

**UNIVERSIDADE DE LISBOA**  
**INSTITUTO SUPERIOR TÉCNICO**

**On the Modelling of Oscillating Foils for Wave Propulsion**

**Diogo Batalha Silva Lopes**

**Supervisor: Doctor José Alberto Caiado Falcão de Campos**  
**Co-Supervisors: Doctor António José Nunes de Almeida Sarmento**  
**Doctor Guilherme Nuno Vasconcelos Beleza Vaz**

**Thesis approved in public session to obtain the PhD Degree in**  
**Mechanical Engineering**

**Jury final classification: Pass**



**UNIVERSIDADE DE LISBOA**  
**INSTITUTO SUPERIOR TÉCNICO**

**On the Modelling of Oscillating Foils for Wave Propulsion**

Diogo Batalha Silva Lopes

**Supervisor:** Doctor José Alberto Caiado Falcão de Campos

**Co-Supervisors:** Doctor António José Nunes de Almeida Sarmento  
Doctor Guilherme Nuno Vasconcelos Beleza Vaz

Thesis approved in public session to obtain the PhD Degree in Mechanical Engineering

**Jury final classification: Pass**

**Jury**

**Chairperson:** Doctor José Carlos Fernandes Pereira, Instituto Superior Técnico, Universidade de Lisboa

**Members of Committee:**

Doctor Sverre Steen, Faculty of Engineering, Norwegian University of Science and Technology, Norway

Doctor José Alberto Caiado Falcão de Campos, Instituto Superior Técnico, Universidade de Lisboa

Doctor Luís Manuel de Carvalho Gato, Instituto Superior Técnico, Universidade de Lisboa

Doctor Luís Rego da Cunha Eça, Instituto Superior Técnico, Universidade de Lisboa

Doctor Matthew Spencer Folley, School of Natural and Built Environment, Queen's University Belfast, UK

**Funding Institutions:**

Fundação para a Ciência e Tecnologia  
Instituto Superior Técnico  
WavEC – Offshore Renewables



# Resumo

O presente trabalho investiga métodos teóricos e numéricos CFD para modelação de um conceito não-tradicional de propulsão para veículos marítimos que envolve perfis hidrodinâmicos oscilantes. Na forma mais simples deste sistema, o perfil oscila com movimentos de arfagem e cabeceio que, quando devidamente configurados, convertem o movimento relativo entre o perfil e o fluido numa força propulsiva. Vários protótipos de veículos com propulsores deste tipo foram já implementados com sucesso, demonstrando o mérito do conceito. A par dos esforços para desenvolver veículos práticos, tem havido um grande volume de investigação, mais teórica, visando melhorar os valores actuais de força propulsiva e rendimento. Embora a investigação principal seja em sistemas activos, onde os perfis são movidos por actuadores, também têm sido estudados dispositivos passivos, onde os perfis são activados pelas ondas. Nestes sistemas os perfis oscilam livremente com movimentos controlados por um sistema de molas. Uma melhoria promissora deste conceito envolve a combinação de dois perfis em *tandem*, um a vante e outro a ré, onde o aumento do rendimento é conseguido através da utilização da energia da esteira do perfil de vante pelo de ré. Embora os resultados tenham demonstrado que esta configuração tem potencial para uma melhoria do desempenho, o problema da selecção apropriada dos parâmetros permanece, em grande medida, uma questão em aberto.

O ponto de partida para o trabalho apresentado nesta tese foi a ideia de que uma configuração de perfis em *tandem* poderia ser utilizada com ondas, para se tornar uma solução prática a ser aplicada em veículos marítimos autónomos propulsionados a energia renovável. Esta tese foca-se no propulsor activo, um passo intermédio para abordar o propulsor com ondas. Sistemas com um perfil isolado e a combinação de dois perfis em *tandem* são estudados para três configurações progressivamente mais complexas, considerando os perfis i) em domínio infinito, ii) submersos e iii) com ondas incidentes.

Na primeira parte desta tese é proposto um modelo semi-analítico para um perfil bidimensional que se desloca a uma velocidade constante e com movimentos harmónicos verticais e de rotação em torno de um eixo transversal. O modelo baseia-se na teoria clássica dos perfis delgados, em particular na abordagem da teoria não-estacionária de Theodorsen. A formulação linear clássica, que é limitada a pequenas oscilações, é modificada neste trabalho para permitir a sua aplicação a oscilações com grandes amplitudes, que implicam grandes ângulos de incidência aparente do escoamento relativo ao perfil. O modelo é complementado para incluir efeitos de envergadura finita, usando a teoria da linha sustentadora, e correcções viscosas quase-estacionárias usando fórmulas empíricas para perfis simétricos NACA. É também estendido para permitir a simulação dos efeitos causados pela presença de uma superfície livre, e por ondas incidentes, adaptando teorias já publicadas. Adicionalmente, é proposto um modelo inovador para captar os principais processos físicos que actuam na configuração de perfis em *tandem*. Os modelos permitem uma previsão das forças horizontais e verticais que actuam no perfil e também do momento, para as várias configurações paramétricas.

A segunda parte deste trabalho investiga o mesmo problema do perfil oscilante com modelação numérica utilizando o código ReFRESCO, baseado em técnicas de dinâmica de fluidos computacional (CFD). Os processos físicos envolvidos no escoamento e na dinâmica do perfil são modelados por equações diferenciais de Navier-Stokes para a conservação da massa e da quantidade de movimento. Nesta abordagem, o primeiro passo para obter uma solução numérica é a discretização do domínio geométrico definindo uma malha numérica composta por células. As equações são aplicadas ao centro de cada célula, estabelecendo a sua relação com as adjacentes. São discretizadas num sistema de equações algébricas que depois é resolvido pelo código iterativamente para obter uma solução numérica. Finalmente são

utilizadas ferramentas de pós-processamento para analisar os resultados numéricos. A precisão dos resultados é avaliada através de procedimentos de verificação e validação. A nível da codificação, verifica-se se os algoritmos são adequados, e a nível de simulação, são estimados os erros iterativos, os erros de precisão digital e os erros de discretização. Finalmente o modelo é validado com dados experimentais. O presente trabalho começa por definir o domínio computacional e gerar as malhas não-estruturadas com zonas de refinamento progressivo junto do perfil. São depois escolhidas as condições de fronteira e iniciais. Para completar a descrição dos fenómenos físicos referentes a este problema específico, são introduzidos modelos para a turbulência, para a superfície livre, para a geração de ondas e para o movimento do perfil. A turbulência é modelada com o modelo  $k-\omega$  SST e a superfície livre é modelada através duma equação de transporte para a fracção de volume do fluido (VOF). A geração de ondas usa a teoria de 5ª ordem de Stokes e uma zona de absorção de ondas junto dos limites do domínio, dependente do caso respectivo. A modelação do movimento do perfil é feita através de um método de deformação da malha (DG) com controlo de deformação através do método das funções de base radiais (RBF), que mostrou ser adequado para resolver este problema hidrodinâmico. Para obter a solução o código usa o algoritmo iterativo SIMPLE com uma linearização com o método de Picard, tratando as equações de forma segregada. O critério para o erro iterativo é definido com uma norma de infinito, a integração no tempo utiliza um método implícito de segunda ordem, e a discretização da equação de transporte das várias quantidades é também de segunda ordem, com excepção da convecção na turbulência que é de primeira ordem.

Os resultados do método semi-analítico, para a força propulsiva média e rendimento, são comparados com dados respectivos disponíveis na literatura, obtidos a partir de métodos numéricos e testes laboratoriais. A comparação mostra boa concordância na gama de frequências correspondente ao regime propulsivo dos perfis oscilantes. Foram obtidas discrepâncias máximas para a força de propulsão média de 4% a 9% nos casos mais simples e até 20% para os casos de maior complexidade. Em particular, o resultado do modelo proposto para a configuração com os perfis em *tandem* mostra uma boa concordância com os dados publicados, permitindo a identificação das diferentes combinações de parâmetros favoráveis e desfavoráveis ao desempenho e gamas de alto e baixo desempenho. Foi possível obter valores da força propulsiva média da combinação de perfis em *tandem* quase três vezes superior aos de um perfil isolado. Os resultados do modelo numérico são analisados, em primeiro lugar quantificando o erro de modelação através de procedimentos de verificação e validação; e em segundo lugar interpretando fisicamente o escoamento e as forças hidrodinâmicas, comparando com os dados publicados disponíveis. Foram obtidos resultados com boa precisão, com erros de modelação relativos às forças médias de propulsão e rendimento de 15%.

A investigação da dinâmica dos vórtices na esteira interacção e no caso do perfil em tandem da interacção do perfil de ré com a esteira do perfil de vante através da visualização dos campos de velocidade e vorticidade permite uma compreensão dos processos e efeitos envolvidos e traçar estratégias para melhoria do desempenho destes sistemas. Os resultados globais sugerem que o modelo semi-analítico tem vantagens de engenharia, uma vez que a sua simplicidade permite a fácil exploração de diferentes configurações. Capturando a física principal envolvida, permite a optimização do projecto com possíveis aplicações no sistema de controlo para o desenvolvimento do conceito de propulsão com perfis passivos em ondas.

O código ReFRESCO demonstrou ser uma ferramenta capaz de fornecer resultados precisos para os casos mais complexos do problema da propulsão com perfis oscilantes e de proporcionar uma compreensão abrangente e detalhada da dinâmica do escoamento. Este estudo ilustra as vantagens da utilização complementar do modelo semi-analítico simples com um modelo CFD. A simples implementação e a rápida simulação dos tempos de execução dos primeiros torna viável a exploração dos parâmetros e das configurações do sistema, enquanto que a ferramenta numérica permite a obtenção de detalhes sobre a dinâmica do escoamento e resultados mais precisos para os casos de interesse. A investigação actual pode ser desenvolvida em trabalhos futuros de modo a incluir a modelação do propulsor com um perfil oscilante passivo, controlado por molas, em ondas.

**Keywords:** Modelação de Hidrofólios Oscilantes; Propulsão com Ondas; Interação na Esteira de Fólios em Tandem; Teoria Linear Não-Estacionária de Perfis Delgados; CFD ReFRESCO



# Abstract

The present work investigates theoretical and CFD numerical methods to model a non-conventional marine vessel propulsion concept involving oscillating hydrofoils. Two configurations are considered, an active oscillating foil propulsor and an enhancement of this concept using two foils in tandem to achieve higher propulsive performance. Infinite domain, free-surface and incident waves test cases are addressed.

In the first part of this work a semi-analytical model is presented for a 2D hydrofoil that travels at constant speed, undergoing heaving and pitching oscillations, based on classical thin airfoil 2D theory and on Theodorsen unsteady theory approach. The classical linear formulation is extended to allow for the application to large heave and pitching amplitude oscillations and flow incident angles. The model is complemented to include finite span effects, and quasi-steady viscous corrections. It is also extended to allow the simulation of the effects due to the presence of a free-surface, and incident waves. An innovative analytical model tool is proposed to capture the main physical processes acting on the tandem foil arrangement.

The second part of this work investigates the oscillating foil problem with numerical modelling using the CFD solver ReFRESKO, that uses a RANS approach to achieve high accuracy and allows flow visualization. In particular, a deforming grid method is used for body motion modelling, enabling the simulation of cases with large motions. Turbulence, free-surface, and wave models provided in ReFRESKO are employed. The appropriate computational domain, grid layout, boundary conditions and numerical settings are investigated.

Results of the semi-analytical model for mean thrust and propulsive efficiency are compared with available published numerical and experimental data, with good agreement within the propulsive foil regime range of frequencies. Maximum discrepancies from 4% to 9% are obtained for the simpler cases and up to 20% for the more complex cases. The outcome of the simulations with the CFD numerical model is analysed through verification and validation procedures. The results allow physical interpretation of the flow and forces and comparison with other sources. Results with good accuracy are obtained, with modelling errors for mean thrust coefficient up to 15%. The tandem foil configuration, if properly optimized, is found to increase single foil's thrust by almost three times.

The overall results suggest that the semi-empirical model has engineering advantages, as its simplicity allows easy exploration of different configurations. By capturing the main physics involved, it allows for design optimization with possible applications to the control system for the passive-type wave foil propulsion concept development. The ReFRESKO code showed to be a tool capable of providing accurate results for the most complex cases of the oscillating foil propulsor problem and of providing a comprehensive and generic understanding of the flow dynamics. The straightforward implementation and quick simulation running times of the first allows identifying the main relevant parameters and response curves, as well as cases of interest, while with the CFD numerical tool it is possible to do the detailed study of the flow, providing information for further refinement of the semi-analytical model.

**Keywords:** Oscillating Hydrofoils Modelling; Wave Propulsion; Tandem Foil Wake Interaction; Unsteady ThinWing Linear Theory; CFD ReFRESKO



# Acknowledgments

I deeply thank my supervisor Professor Falcão de Campos, who has supervised my scientific work during these years, and whose guidance, patience, and availability, with all the numerous enriching discussions we shared, was an inspiring example and great support.

My sincere gratitude to my co-supervisor Professor António Sarmento, with whom I studied and work for over 20 years, and whose unconditional support, care and confidence was very important on many occasions of my life, always providing me all sorts of opportunities.

I gratefully thank my good friend and co-supervisor Dr. Guilherme Vaz, for the guidance, discussions, encouragement, and trust, without whom the completion of this work would not have been possible. His personal support and help with technical expertise and experience, team and resources were inestimable.

I also thank Prof. Luís Gato and Prof. António Pascoal from Instituto Superior Técnico for the chance to learn from them and their help with my thesis. I also thank Prof. Relógio Ribeiro and Prof. Virgínia Infante for the relevant technical advice and help during this work.

Special thanks to my colleagues at WavEC and BlueOasis, Manuel Rentschler, Sebastien Lemaire, António Maximiano, Bénédicte Demergues for the valuable suggestions and help with ReFRESKO, in grid generation, using the graphic tools as well all interesting discussions over CFD and oscillating foils. My gratefulness to my colleagues Pedro Pires, Paulo Chainho and Erica Cruz from WavEC with whom I have shared great and tough moments, always available to help, with perseverance and good spirit.

I wish to extend my gratitude to WavEC – Offshore Renewables and their staff, for providing all the opportunities and assistance during this work.

I acknowledge Dr. Juana Fortes and Eng. Ana Mendonça from the Núcleo de Portos e Estruturas (NPE) of the Laboratório Nacional de Engenharia Civil (LNEC) for the opportunities and assistance. I also acknowledge the Institute for System and Robotics (ISR) Lisboa for the assistance.

I acknowledge the Fundação para a Ciência e a Tecnologia and the Instituto Superior Técnico for the financial support through grants.

I would like to acknowledge to the IRIDIS High Performance Computing Facility, and associated support services at the University of Southampton, in the completion of this work.

I wish to deeply thank Pema Wangyal Rinpoche for inspiring me to do this PhD and his invaluable support and advice.

My gratefulness to my good friends Fernando Santos and Alberto Ramos for their encouragement, confidence, and support.

My thanks to Catarina Rodrigues for her contribution to this work.

I cannot be grateful enough to my parents, Carlos and Lúcia, to my sister Andreia, and all my family for so much support and love throughout this PhD and my life.

Finally, and foremost, my deepest gratitude goes to my partner Maria João, for unwavering support, inspiration and motivation. Your patience, insight, joy, and love have pushed me forwards in all times and allow me to find solutions when I thought it was not possible. I also thank her family, for all the support.



# Contents

<b>RESUMO</b>	<b>III</b>
<b>ABSTRACT</b>	<b>VII</b>
<b>ACKNOWLEDGMENTS</b>	<b>IX</b>
<b>CONTENTS</b>	<b>XI</b>
<b>INDEX OF FIGURES</b>	<b>XV</b>
<b>INDEX OF TABLES</b>	<b>XXIII</b>
<b>NOMENCLATURE</b>	<b>XXVII</b>
<b>CHAPTER 1 INTRODUCTION</b>	<b>1</b>
1.1 Motivation	1
1.2 State of the Art	2
1.2.1 Full-Scale Vessels and Notable Model Boats	2
1.2.2 Theoretical and Experimental Studies on Foil Propulsion	6
1.3 Thesis Outline	9
1.4 Main Contributions	10
<b>CHAPTER 2 SEMI-ANALYTICAL MODELLING</b>	<b>13</b>
2.1 Oscillating Foil Propulsion Overview	13
2.2 Classical Theory	16
2.3 Single Oscillating Foil	20
2.3.1 Drag	20
2.3.2 Free-Surface Effects	24
2.3.3 Incident Wave Effects	26
2.3.4 Propulsive Force and Efficiency	29
2.4 Tandem Oscillating Foils	31
2.5 Model Implementation	33
<b>CHAPTER 3 SEMI-ANALYTICAL MODEL VALIDATION</b>	<b>35</b>
3.1 Methods	35

<b>3.2</b>	<b>Comparison with Published Data</b>	<b>37</b>
3.2.1	Single Foil in an Infinite Domain	37
3.2.2	Submerged Single Foil with Incident Waves	42
3.2.3	Tandem Foils	48
 <b>CHAPTER 4 CFD NUMERICAL MODELLING</b>		<b>53</b>
<b>4.1</b>	<b>CFD Background</b>	<b>53</b>
<b>4.2</b>	<b>CFD Solver ReFRESKO</b>	<b>54</b>
4.2.1	Fundamentals of the Governing Equations	54
4.2.2	Numerical Discretization	56
4.2.3	Free-Surface and Waves Models	57
4.2.4	Solution Methodologies	57
4.2.5	High-Performance Computing (HPC)	59
<b>4.3</b>	<b>Grid Generation</b>	<b>59</b>
4.3.1	Computational Domain and Grid Layout	60
<b>4.4</b>	<b>Numerical Setup</b>	<b>62</b>
4.4.1	Boundary Conditions	62
4.4.2	Body Motion	64
4.4.3	Numerical Settings	64
<b>4.5</b>	<b>Verification &amp; Validation</b>	<b>65</b>
4.5.1	Numerical Error	66
4.5.2	Modelling Error	67
 <b>CHAPTER 5 OSCILLATING FOILS THRUSTERS IN INFINITE DOMAIN</b>		<b>69</b>
<b>5.1</b>	<b>Single Foil</b>	<b>69</b>
5.1.1	Small Oscillations – Grid Study	69
5.1.2	Large Oscillations – Validation & Verification Study	73
5.1.3	High-Performance – Forces and Flow Analysis	78
5.1.4	Three Dimensional Case – Span Effects Analysis	83
<b>5.2</b>	<b>Tandem Foils</b>	<b>84</b>
5.2.1	Low-Performance – Flow and Forces Analysis	84
5.2.2	High-Performance – Flow and Forces Analysis	88
 <b>CHAPTER 6 OSCILLATING FOIL THRUSTERS WITH FREE-SURFACE AND WAVES</b>		<b>93</b>
<b>6.1</b>	<b>Single Foil</b>	<b>93</b>
6.1.1	Free-Surface – 2D Study	93
6.1.2	Free-Surface – 3D Study	96
6.1.3	Incident Waves – No Oscillations Study	98
6.1.4	Incident Waves – Large Oscillations Study	101
<b>6.2</b>	<b>Tandem Foils</b>	<b>104</b>
6.2.1	Free-Surface	104
6.2.2	Incident Waves	107
 <b>CHAPTER 7 CONCLUSIONS</b>		<b>111</b>
<b>7.1</b>	<b>Main Conclusions</b>	<b>111</b>
7.1.1	Introduction	111
7.1.2	Semi-Analytical Model	111
7.1.3	CFD Numerical Model	112
7.1.4	Findings Related to Flow Dynamics and Performance	113

<b>7.2 Future Work</b>	<b>115</b>
<b>REFERENCES</b>	<b>117</b>
<b>APPENDIX A 2D HYDROFOIL POTENTIAL FLOW THEORY</b>	<b>127</b>
<b>APPENDIX B WU'S THEORY FORMULATION</b>	<b>133</b>
<b>APPENDIX C TANDEM FOIL MODEL FORMULATION</b>	<b>137</b>
<b>APPENDIX D CHAPTER 3 CASES</b>	<b>141</b>
<b>APPENDIX E CHAPTER 5 CASES</b>	<b>143</b>
<b>APPENDIX F CHAPTER 6 CASES</b>	<b>145</b>
<b>APPENDIX G SUMMARY OF RESULTS</b>	<b>147</b>
<b>APPENDIX H SUPPLEMENTARY MATERIAL</b>	<b>149</b>



# Index of Figures

Figure 1.1: Kystfangst (Dybdahl, 1988).....	3
Figure 1.2: WDPS ship speed trial (Terao, 1991). ....	3
Figure 1.3: The Wave Glider a) from below and b) principles of operation (Manley, 2010). .....	4
Figure 1.4: Suntory Mermaid II a) The catamaran b) Physical structure (Zhenjiang, 2016).4	
Figure 1.5: a) MS Triade b) O-foil propeller (Cibalia, 2021). ....	5
Figure 1.6: a) The AutoNaut and b) an example of Linden and Jakobsen techniques (Bowker, 2015).....	5
Figure 1.7: WDPS new ASV model.....	5
Figure 1.8: FLEUR a) Underwater view of forward and aft foil setup and b) general arrangement (Bowker, 2015).....	6
Figure 1.9: ASV's performance (Bowker, 2015).....	6
Figure 1.10: Cetacean propulsion (Coffey, 1977).....	7
Figure 2.1: Types of oscillating foil motions; a) pitch, b) heave, c) combined heave and pitch. ....	13
Figure 2.2: Flapping foil kinematics heaving and pitching in a steady flow; a) power generation, b) feathering, c) thrust generation.....	14
Figure 2.3: Simplified example of the wake dynamics with streamwise velocity field perturbation; a) natural BvK wake street b) reverse BvK wake street. ....	14
Figure 2.4: Instantaneous vorticity (left column, $s^{-1}$ ) and mean flow (time averaged horizontal velocity, right column, m/s) of a pitching foil for different dimensionless amplitudes $A_D$ (trailing edge excursion/maximum thickness) at $Re = 1773$ ; a) natural BvK wake. b) natural to reverse BvK transition. c) reverse BvK wake, drag regime. d) reverse BvK wake, propulsion regime. e) deflected reverse BvK, asymmetric regime (Godoy-Diana et al., 2008). ....	15
Figure 2.5: Model coordinate system. ....	17
Figure 2.6: Flattened vortex wake on an oscillating foil. ....	18
Figure 2.7: 3D foil with tip vortex effect. ....	20
Figure 2.8: Lift coefficient reduction with aspect ratio $\Lambda$ . Comparison between Prandtl lifting-line theory, Medan numerical model (van Dyke, 1975) and DuCane (1972) correction, adopted in this work. ....	21
Figure 2.9: Zero-lift profile drag coefficient $C_{Dp0}$ for a NACA0012 foil at low Reynolds numbers. Comparison between experimental data from Ohtake, Sunada, Abbot, and other authors (Ohtake et al., 2007) and the present model, adapted from Hoerner (1965). Blasius (laminar), Prandtl-von Kármán (turbulent-low Reynolds), Prandtl-Schlichting (turbulent-high Reynolds) methods for a flat plate are also plotted. ....	22
Figure 2.10: Separation effect; a) foil exceeds static stall angle, flow reversals appear in boundary layer, b) flow separation at leading edge, formation of a vortex c) vortex convects along the chord, inducing extra lift, d) lift stall, flow enters in full separation state. Adapted from Leishman (2002).....	23

Figure 2.11: Comparison with experimental profile drag coefficient $C_{D,p}$ curve for different angles of attack, for a steady inflow NACA0012 profile at $Re = 4 \times 10^4$ (Ohtake et al., 2007).	24
Figure 2.12: Example of the time history of the free-surface elevation, generated by a travelling and oscillating fully immersed hydrofoil.	24
Figure 2.13: Lift loss varying with non-dimensional depth $d^*$ and Froude number $Fr$ . Comparison between present results and Hough (1969).	25
Figure 2.14: Radiated waves generation by a foil near the surface.	26
Figure 2.15: Incident waves model coordinate system.	27
Figure 2.16: Average horizontal force $F_x$ , total wave resistance $R_w$ and thrust $T$ for a fixed foil $c = 0.328$ m in incident head waves with $Fr = 0.55$ , $d^* = 1.5$ , $\alpha_0^* = \pi/(20ka)$ . Comparison of present method with Isshiki (1982) results.	29
Figure 2.17: Forces acting on the foil.	30
Figure 2.18: Simplified example for the tandem foil wake pattern. $U$ , $U_{for}$ and $U_{aft}$ are the foil advance velocity, fore foil vortex advection velocity and aft foil vortex advection velocity, respectively.	31
Figure 2.19: Flowchart of the present model.	33
Figure 3.1: Number of wave occurrences distribution with the energy period $T_e$ , for waves with significant height $H_s > 0.5$ m, at Leixões, coast of Portugal (WavEC, 2015).	36
Figure 3.2 View of the test carriage, which oscillates the foil in heave and pitch, while moving horizontally in a towing tank (Read et al., 2003)	37
Figure 3.3: Amplitude of lift coefficient of a NACA0012 section, in low-amplitude flapping motion $h_0/c = 0.1$ , $\theta_0 = 10^\circ$ , $\psi = 90^\circ$ , $b^* = 0$ , in infinite domain. Present method results against Filippas numerical with and without the contribution of added mass effects.	38
Figure 3.5 Average thrust coefficient varying with pitch amplitude and Strouhal number for a NACA0012 foil with $\Lambda = 12.5$ , $h_0/c = 1.0$ , $b^* = -1/3$ , $\psi = 90^\circ$ . Present method (red -) compared to Filippas & Belibassakis (2014b) (blue +) and Read et al. (2003) (black o) results. For $St = 0.45$ curve the uncertainty found by Schouveiler (2005) is added.	39
Figure 3.6 Vertical force $C_y$ and thrust coefficients $C_T$ for a NACA0012 hydrofoil with $\Lambda = 12.5$ , $St = 0:3$ , $h_0/c = 0.75$ , $\theta_0 = 23.3^\circ$ , $b^* = -1/3$ and $\psi = 90^\circ$ . Present method (red -) compared to Filippas & Belibassakis (2014b) (blue -) and Schouveiler et al. (2005) (black o) results.	40
Figure 3.7: a) Average thrust coefficient and b) propulsive efficiency varying with Strouhal number for 3 values of maximum angle of attack, for a NACA0012 hydrofoil $\Lambda = 12.5$ with $h_0/c = 0.75$ (first row) and $h_0/c = 1.0$ (second row), $b^* = -1/3$ , $\psi = 90^\circ$ , present method (colour line), compared with experiment (o) (Read, 2005).	41
Figure 3.8: Average thrust coefficient and propulsive efficiency for a NACA0012 foil $\alpha_0 = 15^\circ$ , $b^* = -1/3$ , $\psi = 90^\circ$ , for different heave amplitudes, present method.	42
Figure 3.9: a) Lift loss for different depths and Froude numbers b) Mean wave radiation drag coefficients for the different $k_f$ waves, varying with Froude number, for a NACA0012 section with $\omega_0 = 1.2$ rad/s, $d^* = 1.5$ , $\theta_0 = 15^\circ$ , $b^* = -1/3$ , $\psi = 90^\circ$ , $h_0/c = 1$ , present model results.	42
Figure 3.10: Mean drag coefficients comparison for the wave radiation (total), the profile and the finite span effects, varying with Froude number, for NACA0012 foil with $\omega_0 = 1.2$ rad/s, $d^* = 1.5$ , $\theta_0 = 15^\circ$ , $b^* = -1/3$ , $\psi = 90^\circ$ , $h_0/c = 1$ and $\Lambda = 6$ , present model results.	43
Figure 3.11: Instantaneous vertical $C_y$ and thrust $C_T$ coefficients time series for NACA0015 section with $b^* = -1/3$ , $h_0/c = 1$ , $\theta_0 = 35^\circ$ , $\psi = 90^\circ$ and $\omega_0^2 c/g = 0.25$ at submergence $d^* = 1.28$ , and $Fr = 0.87$ . Comparison of present model (colour) with Silva et al. (2012) (black) results.	44

Figure 3.12: Thrust increase for NACA0012 section at $F_r = 1.5$ with motion parameters $h_0/c = 1$ , $\theta_0 = 35^\circ$ , $\omega_0^2 c/g = 3.55$ . Comparison between results in infinite domain, in calm waters at $d^* = 2.5$ , and in waves $a_0^* = 1.5$ .	45
Figure 3.13: a) Vertical force coefficient and b) thrust coefficients time series comparison for NACA0015 at $F_r = 0.87$ and $d^* = 1.28$ with motion parameters, $h_0/c = 0.6$ , $\theta_0 = 15.65^\circ$ , $\psi = 105^\circ$ with an incident wave with $\omega_0^2 c/g = 0.69$ , $a_0/h_0 = 0.238$ , for two cases: (i), wave phase $\phi w = -180^\circ$ (ii) wave phase $\phi w = 0^\circ$ .	45
Figure 3.14: a) Average thrust coefficient and b) propulsive efficiency versus heave-pitch phase $\psi$ at $F_r = 0.87$ and $d^* = 1.28$ with, $h_0/c = 0.6$ , $\theta_0 = 15.65^\circ$ with an incident wave with $\omega_0^2 c/g = 0.69$ , $a_0/h_0 = 0.238$ , $\phi w = -180^\circ$ .	46
Figure 3.15: a) Average thrust coefficient and b) propulsive versus extended feathering parameter, for at $F_r = 0.87$ and $d^* = 1.71$ , $h_0/c = 0.6$ , $\psi = 40^\circ$ with $\omega_0^2 c/g = 0.69$ , $a_0/h_0 = 0.238$ , $\phi w = -180^\circ$ .	46
Figure 3.16: a) Average thrust coefficient and b) propulsive efficiency versus Froude number for $d^* = 1.28$ and $h_0/c = 0.6$ , $\psi = 40^\circ$ , $\chi = 0.2$ and wave with $\omega_0^2 c/g = 1.5$ , $a_0/h_0 = 0.238$ , $\phi w = -90^\circ$ .	47
Figure 3.17: a) Comparison of the normalized thrust $CT/CT$ and b) normalized vertical force $Cy/CT$ coefficients between the present model results with numerical results (Epps et al., 2016), with $h_{0i}/c = 1$ , $\theta_{0i} = 45^\circ$ , $\psi_i = 90^\circ$ , $\phi_i = 135^\circ$ , $s^* = 8$ , $St = 0.4$ .	48
Figure 3.18: Normalized average thrust coefficient varying with non-dimensional separation and Strouhal number, for inter-foil phase lag $\phi_i = 90^\circ$ , with $h_{0i}/c = 1$ , $\alpha_{0i} = 10^\circ$ , $\psi_i = 90^\circ$ . Comparison of the present model with Muscutt et al. (2017) results.	49
Figure 3.19: Normalized average thrust coefficient varying with inter-foil phase lag, $St = 0.2$ , $s^* = 6$ . Comparison of the present model with Muscutt et al. (2017) results.	50
Figure 3.20: Present model results of the normalized aft foil average thrust in the inter-foil phase lag – separation space, for $St = 0.4$ .	50
Figure 3.21: Normalized average thrust coefficient varying with inter-foil separation distance $s^*$ and Strouhal number, for optimal inter-foil phase lag.	51
Figure 4.1: Cells in a finite volume approach.	55
Figure 4.2: SIMPLE algorithm schematics.	58
Figure 4.3: Hexpress unstructured mesh refinement regions a) around foil and wake, b) close to the foil, c) leading and trailing edge and d) trailing edge.	60
Figure 4.4: GridPro structured grids refinement details a) around foil, b) close to the foil, c) trailing edge and d) foil surface.	61
Figure 4.5: Unstructured Hexpress grid for free-surface or incident wave cases: example of the refinement region used.	61
Figure 4.6: Schematic representation of the 2D computational domain and prescribed boundary conditions, for the infinite domain single foil case.	62
Figure 4.7 Schematic representation of 2D domain with boundary conditions, free-surface and damping zones, for the submerged single foil case (not to scale).	63
Figure 4.8: Grid deformation example in present case. a) single foil b) tandem foils.	64
Figure 4.9: Sources of computational errors.	66
Figure 4.10: Statistical error evaluation (transient state in yellow, statistically converged state in blue).	67
Figure 5.1: Small oscillations test case statistical signal evaluation for simulation with Grid HE_B and $\Delta t_i/\Delta t_f = 4$ , with the discarded transient state in orange and the statistical converged	

state in blue. (a) The horizontal force time series for total iterations and (b) the uncertainty calculated backwards, showing the method of selection of optimal point of transient signal discard. ....	71
Figure 5.2: Statistical error evaluation with number of sampling cycles for 2 simulations with Hexpress grids. Motion parameters $h_0/c = 0.25$ , $\alpha_0 = 15^\circ$ , $\psi = 90^\circ$ , $St = 0.3$ . ....	71
Figure 5.3 Results for 5 simulations using GridPro structured grids (a) average thrust coefficient with experimental data in blue (b) vertical force coefficient (c) moment coefficient. The data points are defined with the grid space refinement ratio $h_i/h_1$ and time refinement ratio $t_i/t_1$ and the uncertainty bar is included. Motion parameters $h_0/c = 0.25$ , $\alpha_0 = 15^\circ$ , $\psi = 90^\circ$ , $St = 0.3$ . ....	71
Figure 5.4: Results for 6 simulations using Hexpress unstructured grids (a) average thrust coefficient with experimental data in blue (b) vertical force coefficient (c) moment coefficient. The data points are defined with the grid space refinement ratio $h_i/h_1$ , time refinement ratio $t_i/t_1$ and the uncertainty bar is included. Motion parameters $h_0/c = 0.25$ , $\alpha_0 = 15^\circ$ , $\psi = 90^\circ$ , $St = 0.3$ . ....	72
Figure 5.5 Average Courant number for grid C and $t_i/t_1 = 2$ . Motion parameters $h_0/c = 1.0$ , $\alpha_0 = 15^\circ$ , $\psi = 90^\circ$ , $St = 0.3$ . ....	74
Figure 5.6: Residuals for the (a) $L_2$ and (a) $L_\infty$ norm for the grid C and $t_i/t_1 = 2$ . Motion parameters $h_0/c = 1.0$ , $\alpha_0 = 15^\circ$ , $\psi = 90^\circ$ , $St = 0.3$ . ....	75
Figure 5.7: Number of used iterations to the equations for (a) vertical velocity and (b) pressure, using the grid C and $t_i/t_1 = 2$ . Motion parameters $h_0/c = 1.0$ , $\alpha_0 = 15^\circ$ , $\psi = 90^\circ$ , $St = 0.3$ . ....	75
Figure 5.8: (a) Residuals averaged over time, for vertical velocity and pressure and (b) average thrust iterative error, for different convergence criteria using the grid C and $t_i/t_1 = 2$ . Motion parameters $h_0/c = 1.0$ , $\alpha_0 = 15^\circ$ , $\psi = 90^\circ$ , $St = 0.3$ . ....	75
Figure 5.9: Large oscillations test case statistical error evaluation for simulation with grid C and $t_i/t_1 = 2$ , with the discarded transient state in orange and the statistical converged state in blue. (a) The thrust coefficient time series for total iterations and (b) the uncertainty calculated backwards, showing the method of selection of optimal point of transient signal discard. ....	76
Figure 5.10: Variation of statistical uncertainty for the average thrust with sampling cycles/periods for grid C and $t_i/t_1 = 2$ simulation. Motion parameters $h_0/c = 1.0$ , $\alpha_0 = 15^\circ$ , $\psi = 90^\circ$ , $St = 0.3$ . ....	76
Figure 5.11: Results for 7 simulations (a) average thrust coefficient with experimental data in blue (b) vertical force coefficient (c) moment coefficient. Motion parameters $h_0/c = 1.0$ , $\alpha_0 = 15^\circ$ , $\psi = 90^\circ$ , $St = 0.3$ . ....	76
Figure 5.12: Example of grid deformation (a) general view and (b) detail of the mesh around the foil. ....	77
Figure 5.13: (a) Average <i>MeshQuality</i> parameter and (b) maximum non-dimensional wall distance $y^+_{max}$ for grid C and $t_i/t_1 = 2$ . Motion parameters $h_0/c = 1.0$ , $\alpha_0 = 15^\circ$ , $\psi = 90^\circ$ , $St = 0.3$ . ....	77
Figure 5.14: Eddy viscosity ratio (log scale) for the single foil in large oscillations case for the simulation with $h_i/h_1 = 2.15$ and $t_i/t_1 = 2.0$ . (a) wake (b) foil boundary layer. Motion parameters $h_0/c = 1.0$ , $\alpha_0 = 15^\circ$ , $\psi = 90^\circ$ , $St = 0.3$ . Laminar flow in dark blue and fully turbulent flow in red. ....	78
Figure 5.15: Variation of statistical uncertainty for the average thrust with sampling cycles/periods for grid C and $t_i/t_1 = 1$ simulation. Motion parameters $h_0/c = 1.0$ , $\alpha_0 = 16.5^\circ$ , $\psi = 90^\circ$ , $St = 0.4$ . ....	79

Figure 5.16: Snapshots of (a) normalized vorticity and (b) normalized velocity fields contours at cycle increments of $t/T = 1/4$ where $T = 1/f$ , for a single foil with motion parameters $h_0/c = 1.0$ , $\alpha_0 = 16.5^\circ$ , $\psi = 90^\circ$ , $St = 0.4$ . Clockwise vorticity is indicated with blue, and anticlockwise with red. In all figures, the vertical lines show the location of 1/3 point pitching axis of the foils. The horizontal lines show the mid foil position as well as the upper and lower limits of heave motion. A video of the vorticity field can be found in the on-line supplementary materials listed in the Appendix H and is entitled ‘Single Foil in Infinite Domain’.....	80
Figure 5.17: Detail of vorticity close to the foil for the snapshots of Figure 5.16. Motion parameters $h_0/c = 1.0$ , $\alpha_0 = 16.5^\circ$ , $\psi = 90^\circ$ , $St = 0.4$ .....	81
Figure 5.18: (a) Thrust and vertical forces coefficient and (b) moment coefficient instantaneous values for the single foil in high frequency test case. The four-time instants marked correspond to the snapshots of Figure 5.16. Motion parameters $h_0/c = 1.0$ , $\alpha_0 = 16.5^\circ$ , $\psi = 90^\circ$ , $St = 0.4$ .....	81
Figure 5.19: Eddy viscosity ratio (log scale) for the single foil in the high-performance test case. Motion parameters $h_0/c = 1.0$ , $\alpha_0 = 16.5^\circ$ , $\psi = 90^\circ$ , $St = 0.4$ . Laminar flow in dark blue and fully turbulent flow in red.....	82
Figure 5.20: Snapshots of (a) normalized vorticity and (b) normalized velocity fields contours at cycle increments of $t/T = 1/4$ where $T = 1/f$ , for a tandem foil low performance case with motion parameters $h_0/c = 1.0$ , $\alpha_0 = 6.5^\circ$ , $\psi = 90^\circ$ , $St = 0.4$ , $s^* = 8$ , $\phi_t = 270^\circ$ . Clockwise vorticity is indicated with blue, and anticlockwise with red. In all figures, the vertical lines show the location of 1/3 point pitching axis of the foils. The horizontal lines show the mid foil position and the upper and lower limits of heave motion. ....	86
Figure 5.21: (a) Thrust and vertical coefficients and (b) moment coefficient instantaneous values for the forward foil and aft foil in the tandem low performance test case. The four time instants marked correspond to the snapshots of Figure 5.20. Motion parameters $h_0/c = 1.0$ , $\alpha_0 = 6.5^\circ$ , $\psi = 90^\circ$ , $St = 0.4$ , $s^* = 8$ , $\phi_t = 270^\circ$ .....	87
Figure 5.22: Eddy viscosity ratio (log scale) for the tandem foil in low performance case. Motion parameters $h_0/c = 1.0$ , $\alpha_0 = 6.5^\circ$ , $\psi = 90^\circ$ , $St = 0.4$ , $s^* = 8$ , $\phi_t = 270^\circ$ . Laminar flow in dark blue and fully turbulent flow in red.....	87
Figure 5.23: Snapshots of (a) vorticity and (b) normalized velocity fields contours at cycle increments of $t/T = 1/4$ where $T = 1/f$ , for a tandem foil high-performance case with motion parameters $h_0/c = 1.0$ , $\alpha_0 = 10^\circ$ , $\psi = 90^\circ$ , $St = 0.4$ , $s^* = 8$ , $\phi_t = 180^\circ$ . Clockwise vorticity is indicated with blue, and anticlockwise with red. In all figures, the vertical lines show the location of 1/3 point pitching axis of the foils. The horizontal lines show the mid foil position and the upper and lower limits of heave motion. A video of the vorticity field can be found in the on-line supplementary materials listed in the Appendix H and is entitled ‘Tandem Foil in Infinite Domain’.....	89
Figure 5.25: Example of grid deformation (a) general view and (b) detail of the mesh around the aft foil. ....	91
Figure 5.26: Eddy viscosity ratio (log scale) for the high-performance tandem foil case. (a) wake (b) Aft foil boundary layer. Motion parameters $h_0/c = 1.0$ , $\alpha_0 = 10^\circ$ , $\psi = 90^\circ$ , $St = 0.4$ , $s^* = 8$ , $\phi_t = 180^\circ$ . Laminar flow in dark blue and fully turbulent flow in red.....	91
Figure 6.1: Snapshots of (a) vorticity and (b) normalized velocity fields contours at cycle increments of $t/T = 1/4$ where $T = 1/f$ , for a submerged foil in large oscillations with motion parameters $h_0/c = 1.0$ , $\alpha_0 = 15^\circ$ , $\psi = 90^\circ$ , $St = 0.3$ , $d^* = 1.25$ . Clockwise vorticity is indicated with blue, and anticlockwise with red. In all figures, the vertical lines show the location of 1/3 point pitching axis of the foils. The horizontal lines show the mid foil position and the upper and lower limits of heave motion. A video of the vorticity field can be found in the on-line supplementary materials listed in the Appendix H and is entitled ‘Single Foil with Free-Surface’.....	94

Figure 6.3: Eddy viscosity ratio (log scale) for the submerged single foil case: (a) wake (b) foil boundary layer. Motion parameters $h_0/c = 1.0$ , $\alpha_0 = 15^\circ$ , $\psi = 90^\circ$ , $St = 0.3$ , $d^* = 1.25$ . Laminar flow in dark blue and fully turbulent flow in red.....	96
Figure 6.4: Grid refinement near the free-surface for a wave with non-dimensional wavelength $ka = 0.118$ and amplitude $a_0/a = 1.5$ : (a) Normalized vorticity (b) Eddy viscosity ratio (turbulence) (c) Turbulent kinetic energy $k$ (d) Dissipation rate per unit kinetic energy $\omega$ .....	96
Figure 6.6: Snapshots of (a) vorticity and (b) normalized velocity fields contours at cycle increments of $t/T = 1/4$ where $T = 1/f$ , for a fixed foil in incident waves with parameters $a_0^* = 1.5$ , $d^* = 2.5$ . The blue indicates the clockwise vorticity, and the red the anticlockwise vorticity.....	99
Figure 6.7: (a) Thrust and vertical coefficient and (b) moment coefficient for the fixed foil in incident waves test case. The four time instants marked correspond to the snapshots of Figure 5.20 $t/T = 0, 0.25, 0.5, 0.75$ . Parameters are $a_0^* = 1.5$ , $d^* = 2.5$ .....	100
Figure 6.8: Wave height at $x = 1/3$ -chord for the fixed foil in waves test case. The four time instants marked correspond to the snapshots of Figure 5.20 $t/T = 0, 0.25, 0.5, 0.75$ . Parameters are $a_0^* = 1.5$ , $d^* = 2.5$ .....	100
Figure 6.9: Grid refinement for an incident wave with a fixed foil a) general view b) detail near the foil. Parameters are $a_0^* = 1.5$ , $d^* = 2.5$ .....	100
Figure 6.10: Eddy viscosity ratio (log scale) for the submerged fixed single foil case: (a) wake (b) foil boundary layer. Parameters are $a_0^* = 1.5$ , $d^* = 2.5$ . Laminar flow in dark blue and fully turbulent flow in red.....	101
Figure 6.11: Snapshots of (a) vorticity and (b) normalized velocity fields contours at cycle increments of $t/T = 1/4$ where $T = 1/f$ , for a single foil in incident waves with motion and wave parameters $h_0/c = 0.6$ , $\theta_0 = 15.2^\circ$ , $\psi = 90^\circ$ , $\omega_0^2 c/g = 0.69$ , $d^* = 1.28$ , $a_0/h_0 = 0.238$ . Clockwise vorticity is indicated with blue, and anticlockwise with red. In all figures, the vertical lines show the location of $1/3$ point pitching axis of the foils. The horizontal lines show the mid foil position and the upper and lower limits of heave motion. A video of the vorticity field can be found in the on-line supplementary materials listed in the Appendix H and is entitled ‘Single Foil in Waves’.....	102
Figure 6.12: (a) Thrust and vertical and (b) moment coefficients instantaneous values for the forward foil and aft foil in tandem test case. The four time instants marked correspond to the snapshots of Figure 6.11 $t/T = 0, 0.25, 0.5, 0.75$ . Motion and wave parameters $h_0/c = 0.6$ , $\theta_0 = 15.2^\circ$ , $\psi = 90^\circ$ , $\omega_0^2 c/g = 0.69$ , $d^* = 1.28$ , $a_0/h_0 = 0.238$ .....	103
Figure 6.13: Eddy viscosity ratio (log scale) for the single foil in incident waves case. Motion and wave parameters $h_0/c = 0.6$ , $\theta_0 = 15.2^\circ$ , $\psi = 90^\circ$ , $\omega_0^2 c/g = 0.69$ , $d^* = 1.28$ , $a_0/h_0 = 0.238$ . Laminar flow in blue and turbulent flow in red.....	103
Figure 6.14: Snapshots of (a) vorticity and (b) normalized velocity fields contours at cycle increments of $t/T = 1/4$ where $T = 1/f$ , for a tandem foil in large oscillations with motion parameters $h_0/c_i = 1.0$ , $\alpha_{0i} = 10^\circ$ , $\psi_i = 90^\circ$ , $St = 0.4$ , $d^* = 2.5$ , $s^* = 8$ , $\phi_t = 180^\circ$ . Clockwise vorticity is indicated with blue, and anticlockwise with red. In all figures, the vertical lines show the location of $1/3$ point pitching axis of the foils, and the horizontal lines show the mid foil position and the upper and lower limits of heave motion. A video of the vorticity field can be found in the on-line supplementary materials listed in the Appendix H and is entitled ‘Tandem Foil with Free-Surface’.....	105
Figure 6.15. (a) Thrust and vertical and (b) moment coefficients instantaneous values for the forward foil and aft foil in submerged tandem test case. The four time instants marked correspond to the snapshots of Figure 6.14 $t/T = 0, 0.25, 0.5, 0.75$ . Motion parameters $h_0/c_i = 1.0$ , $\alpha_{0i} = 10^\circ$ , $\psi_i = 90^\circ$ , $St = 0.4$ , $d^* = 2.5$ , $s^* = 8$ , $\phi_t = 180^\circ$ .....	106

Figure 6.16: Eddy viscosity ratio (log scale) for the submerged tandem foil case. Motion parameters  $h_0/c_i = 1.0$ ,  $\alpha_{0i} = 10^\circ$ ,  $\psi_i = 90^\circ$ ,  $St = 0.4$ ,  $d^* = 2.5$ ,  $s^* = 8$ ,  $\phi_t = 180^\circ$ . Laminar flow in blue and turbulent flow in red. .... 106

Figure 6.17: Snapshots of (a) vorticity and (b) normalized velocity fields contours at cycle increments of  $t/T = 1/4$  where  $T = 1/f$ , for a tandem foil oscillating in waves with motion parameters  $h_0/c_i = 1.0$ ,  $\chi_{0i} = 0.41$ ,  $\psi_i = 90^\circ$ ,  $\omega_0^2 c/g = 0.24$ ,  $s^* = 8$ ,  $\phi_t = 180^\circ$ ,  $d^* = 2.5$ ,  $a_0/h_o = 0.75$ ,  $\phi_w = -90^\circ$ . Clockwise vorticity is indicated with blue, and anticlockwise with red. In all figures, the vertical lines show the location of 1/3-point pitching axis of the foils. The horizontal lines show the mid foil position and the upper and lower limits of heave motion. A video of the vorticity field can be found in the on-line supplementary materials listed in the Appendix H and is entitled ‘Tandem Foil in Waves’..... 108

Figure 6.18: (a) Thrust and vertical and (b) moment coefficients instantaneous values for the forward foil and aft foil in tandem in waves test case. The four time instants marked correspond to the snapshots of Figure 6.17  $t/T = 0, 0.25, 0.5, 0.75$ . Motion parameters  $h_0/c_i = 1.0$ ,  $\chi_{0i} = 0.41$ ,  $\psi_i = 90^\circ$ ,  $\omega_0^2 c/g = 0.24$ ,  $s^* = 8$ ,  $\phi_t = 180^\circ$ ,  $d^* = 2.5$ ,  $a_0/h_o = 0.75$ ,  $\phi_w = -90^\circ$ .... 109

Figure 6.19: Example of grid deformation for the tandem foil in waves (a) general view and (b) detail of the mesh around the aft foil. .... 109

Figure 6.20: Eddy viscosity ratio (log scale) for the tandem foil case in waves. (a) general view (b) detail of the fore foil (c) and detail on the aft foil. Motion and wave parameters  $h_0/c_i = 1.0$ ,  $\chi_{0i} = 0.41$ ,  $\psi_i = 90^\circ$ ,  $\omega_0^2 c/g = 0.24$ ,  $s^* = 8$ ,  $\phi_t = 180^\circ$ ,  $d^* = 2.5$ ,  $a_0/h_o = 0.75$ ,  $\phi_w = -90^\circ$ . Laminar flow in blue and turbulent flow in red. .... 110



# Index of Tables

Table 3.1 Comparison of average thrust coefficient between experimental, numerical, and theoretical methods for $Fr = 0.2$ , $\omega_0^2 c/g = 0.38$ (Silva et al., 2012).....	47
Table 3.2 Comparison of present model results with Epps et al. (2016) numerical results, with $h_0/c = 1$ , $\theta_{0i} = 45^\circ$ , $\psi_i = 90^\circ$ , $\phi_i = 135^\circ$ , $s^* = 8$ , $St = 0.4$ . ....	49
Table 4.1: Available details of the machines used in the present work. ....	59
Table 4.2: Dimensions of the computational domains. ....	60
Table 4.3 Boundary condition settings for the different test cases both with single foil and tandem foil.....	63
Table 4.4: Numerical settings for the different test cases with a single foil. ....	65
Table 4.5 Numerical settings for the different test cases with tandem foils. ....	65
Table 5.1: Small oscillations test case simulation parameters. ....	70
Table 5.2: Simulation grid and time refinement: total number of cells $N_C$ , space refinement ratio $h_i/h_1$ , number of timesteps per period $n_i/T$ , time refinement ratio $t_i/t_1$ and $CFL_{\max}$ for GridPro (GP) and Hexpress (HE) grids. Motion parameters $h_0/c = 0.25$ , $\alpha_0 = 15^\circ$ , $\psi = 90^\circ$ , $St = 0.3$ . ....	70
Table 5.3: Results for discretization error and uncertainty for the different data sets. The errors are given in percentage based on extrapolated value. Motion parameters $h_0/c = 0.25$ , $\alpha_0 = 15^\circ$ , $\psi = 90^\circ$ , $St = 0.3$ . ....	72
Table 5.4. Comparison between present numerical model and experimental data (Anderson et al., 1998). Motion parameters $h_0/c = 0.25$ , $\alpha_0 = 15^\circ$ , $\psi = 90^\circ$ , $St = 0.3$ . ....	72
Table 5.5: Large oscillations test case simulation parameters. ....	74
Table 5.6: Large oscillations test case simulation grid and time refinement: total number of cells $N_C$ , space refinement ratio $h_i/h_1$ , number of timesteps per period $n_i/T$ , time refinement ratio $t_i/t_1$ and CFL. Motion parameters $h_0/c = 1.0$ , $\alpha_0 = 15^\circ$ , $\psi = 90^\circ$ , $St = 0.3$ . ....	74
Table 5.7: Results for discretization error and uncertainty of the data set for the large oscillations test case. The errors are given in percentage based on extrapolated value. Comparison with semi-analytical results and measured data (Read et al. 2003). Motion parameters $h_0/c = 1.0$ , $\alpha_0 = 15^\circ$ , $\psi = 90^\circ$ , $St = 0.3$ . ....	77
Table 5.8: Comparison of the results with and without turbulence model for the large oscillations test case, for the simulation with $h_i/h_1 = 2.15$ and $t_i/t_1 = 2.0$ . Motion parameters $h_0/c = 1.0$ , $\alpha_0 = 15^\circ$ , $\psi = 90^\circ$ , $St = 0.3$ . ....	78
Table 5.9: Simulation parameters for the single foil high-performance case. ....	79
Table 5.10: Simulation grid and time refinement: total number of cells $N_C$ , space refinement ratio $h_i/h_1$ , number of timesteps per period $n_i/T$ , time refinement ratio $t_i/t_1$ , $CFL_{\max}$ and grid quality values. Motion parameters $h_0/c = 1.0$ , $\alpha_0 = 16.5^\circ$ , $\psi = 90^\circ$ , $St = 0.4$ . ....	79
Table 5.11 Results for discretization error and uncertainty of the data set for the flow & forces study test case. The errors are given in percentage based on the extrapolated value. Motion parameters $h_0/c = 1.0$ , $\alpha_0 = 16.5^\circ$ , $\psi = 90^\circ$ , $St = 0.4$ . ....	79

Table 5.12: Comparison of the average thrust coefficient, vertical force coefficients, moment coefficient and propulsive efficiency between the semi-analytical and CFD model developed in the present work with experimental measured values from Read et al. (2003). Motion parameters $h_0/c = 1.0$ , $\alpha_0 = 16.5^\circ$ , $\psi = 90^\circ$ , $St = 0.4$ .....	82
Table 5.13: Comparison of the results with and without turbulence model for the single foil in the high-performance test case, for the simulation with $h_i/h_1 = 1.21$ and $t_i/t_1 = 5.0$ . Motion parameters $h_0/c = 1.0$ , $\alpha_0 = 16.5^\circ$ , $\psi = 90^\circ$ , $St = 0.4$ .....	83
Table 5.14: Simulation parameters for the span effect test case. ....	83
Table 5.15: Simulation refinement and $CFL_{\max}$ : total number of cells $N_c$ , space refinement ratio $h_i/h_1$ , number of timesteps per period $n_i/T$ , time refinement ratio $t_i/t_1$ and $CFL_{\max}$ . Motion parameters $h_0/c = 1.0$ , $\alpha_0 = 15^\circ$ , $\psi = 90^\circ$ , $St = 0.3$ , $s/c = 8$ .....	83
Table 5.16: Comparison of the average thrust, vertical force and moment coefficients results between the CFD and semi-analytical models for the 3D with the results for the 2D case from CFD model, semi-analytical model, experimental data from Read et al. (2003) and panel model results from Filippas & Belibassakis (2014b). Motion parameters $h_0/c = 1.0$ , $\alpha_0 = 15^\circ$ , $\psi = 90^\circ$ , $St = 0.3$ , $s/c = 8$ .....	84
Table 5.17: Tandem foil low performance test case simulation parameters. ....	85
Table 5.18: Simulation parameter details: total number of cells $N_c$ , number of timesteps per period $n_i/T$ , space refinement ratio $h_i/h_1$ , time refinement ratio $t_i/t_1$ , $CFL_{\max}$ and $y^+_{\max}$ . Motion parameters $h_0/c = 1.0$ , $\alpha_0 = 6.5^\circ$ , $\psi = 90^\circ$ , $St = 0.4$ , $s^* = 8$ , $\phi_t = 270^\circ$ .....	85
Table 5.19 Results for discretization error and uncertainty of the data set for the tandem foil low performance test case. Motion parameters $h_0/c = 1.0$ , $\alpha_0 = 6.5^\circ$ , $\psi = 90^\circ$ , $St = 0.4$ , $s^* = 8$ , $\phi_t = 270^\circ$ .....	85
Table 5.20: Comparison of the average thrust coefficient for single, fore, aft and total tandem foils between the CFD model, semi-analytical model and CFD LilyPad solver numerical data (Epps et al., 2016) and experimental data (Read et al., 2003). Results for tandem foil propulsive efficiency. Motion parameters $h_0/c = 1.0$ , $\alpha_0 = 6.5^\circ$ , $\psi = 90^\circ$ , $St = 0.4$ , $s^* = 8$ , $\phi_t = 270^\circ$ .....	87
Table 5.21: Simulation parameters for the tandem foil high-performance test case.....	88
Table 5.22: Simulation parameter details: total number of cells $N_c$ , number of timesteps per period $n_i/T$ , space refinement ratio $h_i/h_1$ , time refinement ratio $t_i/t_1$ and $CFL_{\max}$ . Motion parameters $h_0/c = 1.0$ , $\alpha_0 = 10^\circ$ , $\psi = 90^\circ$ , $St = 0.4$ , $s^* = 8$ , $\phi_t = 180^\circ$ .....	88
Table 5.23: Results of the average thrust coefficient and propulsive efficiency for the fore, aft and tandem foil. Motion parameters $h_0/c = 1.0$ , $\alpha_0 = 10^\circ$ , $\psi = 90^\circ$ , $St = 0.4$ , $s^* = 8$ , $\phi_t = 180^\circ$ .....	90
Table 5.24: Comparison of the normalized aft foil average thrust coefficient and efficiency between CFD model, the semi-analytical model and CFD LilyPad solver numerical data (Muscutt et al., 2017). Motion parameters $h_0/c = 1.0$ , $\alpha_0 = 10^\circ$ , $\psi = 90^\circ$ , $St = 0.4$ , $s^* = 8$ , $\phi_t = 180^\circ$ .....	91
Table 6.1: Submerged single foil test case simulation parameters.....	93
Table 6.2: Simulation parameter details: total number of cells $N_c$ , number of timesteps per period $n_i/T$ , space refinement ratio $h_i/h_1$ , time refinement ratio $t_i/t_1$ and $CFL_{\max}$ . Motion parameters $h_0/c = 1.0$ , $\alpha_0 = 15^\circ$ , $\psi = 90^\circ$ , $St = 0.3$ , $d^* = 1.25$ .....	94
Table 6.3: Comparison of the average thrust coefficient, between the semi-analytical and numerical model developed in the present work with respective results in an infinite domain of Section 5.1.2. Motion parameters $h_0/c = 1.0$ , $\alpha_0 = 15^\circ$ , $\psi = 90^\circ$ , $St = 0.3$ , $d^* = 1.25$ .....	95
Table 6.4: Simulation parameters for the free-surface span effect test case. ....	97

Table 6.5: Simulation parameter details: total number of cells $N_c$ , number of timesteps per period $n_i/T$ . Motion parameters $h_0/c = 1.0$ , $\alpha_0 = 15^\circ$ , $\psi = 90^\circ$ , $St = 0.3$ , $d^* = 1.25$ , $s/c = 8$ .....	97
Table 6.6: Comparison of the average thrust coefficient, between the semi-analytical and numerical model developed in the present work with respective results in 3D infinite domain, 2D free-surface and 2D infinite domain. Motion parameters $h_0/c = 1.0$ , $\alpha_0 = 15^\circ$ , $\psi = 90^\circ$ , $St = 0.3$ , $d^* = 1.25$ , $s/c = 8$ .....	98
Table 6.7: Simulation parameters for the fixed foil in incident waves test case. ....	98
Table 6.8: Simulation parameter details: total number of cells $N_c$ , number of timesteps per period $n_i/T$ , and $CFL_{\max}$ . Parameters $a_0^* = 1.5$ , $d^* = 2.5$ .....	98
Table 6.9: Results of the average thrust, vertical and moment coefficients for the fixed foil in waves and comparison with the semi-analytical model. Parameters are $a_0^* = 1.5$ , $d^* = 2.5$ . ....	100
Table 6.10: Simulation parameters for oscillating foil in incident wave test case. ....	101
Table 6.11: Simulation parameter details: total number of cells $N_c$ , number of timesteps per period $n_i/T$ , and $CFL_{\max}$ . Motion and wave parameters $h_0/c = 0.6$ , $\theta_0 = 15.2^\circ$ , $\psi = 90^\circ$ , $\omega_0^2 c/g = 0.69$ , $d^* = 1.28$ , $a_0/h_0 = 0.238$ .....	102
Table 6.12: Comparison of the average thrust coefficients results between the CFD, semi-analytical models and FLUENT results from Silva et al. (2012). Motion and wave parameters $h_0/c = 0.6$ , $\theta_0 = 15.2^\circ$ , $\psi = 90^\circ$ , $\omega_0^2 c/g = 0.69$ , $d^* = 1.28$ , $a_0/h_0 = 0.238$ .....	103
Table 6.13: Simulation parameters for the submerged tandem foil test case. ....	104
Table 6.14: Simulation parameter details: total number of cells $N_c$ , number of timesteps per period $n_i/T$ , and $CFL_{\max}$ . Motion parameters $h_0/c_i = 1.0$ , $\alpha_{0i} = 10^\circ$ , $\psi_i = 90^\circ$ , $St = 0.4$ , $d^* = 2.5$ , $s^* = 8$ , $\phi_t = 180^\circ$ . ....	104
Table 6.15: Results of the average thrust coefficient for the fore, aft and tandem foil. Motion parameters $h_0/c_i = 1.0$ , $\alpha_{0i} = 10^\circ$ , $\psi_i = 90^\circ$ , $St = 0.4$ , $d^* = 2.5$ , $s^* = 8$ , $\phi_t = 180^\circ$ . ....	106
Table 6.16: Simulation parameters for the tandem foil in waves test case. ....	107
Table 6.17: Simulation parameter details: total number of cells $N_c$ , number of timesteps per period $n_i/T$ , and $CFL_{\max}$ . Motion parameters $h_0/c_i = 1.0$ , $\chi_{0i} = 0.41$ , $\psi_i = 90^\circ$ , $\omega_0^2 c/g = 0.24$ , $s^* = 8$ , $\phi_t = 180^\circ$ , $d^* = 2.5$ , $a_0/h_0 = 0.75$ , $\phi_w = -90^\circ$ .....	107
Table 6.18: Results of the average thrust coefficient and propulsive efficiency for the fore, aft and tandem foil. Motion and wave parameters $h_0/c_i = 1.0$ , $\chi_{0i} = 0.41$ , $\psi_i = 90^\circ$ , $\omega_0^2 c/g = 0.24$ , $s^* = 8$ , $s^* = 8$ , $\phi_t = 180^\circ$ , $d^* = 2.5$ , $a_0/h_0 = 0.75$ , $\phi_w = -90^\circ$ . ....	109



# Nomenclature

## Acronyms and Abbreviations

2D – Two-dimensional  
3D – Three-dimensional  
AoA – Angle of attack  
ASV – Autonomous Surface Vehicle  
BvK – Bernard-Von-Kármán  
CFD – Computational Fluid Dynamics  
CFL – Courant-Friedrichs-Lewy  
HPC – High-Performance Computing  
LE – Leading Edge  
LEV – Leading Edge Vortex  
TEV – Trailing Edge Vortex  
MARIN – Maritime Research Institute Netherlands  
NACA – National Advisory Committee for Aeronautics  
NUA – Numerical Uncertainty Analysis  
ReFRESKO – Reliable & Fast Rans Equations solver for Ships and Constructions Offshore  
SIMPLE – Semi-Implicit Pressure-Linked Equations  
SST – Shear Stress Transport  
TE – Trailing Edge  
TST – Transient Scanning Technique  
URANS – Unsteady Reynolds Averaged Navier Stokes Equations

## Greek Letters

$\alpha$  – Foil effective angle of attack; volume-fraction variable  
 $\alpha_0$  – Foil maximum effective angle of attack  
 $\alpha_s$  – Error constant spatial component  
 $\alpha_t$  – Error constant temporal component  
 $\Delta\alpha_{fs}$  – Free-surface angle of attack correction  
 $\eta$  – Foil camber  
 $\eta_P$  – Propulsive efficiency  
 $\gamma$  – Wake vorticity  
 $\Lambda$  – Foil aspect ratio  
 $\lambda$  – Wavelength  
 $\omega$  – Incident wave angular frequency  
 $\omega_0$  – Foil oscillation angular frequency; wave angular frequency of encounter  
 $\phi$  – Velocity potential  
 $\phi_\infty$  – Velocity potential at infinity  
 $\phi_0$  – Encounter velocity potential; extrapolated value  
 $\phi_1$  – Finest exact solution  
 $\phi_t$  – Tandem configuration inter-foil phase lag  
 $\phi_w$  – Phase between heave motion and incident wave  
 $\Phi_0$  – Exact solution  
 $\Phi_{cit}$  – Numerical solution obtained at a given criterion  
 $\Phi_{ref}$  – Numerical solution obtained with the tightest iterative criterion  
 $\rho$  – Fluid density

$\varphi$  – Quasi-steady inflow angle  
 $\theta$  – Foil pitch angle  
 $\theta_0$  – Foil pitch angle complex amplitude  
 $\theta_0^*$  – Non-dimensional pitch angle amplitude  
 $\psi$  – Phase between pitch and heave motion  
 $\mu$  – Dynamic viscosity  
 $\nu$  – Kinetic viscosity  
 $\varepsilon$  – Feather parameter  
 $\xi$  – Non-dimensional horizontal coordinate  
 $\zeta_0$  – Wave free-surface profile  
 $\chi$  – Extended feather parameter

### Latin letters

$A$  – Planform foil area  
 $A_0$  – Wave orbital velocity amplitude  
 $a$  – Half-chord length  
 $a_0$  – Wave amplitude  
 $a_0^*$  – Non-dimensional wave amplitude  
 $b$  – Rotating axis position  
 $b^*$  – Non-dimensional rotating axis position  
 $C(k)$  – Theodorsen Function  
 $C_D$  – Drag coefficient  
 $C_{D,p}$  – Foil profile drag coefficient  
 $C_{D,p0}$  – Zero-lift profile drag coefficient  
 $C_{D,pa}$  – Lift profile drag coefficient  
 $C_{D,ps}$  – Flow separation drag coefficient  
 $C_{D,i}$  – Induced drag coefficient  
 $C_F$  – Friction coefficient  
 $C_L$  – Lift coefficient  
 $C_{Lo}$  – Lift factor for drag calculation  
 $C_{L2D}$  – Lift coefficient without span effects  
 $C_{L\infty}$  – Lift coefficient in infinite domain  
 $C_L^t$  – Tandem foil thrust coefficient  
 $C_L^s$  – Single foil thrust coefficient  
 $C_P$  – Power coefficient  
 $C_T$  – Thrust coefficient  
 $C_{T,qs}$  – Quasi steady thrust coefficient  
 $C_{T,us}$  – Unsteady thrust coefficient  
 $C_y$  – Vertical force coefficient  
 $c$  – Foil chord length  
 $D$  – Foil drag  
 $d$  – Foil submersion depth  
 $d^*$  – Non-dimensional foil submersion depth  
 $d^*(t)$  – Instantaneous non-dimensional effective foil submersion depth  
 $E_0$  – Tandem foil constant  
 $E_c$  – Comparison error  
 $E_d$  – Discretization error  
 $E_e$  – Experimental error  
 $E_{it}$  – Iteration error  
 $E_m$  – Modelling error  
 $e$  – Foil planform efficiency factor  
 $F_r$  – Froude number  
 $F_x$  – Foil horizontal force

$F_y$  – Foil vertical force  
 $f$  – Foil oscillating frequency  
 $g$  – Acceleration of gravity  
 $H_0^*$  – Non-dimensional wave orbital velocity amplitude  
 $h$  – Foil heave motion  
 $h_0$  – Heave motion complex amplitude  
 $h_0^*$  – Non-dimensional heave amplitude  
 $h_{0w}^*$  – Non-dimensional wave heave amplitude  
 $h_{ep}$  – Endplate height  
 $i$  – Imaginary unit  
 $k$  – Wave number  
 $ka$  – Non-dimensional wave number  
 $k_{fs}$  – Free-surface lift-loss factor  
 $k_f$  – Reduced frequency  
 $L$  – Foil lift  
 $L_C$  – Circulatory lift  
 $L_{NC}$  – Non-circulatory lift or added-mass  
 $L'_C$  – Circulatory lift in tandem configuration  
 $L^s_C$  – Circulatory lift in single foil  
 $L_\infty$  – Infinity norm  
 $M$  – Foil pitching moment  
 $M_C$  – Circulatory pitching moment  
 $M_{NC}$  – Non-circulatory pitching moment  
 $M_{NC1/2}$  – Non-circulatory pitching moment at mid-chord point  
 $M_{NC1/4}$  – Non-circulatory pitching moment at quarter-chord point  
 $\bar{P}$  – Average input power  
 $p$  – Pressure  
 $p_I$  – Pressure disturbance  
 $p_x$  – Space order of convergence  
 $q_t$  – Time order of convergence  
 $\bar{R}_{wd}$  – Mean wave diffraction resistance  
 $\bar{R}_{wr}$  – Mean wave radiation resistance  
 $R_e$  – Reynolds number  
 $S_t$  – Strouhal number  
 $s$  – Tandem inter-foil separation distance; foil span length  
 $s^*$  – Non-dimensional inter-foil separation distance  
 $T$  – Foil thrust; motion period  
 $\bar{T}$  – Average thrust force  
 $t$  – Time; foil maximum thickness  
 $t^*$  – Non-dimensional maximum foil thickness  
 $t_i$  – Time iteration step  
 $U$  – Ship speed or foil advance horizontal speed  
 $U_{for}$  – Fore foil vortex advection velocity  
 $U_d$  – Discretization uncertainty  
 $U_e$  – Experimental uncertainty  
 $U_v$  – Modelling validity uncertainty  
 $u_T$  – Friction velocity  
 $V_0$  – Wave orbital vertical velocity  
 $V_A$  – Apparent incident velocity  
 $v$  – Vertical velocity of fluid  
 $v_0$  – Vertical velocity of foil surface  
 $x_0y_0$  – Origin of the coordinate system  
 $y^+$  – Non-dimensional wall distance  
 $y^+_{max}$  – Maximum non-dimensional wall distance



# Chapter 1

## Introduction

### 1.1 Motivation

Flying and swimming animals have long been an inspiration for human inventors seeking to create aircraft or watercraft. Today, due to the widespread concern over the environment and global warming, the way animals use natural energy resources like the wind, currents, and waves to travel with minimal energy consumption provides innovative solutions to meet the current economic targets to reduce the use of fossil fuel for ship propulsion. Moreover, there is a revived interest in renewable energy for the supplementary propulsion of ships. Remaining almost unexplored, the major renewable energy resource in the ocean is wave energy, and the idea of propelling a boat using waves is an unavoidable concept. Wave-powered boats have been proposed and studied for already more than one century.

The simplest and most common type of wave-powered boat uses hydrofoils which convert the relative motion between the foil and the water into propulsive thrust. Nowadays, mechanical systems which propel airplanes and ships differ distinctly from this biological source of inspiration by the use of rotating rather than oscillating blades. Nevertheless, modern research (Wu et al., 2020) has revitalized the interest in the development of mechanical propulsion systems based on oscillating blades or foils. Various researchers have successfully implemented oscillating foils in proof-of-concept prototype vehicles. MARIN (Maritime Research Institute Netherlands) has built the first inland ship with O-foil propulsion, resulting in 50% better efficiency to conventional propellers and both Liquid Robotics and MOST are commercializing wave propelled ASVs (Autonomous Surface Vehicle) (Wu et al., 2020). Alongside these efforts to develop practical vehicles, there has been a large body of research that examined the operation of oscillating foils from a more theoretical standpoint to improve the thrust production and efficiency of foil propulsors. The main effort has been on the research of active foil propulsors using actuators. To a lesser extent, it has also been studied passively wave propelled devices, where foils that are free to oscillate in waves, with motion limited by properly tuned system of springs, are able to generate thrust. However, single-foil propulsion has shortcomings, such as large oscillations in thrust and large unsteady side forces, as well as efficiency issues (Akhtar et al., 2007, Boschitsch et al., 2014). A promising approach to enhance this concept involves in-line tandem flapping foils, i.e., a configuration of two parallel hydrofoils, one after the other, to mitigate unbalanced forces and potentially increase efficiency by utilizing the energy in the wake of the forward foil. This line of research has been mainly applied to the active foil propulsor concept. While the results have demonstrated the potential to improve thrust production and efficiency (Lagolopoulos, 2020), the selection of the appropriate parameters to improve performance under a given set of oscillation and forward travel kinematics remains, to a large extent, an open question.

The starting point for the study presented in this thesis is the idea that a tandem foil configuration could be used as wave foil propulsor, improving the performance of single hydrofoils to become a practical solution to be applied in renewable autonomous marine vehicles. These vehicles have a broad scope of applications ranging from scientific survey, offshore exploration support, over-the-horizon data telemetry and navigation security. This work is part of the effort to develop technology for Portuguese EEZ ocean monitoring and surveillance according to national needs. Unmanned vehicles are emerging as a response to

these needs. Although some solutions have already been advanced, the operation range and power supplying still represent significant limitations. The wave foil propulsor concept could provide a solution for such devices.

The design of an oscillating-foil propulsion system requires the optimization of parameters related to the kinematics of the oscillating motion, as well as the shape and structure of the foils. The primary aim in the optimal selection of these parameters is to have the system develop sufficient thrust forces that the vehicle can move forward against resisting forces such as profile and separation drag or wave making resistance. The secondary objective is to produce this thrust force with the minimum power input to the system or, in other words, to have high propulsive efficiency. Typically, the parameters must be chosen from within ranges set by various constraints such as the vehicle size, material properties and the limitations of the drive mechanism actuating the flapping motion or the wave conditions under which it is expected to operate. To meet the performance goals in the design of a propulsion system, engineers must understand the effect of the various design parameters on the thrust generation and efficiency. The concept regarding a single foil has been broadly studied (Read et al., 2003), while the tandem hydrofoil as an active foil propulsor has been more thoroughly investigated in recent years. Studies of tandem foil in waves are still almost inexistent in published literature. Understanding of the hydrodynamics of the tandem in waves remains a large field of study to explore.

The objective of the thesis is to develop tools that capture the main physical processes acting on the active foil tandem foil propulsor arrangement, allowing the understanding of the various effects on the forces and moments involved. It proposes using theoretical and numeric models in a complementary manner to allow exploring the foil propulsor in the tandem configuration and in waves. We demonstrate that this is a significant step towards engineering development of wave tandem foil propulsor solutions for ship propulsion that can rely only on wave energy. It can contribute to reducing the fuel consumption of vessels traveling in waves or the autonomy of ASVs. To reach this objective this thesis intends to provide: i) a simple semi-analytical tool that captures the main physical processes acting on the tandem foil arrangement. Its straightforward implementation and quick simulation running times turns viable the exploration of system parameters and configurations. It also allows simple coupling with vehicle seakeeping equations of motion and control system. ii) a numerical tool where the detailed dynamics of the flow are visualized, allowing the understanding of the various effects on the forces and moments involved, together with more accurate results on the cases of interest, with the main effects included, like viscosity, turbulence and waves.

## **1.2 State of the Art**

### **1.2.1 Full-Scale Vessels and Notable Model Boats**

Wave-powered boats exist since the 1890s and were introduced as early as 1858. The wave propulsion system was first coined in a US patent by Daniel Vrooman (1858), in which was described a new improvement in ships. These relied on the rolling sea as propelling aid to get their motion. It is not known whether anyone built Vrooman's boat. In 1895, Herman Linden from the Zoological Station in Naples, Italy, patented his wave powered boat called AutoNaut (Linden, 1895). It was a 4-meter-long boat that could move against the waves at speeds between 2.6 to 3.5 knots (1.3-1.8 m/s) and its propulsion was provided only by wave energy. It had two underwater steel plates, one at the bow and one at the stern, fixed to the hull, that behave like fish fins with the heave motion of the boat, propelling it.

In 1978, Einar Jakobsen carried out some experiments on wave powered boats at the Norwegian Hydrodynamics Laboratories in Trondheim, Norway (Jakobsen, 1981). His model boat had a total length of 1.025 meters. The wave propulsion system was based on a spring-loaded foil on an extension out from the bow, and another spring-loaded foil on an extension aft of the stern. The results presented a speed between 0.55 to 0.824 m/s in regular sea waves of 0.05 m height and 1.2 s period. Jakobsen's vessel was named the "Foilpropeller", and his Wave Control Company applied this technology on a sailboat hull 7.5 meters long and tested it

with combinations of 2 and 4 foils, each with an area measuring  $0.5 \text{ m}^2$ . The Norwegian government sponsored the research to fit the vessel *Kystfangst* (20 m long and 180 tonnes), owned by the Institute of Fishery Technology Research, with a bulbous bow and two foils with a total area of  $3 \text{ m}^2$  (Anon, 1983; Berg, 1985) (see Figure 1.1). In a sea state of about 3 m wave height, the foils produced a propulsive force corresponding to 15-20 % of the vessel's total resistance (Berg, 1985).



Figure 1.1: Kystfangst (Dybdahl, 1988).

During this period, Hiroshi Isshiki, of the Technical Research Institute, Hitachi Shipbuilding & Engineering Co., Ltd. in Osaka, Japan developed a theoretical and experimental study on wave-powered boats. He named his research “Wave Devouring Propulsion System” (WDPS). At the same time, Yutaka Terao of Tokai University in Japan was also working in this very same system (Terao, 1982). The WDPS consists of a ship hull and hydrofoil acting in a similar way as the dolphin's fin. Experimental studies were carried between December of 1988 and January of 1989 on a 20 ton and 15.7-meter-long fishing vessel equipped with a hydrofoil with an area of 7.4% of the ship's waterline area (Figure 1.2). With the use of the hydrofoil, the ship registered an improvement of propulsion in waves (Terao et al., 1991).

In the early 2000's, there was a growing interest in unmanned vehicles, that used dynamic positioning to follow a course or to station keeping within a watch radius. These vehicles are in general powered by batteries, fuel, solar radiation, wind, or waves, but have a limited range of operation.

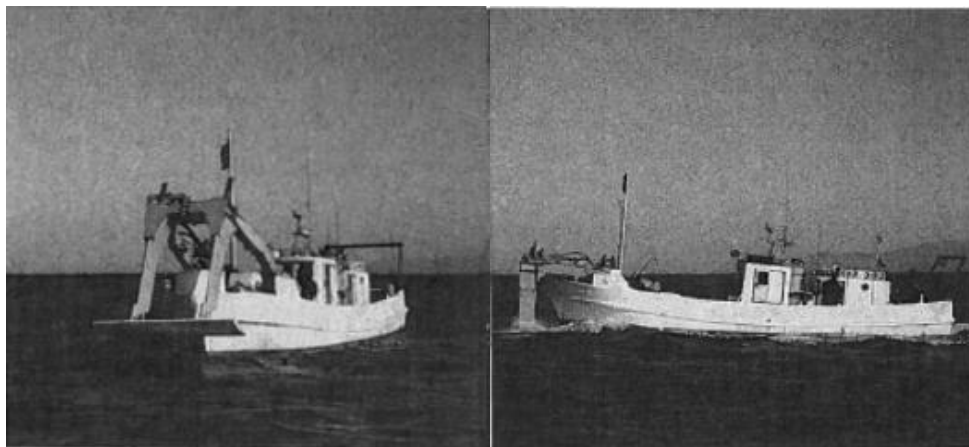


Figure 1.2: WDPS ship speed trial (Terao, 1991).

In 2007, Liquid Robotics, an American robotics marine corporation, developed an ASV named WaveGlider. The WaveGlider was a new class of ASV because it used only wave energy for basic propulsion, overcoming the problem of autonomy. It has a submerged glider

with a set of foils attached to the main vessel, from 2.1 to 3.05 m in length, through a tether (Manley, 2010) As the float heaves in response to the ocean waves, the submerged glider heaved and plunged through the water, generating thrust that drives the float forward. In one of the trials, the glider and the float endured over 440 days at sea and the second tether endured 365 days. Despite the advantage of limitless propulsion, the speed generated by this mechanism is limited and it only reaches speeds between 1-3 knots (0.5-1.5 m/s) (Rochholz, 2012).

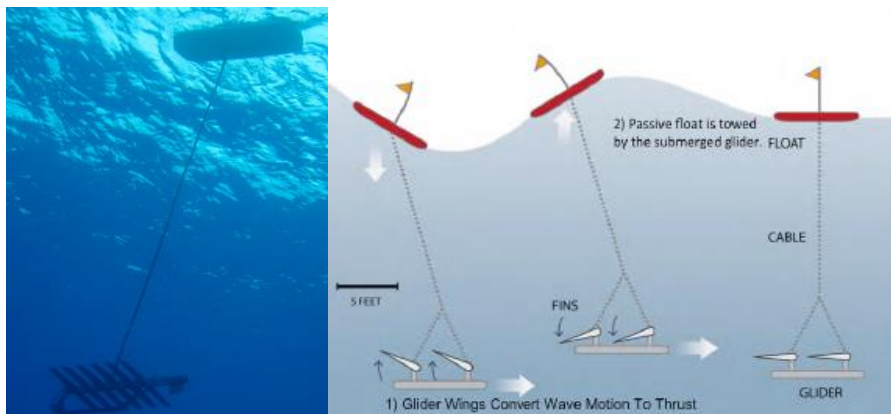


Figure 1.3: The Wave Glider a) from below and b) principles of operation (Manley, 2010).

In 2008, Japanese Kenichi Horie sailed a 10 m wave-powered catamaran, the Suntory Mermaid II, from Honolulu, Hawaii to the Kii Channel in Japan (Geoghegan, 2008). The vessel's propulsion system was designed by Yutaka Terao and worked like the WDPS. The propulsion system is mounted under the bow and consists of two side-by-side horizontal foils that move up and down with the motion of the waves (Zhenjiang, 2016) The Mermaid completed its journey in 110 days and cruised using only the thrust generated by the WDPS with a maximum speed of 3-4 knots (1.5-2.0 m/s) (see Figure 1.4).

Nagata et al. (2010) performed model tests of a 1:40 scale model of an 80 m long container ship. The ship was equipped with a hydrofoil in the bow, of span 2.34 times the ship beam. In head sea waves of wavelength 3.12 times the ship length, and height 0.10 m, the ship cruised at about 0.7 m/s, powered only by the waves. The same speed was almost achieved in following seas with the same wave height, but with a wavelength of 0.96 times the ship length. Froude-scaled to full scale, this is equivalent to an 80 m ship sailing at 8.6 knots (4.4 m/s) in waves of 4 m height.



Figure 1.4: Suntory Mermaid II a) The catamaran b) Physical structure (Zhenjiang, 2016).

Based on a similar concept of WDPS, in 2012 MARIN announced that the first inland ship with O-foil propulsion and integrated power system was under construction. O-foil stands for “oscillating foil”, a flapping wing propulsor that covers the entire width of the ship. As a result, the propulsion surface is much larger, resulting in 50% better efficiency and a cut in fuel consumption by 33-50%, (Wu et al., 2020). The first ship to be fitted with the O-foil wing

propulsion, in 2013, the MS Triade, is already in use. The conversion of this inland vessel was a complete success (see Figure 1.5).



Figure 1.5: a) MS Triade b) O-foil propeller (Cibalia, 2021).

Also in 2012, MOST – Autonomous Vessels started to develop the ASV AutoNaut (AutoNaut, 2021) using the same Linden and Jakobsen techniques (Caccia, 2005; Curcio, 2005). The vessel consists of two flapping foils, one at the bow and one at the stern, and propels itself using the wave-induced vessel motions to generate thrust from spring-loaded foils. It had its successful first mission in 2014, and in 2016 during the performance ocean test in Plymouth its 5 m vessel in length version could achieve 3.5 knots in wave heights of 0.6m.

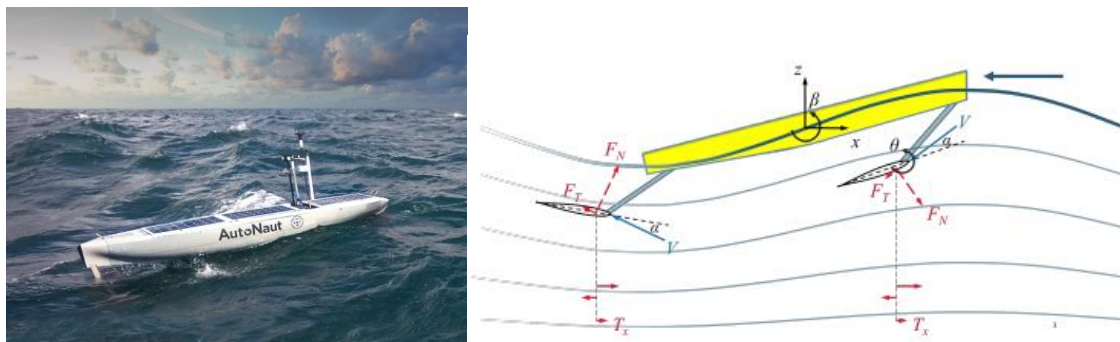


Figure 1.6: a) The AutoNaut and b) an example of Linden and Jakobsen techniques (Bowker, 2015).

In 2012 Terao and Sakagami developed a new small, lightweight WDPS ASV vessel, with 1.3 m length, with dual parallel fins installed under the bow. Each fin has a pitch restoring spring and travels along a pivot axis, as shown in Figure 1.7, with the maximum pitch amplitude angle set at 45 degrees. The new model was tested in Orido Bay, Japan. All systems worked properly in this trial and the experimental WDPS vessel advanced toward the set waypoints at an estimated speed of 0.18 m/s. (Terao et al., 2012)

Bowker (2015), a researcher and team member of the Fluid Structure Interactions Group at the University of Southampton, conducted an experimental study of a wave energy scavenging system onboard ASVs.



Figure 1.7: WDPS new ASV model.

Its purpose was to develop a foil system that can generate thrust and convert wave energy into electricity for onboard later use. The system was named Flapping Energy Utilization and Recovery (FLEUR). Two sets of flapping foils are submerged and fixed to the hull beneath the bow and the stern through a rigid pivot arm. The model trials were carried out at the Solent University towing tank. The results showed that the model was able to generate an average power close to 0.15 W and 0.5 W for the fore and the aft foil respectively, with 0.23 m chord and 1 m span foils, and waves of 0.04 m amplitude and 0.8 Hz frequency. It proved that it's possible to generate power using this technology and improve ASV autonomy.

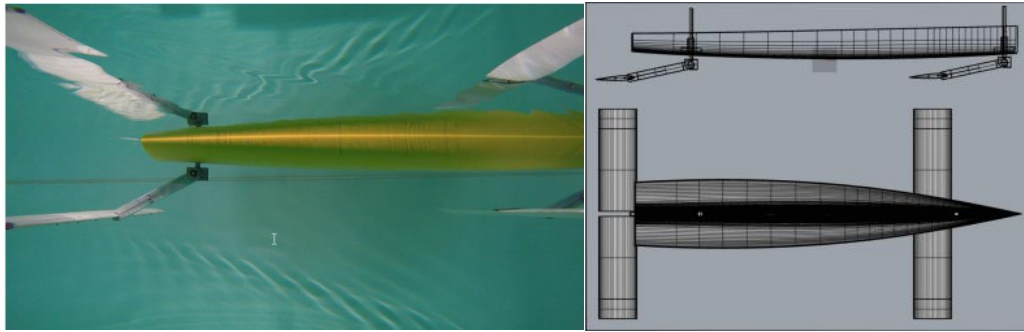


Figure 1.8: FLEUR a) Underwater view of forward and aft foil setup and b) general arrangement (Bowker, 2015).

A new version of the Autonaut was recently announced, with four keel-mounted foils (Wu et al., 2020).

Figure 1.9 presents a comparison of several commercially available ASVs endurance and capability. The lines highlight the trade-off tendency convergence of both these characteristics. All devices have photovoltaic and batteries power systems capability. However, there are few solutions available for ASVs to travel long distances across the ocean with the sole use of renewable energy systems. At the moment, the WaveGlider continues to be the ASV that provides a better trade-off between endurance and power. Despite all the advances and innovations, there are still many challenges in the ASV conception, namely autonomy and speed. The latter is mainly due to propulsion issues.

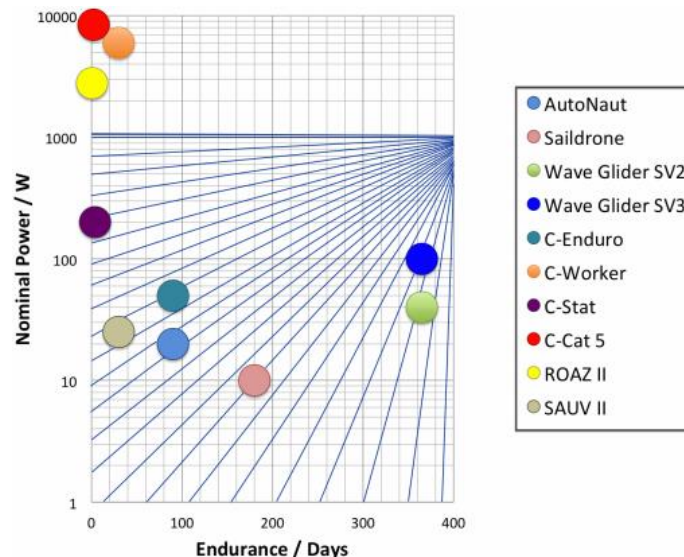


Figure 1.9: ASV's performance (Bowker, 2015).

## 1.2.2 Theoretical and Experimental Studies on Foil Propulsion

Fuelled by the need to understand the problem of wing flutter, the foundation of two-dimensional unsteady foil theory was laid in the 1920s and 1930s by pioneers such as Wagner

(1925), Theodorsen (1935), Küssner (1935), Garrick (1936), and von Kármán and Sears (1938). They all assumed incompressible and inviscid flow, that the effect of airfoil thickness is negligible, and that the shed vortices in the wake remain on a straight line behind the foil, thereby assuming small transverse motions. Despite its simplifying assumptions, this classical unsteady thin-airfoil theory is often applied when studying oscillating foils, primarily because its analytical solutions allow separating the various components, providing insight into the problem. The resulting expression for the unsteady lift in the highly mathematical approach of Theodorsen's paper (1935) can easily be implemented in a computer program. In addition, reasonably accurate values for the unsteady lift can quickly be obtained, even for the relatively large transverse oscillation amplitudes of practical importance, which may then be confirmed through more advanced methods.

Lighthill was a pioneer in applying the hydrodynamic perspective to the study of fish swimming, with his theory for the swimming of slender fish (Lighthill, 1960). Wu (1961) analysed fish swimming by studying the two-dimensional potential flow over a waving thin plate of finite chord, building on results from classical unsteady thin-airfoil theory. Lighthill (1970) also applied unsteady foil theory to analyse the uniform swimming, i.e., fish locomotion where virtually all lateral motion occurs in the caudal fin and the region connecting the caudal fin to the main body.

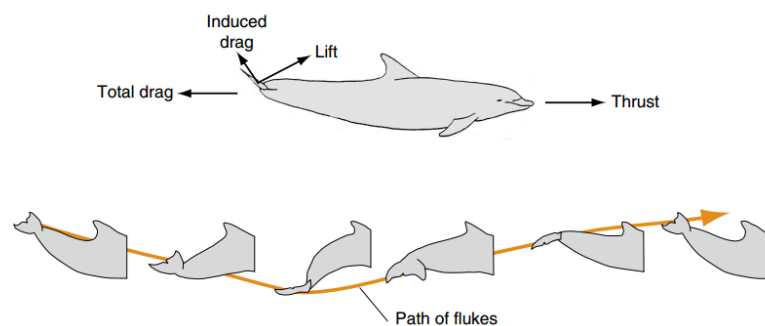


Figure 1.10: Cetacean propulsion (Coffey, 1977).

Wu (1971b) and Wu & Chang (1975) addressed the thrust generation of an oscillating hydrofoil advancing in waves but neglected the effect of the free-surface and the solid bottom. This is a reasonable simplification when the hydrofoil is farther than two chord lengths away from each of these boundaries (Wu, 1972), valid above a certain advance speed (Hough, 1969).

In four reports, Isshiki (1982a,b) and Isshiki and Murakami (1983, 1984) presented theoretical and experimental researches on thrust generation of a hydrofoil advancing in waves. In his first report, Isshiki (1982a) improved Wu's theory by including an approximation of the free-surface effect and studied the thrust from a non-oscillating hydrofoil advancing in waves. In his second report, Isshiki (1982b) explored optimized foil motions in heave and pitch given that the power required to heave and pitch the foil was zero. In the third and fourth reports (Isshiki and Murakami, 1983, 1984), experiments were carried out to verify thrust generation through absorption of wave energy by an advancing hydrofoil, heaving and pitching passively through a set of springs, and compared with theory. The effects of foil draft, heave and pitch springs, and an auxiliary float were studied theoretically in the fourth report (Isshiki and Murakami, 1984). When the foil was attached to the float in a suitable position, a larger thrust was obtained than without the boat. More experimental results are given in Isshiki et al. (1984).

Veritec, a former subsidiary of Det Norske Veritas (today DNV Group), analysed the propulsive effect of hydrofoils near the bow of vessels 20 m, 40 m, and 70 m long (Veritec, 1985, 1986) operating in the North Sea. Foil areas of 2%, 4%, and 6% of the vessel water plane area were studied. The fuel saving percentage increased with increasing foil area for all three ships. For the 70 m long vessel with a foil of 6% of the vessel water plane area, the fuel saving was 43% at 10.6 knots (5.4 m/s) and 10% at 15.9 knots (8.2 m/s). A strip theory

program calculated the vessel motions, but the heave and pitch damping due to the foils was not accounted for. Foil drag and dynamic effects on the foil lift were not accounted for either.

Grue et al. (1988) examined the propulsion of a foil moving through water close to a free-surface in 2D. They applied a vortex distribution along the centreline of the foil and the wake and solved for the local vortex strength. All equations were linearized. The ability of the foil to propel a ship in waves was studied, and they found that a 40 m long ship in 1 m high regular waves would travel at a speed of 8 knots (4.1 m/s). They assumed that the foil moved downward when the wave field velocity was upward, and that the heave motion of the ship was of the same order of magnitude as the amplitude of the incoming waves. Finally, the theory was compared with Isshiki et al.'s experiments (1984), providing different degrees of success.

Potentially, if ships can save large amounts of fuel in waves, whales and dolphins could also minimize their energy consumption through wave energy. Bose and Lien (1990) showed that in seas corresponding to a windspeed of 20 knots (10.3 m/s), a 14.5 m long fin whale could save about 25% propulsive power in head seas and 33% in following seas, when swimming at a depth of 2.0 m and a forward speed of 2.5 m/s. The power savings dropped with increasing submergence depth.

The Massachusetts Institute of Technology (MIT) has been one of the most prominent institutes researching on oscillating foil propulsion. Its research group has a towing tank 30 m long, 2.6 m wide, and 1.3 m deep, with equipment for power and force measurement on a foil oscillated in heave and pitch. Since the 90's several researchers used this equipment for research on oscillating hydrofoils (Hover et al., 2004; Read et al., 2003; Anderson et al., 1998; Triantafyllou, Triantafyllou & Grosenbaugh, 1993). Until recently, the issues of a two-dimensional foil are still being studied. Studies on the thrust forces generated by an oscillating foil have shown the potential for impressive thrust coefficients and efficiency in regions of 50-60% (Read et al., 2003).

Silva and Yamaguchi (2012) used the commercially available code FLUENT to study a two-dimensional hydrofoil oscillating harmonically in heave and pitch under the influence of free-surface waves. Simulation results were found to be in good agreement with experimental results in Isshiki and Murakami (1984).

Researchers from the National Technical University of Athens (NTUA) carried out many numerical works on this issue (Belibassakis et al., 1997; Belibassakis, 2011; Belibassakis and Politis, 2013; Belibassakis and Filippas, 2015; Filippas et al., 2018; Politis, 2004; Politis and Tsarsitalidis, 2009, 2013, 2014; Politis and Politis, 2014; Tsarsitalidis and Politis, 2015). They numerically investigated the hydrodynamic performance of flapping foils for ship propulsion under different conditions. They employed the Unsteady Boundary Element Modelling code (Politis, 2009, 2011). Filippas and Belibassakis (2013, 2014a,b) used a boundary element method while focused on the free-surface effects, by studying a two-dimensional hydrofoil under-going heaving and pitching oscillations underneath the free-surface, with constant forward speed. There was good agreement with results in Silva and Yamaguchi (2012). Almost all results show flapping foils to be a promising system with propulsion efficiency and energy extraction from ship motion that compare to conventional propellers.

Furthermore, Bøckmann and Steen from the Norwegian University of Science and Technology (NTNU) performed an experimental investigation to determine the effect of fixed wave foils on ship motion and propulsion (Bøckmann and Steen, 2013, 2016), as well as the effect of control methods of oscillating motion on the performance of foils (Bøckmann and Steen, 2014). They have reached two conclusions: both ship resistance and motion were reduced by the wave foils; the oscillating foils can be used as a major or auxiliary driving force of a ship. In addition, Thaweewat et al. (2018) studied the performance of semi-active flapping foils for ship propulsion. Similar investigations were also conducted by Liu et al. (2019), Bøckmann and Steen (2014), Belibassakis and Filippas (2015) and Filippas et al. (2018).

To improve the propulsive performance of a flapping system, various researchers have proposed the use of multiple foil configurations. Early studies focusing on tandem flapping configurations e.g., insect wings (Alexander 1984; Thomas et al. 2004) have shown that they outperform single flappers under certain wake-to-wake interactions. This was achieved by observing that dragonflies change the phasing of the flapping motion between their fore and hind wings depending on the flight manoeuvres. Floc'h et al. (2012) performed a comparison

between an oscillating foil as propulsion and a conventional propeller. Results indicated that the two propulsion systems had a similar hydrodynamic performance despite their different nature.

Concerning tandem configurations Muscutt et al. (2014) from the University of Southampton presented the results of a comprehensive series of 2D numerical simulations of tandem foils in heave and pitch using the boundary data immersion method. Epps et al. (2016) investigated the use of tandem flapping foils to mitigate the unbalanced forces and potentially increase efficiency by utilizing energy in the wake of the forward foil. This was shown both numerically (Muscutt et al., 2017b; Broering & Lian, 2012; Akhtar et al., 2007) and experimentally (Muscutt et al., 2017a; Warkentin & DeLaurier, 2007; Usherwood & Lehmann, 2008).

Within these abovementioned articles, the extent of the phase-spacing-frequency parameter space that has been explored is very limited. Work has focussed on the effects of phase alone (Rival et al., 2011; Lian et al., 2014), or the effect of phase and frequency (Broering et al., 2012), or spacing and frequency (Kinsey & Dumas, 2012). Many studies have investigated both phase and spacing, but at only one flapping frequency (Broering & Lian, 2012; Kumar & Hu, 2011; Boschitsch et al., 2014; Gong et al., 2015, 2016). One study has considered the effects of both spacing and phase at different flapping frequencies, or Strouhal numbers (Broering & Lian, 2010), although the parameter space was sparse and the experimental data consisted of combined forces of both foils, with very little information on the flow field. Therefore, the details of the mechanism responsible for the thrust augmentation and the dependence of this mechanism on the phase-spacing-frequency space remain unresolved. Moreover, the effects of all these parameters on hydrodynamic performances such as thrust, lift and propulsion efficiency are not an easy issue.

### 1.3 Thesis Outline

The structure of this thesis first and foremost reflects the way this research was conducted. Yet, it is also guided by the sequential exploration of the model, from the single oscillating foil to the tandem foil configuration in an infinite domain to the examination of more complex cases with free-surface and incident waves. The numerous results presented aim at studying both the semi-analytical and numerical models implemented and used for the oscillating foil propulsor in various situations. Moreover, they aim at demonstrating its capabilities, limitations, and performance. Throughout the text, clarity and accuracy were pursued to put forward the research's main objectives. To meet this purpose some results are explored in more depth than others.

The present chapter first introduces a chronological state-of-art review on the development of full-scale vessels and remarkable model boats propelled by wave energy. Following this introduction, the literature review offers an overview of the relevant theoretical and experimental studies in this field, giving special attention to the ones addressing the themes dealt with in this thesis.

Chapter 2 starts by discussing the oscillating foil propulsion problem introducing the main physical phenomena. It is followed by a review on 2D classical thin-wing theory, from quasi-steady to unsteady regime. The model, the physics, the phenomena involved, and the assumptions that are usually made are described. The main theoretical aspects that permeate the entire thesis are addressed. Then a 2D semi-analytical model of a single foil, building on the unsteady linear classical theory, is presented. It is first extended to include large incident flow angles, followed by analytical and empirical corrections to account for the different drag components, namely finite-span, profile, and separation effects. The model is after complemented to account for free-surface effects and then the incident wave case. Finally, an innovative analytical model for an in-line tandem foil configuration is proposed.

Chapter 3 focus on comparing both models developed in Chapter 2 with other sources. Firstly, it discusses the practical range of values for the different parameters. The results of the model, for the different cases, are compared with publish data, both numerical and experimental. The influence of the different effects on foil hydrodynamics is discussed. The

limits of the models' accuracy are studied, and the results are discussed. An example of the application of the models to parametric studies is shown.

Chapter 4 starts by reviewing numerical methods used to study this problem. It then introduces the CFD code ReFRESKO (MARIN, 2022b), which is used to solve the present numerical model, and its associated auxiliary tools. The fundamentals of the governing equations, numerical discretization schemes used to define the problem, as well as the solution methodologies are briefly presented. The computational domains, grids, and numerical set-up employed in this work are explained and detailed. This chapter concludes with basic theoretical aspects of the Verification and Validation steps that are adopted in this work.

Chapter 5 presents the results of CFD simulations for a single oscillating foil and for a tandem configuration oscillating foils, in infinite domain. The accuracy is evaluated for the different test cases, analysing the results for different types of grids as well as different amplitudes and frequencies of oscillation. The importance of turbulence is addressed. 2D and 3D simulations are compared. The errors and accuracies are studied following verification & validation procedures. Flow solutions and hydrodynamic forces are then discussed with emphasis on the understanding of the physical phenomena involved.

Chapter 6 first assesses the results for a single foil with free-surface and then with incident waves, emphasising on the understanding of the flow dynamics. Moreover, it focuses on demonstrating and discussing the capabilities of the numerical model to simulate these cases of increased complexity. It is followed by an exploratory and pioneer study of the tandem foil physical processes and performance, again both with free-surface and incident waves, following the same approach and structure of the single foil cases.

Chapter 7 summarizes the key findings of the thesis and provides suggestions for future work.

## 1.4 Main Contributions

The main contributions of the present work are:

1. A concise review of oscillating foil propulsion systems, including the role of the relevant parameters, including the hydrodynamics and physical effects involved, as well as their application limits.
2. A simple semi-analytical tool, modelling the performance of an oscillating foil propulsor is implemented. This model has enough accuracy in the interesting range of parameters and very short simulation times, showing to be a useful tool in the design optimization of these systems. It is also a suitable engineering tool for prototypes in a wide range of operating conditions. Furthermore, it is easily coupled with both the equations of motion for a passive-type spring control system and with the ship seakeeping equations of motion, allowing further research of control schemes for this system. It can also be linked to parameter optimization tools.
3. An innovative analytical model for the tandem oscillating foil propulsor is proposed that allows a wide range of studies in the very broad parameter space of these propulsion systems. The results show that this tool can be used for further optimization studies and concept development, presenting simulation times less than one minute for the most complex test cases, using a personal computer, while for the same test cases the CFD model calculations can last up to 10 days using the *Iridis5* supercomputer.
4. A numerical model for oscillating foils, both single and tandem, in calm waters and in incident waves, was implemented using the CFD code ReFRESKO. This novel approach method allows the study of large oscillations cases and pushing the limits of deforming grid CFD techniques for renewable wave energy applications. It is applicable to higher ranges of Reynolds numbers with accurate evaluation of the hydrodynamic forces and moments, and the resulting turbulence and flow visualization. It allows careful modern verification and validation of all CFD results.

5. Preliminary conclusions of the application of the developed tools to tandem foils propulsor: The simulations show the advantages of using theoretical and numeric models in a complementary manner; the results indicate that with the right parameter tuning the tandem foil can attain thrust forces almost thrice the thrust force of a single isolated foil; it was possible to obtain flow dynamics visual media to study the tandem foil in incident waves.



# Chapter 2

## Semi-Analytical Modelling

This chapter presents the formulation of the semi-analytical single and tandem foil models. The models focus on the evaluation of the different forces and propulsion efficiency generated by the oscillating foils.

### 2.1 Oscillating Foil Propulsion Overview

The work of Xiao & Zu (2014) provides a complete description of the state-of-the-art on the use of oscillating foils, as well as many important references on this topic. The hydrofoil propulsion can be classified based on several criteria, the most important of which is the type of movement (Figure 2.1). Usually, a symmetrical oscillating foil used for propulsion, immersed in a uniform incoming flow, will undergo a heaving motion in which the foil translates perpendicular to the direction of travel. It can also make a pitching motion in which the foil rotates about a spanwise axis. The combination of pitching and heaving concept (Rozhdestvensky & Ryzhov, 2003) is considered the most effective and will be used in this work.

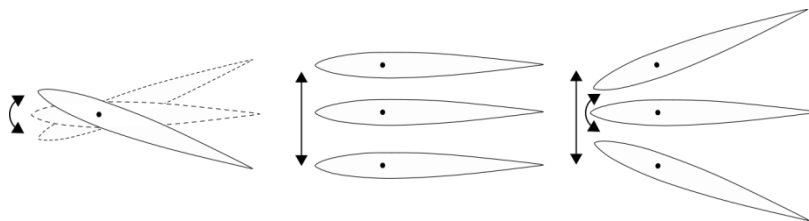


Figure 2.1: Types of oscillating foil motions; a) pitch, b) heave, c) combined heave and pitch.

These devices can also be classified into the following three categories according to the activating mechanism: with forced pitching and heaving motions, requiring powered actuators; with forced pitching and induced heaving motions (semi-activated systems), where only the pitch is controlled; and systems with self-sustained pitching and heaving motions (self-sustained systems), that rely on flow-induced instabilities (e.g. ocean waves or currents) to generate oscillatory motions in the heaving and pitching directions, using springs to provide a restitution force. In this work the first category is addressed.

The method of generating force can be classified as lift-based or drag-based. In drag-based propulsion, the foil moves in a rowing motion. This method of force generation allows more precise control of force direction useful for the low-speed, high-precision manoeuvring of a vehicle. However, lift-based propulsion is generally more efficient than drag-based force generation. It is also more suitable for travelling over long distances and at high speeds (Rozhdestvensky & Ryzhov, 2003). For this reason, the research conducted in this thesis will consider lift-based propulsion.

Depending on the incoming stream velocity and the heaving and pitching amplitudes, phases and frequencies, different foil kinematics will occur. Figure 2.2 shows three ideal cases,

with a sequence of images showing the typical positioning with respect to time: when the forces are mainly in the backward direction (power generation, where the energy flux is in the opposite direction), where the angle of attack is negative (pitch angle is larger than apparent incident flow angle); when no forces act on the foil (feathering), corresponding to zero angle of attack between the apparent incoming flow and the foil; and when the forces are mainly in the forward direction (thrust generation case where the energy flux is from the foil to the fluid), corresponding to a positive angle of attack. An example of an application for the first case is explored in the hydrokinetic turbine 2KW prototype for water current power extraction developed by Kinsey & Dumas (2012b).

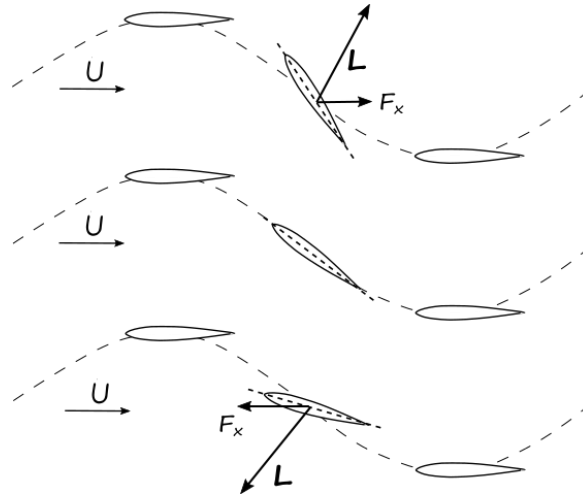


Figure 2.2: Flapping foil kinematics heaving and pitching in a steady flow; a) power generation, b) feathering, c) thrust generation.

These different fluxes of energy suggest different stability properties of the wakes, subsequently, different features in wake-body interactions. When the foil or incident flow are perturbed so that the forces on the foil change, a change in the flow field surrounding the foil will also occur. It causes a vortex to be immediately shed from the trailing edge into the wake and convected downstream, oppositely directed to the change in circulation experienced during the perturbation. Figure 2.3 shows two typical wake vortex patterns and transversal velocity perturbations, for an oscillating foil in a flow. In the former case, it forms the natural Bénard-von Kármán (BvK) vortex street, where vortices are shed in alternating sides of the foil, rotating outwardly, and creating a slower speed behind the foil, thus a drag force. This is the principle used in power generation applications mentioned above. The second case, because of the dynamics of the oscillating foil, the vortices shed are reversed, rotating inwardly (reverse BvK vortex street), and giving rise to a downstream jet profile, used for propulsion.

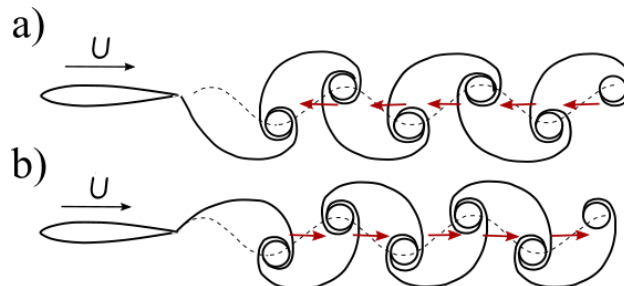


Figure 2.3: Simplified example of the wake dynamics with streamwise velocity field perturbation; a) natural BvK wake street b) reverse BvK wake street.

This last case can be better understood by looking into the different regimes of the wake of a foil in pitching oscillations and in its transitions. Figure 2.4 presents several cases in which, for a given freestream velocity and flapping frequency, the amplitude is progressively increased: the typical case of low-amplitude oscillations in case a) produces a forced wake

with features resembling a natural BvK vortex street with shedding locked in the oscillation frequency. Increasing the oscillation amplitude allows a very clear-cut view of the mechanism of reversal of vortex position: in case b) vortices of alternating signs align in the wake symmetry line and the velocity deficit is almost erased whereas in case c), the vortices shed on one side of the stroke organize themselves in the wake on the other side of the symmetry line constituting the reverse BvK vortex street, prior to the appearance of the jet profile, more clearly evident on case d), in which the relative thrust engendered overcomes the total mean drag.

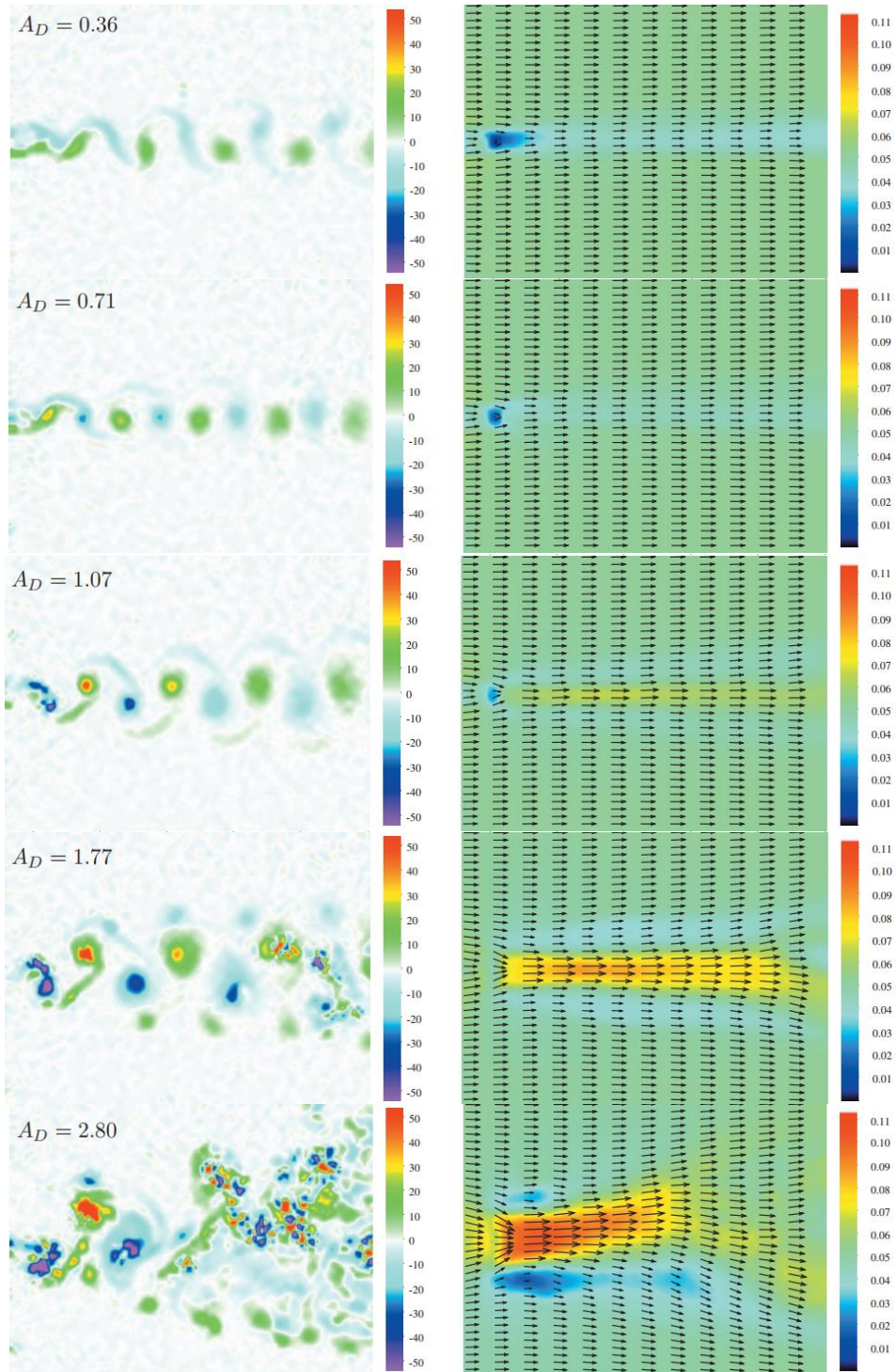


Figure 2.4: Instantaneous vorticity (left column,  $s^{-1}$ ) and mean flow (time averaged horizontal velocity, right column, m/s) of a pitching foil for different dimensionless amplitudes  $A_D$  (trailing edge excursion/maximum thickness) at  $Re = 1773$ ; a) natural BvK wake. b) natural to reverse BvK transition. c) reverse BvK wake, drag regime. d) reverse BvK wake, propulsion regime. e) deflected reverse BvK, asymmetric regime (Godoy-Diana et al., 2008).

Further increase in the oscillation amplitude triggers a symmetry breaking in the reverse BvK wake: in case e) a strong dipolar structure that propagates obliquely to one side of the symmetry line of the wake is formed in each flapping cycle, while a much weaker single vortex is shed on the other side (Godoy-Diana et al., 2008). The great majority of foil propulsion applications aim using the propulsion regime of case d). The regime of asymmetric deflected wake only very recently has been studied for tandem configuration enhancement (Lagopoulos et al., 2020).

The first set of parameters involved in the study of this system, referring to the foil, is defined by the cross-section profile, transversal planform, and aspect ratio, to which is added the position of the foil pitching axis. Symmetric NACA wing profiles and rectangular planforms are mainly adopted. The second set of parameters regards flow characteristics, namely the freestream velocity as well as the fluid density and viscosity. The Reynolds number is broadly used to characterize the flow. In most existing studies, there is the assumption that the foil undergoes sinusoidal motions in both heaving and pitching directions. Several kinematic parameters describe this problem quantitatively, including heaving and pitching amplitudes, frequency, and the phase lag between both motions. Among them, two forms of non-dimensional frequency are adopted by most researchers: reduced frequency based on chord and Strouhal number based on heaving amplitude that denotes the characteristic width of the created jet flow (see Figure 2.4). Additionally, the feathering parameter denotes the ratio of the foil slope to the slope of the path travelled by the pitching axis of the oscillating foil. This last parameter defines the different cases presented in Figure 2.2. These parameters will be defined in the following sections.

In addition to parameter optimization, different mechanisms have been explored to enhance propulsion performance. Most investigations of the effect of kinematic parameters on propulsion efficiency are based on sinusoidal motions, which are the most fundamental harmonic profile for a flapping motion. However, in nature, the high propulsion efficiency of flying and swimming animals might be achieved by non-sinusoidal locomotion trajectories. Inspired by this biological mechanism, the influence from non-sinusoidal oscillation motions has been studied (Ashraf et al., 2011). Biomechanical studies on the surface pattern of a dragonfly wing indicate that a corrugated structure with various ‘tabulators’ on it can enhance the aerodynamic performance via increased lift and reduced drag (see for example Kesel, 2000). The unsteady vortices generated inside valleys formed by the pleats can effectively control the flow separation size by changing the laminar boundary layer to a turbulent one. Inspired by this biological concept, new models with corrugated foils have been proposed (Le et al., 2013). Structural flexibility is known to have beneficial effects on the performance of flapping foils in force generation. For example, previous studies on insect wings and fish fins suggest that a certain degree of flexibility may lead to the generation of higher thrust or lift forces. In nature, fish swim in schools and birds fly in flocks to save energy expenditure through interactions between neighbours. Previous studies on live fish or tandem/parallel oscillating foil propulsors have proven that, with a proper distance between two adjacent foils, the energy of previously shed vortices can be effectively utilized to increase the thrust generation (e.g., Zhu et al., 2012; Deng et al., 2007). This latter mechanism has been predominantly adopted by commercial ASVs in either parallel (WDPS) or tandem configurations (WaveGlider and Autonaut). Thus, since the concept of tandem configuration is currently the one that presents the best results, this investigation takes it up as its object of study.

## 2.2 Classical Theory

In this section we briefly review the potential flow theory formulation of the hydrodynamics of 2D hydrofoils. The focus is on the propulsion characteristics of rigid hydrofoils performing periodic oscillations in combined heave and pitch motions while advancing with a constant speed.

Firstly, we consider the problem of a two-dimensional infinitely thin hydrofoil moving in an unbounded ideal fluid at rest at infinity. Its core assumption is that the camber and thickness

of the foil are small compared to its chord  $c$  (typically foils with  $t/c = 0.06-0.12$ ) (Minsaas & Steen, 2008). Assumptions for an ideal fluid are that there is no vorticity in the flow field except with a net circulation around the foil and there are no viscous effects. It will be further considered that the heave and pitch motions introduce small perturbations to the steady forward motion of the foil. In this case, it is possible to linearize the kinematic boundary condition on the foil surface and separate the effect of thickness from the effect of camber. To determine the lift force acting on the hydrofoil it suffices to consider the infinitely thin camber line of the foil performing the heave and pitch motions while advancing at a constant speed. The foil motions are assumed to consist of a constant forward velocity  $U$  directed to the negative  $x_0$  axis of a space-fixed Cartesian coordinate system  $(x_0, y_0)$ , and a small lateral motion in the  $y_0$  direction. A moving coordinate system  $(x, y)$  with undisturbed velocity  $U$  is defined by the transformation

$$x = x_0 + Ut, y = y_0. \quad (2.1)$$

Accordingly, at infinity the fluid velocity in the moving reference frame is  $(U, 0)$  pointing in the positive  $x$  direction. The origin  $O$  of the coordinate system  $(x, y)$  is considered to be at mid-chord of the foil (see Figure 2.5).

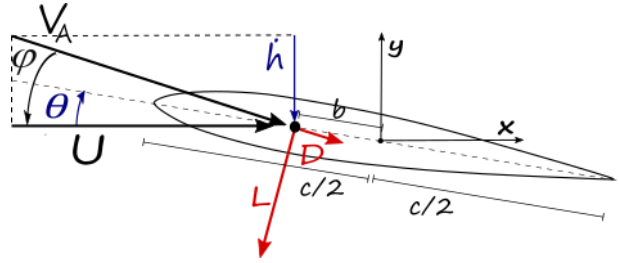


Figure 2.5: Model coordinate system.

The fluid motion due to the unsteady motion of the foil is described by the gradient of a perturbation velocity potential  $\phi(x, y, t)$  to the free-stream potential  $\phi_\infty = Ux$ , satisfying the Laplace equation in the fluid domain. The potential must satisfy the boundary conditions set for this problem: the kinematic condition in which no fluid can flow through the foil surface i.e., the velocity vector is tangential to the surface, and the infinite condition, where the perturbation of the velocity should tend to zero at infinity. In addition, a Kutta condition should impose smooth tangential flow at the sharp trailing edge or in other words that the velocity vector must be finite.

To solve this problem, the circulation around the foil is modelled by a vortex distribution along the chord length, aligned with the  $x$  axis. This vortex distribution specifies the difference in velocities at the upper and lower sides of the foil, giving rise to pressure differences between the two sides. The resultant pressure force or lift  $L$ , is directed perpendicular to the incoming flow direction. Also, the foil is subject to a rotational force moment  $M$ , with axis at the pressure centre point. In a real situation there is also a resistance force in-line with the motion, which will be considered in the next section. However, such force is not considered within 2D linear foil theory. It is also assumed that the heave and pitch motions of the plate are harmonic, with angular frequency  $\omega_0$  respectively:

$$h = h_0 e^{i\omega_0 t} \text{ and } \theta = \theta_0 e^{i\omega_0 t}, \quad (2.2)$$

where  $h_0$  and  $\theta_0$  are complex constant amplitudes with heave-pitch phase difference  $\psi$ . Assuming a quasi-steady approach, both the heave and pitch angular motion will cause a perturbation on the vertical velocity field, resulting in an apparent opposite direction velocity: The apparent incident velocity  $V_A$  will be at a quasi-steady inflow angle  $\varphi$  (Bøckman, 2015):

$$\varphi = \text{atan} \left[ \frac{\dot{h} + a \left( b^* - \frac{1}{2} \right) \dot{\theta}}{U} \right], \quad (2.3)$$

with the half-chord length,  $a=c/2$  and  $b^* = b/a$ .  $b$  is the coordinate of the rotating axis, negative from leading edge to mid-chord. Based on the assumptions taken, Equation (2.3) is then linearized. The effective angle of attack is  $\alpha = \varphi - \theta$ . The quasi-steady lift coefficient, defined perpendicular to the apparent incident velocity can be written:

$$C_{L,qs} = -2\pi(\varphi - \theta). \quad (2.4)$$

The actual lift force is defined by:

$$L = \frac{1}{2}\rho U^2 c C_{L,qs}, \quad (2.5)$$

with  $\rho$  the water density. In the unsteady case, the time dependence of the foil or incident flow perturbations causes the forces on the foil to change. Therefore, it affects the flow field surrounding the foil, implying that the circulation around the foil also changes. In order to comply with Kelvin's theorem, a vortex is immediately shed from the trailing edge into the wake and convected downstream. The vortex is oppositely directed to the change in circulation experienced during the perturbation. Thus, for a 2D foil experiencing a continuous oscillating flow situation, a continuous vortex sheet will be shed into the wake, as presented in the previous section. This vortex street will induce velocities in the fluid domain, in turn influencing the velocities in front of the foil, hence also the instantaneous angle of attack. Since the magnitude of the shed vortices depend on the magnitude of the perturbations the foil experience, the time history of the foil oscillation will influence the instantaneous angle of attack, hence the magnitude and direction of the lift.

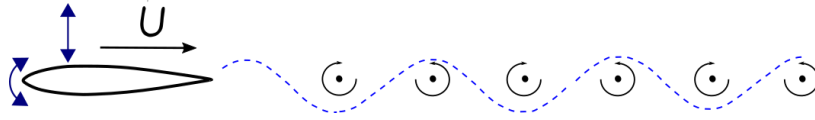


Figure 2.6: Flattened vortex wake on an oscillating foil.

Theodorsen (1935) unsteady theory provides a model to account for these memory effects associated with the vortex shedding. The wake is modelled by a straight-line vortex distribution behind the foil, extending from the trailing edge to infinity, and the wake vorticity travels at free stream speed (Figure 2.6). The theory is presented in Newman (1978), and it is described in Appendix A for the sake of completeness. The important result of this theory is that the unsteady lift  $L$  can be written as the sum of two terms: a non-circulatory lift term  $L_{NC}$  due to time rate of change on the foil velocity resulting in flow acceleration, called added mass, and the time rate change on circulation around the foil that is balanced by vortex shedding into the wake, which results in a change in the circulatory lift term  $L_C$ . This last term can be expressed by the quasi-steady term  $L_{C,qs}$ , multiplied by the Theodorsen function  $C(k_f)$ . The argument in this function is the reduced frequency  $k_f = \omega_0 c / 2U$ . The modulus of this function gives the lift loss caused by the wake and the imaginary part introduces its change in phase:

$$L = L_C + L_{NC} = C(k_f)L_{C,qs} + L_{NC}. \quad (2.6)$$

The non-circulatory lift or added mass term is the inertia added by the acceleration of the fluid surrounding the foil in its motion. One component results from heave motion, which is vertical, and other from the pitch motion, which is normal to the plate. Since it is assumed that

the horizontal velocity field perturbations are negligible, the total lift vector  $L_{NC}$  is considered to be vertical with amplitude given by (Bøckman, 2015):

$$L_{NC} = -\pi\rho a^2[\ddot{h} - U\dot{\theta} + ab^*\ddot{\theta}]. \quad (2.7)$$

The total moment acting on the foil depends on the point of rotation  $b$ , positive with nose down (counterclockwise), and has also two components:

$$M = M_C + M_{NC}. \quad (2.8)$$

The circulatory moment caused by the circulatory lift, that is zero on the pressure center at quarter chord point of the foil, is given by

$$M_C = -a\left(b^* + \frac{1}{2}\right)L_C. \quad (2.9)$$

The non-circulatory moment is given by

$$M_{NC} = M_{NC1/4} - a\left(b^* + \frac{1}{2}\right)L_{NC}, \quad (2.10)$$

or alternatively (Bøckman, 2015)

$$M_{NC} = \pi\rho a^2\left[ab^*\ddot{h} - a\left(b^* - \frac{1}{2}\right)\dot{\theta}U + a^2\left(b^{*2} + \frac{1}{8}\right)\ddot{\theta}\right]. \quad (2.11)$$

With the moment coefficient defined by

$$C_M = \frac{M}{\frac{1}{2}\rho U^2 c^2}, \quad (2.12)$$

the lift and moment expressions of Equations (2.6), (2.7) and (2.11) can be rewritten using non-dimensional parameters (see Equations (A.36), (A.37) and (A.40)):

$$L_C = (\rho a U^2)[-2\pi C(k_f)h_0^*]\left\{ik_f\left[1 + \left(b^* - \frac{1}{2}\right)\theta_0^*\right] - \theta_0^*\right\}e^{i\omega_0 t}, \quad (2.13)$$

$$L_{NC} = (\rho a U^2)[- \pi h_0^*]\{-k_f^2[1 + b^*\theta_0^*] - ik_f\theta_0^*\}e^{i\omega_0 t}, \quad (2.14)$$

$$M_C = (2\rho a^2 U^2)\left[\pi C(k_f)h_0^*\left(b^* + \frac{1}{2}\right)\right]\left\{ik_f\left[1 + \left(b^* - \frac{1}{2}\right)\theta_0^*\right] - \theta_0^*\right\}e^{i\omega_0 t}, \quad (2.15)$$

$$M_{NC} = (2\rho a^2 U^2)\left[\frac{\pi}{2}h_0^*\right]\left\{-k_f^2\left[b^* + \left(b^{*2} + \frac{1}{8}\right)\theta_0^*\right] - ik_f\left(b^* - \frac{1}{2}\right)\theta_0^*\right\}e^{i\omega_0 t}, \quad (2.16)$$

where  $h_0^* = h_0/a$ ,  $\theta_0^* = \theta_0/h_0^*$ . The Strouhal number can be related with reduced frequency with  $\pi S_t = h_0^* k_f$ .

Usually, in the classic theory, to evaluate the thrust produced by the foil motions, two basic contributions to the force component in the direction of the foil advance velocity (Lighthill, 1970) are considered: The component of the foil lift force acting in the direction of motion when the foil is inclined at the instantaneous pitch angle and the suction force at the sharp cusped leading edge for a foil with zero thickness. The thrust is a second order quantity when the motions are assumed small as considered in the linearized theory described previously. The first contribution results from the product of the first order lift with the first order pitch angle which is a second order quantity. The suction force, on the other hand, is known to be a second order quantity resulting from the squared velocity neglected in the linearization. However, in this thesis the evaluation of thrust follows a different method, presented in the next section.

## 2.3 Single Oscillating Foil

In this Section, the 2D semi-analytical model is developed, first by extending the classical unsteady theory approach to account for large inflow angles that arise in the hydrofoil propulsion problem, and then by introducing the drag effects. Instead of using the suction force approach, here we account for the apparent inflow velocity as reference.

In the derivation of the Theodorsen function, small disturbances are assumed. However, Leishman (2006) states that the Theodorsen function is suitable for flow oscillation amplitudes of up to 70% of the uniform incoming flow. Thus, the linear theory limitation for large incident angles can be overcome replacing  $U$  by  $V_A = U/\cos \varphi$  in the lift definition in Equations (2.13) to (2.16) (Leishman, 2006). The quasi-steady angle  $\varphi$  is then given by using Equation (2.3) instantaneously without the usual linearization, here rewritten using the non-dimensional parameters

$$\varphi(t) = \text{atan} \left( ik_f h_0^* \left[ 1 + \left( b^* - \frac{1}{2} \right) \theta_0^* \right] \right) e^{i\omega_0 t}. \quad (2.17)$$

The circulatory lift is then perpendicular to the apparent inflow while the non-circulatory lift is here assumed to be perpendicular to the plate.

### 2.3.1 Drag

The drag is a force perpendicular to the lift that counter acts the forward motion of the foil and represents energy losses. It has several contributions that can be evaluated with both analytical and empirical methods, including viscous effects that are not included in the previous potential theory. This force can be decomposed in inviscid induced drag, profile drag, separation drag, and wave drag. The first arises from 3D pressure effects due the foil finite aspect ratio, and the second accounts for the friction and form drag of the foil. The separation drag becomes important for large amplitudes of the angle of attack. The last is caused by the presence of a free-surface. The drag coefficient is given by

$$C_D = \frac{D}{\frac{1}{2} \rho c U^2}. \quad (2.18)$$

The modelling of the first three effects is first approached by quasi-steady modelling and then included in the unsteady model of the previous section.

Induced drag or potential drag arises due to a spanwise circulation distribution over the foil (Figure 2.7) and it depends on its shape.

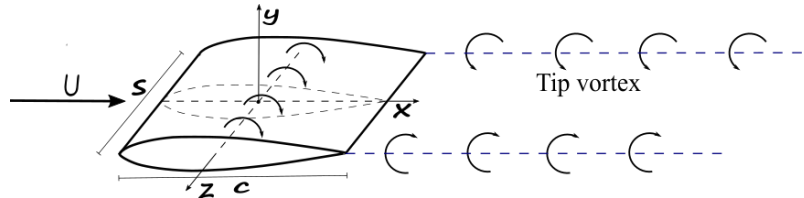


Figure 2.7: 3D foil with tip vortex effect.

When finite span or 3D effects are taken into account in the 2D model, the work per unit of time done by the induced drag will equal the kinetic energy passed to the fluid per unit of time on the trailing vortex sheet downstream the foil trailing edge. It causes the reduction of lift and increases the drag. For a steady elliptical foil with high-aspect-ratio, the Lifting-Line Theory of Prandtl (Newman, 1978) shows that the lift reduction can be rewritten in terms of the aspect ratio and the induced drag can be expressed in terms of the lift:

$$\frac{C_L}{C_{L2D}} = \frac{1}{1 + 2/\Lambda}, \quad (2.19)$$

and

$$C_{Di} = \frac{1}{\pi e \Lambda} C_L^2, \quad (2.20)$$

being the aspect ratio given by  $\Lambda = s^2/A$ , where  $A$  is the planform area of the foil,  $s$  the foil span length and  $e$  the planform efficiency factor.  $C_{L2D}$  is the lift coefficient for infinite span. According to Doctors (1986) the lift coefficient ratio between rectangular and elliptic foils is 96.7-96.2% for aspect ratios  $\Lambda = 4$  to 10. Thus, this theory can also be extended to rectangular shaped foils. Because Prandtl's theory over predicts the lift coefficient, DuCane (1972) proposes the following approximation:

$$\frac{C_L}{C_{L2D}} = \frac{1 - 2/\Lambda^2}{1 + 2/\Lambda}. \quad (2.21)$$

Figure 2.8 presents the variation of the lift coefficient with the aspect ratio, showing the approximation Equation (2.21) used in this work and other methods. The present approximation has a discrepancy from numerical results (van Dyke, 1975) of less than 2.5% for aspect ratios  $\Lambda > 4$ .

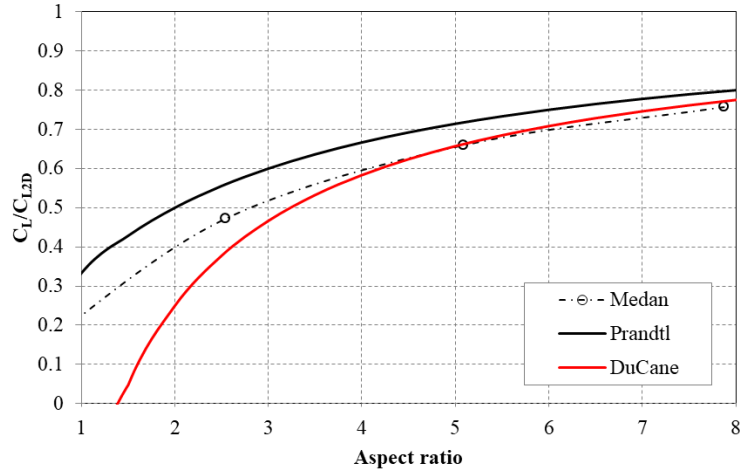


Figure 2.8: Lift coefficient reduction with aspect ratio  $\Lambda$ . Comparison between Prandtl lifting-line theory, Medan numerical model (van Dyke, 1975) and DuCane (1972) correction, adopted in this work.

Profile drag arises from the effect of viscosity including the friction on the foil surface and the contrary pressure forces due to the foil form. This work uses the expression provided by Hoerner (1965) that estimates the drag of a symmetrical foil with smooth surface in steady inflow. The zero-lift profile drag coefficient  $C_{D,p0}$  is given by (Faltinsen, 2005):

$$C_{Dp0} = 2C_F(1 + t^* + 3.75t^{*4}), \quad (2.22)$$

where  $t^* = t/a$  is the non-dimensional foil thickness. The first term is the skin friction of a flat plate, the second introduces the thickness correction and the last is the adverse pressure forces originating on the frontal area and rear section of the foil. This last term applies to foils with maximum thickness located near 30% of the chord.  $C_F$  is the flat plate friction coefficient. The viscosity only matters within a thin layer close to the plate, referred to as the boundary layer where the flow can be laminar or turbulent. Turbulent flow is characterized by the irregular movement of fluid's particles, in contrast to laminar flow where fluid flows in parallel layers.

Hoerner considers combined laminar and turbulent flow, where the friction coefficient depends on the chordwise location of the boundary transition point. This transition point is function of foil geometry, angle of attack and Reynolds number  $R_e = \rho U c / \mu$  with  $\mu$  being the dynamic viscosity. Blasius solution (Hoerner, 1965) for the case of laminar flow along a smooth flat plate is:

$$C_F = \frac{1.328}{\sqrt{R_e}}, \quad (2.23)$$

and the Prandtl-von Kármán expression (Hoerner, 1965) for turbulent flow is given by:

$$C_F = \frac{0.074}{\sqrt[5]{R_e}}. \quad (2.24)$$

Both these expressions are seen to be good approximations at low Reynolds numbers  $10^3 < R_e < 10^6$  while Prandtl-Schlichting formula (Hoerner, 1965) is recommended for turbulent boundary layers at higher Reynolds  $10^6 < R_e < 10^9$ :

$$C_F = \frac{0.445}{(\log_{10} R_e)^{2.58}}. \quad (2.25)$$

Based on Ohtake et al. (2007) data, the present model, for simplicity, assumes that the flow has a transition from laminar to turbulent regime at  $R_e = 1.5 \times 10^4$  and to high Reynolds at  $R_e = 2.5 \times 10^5$ . Figure 2.9 shows a comparison of the zero-lift profile drag coefficient  $C_{Dp0}$  for a NACA0012 between the present method and experimental data (Ohtake et al., 2007). Results of Blasius, Prandtl-von Kármán and Prandtl-Schlichting expressions for a flat plate are also shown. The results of the present method agree sufficiently well with experimental data for the intended application.

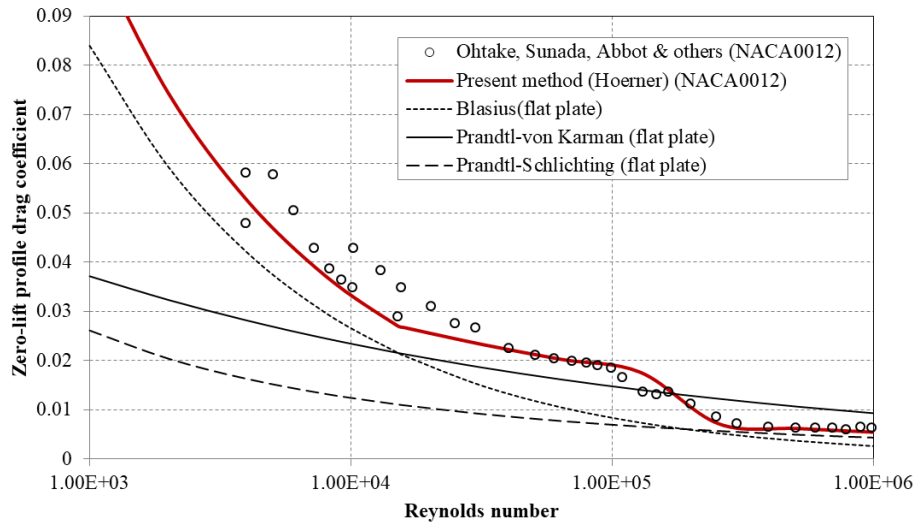


Figure 2.9: Zero-lift profile drag coefficient  $C_{Dp0}$  for a NACA0012 foil at low Reynolds numbers. Comparison between experimental data from Ohtake, Sunada, Abbot, and other authors (Ohtake et al., 2007) and the present model, adapted from Hoerner (1965). Blasius (laminar), Prandtl-von Kármán (turbulent-low Reynolds), Prandtl-Schlichting (turbulent-high Reynolds) methods for a flat plate are also plotted.

The drag increases with the angle of attack because of the flow around the leading-edge and subsequent moment losses. The pressure drag correction for a foil with an angle of attack can be empirically related with the lift coefficient. In this work, the lift profile coefficient  $C_{D,pa}$  is approximated using the following expression (Hoerner, 1965):

$$C_{D,p\alpha} = C_{D,p0} K_{\alpha} C_L^2, \quad (2.26)$$

with  $K_{\alpha} = 2.5$  an empirical factor, obtained here using Ohtake experimental data (see Figure 2.11).

Drag separation or stall results of flow detachment from the foil, with the increase of effective angle of attack beyond a certain critical point. Physically, the phenomenon is characterized first by the building-up of a vortex at the leading edge, which detaches and is convected downstream in the wake, see Figure 2.10 (Leishman, 2002). In an unsteady regime the foil can operate beyond static stall angles, as the flow on the upper surface only becomes fully separated when trailing edge vortex shedding starts to happen. Since the present approach uses a steady model for the profile drag, dynamic stall modelling is not included. The separation drag coefficient  $C_{D,ps}$  is accounted for with Migeotte (1997) empirical expression (see also Hoerner, 1965), assuming steady inflow and laminar flow separation:

$$C_{D,ps} = 2C_F 70(t^* + \sin\alpha_0)^4, \quad (2.27)$$

where  $\alpha_0$  is the maximum amplitude of the angle of attack.

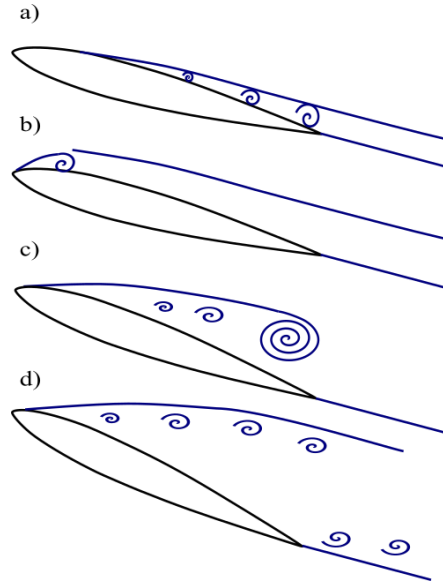


Figure 2.10: Separation effect; a) foil exceeds static stall angle, flow reversals appear in boundary layer, b) flow separation at leading edge, formation of a vortex c) vortex convects along the chord, inducing extra lift, d) lift stall, flow enters in full separation state. Adapted from Leishman (2002).

The total profile drag is then:

$$C_{D,p} = C_{D,p0} + C_{D,p\alpha} + C_{D,ps}. \quad (2.28)$$

This method is compared with the experimental steady inflow profile drag coefficient - angle of attack curve for a NACA0012 at  $Re = 4 \times 10^4$  given by Ohtake (Figure 2.11). The curve shows a bucket form of low drag near the zero-lift point, also reported by other authors (Faltinsen, 2005), that is not captured by the model, with discrepancies up to 23% for  $AoA = \pm [5^\circ - 15^\circ]$ . For the present work, aiming at simplicity, it is considered acceptable, since profile drag is not expected to be the major effect.

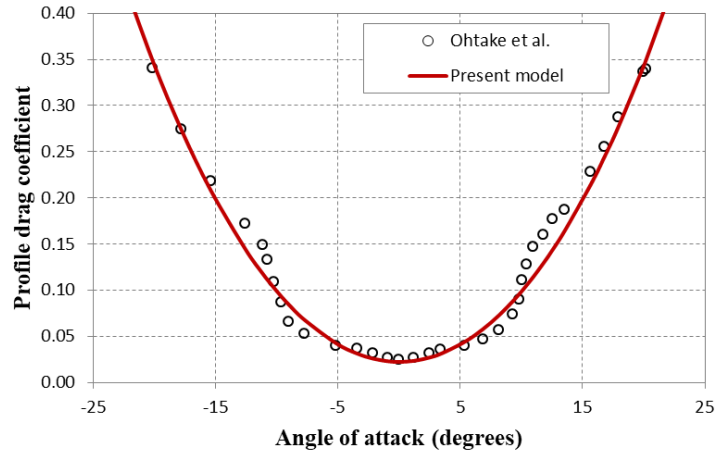


Figure 2.11: Comparison with experimental profile drag coefficient  $C_{D,p}$  curve for different angles of attack, for a steady inflow NACA0012 profile at  $Re = 4 \times 10^4$  (Ohtake et al., 2007).

### 2.3.2 Free-Surface Effects

The radiation wave drag is caused by the presence of a free-surface. While the previous effects referring to an infinite domain have been often studied and the analytical approaches have proven to be reliable, the introduction of a free-surface boundary presents a more complicated problem. The presence of a free-surface induces different effects that decrease with the submergence depth of the foil. The pressure variation above the moving hydrofoil distorts the water surface, radiating waves associated with both steady translation of the body and flapping oscillation. This energy loss affects the lift of the foil (Figure 2.12). DuCane (1972) explains that this effect is relatively complex, but approximations can be made: by considering the lift loss due to pressure relief as a function of foil depth calculated at an infinite Froude number and calm water; and by considering the change in angle of the lift vector due to the wave radiation effect. The Froude number relates the inertial forces with the gravity forces and can be used as a non-dimensional flow velocity, given by

$$F_r = \frac{U}{\sqrt{gc}}. \quad (2.29)$$

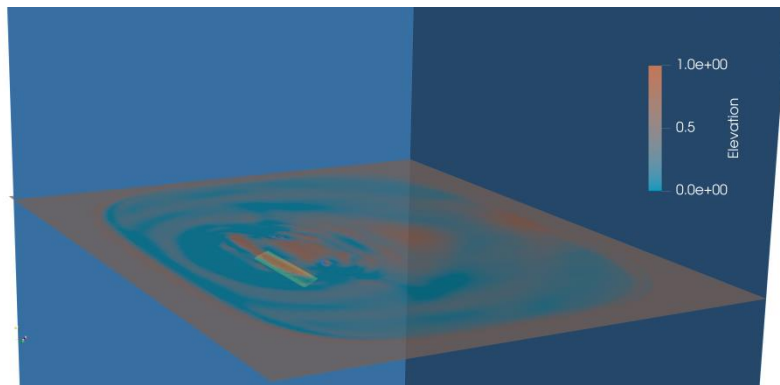


Figure 2.12: Example of the time history of the free-surface elevation, generated by a travelling and oscillating fully immersed hydrofoil.

DuCane proposes an approximation for the lift loss ratio, by multiplying the lift-curve slope by a lift-loss factor  $k_{fs}$  given by the quarter-three-quarter-chord Weissinger approximation for high Froude numbers (Doctors, 1985). In this work we include also the Weissinger approximation for low Froude numbers (Faltinsen, 2005)

$$k_{fs} = 1 + \frac{1}{(4d^*)^2} \quad \text{when } F_r \rightarrow 0 \quad (2.30)$$

$$k_{fs} = \frac{(4d^*)^2 + 1}{(4d^*)^2 + 2} \quad \text{when } F_r > 10, \quad (2.31)$$

assuming Equation (2.30) for  $F_r \leq 1$  and Equation (2.31) for  $F_r > 1$ . The correction in the angle of attack is accounted for by (Doctors, 1985)

$$\frac{\Delta\alpha_{fs}}{C_L} = \frac{1}{2F_r^2} e^{-\frac{2d^*}{F_r^2}}, \quad (2.32)$$

with  $d^* = d/c$ . Combining these two expressions it is possible to obtain:

$$\frac{C_L}{C_{L\infty}} = 1 / \left[ \frac{1}{k_{fs}} + 2\pi \left( \frac{1}{2F_r^2} e^{-\frac{2d^*}{F_r^2}} \right) \right], \quad (2.33)$$

where  $C_{L\infty}$  is the lift coefficient in infinite domain.

The free-surface effect on the lift of a steady flat plate with given speed and angle of attack in calm waters is studied in detail by Hough (1969), based on a vortex distribution nonlinear method using a Neumann type boundary condition. The present expression is compared in Figure 2.13 with his results, with good agreement, but with quantitative differences for  $F_r < 0.8$  and  $d^* < 1$ .

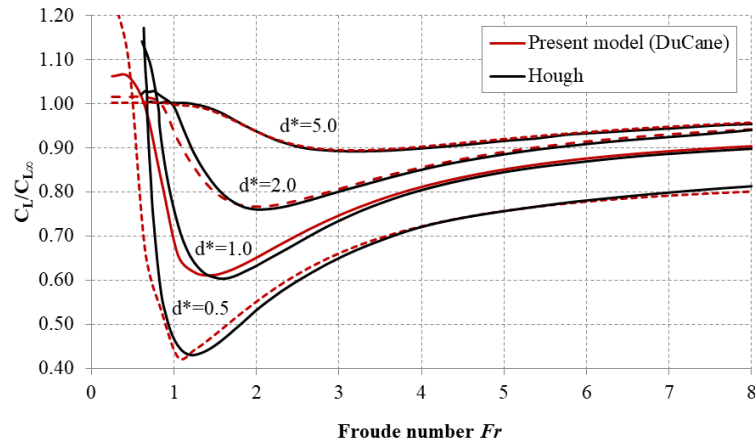


Figure 2.13: Lift loss varying with non-dimensional depth  $d^*$  and Froude number  $F_r$ . Comparison between present results and Hough (1969).

The expression is then incorporated in the unsteady model through the replacement of  $d^*$  in Equations (2.30), (2.31) and (2.33) by the instantaneous non-dimensional effective depth

$$d^*(t) = d^* - h/a, \quad (2.34)$$

where  $h$  is the heave motion of the foil given by Equation (2.2).

The wave resistance is due to the movement of the foil, which in the presence of the free-surface generates surface waves that may transport a considerable amount of momentum. This momentum can be positive or negative leading to increase or decrease of thrust, depending on properties of the waves. At a large distance from the foil the waves will be sinusoidal with wavenumbers  $k_1$ ,  $k_2$ ,  $k_3$  and  $k_4$  (Isshiki, 1984; Grue et al., 1988) (Figure 2.14). The first two waves are following waves because they have positive phase velocities. However, because the  $k_2$  wave also has positive group velocity, it will be located upstream, while the  $k_1$  has negative

group velocity so is located downstream.  $k_3$  e  $k_4$  are heading waves, and have both negative phase and group velocities so, they are located downstream.

All the other waves add to negative thrust or resistance but  $k_4$  contributes to positive thrust (Grue et al., 1988). The respective non-dimensional wavenumbers are:

$$k_{1,2}a = \frac{1}{4F_r^2} \left( 1 - 4F_r^2 k_f \pm \sqrt{1 - 8F_r^2 k_f} \right) \quad (2.35)$$

$$k_{3,4}a = \frac{1}{4F_r^2} \left( 1 + 4F_r^2 k_f \pm \sqrt{1 + 8F_r^2 k_f} \right), \quad (2.36)$$

where  $\pm$  corresponds to 1 and 2 in Equation (2.35) and to 3 and 4 in Equation (2.36), respectively. For  $F_r^2 k_f < 1/8$ , corresponding to the critical wavenumber, all four waves exist and  $k_1$  and  $k_2$  are dominant. When  $F_r^2 k_f > 1/8$ , corresponding to higher speed or frequency, only  $k_3$  and  $k_4$  exist, i.e., there are no radiated waves in front of the foil, and  $k_4$  is most pronounced (Grue et al., 1988).

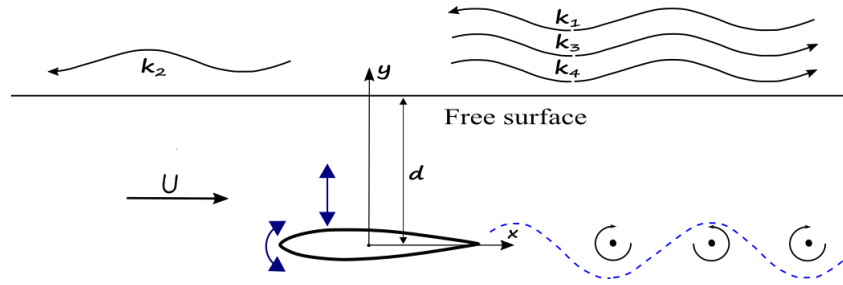


Figure 2.14: Radiated waves generation by a foil near the surface.

Maruo's (1963) theory for an oscillating foil estimates the resistance force caused by the radiated waves by using their amplitudes generated by the concentrated singularities expressing the lift and the moment obtained in the infinite domain case. It may be reduced to the 2D case by comparing the derived expression to the resistance of an infinite cylinder moving in head seas. This work is presented in Isshiki (1982) from which the following expressions are borrowed. The mean wave radiation resistance for following waves  $i = 1,2$  and for heading waves  $i = 3,4$  is given by

$$\bar{R}_{wr,12,34} = \frac{(k_i a)^2 F_r^2 e^{-(k_i a) 4d^*} [\tilde{L}^2 + (k_i a)^2 \tilde{M}^2]}{2\sqrt{1 \mp 8F_r^2 k_f} \rho a U^2}, \quad (2.37)$$

where  $\tilde{L}$  and  $\tilde{M}$  are the complex amplitudes of the total lift and moment, for mid-chord ( $b^* = 0$ ), given by Equations (2.13) to (2.16),  $L = L_C + L_{NC} = \tilde{L} e^{i\omega_0 t}$  and  $M = M_C + M_{NC} = \tilde{M} e^{i\omega_0 t}$ . The total mean wave radiation resistance is given by

$$\bar{R}_{wr} = \sum_{i=1,2,3} \bar{R}_{wr,i} - \bar{R}_{wr,4}. \quad (2.38)$$

### 2.3.3 Incident Wave Effects

The presence of incident waves adds highly relevant effects on oscillating foil dynamics. Henceforth, we will consider the effect on the forces acting on the hydrofoil from a fluid velocity field created by an incoming wave with amplitude  $a_0$  and wavelength  $\lambda$  (Figure 2.15).

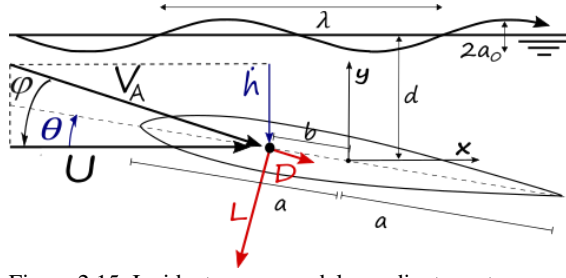


Figure 2.15: Incident waves model coordinate system.

The foil advances with constant horizontal velocity  $U$  at the average depth  $d$ . In addition, it performs heave and pitch harmonic oscillations of small amplitude, such that it may be assumed that the undisturbed incident wave field velocity on the foil may be evaluated at the constant depth  $d$ . The wave phase lag  $\phi_w$  is defined to be at  $0^\circ$  when the wave frame of reference has been fixed at the wave crest i.e., the foil is at its topmost position and about to go downwards, and the vertical component of the wave orbital velocity is also about to go downwards. Similarly,  $\phi_w = -180^\circ$  when the wave frame it is at the wave trough. For the present analysis, we consider that the incident wave problem is independent of the free-surface effects. The heading wave profile  $\zeta_0$  can be given by

$$\zeta_0(x, t) = a_0 e^{i(\omega_0 t - kx + \phi_w)}, \quad (2.39)$$

where the wavenumber is  $k = 2\pi/\lambda$  and the encounter angular frequency is

$$\omega_0 = \sqrt{gk} + kU. \quad (2.40)$$

Maintaining the assumption of an infinite domain, the vertical component of the water particles velocity  $V_0$  at the foil surface, considering the foil at the submergence of  $d$  is:

$$V_0(x, t) = iA_0 e^{i(\omega_0 t - kx + \phi_w)}, \quad (2.41)$$

with the wave orbital velocity amplitude

$$A_0 = a_0^* \sqrt{g(ka)} e^{-(ka)2d^*} e^{i\phi_w}, \quad (2.42)$$

using  $a_0^* = a_0/a$  and the non-dimensional wavenumber  $ka$ .

Physically, as stated before, perturbations on the incident flow will also cause a vortex sheet to be shed downstream, influencing the instantaneous angle of attack. Isshiki (1983), in his third report, also based on the unsteady foil theory, describes the interaction of the fluid and the foil in terms of the Theodorsen function and Bessel functions of first kind for zeroth, first and second integer order. The complete formulation can be found in Appendix B, where it is presented a simplified solution to the problem, considering a fixed foil in incident waves. The complete solution is now provided: the solution of the oscillating foil without waves is added to the solution of a fixed foil in incident waves, with the  $U$  replacement by  $V_a$ , Equations (2.13) to (2.17) become:

$$L_C = \frac{\rho a U^2 [-2\pi C(k_f) h_0^*]}{\cos^2 \varphi} \left\{ ik_f \left[ 1 - H_0^* J_0(ka) - iJ_1(ka) \right] + \left( b^* - \frac{1}{2} \right) \theta_0^* \right. \\ \left. - \theta_0^* \right\} e^{i\omega_0 t}, \quad (2.43)$$

$$L_{NC} = \frac{\rho a U^2 [-\pi h_0^*]}{\cos^2 \varphi} \left\{ -k_f^2 \left[ 1 - H_0^* \frac{2J_1(ka)}{ka} + b^* \theta_0^* \right] - ik_f \theta_0^* \right\} e^{i\omega_0 t}, \quad (2.44)$$

$$M_C = (2\rho a^2 U^2) \left[ \pi C(k_f) h_0^* \left( b^* + \frac{1}{2} \right) \right] \left\{ ik_f \left[ 1 - H_0^* J_0(ka) - iJ_1(ka) \right] + \left( b^* - \frac{1}{2} \right) \theta_0^* \right\} e^{i\omega_0 t}, \quad (2.45)$$

$$M_{NC} = \frac{2\rho a^2 U^2}{\cos^2 \varphi} \left[ -\frac{\pi}{2} h_0^* \right] \left\{ k_f^2 \left[ b^* - H_0^* \left( b^* \frac{2J_1(ka)}{ka} + i \frac{J_2(ka)}{ka} \right) + \left( b^{*2} + \frac{1}{8} \right) \theta_0^* \right] - k_f \left[ H_0^* (J_1(ka) - iJ_2(ka)) + i \left( b^* - \frac{1}{2} \right) \theta_0^* \right] \right\} e^{i\omega_0 t}, \quad (2.46)$$

$$\varphi = \text{atan} \left( ik_f h_0^* \left[ 1 - H_0^* J_0(ka) - iJ_1(ka) \right] + \left( b^* - \frac{1}{2} \right) \theta_0^* \right) e^{i\omega_0 t}, \quad (2.47)$$

with the non-dimensional wave orbital velocity amplitude:

$$H_0^* = \frac{A_0}{U k_f h_0^*} = \frac{a_0^*}{h_0^*} \left( \frac{\sqrt{ka}}{\sqrt{2} F_r k_f} \right) e^{-(ka)2d^*} e^{i\phi_w}, \quad (2.48)$$

where  $J_n(ka)$  are Bessel functions of the first kind. For the present application, considering the typical wavenumbers in West Coast of Portugal and chord length smaller than 1 m,  $ka \ll 1$  (see Section 2.5 for details), allows the approximations  $J_0(ka) \approx 1$ ,  $J_1(ka) \approx J_2(ka) \approx J_2(ka)/ka \approx 0$  and  $J_1(ka)/ka \approx 1/2$  through the use of the Bessel functions' Taylor series and recursive relations (Abramowitz & Stegun, 1972). To better understand this effect, its application to the previous Equations leads to the simplifications:

$$\varphi = \text{atan} \left( ik_f h_0^* \left[ 1 - H_0^* \left( b^* - \frac{1}{2} \right) \theta_0^* \right] e^{i\omega_0 t} \right), \quad (2.49)$$

$$L_C = \frac{\rho a U^2 [-2\pi C(k_f) h_0^*]}{\cos^2 \varphi} \left\{ ik_f \left[ 1 - H_0^* + \left( b^* - \frac{1}{2} \right) \theta_0^* \right] - \theta_0^* \right\} e^{i\omega_0 t}, \quad (2.50)$$

$$L_{NC} = \frac{\rho a U^2 [-\pi h_0^*]}{\cos^2 \varphi} \left\{ -k_f^2 [1 - H_0^* + b^* \theta_0^*] - ik_f \theta_0^* \right\} e^{i\omega_0 t}, \quad (2.51)$$

$$M_C = (2\rho a^2 U^2) \left[ \pi C(k_f) h_0^* \left( b^* + \frac{1}{2} \right) \right] \left\{ ik_f \left[ 1 - H_0^* + \left( b^* - \frac{1}{2} \right) \theta_0^* \right] - \theta_0^* \right\} e^{i\omega_0 t}, \quad (2.52)$$

$$M_{NC} = \frac{2\rho a^2 U^2 \left[ -\frac{\pi}{2} h_0^* \right]}{\cos^2 \varphi} \left\{ k_f^2 \left[ b^* (1 - H_0^*) + \left( b^{*2} + \frac{1}{8} \right) \theta_0^* \right] - ik_f \left( b^* - \frac{1}{2} \right) \theta_0^* \right\} e^{i\omega_0 t}, \quad (2.53)$$

that makes it easier to see that the vertical wave velocity adds positively or negatively, depending on  $\phi_w$ , to the foil heave velocity, resulting in higher or lower incident flow angles. Following this conclusion, using (2.42), we propose the non-dimensional wave heave amplitude, given by

$$h_{0w}^* = h_0^* [1 - H_0^*], \quad (2.54)$$

whereby simply replacing  $h_0^*$  by  $h_{0w}^*$ , all the expressions for the single foil in infinite domain in Section 2.2 can be used for the case with incident waves.

Wave diffracted resistance is caused by the scattering of the incoming waves when encounter the body, and the corresponding energy loss. Heading waves result in an increase in

wave resistance, following waves result in thrust increase (Grue, 1988). For simplicity only the former case is considered. It can be evaluated by the expression derived from Isshiki (1982) assuming, for this effect, that the foil does not oscillate, and the moment refers to mid-chord:

$$\begin{aligned} \bar{R}_{wd} = \rho a U^2 \frac{\pi a_0^{*2}}{\sqrt{2} F_r} (ka)^{3/2} e^{-(ka)4d^*} \left\{ F(k_f) J_0(ka) + G(k_f) J_1(ka) \right. \\ \left. + \frac{ka}{2} \left[ (1 - F(k_f)) J_1(ka) + G(k_f) J_0(ka) \right] \right\}, \end{aligned} \quad (2.55)$$

with  $C(k_f) = F(k_f) + iG(k_f)$ . Using the previous approximations of the Bessel functions for  $ka \ll 1$  it simplifies to:

$$\bar{R}_{wd} = \rho a U^2 \frac{\pi a_0^{*2}}{\sqrt{2} F_r} (ka)^{3/2} e^{-(ka)4d^*} \left[ F(k_f) + \frac{ka}{2} G(k_f) \right]. \quad (2.56)$$

Figure 2.16 compares the present method with Isshiki (1982) results for a fixed foil in incident head waves with  $F_r = 0.55$ ,  $d^* = 1.5$ ,  $a_0^* = \pi/(20ka)$  with a good agreement. It is visible the critical wavelength value  $ka = 0.067$  where the wave resistance tends to infinity. For  $ka > 0.067$  there are no radiated waves in front of the foil.

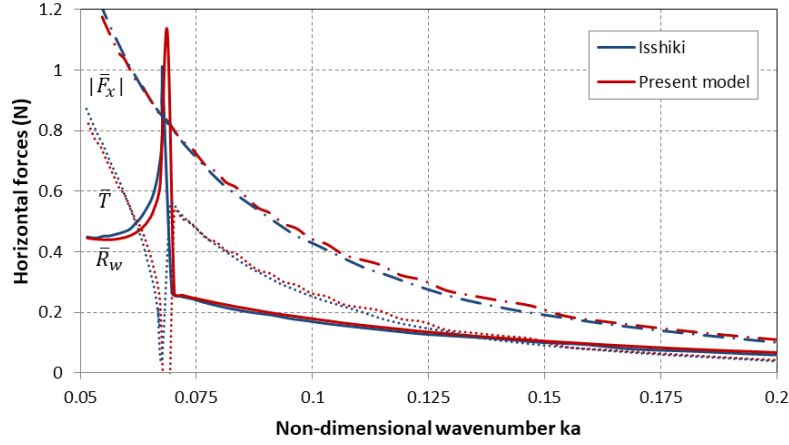


Figure 2.16: Average horizontal force  $\bar{F}_x$ , total wave resistance  $\bar{R}_w$  and thrust  $\bar{T}$  for a fixed foil  $c = 0.328$  m in incident head waves with  $F_r = 0.55$ ,  $d^* = 1.5$ ,  $a_0^* = \pi/(20ka)$ . Comparison of present method with Isshiki (1982) results.

### 2.3.4 Propulsive Force and Efficiency

The empirical lift-drag relations presented in Section 2.3.1 for the induced and profile drag are based on quasi-steady theory. To combine it with Theodorsen unsteady model an engineering approach is used (Hauge, 2013). Therefore,  $L_C$  and  $M_C$  are multiplied by the lift loss given by Equations (2.21) and (2.32), and it is simply assumed that the drag is in phase with the lift, as this will fulfil the lift-drag relation at all instants in time. Since the drag oscillates with double frequency of the lift, the second-order terms of the lift coefficient of Equations (2.20) and (2.26) can be written as follows

$$C_L^2(t) = C(k_f) \alpha_0 |C(k_f) \alpha_0| C_{L0}^2 e^{i2\omega_0 t}, \quad (2.57)$$

with  $C_{L0}$  being the lift factor for drag calculation, that include the lift losses for finite span and free-surface effects

$$C_{L0} = 2\pi \left[ \frac{1}{k_d} + 2\pi \left( \frac{1}{2F_r^2} e^{-\frac{2d^*}{F_r^2}} \right) \right] \left( \frac{1 - 2/\Lambda^2}{1 + 2/\Lambda} \right). \quad (2.58)$$

The total drag coefficient is given by:

$$C_D = (C_{D,i} + C_{D,p}) / \cos^2 \varphi, \quad (2.59)$$

and the total drag can be calculated using Equation (2.18).

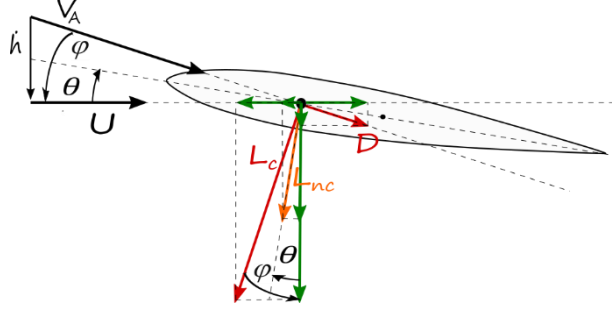


Figure 2.17: Forces acting on the foil.

Finally, the horizontal (positive thrust) and vertical forces (Figure 2.17) are given by:

$$F_x = -L_C \sin \varphi + D \cos \varphi - L_{NC} \sin \theta, \quad (2.60)$$

$$F_y = L_C \cos \varphi + D \sin \varphi + L_{NC} \cos \theta, \quad (2.61)$$

$$M = M_C + M_{NC}. \quad (2.62)$$

If  $T$  is the period of oscillation, we denote by  $\bar{T}$  the time-averaged value of  $-F_x(t)$  (negative horizontal force corresponds to positive thrust), and by  $\bar{P}$  the average input power per cycle, i.e., the mean rate of working power on the fluid per unit span is the vertical force times the rate of transverse motion plus the moment about the pitching axis times the rate of pitching

$$\bar{T} = -\frac{1}{T} \int_0^T F_x dt - (\bar{R}_{wr} + \bar{R}_{wd}), \quad (2.63)$$

$$\bar{P} = \frac{1}{T} \left[ \left| \int_0^T F_y h dt \right| + \int_0^T M_b \dot{\theta} dt \right]. \quad (2.64)$$

The absolute value sign in Equation (2.64) is needed to get a positive  $\bar{P}$ , because the heave velocity is defined to be positive when the foil is heaving upward, which is when the vertical force points downward. It is thus negative by the present definition. We define the average power coefficient  $\bar{C}_P$  as

$$\bar{C}_P = \frac{\bar{P}}{\rho c U^3 |h_0|}, \quad (2.65)$$

and the average thrust force,  $\bar{T}$ , is non-dimensionalized as follows, to provide the average thrust coefficient  $\bar{C}_T$ :

$$\bar{C}_T = \frac{\bar{T}}{\rho U^2 |h_0|}. \quad (2.66)$$

The propulsive efficiency  $\eta_P$  is defined to be the ratio of useful power to input power, as

$$\eta_P = \frac{U\bar{T}}{\bar{P}} = \frac{\bar{C}_T}{\bar{C}_P}. \quad (2.67)$$

## 2.4 Tandem Oscillating Foils

This section considers two 2D identical foils, with chord  $c = 2a$ , in tandem configuration, in the same plane, separated by a distance  $s$  (see Figure 2.18), travelling at constant forward velocity  $U$  and oscillating harmonically in heave and pitch at the same frequency, with inter-foil phase lag  $\phi_i$  (fore foil leading the aft). The aft foil encounters a constant velocity  $U_{for}$  induced by the vortex street of the fore foil.

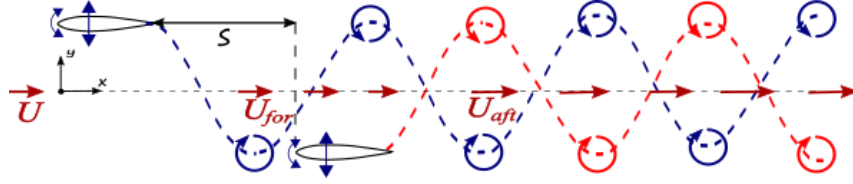


Figure 2.18: Simplified example for the tandem foil wake pattern.  $U$ ,  $U_{for}$  and  $U_{aft}$  are the foil advance velocity, fore foil vortex advection velocity and aft foil vortex advection velocity, respectively.

The heave and pitching motions, with phase differences  $\psi_i$ , for the fore and aft foil, both with rotation axis at  $b^* = b/a$ , are defined as, with  $i = 1, 2$ , respectively:

$$h_i = h_{0i}e^{i\omega_0 t} \text{ and } \theta_i = \theta_{0i}e^{i\omega_0 t}. \quad (2.68)$$

For the formulation of this problem, the assumptions of classical unsteady theory previously presented in Section 2.2 are adopted. The fore foil effect on the aft foil is accounted for in the following way: Firstly, the horizontal vortex advection velocity ratio  $r_{va} = U_{for}/U$ , accounts for the higher aft foil flow speed due to the jet of the fore foil. Epps et al. (2016) propose  $r_{va} = 1.2$ . Secondly, we postulate that there is a vertical velocity component induced on the aft foil by the fore foil vorticity that only affects the foil apparent inflow angle:

$$\varphi_2 = \text{atan} \left( ik_f h_0^* \left[ 1 + \left( b^* - \frac{1}{2} \right) \theta_0^* \right] - \frac{C_L^s}{2\pi(s^* + 2)} \right) e^{i\omega_0 t}, \quad (2.69)$$

where  $s^* = s/a$  and  $C_L^s$  the lift coefficient for a single foil that can be obtained from Equation (2.13). Moreover, it is assumed that the main additional effect of the fore foil on the aft foil is the interference of the two wakes. It is then assumed that the vortex shedding is independent for the two foils. Hence, the Kutta condition can be applied locally to each of them, where the superimposition of the vortices shed by both foils starts on the trailing edge of the aft foil and continues downstream. Finally, we also assert that the aft foil wake effect on the fore foil is minimal, with sufficient inter-foil distance (Epps et al. 2016). The detailed formulation is in Appendix C. Due to the linearity, the circulatory lift of the aft foil in tandem configuration can then be expressed in terms of the circulatory lift of the isolated (single) fore and aft foils:

$$L_{C2}^t = L_{C2}^s + L_{C1}^s \left[ 1 - \frac{E(k_f, s^*)}{C(k_f)} \right] e^{-ik_f(s^*+2)}, \quad (2.70)$$

$$E(k_f, s^*) \approx -\frac{2/\pi}{H_1^{(2)}(k_f) + iH_0^{(2)}(k_f)} \left[ \int_{-(s^*+1)}^{-1} \frac{e^{-ik_f\xi}}{(\xi^2 - 1)^{1/2}} d\xi - 2.5538k_f^{-0.649} \right], \quad (2.71)$$

with  $H_n^{(2)}(k_f)$  being the Hankel functions of second kind and  $L_{C2}^S$  reference velocity is  $U_{for}$ . The constants were found by solving the equation  $E(k_f, s^* \rightarrow \infty) = C(k_f)$ . This expression can be calculated numerically, with errors less than 7% and 3% for  $k_f > 0.05$  and  $k_f > 0.5$  respectively.

Equation (2.70) can estimate the circulatory lift of the aft foil. In a general case with a large number of parameters, including geometric parameters of each foil (planforms, camber ratio, thickness ratio), and kinematic parameters  $h_{oi}/c_i$ ,  $\theta_{oi}$ ,  $S_{ii}$ ,  $\psi_i$ ,  $\phi_0$ , and  $s$ , the design space for tandem flapping foil propulsion is enormous. Thus, applying this result to a practical case where heave and pitch amplitudes and heave-pitch phases are set equal in both foils, Equation (2.70) can be simplified to:

$$C_{L2}^t = \frac{C_L^s}{\cos^2 \varphi_2} \left\{ 1 + r_{va}^2 \left[ 1 - \frac{E(k_f, s^*)}{C(k_f)} \right] e^{i[\phi_t - k_f(s^* + 2)]} \right\}. \quad (2.72)$$

From this expression, it is possible to conclude that there exists a natural relationship between the inter-foil separation  $s$  and the optimum phase lag  $\phi$ , which maximizes efficiency for a given value of the reduced frequency.

Because the non-circulatory lift  $L_{NC2}^t$  does not depend on the wake, the formulas presented in the previous section for a single foil can be applied. This is also the case for the non-circulatory moment  $M_{NC2}^t$ . The circulatory moment of the aft foil  $M_{C2}^t$  can be easily obtained using Equation (2.9). The drag  $D_2^t$  is estimated using the Equations on Section 2.3.1 with  $C_{L2}^t$ . 3D, free-surface and incident wave effects are accounted in  $C_L^s$  of Equation (2.72) using Section 2.3's methods. Finally, the horizontal and vertical forces (negative horizontal force corresponds to positive thrust) for the aft foil are calculated as before by:

$$F_{x2}^t = -L_{C2}^t \sin \varphi_2 + D_2^t \cos \varphi_2 - L_{NC2}^t \sin \theta, \quad (2.73)$$

$$F_{y2}^t = L_{C2}^t \cos \varphi_2 + D_2^t \sin \varphi_2 + L_{NC2}^t \cos \theta, \quad (2.74)$$

$$M_2^t = M_{C2}^t + M_{NC2}^t. \quad (2.75)$$

The fore foil forces are calculated as for a single isolated foil. The total thrust and vertical forces of the foil tandem system is the sum of the instantaneous forces of both foils. The tandem foil propulsive efficiency is evaluated by calculating the individual foil average thrust and input power using Equations (2.65), (2.66) and (2.67).

## 2.5 Model Implementation

The semi-analytical models developed in the previous section are implemented using MATLAB™ (MathWorks, 2021). The model takes as input the foil and tandem geometry i.e., span, section chord, maximum relative thickness, pitching axis position and submergence depth; the tandem foil separation distance, tandem fore-aft phase lag and foil analysis selection within the tandem. The fluid characteristics are given by the density and kinematic viscosity; the inflow data are free-stream velocity, wave amplitude, wavelength, and wave-heave phase lag. The foil motion parameters are heave and pitch amplitudes, heave-pitch phase, and oscillating frequency. The effects of physical phenomena modelled in the simulation are also set, namely unsteady, viscous, finite span and free-surface effects. The flowchart of the model is presented in Figure 2.19.

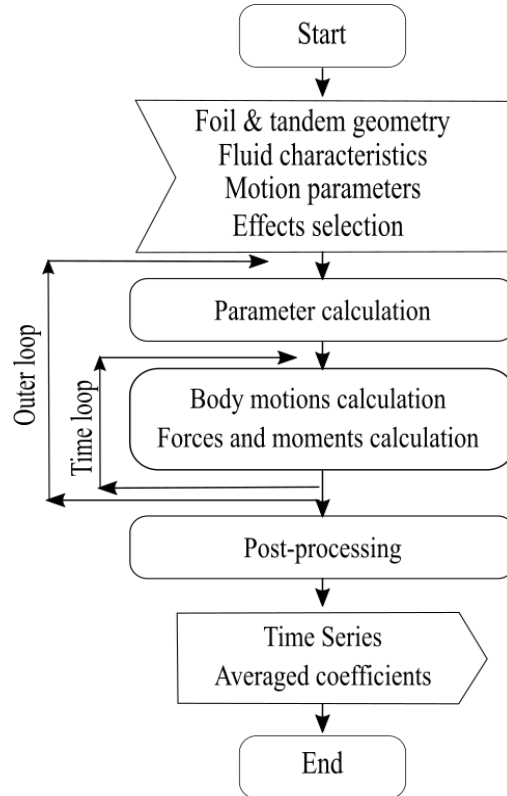


Figure 2.19: Flowchart of the present model.

The model allows the variation of a chosen single parameter within a range, evaluated in the outer loop. The body motions, the vertical position and pitch angle, are then evaluated in a time loop. The apparent inflow angle, the horizontal and vertical forces as well as the moment are calculated in each time step. The post-processing stage calculates the averaged values and the propulsive efficiency. The output produces the time series for the body motions and hydrodynamic forces coefficients and the averaged coefficients for the hydrodynamic forces coefficients as well as the propulsive efficiency.

All calculations are executed on double-precision; thus, the round-off error influence is considered negligible. The integral in Equation (2.71) is numerically evaluated using the Gauss-Kronrod quadrature formula, with an absolute error tolerance of  $10^{-10}$ , and the iterative error is of  $10^{-12}$  order.



# Chapter 3

## Semi-Analytical Model Validation

This chapter presents the methodology followed in the application of the foil performance prediction models and its validation with published data in order to estimate the accuracy of calculations and limits of usage. One of the main objectives of this chapter is to understand in which degree the different physical effects are well captured by the models. It starts by an ideal situation of an oscillating foil propulsor in unbounded fluid. Then, in calm water, which would correspond to an application to inland waters. Finally, it includes incident waves, to address an open sea situation. In all cases the oscillations motion of the foils is imposed *a priori*. The analysis is limited to solving the hydrodynamic problem of predicting the foil performance. This stage is prior to considering the modelling of a passive-type wave foil propulsor concept (Isshiki, 1984), in which the heave and pitch motions are passively controlled by a set of springs, and thus the hydrodynamic and control problems are coupled. The validation of the tandem foil model follows the same line, but at this stage only the infinite domain case is addressed. Examples of the application of these modelling tools are given and discussed.

### 3.1 Methods

The first step for studying the models is to delimit the value range space for the model parameters in the oscillating foil propulsor application. Rectangular foils with NACA symmetric profiles are universally adopted. In particular, NACA0012 and NACA0015 profiles are used. NACA0016 sections started recently to be used in tandem foil studies. For this type of application, the chord length usually is within  $c = 0.1 - 1.0$  m. For practical cases it is reasonable to assume flow velocities in the range  $U = 0.4 - 4.0$  m/s, resulting in Reynolds numbers of  $Re = 4 \times 10^4 - 4 \times 10^6$ . Regarding to the motion parameters, the heave and pitch amplitudes main testing range is  $h_0/c = 0.1 - 1.0$  and  $\theta_0 = 0 - 55^\circ$ , which will be further explored in this section. With respect to the heave-pitch phase  $\psi$ , Read (2003) states that, for a single foil in an infinite domain, there is little benefit in phase angles other than  $90^\circ$ , although there are a few interesting exceptions. A distinct decrease in thrust coefficient eventually occurs with increasing Strouhal number for any phase angle, but the value  $\psi = 90^\circ$  appears to be the most robust so, this value is adopted. Both the one-quarter-chord and one-third-chord point are commonly used as the pivot point, i.e., normalized distance to mid-chord  $b^* = -1/2$  and  $b^* = -1/3$  respectively. The range for the Strouhal number

$$S_t = \frac{\omega_0 h_0}{\pi U}, \quad (3.1)$$

studied is  $S_t = 0.1 - 0.6$  corresponding, approximately, to the lower and higher limits for the wake vortex propulsion regime. For the heave amplitudes selected above, the values correspond approximately to oscillation frequencies from 0.02 to 5 Hz. A derivative parameter of importance to the performance of a foil is the maximum nominal effective angle of attack. The instantaneous effective angle of attack is related to the heave velocity and pitch angle by

$$\alpha = \arctan \left[ \frac{\dot{h}}{U} - a \left( \frac{1}{2} - b^* \right) \frac{\dot{\theta}}{U} \right] - \theta, \quad (3.2)$$

with  $a$  denoting the half-chord length. The maximum effective angle of attack must be determined numerically and is denoted as  $\alpha_0$ . An approximation for the maximum effective angle of attack which is valid only if the phase angle between heave and pitch is  $90^\circ$ , and if the pivot point is close to quarter-chord-point, can be given by

$$\theta_0 \approx \text{atan}(\pi S_t) - \alpha_0. \quad (3.3)$$

The ranges of the maximum angle of attack are discussed more in detail later in this chapter. The feathering parameter is another additional parameter often used:

$$\chi = \frac{\theta_0 U}{h_0 \omega_0}. \quad (3.4)$$

This parameter characterizes the non-dimensional pitching angle with respect to the foil trajectory but is not independent of the Strouhal number. For large angles a better definition of this parameter is

$$\chi = \frac{\theta_0}{\text{atan}(\pi S_t)}. \quad (3.5)$$

In the cases with free-surface, the range of foil submerging depth used is  $d^* = 1.25 - 2.50$  ( $d^* = d/c$ ) corresponding approximately to the extremes where the foil trailing edge touches the surface and where the free-surface effect becomes negligible. For incident waves this study uses as reference the wave occurrences data in the West Coast of Portugal from ONDATLAS monitoring program (WavEC, 2015). The range of wave periods of highest energy  $T_e$ , during the year, where there are 97% of occurrences of waves with significant height above 0.5 m, is from 5 to 12 seconds. The corresponding wave angular frequencies are  $\omega = 0.5 - 1.2$  rad/s and wavenumbers  $k$  range from 0.02 to 0.15 rad/m. The velocities selected above correspond to oscillating foil encounter frequencies of  $f_0 = 0.08 - 0.28$  Hz, a narrower range than the case without waves.

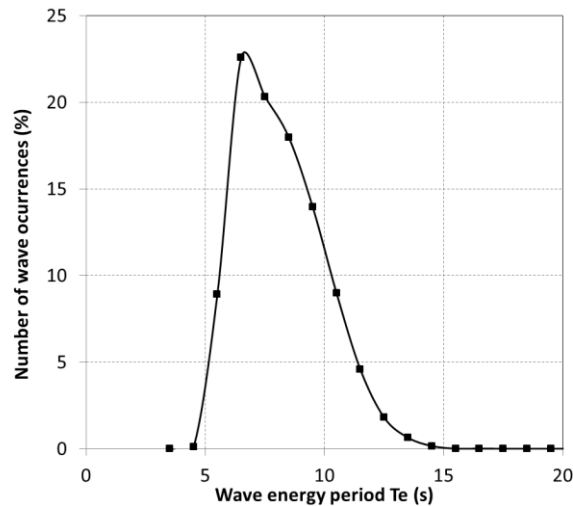


Figure 3.1: Number of wave occurrences distribution with the energy period  $T_e$ , for waves with significant height  $H_s > 0.5$  m, at Leixões, coast of Portugal (WavEC, 2015).

In the present study we use mainly the parameters  $\theta_0$  and  $S_t$ , because of their direct relevance to the thrust coefficient and the dynamics of the wake.

## 3.2 Comparison with Published Data

### 3.2.1 Single Foil in an Infinite Domain

Three main sources of data are used to compare with the present model: the numerical data from Filippas & Belibassakis (2014b) and the experimental data both from Read et al. (2003) and Schouveiler et al. (2005). The former uses an ideal flow 2D panel method to solve numerically the potential flow problem of estimating the hydrodynamic forces. Read and Schouveiler experimental data were obtained in the MIT Department of Ocean Engineering Testing Tank. The water tank is rectangular, with 18 m working length, 2.6 m width and 1.4 m depth, equipped with a mobile carriage that contains the complete motion control and sensor system (see Figure 3.2). The foil used in all the experiments is rectangular with constant NACA0012 section, chord length  $c = 10$  cm, and span  $s = 60$  cm with pivot point at the 1/3-chord position. In the experiments 35 cm diameter endplates were used on each strut to prevent flow around the ends of the foil and maintain approximately a two-dimensional flow. The towing speed  $U$  was 0.40 m/s, corresponding to  $Re = 4 \times 10^4$ . In addition to regular calibration, the pitch zero position was adjusted until the foil produced no lift.

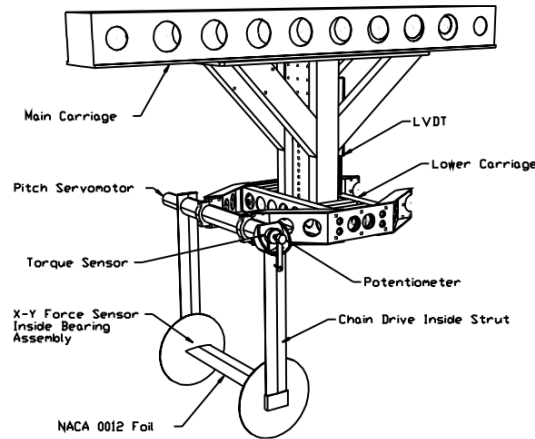


Figure 3.2: View of the test carriage, which oscillates the foil in heave and pitch, while moving horizontally in a towing tank (Read et al., 2003).

We start to show the compatibility of the present method with thin hydrofoil theory by comparing the lift coefficient amplitude in very small oscillations with Filippas numerical model, in Figure 3.3. The amplitude of heaving and pitching oscillations is  $h_0/c = 0.1$  and  $\theta_0 = 10^\circ$ , respectively, the pivot axis is located at  $b^* = 0$  (mid-chord) and the heave-pitch phase is  $\psi = 90^\circ$ . The amplitude of the vertical force coefficient  $C_y = F_y/\rho a U^2$  ( $a = c/2$ ) is plotted for various values of the reduced frequency  $k_f = \omega a/U$ , within the interval  $0.3 < k_f < 3$ . The current results are in very good agreement with the numerical model. Furthermore, to illustrate the significance of the added mass effect to the unsteady responses of the flapping hydrofoil, the predictions obtained without the added mass effect are also shown. It is clear that the present method is fully capable of providing the responses and account for the contribution of added mass effects in a case with small oscillations, i.e., close to linear theory. It is worth noticing the increasing importance of the added mass with the increasing frequency, which is related to the acceleration terms. This is connected to the two methods of force mentioned before, with the acceleration-based propulsion for  $k_f > 1$  i.e., high frequencies or low-speed, and  $k_f < 1$  for the lift-based propulsion that is the present interest.

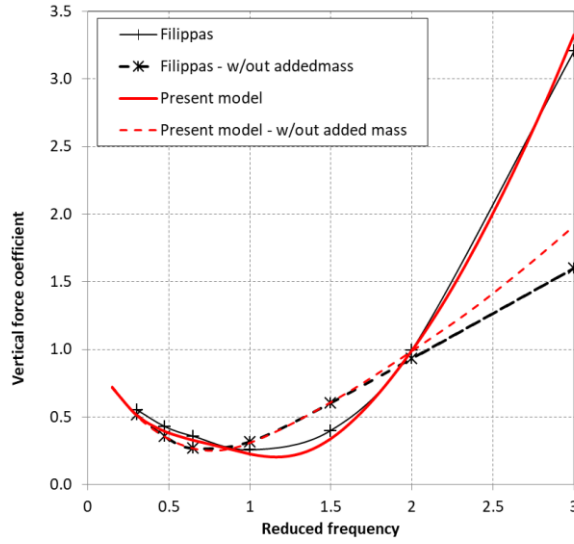


Figure 3.3: Amplitude of lift coefficient of a NACA0012 section, in low-amplitude flapping motion  $h_0/c = 0.1$ ,  $\theta_0 = 10^\circ$ ,  $\psi = 90^\circ$ ,  $b^* = 0$ , in infinite domain. Present method results against Filippas numerical with and without the contribution of added mass effects.

We follow by exploring step by step how the present model evaluates the different physical effects. Figure 3.4 shows the results of different simulations and their comparison with Filippas's numerical data (NACA0012 section) and Read's measured data (NACA0012 hydrofoil  $\Lambda = 6$  with endplates). The average thrust coefficient  $\bar{C}_T = -\bar{F}_x/\rho a U^2$  is plotted for large oscillations  $h_0/c = 1.0$  and  $\theta_0 > 15^\circ$  with one-third-pitching point,  $90^\circ$  of heave-pitch phase and  $St = 0.3$ . It is possible to see that the results with a simple quasi-steady model largely over predict the thrust, as expected. When introducing the wake and added-mass effects in the unsteady model a clear improvement can be observed, in a very good agreement with Filippas results, presenting slope over-predictions of 4% and average coefficient amplitudes discrepancies less than 9% at high AoA ( $\theta_0 = 25^\circ$ ).

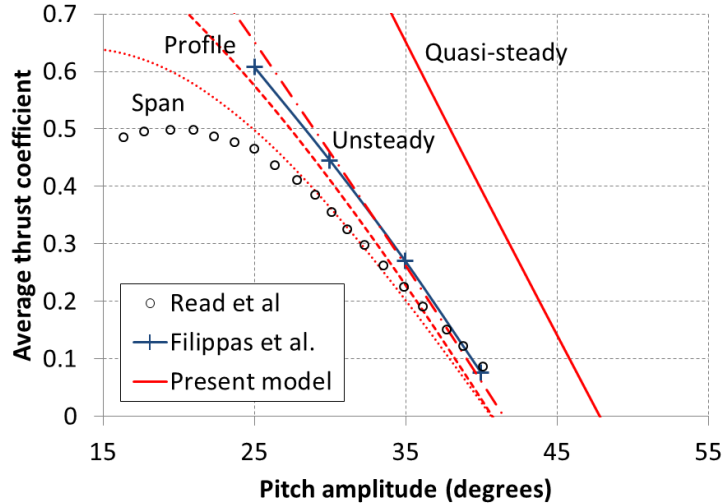


Figure 3.4: Average thrust coefficient of NACA0012 hydrofoil varying with pitch amplitude, using  $\Lambda = 12.5$ ,  $St = 0.3$ ,  $h_0/c = 1.0$ ,  $\psi = 90^\circ$ ,  $b^* = -1/3$ , in infinite domain. The present model is shown with step-by-step adding of the different effects. It is compared with Filippas panel method (+) and Read experiment (o).

This difference with numerical results could be due to non-linearization second order terms not accounted for in the present model. But it is possible to observe that both models do not provide satisfactory predictions when compared with measured data, with overestimation of the slope  $|d\bar{C}_T/d\theta_0|$  higher than 15%. Discrepancies at high angles of attack can be attributed to

the effects not accounted for in both models, namely due to viscosity, separation, and finite span, despite the foil tip endplates. When adding profile drag, simulations of the present model do not present a significant difference, indicating that the skin friction and form drag at this Reynolds number does not play a relevant role. However, these results still present a significant discrepancy with Read's experimental data. Filippas & Belibassakis (2014b) proposes, when assessing this discrepancy, that a possible cause could be 3D effects affecting Read's experiments, due to the fact that the endplates did not completely cancel out the span effects. Thus, the present model adds the finite span effects using  $\Lambda = 12.5$ . The increase in aspect ratio due to the effect of the endplates is approximated by using the expression (Hoerner, 1965)

$$\Delta\Lambda_i = \left(1.9 \frac{h_{ep}}{s}\right) \Lambda, \quad (3.6)$$

where  $h_{ep}$  is the endplate height and  $s$  the actual foil span. The results have a fair qualitative agreement with the measured values, which is congruent with the hypothesis of Filippas & Belibassakis. The extra drag observed in Read's data is explained by the full separation of the flow, due to the large AoA, effect not included in the present model.

The next step taken is a frequency study, through a comparison in parameter space  $St - \theta_0$  with both Filippas & Belibassakis and Read results. In Figure 3.5 the average thrust coefficient is plotted for different pitching amplitudes and Strouhal numbers, for the same case of Figure 3.4 (NACA0012,  $h_0/c = 1.0$  and  $\theta_0 > 15^\circ$ , 1/3-pitching point and  $\psi = 90^\circ$ ). The profile and finite span effects are included, using the equivalent aspect ratio  $\Lambda = 12.5$  as in the case before. In terms of measured values, using the same apparatus of Read, Schouveiler (2005) found that the experimentally determined thrust coefficient and propulsive efficiency had an uncertainty of less than 4% and 7%, respectively, which are plotted for one case. It can be seen the main operating region of propulsion regime that occupies  $St = 0.20 - 0.45$  and  $\theta_0 = 15^\circ - 55^\circ$ .

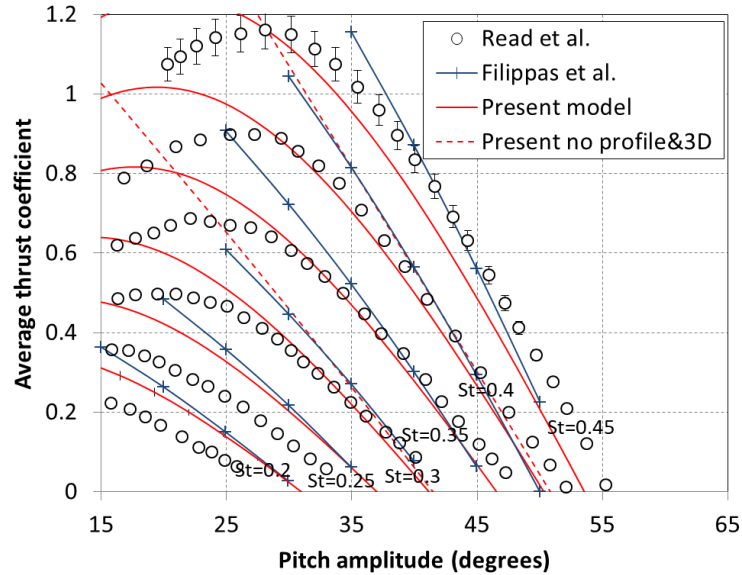


Figure 3.5 Average thrust coefficient varying with pitch amplitude and Strouhal number for a NACA0012 foil with  $\Lambda = 12.5$ ,  $h_0/c = 1.0$ ,  $b^* = -1/3$ ,  $\psi = 90^\circ$ . Present method (red -) compared to Filippas & Belibassakis (2014b) (blue +) and Read et al. (2003) (black o) results. For  $St = 0.45$  curve the uncertainty found by Schouveiler (2005) is added.

There is optimal wake formation within this region, characterized by two vortices per cycle in a reverse BvK pattern as discussed previously in Section 2.1. Reducing the frequency of oscillation, i.e., decreasing  $St$ , causes the vortices shed to become closer to the wake midline until the transition to the drag regime begins to occur. Read verified that in terms of the Strouhal number this transition occurs consistently in the neighbourhood of  $St = 0.10$ . Alternatively, although not visible in this figure, when increasing frequency, for

$St = 0.55 - 0.60$  both thrust and efficiency curves start to drop off (Read, 2005). This is explained by the switch to the deflected asymmetric regime, with the formation of dipole dynamics in the wake pattern that causes the deflection of the jet. As for the pitching angle, as its amplitude increases, the effective angle of attack is reduced until reaching zero and entering the feathering regime. Further increase in the pitch angle amplitude will lead to a power generation regime. By opposition, reducing the pitching amplitude causes the effective AoA to increase, and makes the foil enter the flow separation region. This is characterized by a thrust-type vortex street that is formed by a weak leading edge separation, which travels down the foil and constructively merges with the trailing edge vortex. Even larger angles of attack result in strong leading edge separation, resulting in a pattern with four vortices per cycle, which weakens the thrust producing qualities of the vortex wake, clearly visible in experimental data of Figure 3.5. In this figure, we also compare the two present results without profile and finite span effects with Filippas 2D ideal-flow method, in strong agreement, as seen before. However, when comparing with measured data it is possible to observe discrepancies at low values of AoA i.e., when  $\bar{C}_T$  approaches zero, especially for limit values of frequency (low and high  $St$ ). These discrepancies were not addressed in Filippas work. These effects seem clearly of a different nature from the ones addressed before. They may be due to non-linear effects of vortex wake rollup dynamics or added mass caused by endplates or apparatus heave motion. Namely, because it depends on  $St$  and is more significant when the foil approaches the thrust-drag transition, i.e., the thrust forces from the foil oscillation are smaller. From an engineering point of view this region is of less interest since what is targeted is high thrust and efficiency.

A specific example, comparing time series results, corresponding to one operating condition, for  $St = 0.3$  and heave amplitude  $h_0/c = 0.75$ , is shown in Figure 3.6, concerning the time history of thrust  $C_T$  and vertical force  $C_y$  coefficients, against both Filippas numerical and Schouveiler (2005) experimental data. Schouveiler uses the same experimental set-up of Read. In general, a satisfactory agreement with both the amplitude and the phase lag. Small differences in the peak values of the vertical force coefficient could be due to non-linear second order terms of the added mass not accounted for in the model.

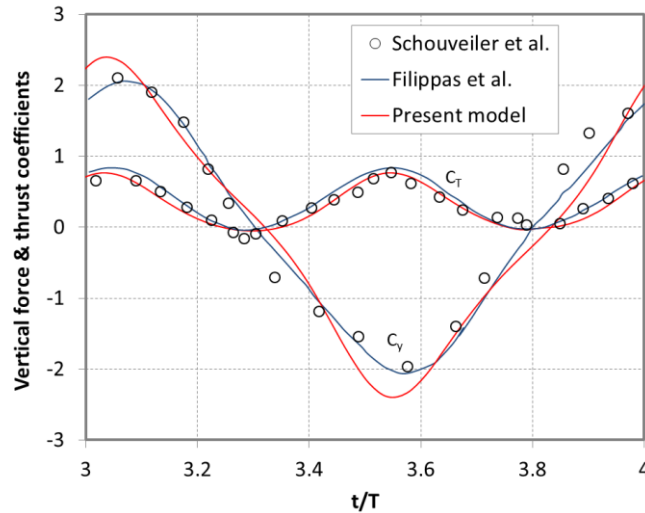


Figure 3.6 Vertical force  $C_y$  and thrust coefficients  $C_T$  for a NACA0012 hydrofoil with  $\Lambda = 12.5$ ,  $St = 0.3$ ,  $h_0/c = 0.75$ ,  $\theta_0 = 23.3^\circ$ ,  $b^* = -1/3$  and  $\psi = 90^\circ$ . Present method (red -) compared to Filippas & Belibassakis (2014b) (blue -) and Schouveiler et al. (2005) (black o) results.

In both in Figure 3.5 and Figure 3.6 one can see the agreement with experimental data, presenting discrepancies in the middle of the range of 4% and maximum discrepancies up from 7% to 13%. The present model is a step forward in refinement from Filippa's numerical model. However, it still shows a growing overestimation of the average thrust coefficient with the decrease of frequency and an underestimation for higher frequencies in relation with experimental data. In spite of its simplicity, it is found that the present model captures some viscous effects with fair agreement up to an AoA of  $21^\circ$ - $23^\circ$ .

Figure 3.7 presents the comparison of the average thrust  $\bar{C}_T$  and propulsive efficiency  $\eta_p$  from the present method with the experimental data of Read, for the same configuration in Figure 3.6, for  $h_0/c = 0.75$  and  $h_0/c = 1.0$ , considering  $\alpha_0 = [10^\circ, 15^\circ \text{ and } 20^\circ]$ . The main purpose is to assess the accuracy of the current method for propulsive efficiency prediction and the effect of heaving amplitude. In the measured values, the limits of the propulsion regime region are evident, with a drop-off both in the  $\bar{C}_T$  and efficiency. Also the mean thrust coefficient increases with the AoA but the maximum of efficiency occurs in both cases for  $\alpha_0$  of  $15^\circ$ . Efficiency is quite high in some cases e.g., with  $St = 0.15$  for  $h_0/c = 0.75$ . The result indicates that these peaks are not paired with good thrust performance. However, it is possible to attain large thrust coefficients with moderate to good efficiency, at high  $St$  values for  $h_0/c = 1.0$  (Read et al., 2003). Both heave amplitudes show similar thrust performance, but lower mechanical (oscillating) frequencies allow reaching higher Strouhal numbers with the higher heave amplitude. The model, including both profile and finite span effects, shows a good agreement with experimental data in the main region of the propulsion regime. As expected, it does not capture the drop-off for high  $St$  as the dynamics of the wake change and Theoderson's theory cease to be valid. And it can be seen that the discrepancy for low  $St$  is lower for small heave amplitudes, in agreement with the early supposition that the heave motion of the endplates and apparatus might be affecting the experiment. Despite the observed agreement, the present method over predicts the measured propulsive efficiency by 8% for central values and does not capture the peaks shown in the measured data. It can indicate a lack of accuracy in the vertical force and moment prediction.

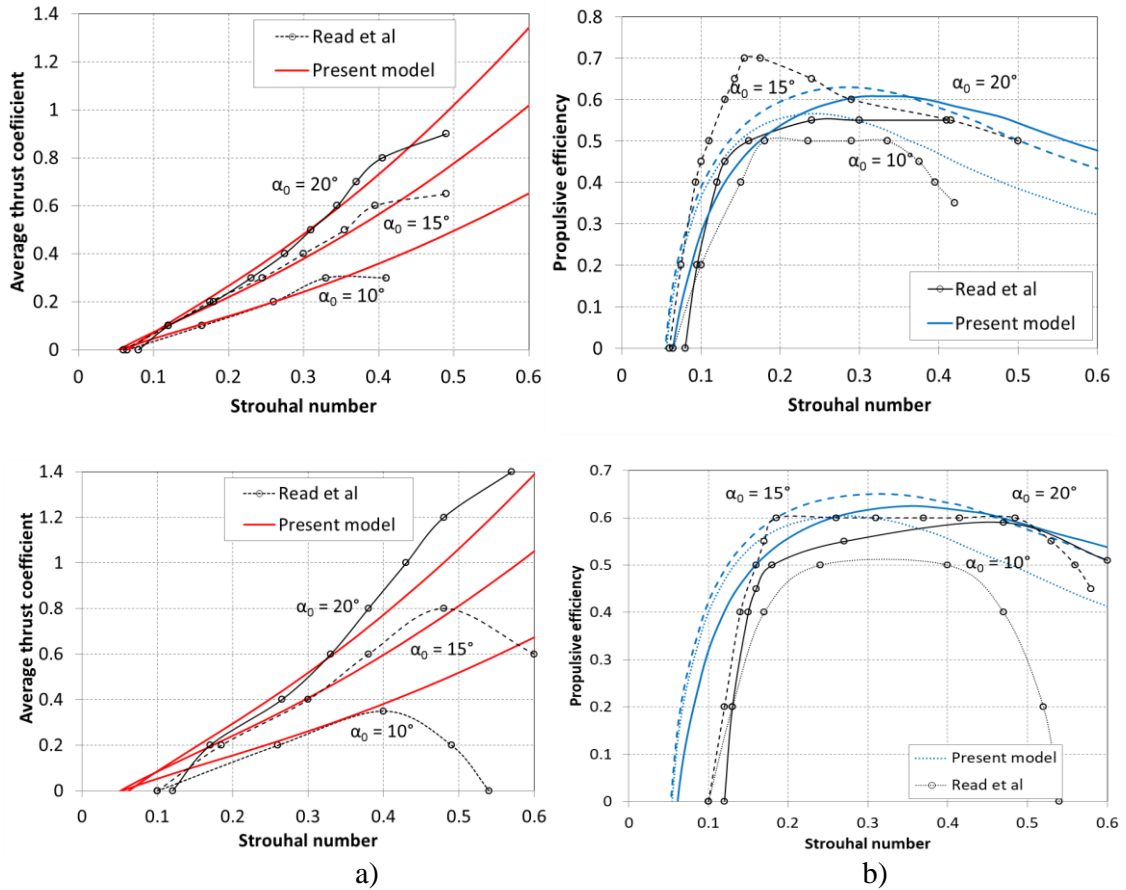


Figure 3.7: a) Average thrust coefficient and b) propulsive efficiency varying with Strouhal number for 3 values of maximum angle of attack, for a NACA0012 hydrofoil  $\Lambda = 12.5$  with  $h_0/c = 0.75$  (first row) and  $h_0/c = 1.0$  (second row),  $b^* = -1/3$ ,  $\psi = 90^\circ$ , present method (colour line), compared with experiment (o) (Read, 2005).

As concluding remarks for this section, one can affirm that the developed model presents enough agreement for the main range of the propulsion regime and is considered satisfactory for the present purpose. Enhancements can be made by introducing a more complex dynamic stall model (e.g., see the work of Bøckman, 2014), and undertaking further studies to

understand the discrepancies in the thrust-drag transition. Another possible extension is to introduce some sort of modelling that tries to capture the switch of the wake regime from propulsion to deflected. One possible idea is to empirically relate the vortex strength with the angle of the jet deflection and estimate the horizontal component of the thrust force. Finally, one can see a promising high-performance configuration, choosing a trade-off between thrust and efficiency, at  $\alpha_0 = 20^\circ$ ,  $h_0/c = 1$  and  $St = 0.5$ . For these parameters, values of propulsive efficiency  $\eta_p$  of 60% and swept area mean thrust coefficient  $\bar{C}_{TSA}$  of 0.6 ( $\bar{C}_{TSA} = -F_x/\rho U^2 h_0$ ) can be achieved, comparing with standard screw propeller that will attain efficiencies in the range 0.65–0.75 for thrust coefficients in the range 0.25–0.75 (Epps et al., 2016). Figure 3.8 presents an example of worthwhile exploring with the present model, where propulsive efficiency is plotted for different heave amplitudes going further than one chord, not often seen in the literature. It is possible to see that for  $h_0/c > 1$  the efficiency does not increase much.

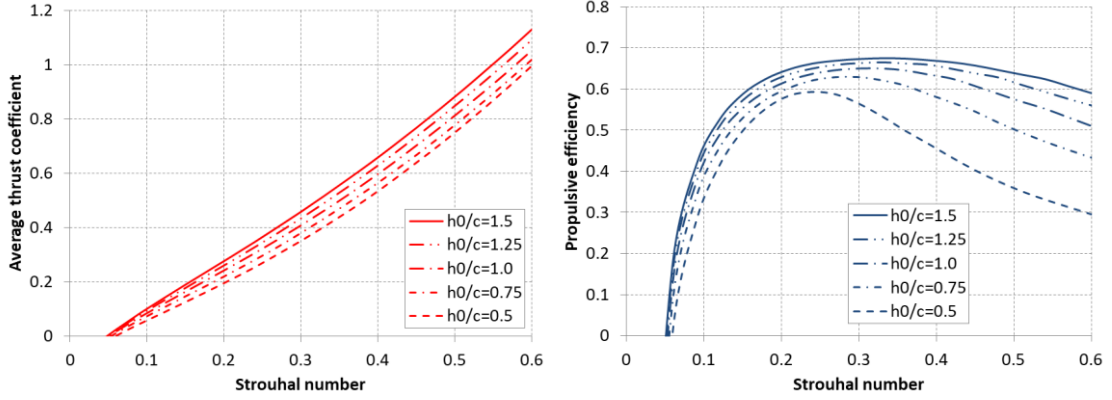


Figure 3.8: Average thrust coefficient and propulsive efficiency for a NACA0012 section  $\alpha_0 = 15^\circ$ ,  $b^* = -1/3$ ,  $\psi = 90^\circ$ , for different heave amplitudes, present method.

### 3.2.2 Submerged Single Foil with Incident Waves

In this Section, we start by exploring the wave radiation effect due to the presence of a free-surface, without incident waves. Figure 3.9 a) presents the lift loss due the presence of free-surface dependence on depth and velocity, significantly visible  $Fr = [1, 3]$ . We have seen in Section 2.3.2 that depending on the critical wavenumber, which is connected with the foil velocity and frequency of oscillation, four different waves can be radiated. A typical example is shown in Figure 3.9 b), which presents the mean wave radiation resistance coefficients for the various waves, varying with the Froude number, for a NACA0012 section oscillating at  $\omega_0 = 1.2$  rad/s,  $d^* = 1.5$ ,  $\theta_0 = 15^\circ$ ,  $b^* = -1/3$ ,  $\psi = 90^\circ$ ,  $h_0/c = 1$ .

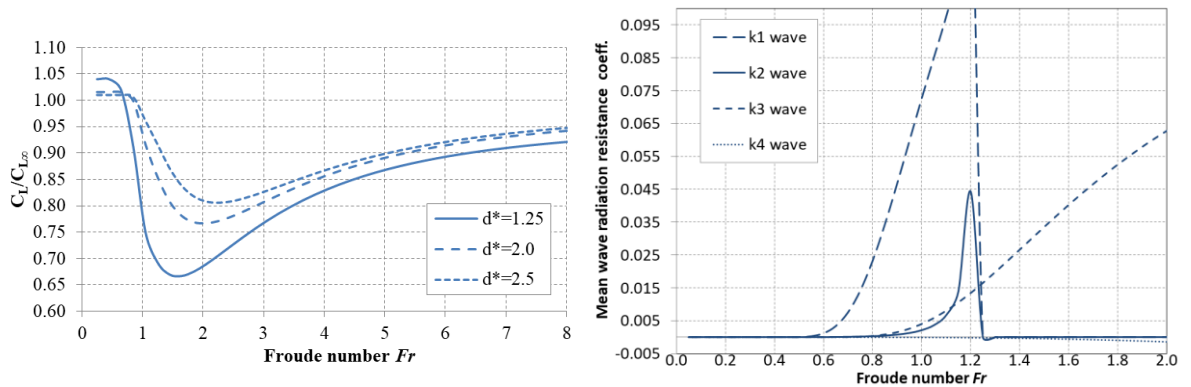


Figure 3.9: a) Lift loss for different depths and Froude numbers b) Mean wave radiation resistance coefficients for the different  $k_i$  waves, varying with Froude number, for a NACA0012 section with  $\omega_0 = 1.2$  rad/s,  $d^* = 1.5$ ,  $\theta_0 = 15^\circ$ ,  $b^* = -1/3$ ,  $\psi = 90^\circ$ ,  $h_0/c = 1$ , present model results.

It is possible to observe that the critical wavenumber corresponds to  $F_r = 1.2$ , and below that Froude number  $k_1$  and  $k_2$  waves dominate. As velocity increases above that critical value,  $k_3$  becomes dominant and  $k_4$  produces negative resistance (i.e., reinforcing thrust). This analysis is relevant for engineering design and project of vehicle nominal speed, especially if taking into account the effects of drag in the vicinity of the critical wavenumber.

A comparison study of the significance of wave radiation resistance with profile and finite span drag is presented in Figure 3.10, for a NACA0012 foil,  $\Lambda = 6$ , with  $\omega_0 = 1.2$  rad/s,  $d^* = 1.5$ ,  $\theta_0 = 15^\circ$ ,  $b^* = -1/3$ ,  $\psi = 90^\circ$ ,  $h_0/c = 1$ . It is possible to observe that this effect mainly becomes important for velocities close to and above the critical value.

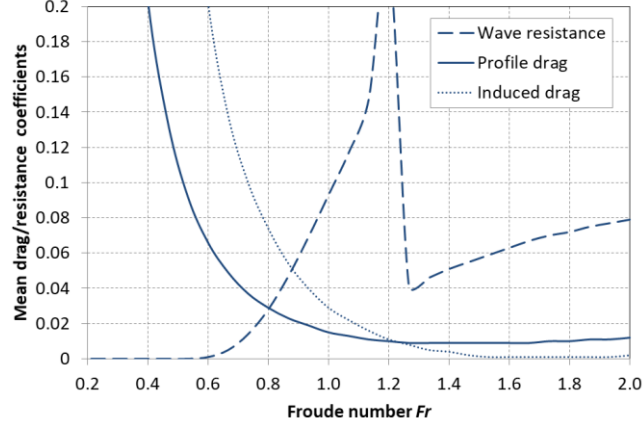


Figure 3.10: Mean drag coefficients comparison for the wave radiation (total), the profile and the finite span effects, varying with Froude number, for NACA0012 foil with  $\omega_0 = 1.2$  rad/s,  $d^* = 1.5$ ,  $\theta_0 = 15^\circ$ ,  $b^* = -1/3$ ,  $\psi = 90^\circ$ ,  $h_0/c = 1$  and  $\Lambda = 6$ , present model results.

Next, the present model in a finite submersion is compared with Silva et al. (2012) results. Silva provides an extensive analysis of the different parameters using CFD, with free-surface and incident waves, and provides a good basis for verification. The CFD code FLUENT was used in this study. His results have an estimated discretization uncertainty of 0.17%. The base case studied considers a NACA0015 section with a 7 m length chord, 9 m submergence, 1/3-pitching point and advancing speed of 7.2 m/s in waves of 1 m amplitude, with active oscillation foil in wave induced flow.

The foil oscillating frequency is always equal to the encounter frequency. The main parameters studied are the phase between wave and heave, the phase between heave and pitch, the feathering parameter (pitching amplitude) and the Froude number (accounting for foil speed). The effects of incident wave are now addressed. As seen before in Equations (2.49), (2.52) and (2.53), the vertical wave velocity adds to the foil heave velocity, allowing higher incident flow angles. Therefore, it is not suitable to use the Strouhal number as defined before as a measure of frequency, so in this section the non-dimensional encounter wavenumber  $\omega_0^2 c/g = (\pi S_t F_r)^2$  is used. Likewise, the feathering parameter is extended to provide a measure of the relative magnitude of pitch and heave velocities with the inclusion of vertical wave velocity for a given encounter frequency

$$\chi = \frac{\theta_0}{\pi S_t (1 + H_0^*)}. \quad (3.7)$$

First, we assess the effect of the free surface in calm water with heave  $h_0/c = 1.0$ ,  $\theta_0 = 35^\circ$ ,  $\psi = 90^\circ$  and  $\omega_0^2 c/g = 0.25$  at submergence  $d^* = 1.28$  and Froude number  $F_r = 0.87$ . Figure 3.11 shows a comparison of the present model with the results of Silva's thrust and vertical force coefficients time history. Although there is a general agreement, there are some discrepancies. One main difference is that Silva's model captures the difference between the upstroke and the downstroke due to the foil closing and moving away from the free-surface. The positive vertical force peak happens for the maxima of vertical velocity when the foil is in the middle of

the downstroke i.e., moving away from the surface, and the negative maxima of vertical force when the foil is in the middle of the upstroke. In the present model the vertical force coefficient is symmetrical. Concerning the thrust coefficient, it can be seen in Silva's results that the difference in maxima is almost negligible, and thus, for the thrust, the limitations of the present model are not significant. But in terms of average thrust coefficient values the present model gives  $C_T = 0.283$  against Silva's value of  $C_T = 0.197$ , which is a discrepancy of +43%. This difference might be due to two reasons. One could see the discrepancies identified in previous section for a single foil in an infinite domain for low  $S_r$ , which is the case of this simulation. Other possible main reason is that the present model is not correctly accounting the lift loss due to the free-surface presence, especially in the upstroke where it is more significant. The model only considers the average submersion depth effect and maybe disregarding that lift loss decrease in the downstroke does not balance the lift loss when the foil goes close the free-surface.

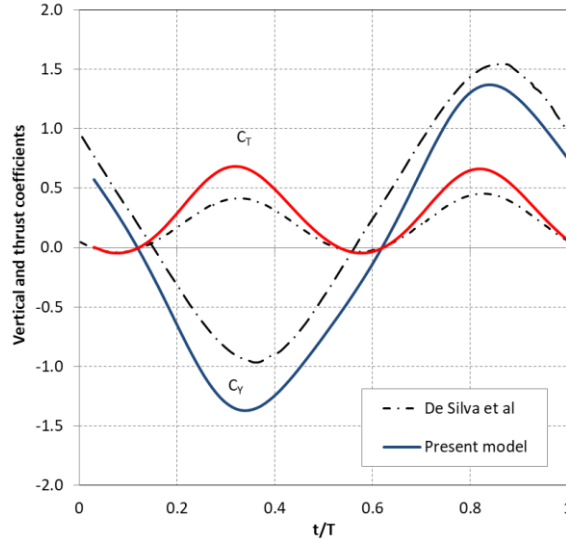


Figure 3.11: Instantaneous vertical  $C_y$  and thrust  $C_T$  coefficients time series for NACA0015 section with  $b^* = -1/3$ ,  $h_0/c = 1$ ,  $\theta_0 = 35^\circ$ ,  $\psi = 90^\circ$  and  $\omega_0^2 c/g = 0.25$  at submergence  $d^* = 1.28$ , and  $Fr = 0.87$ . Comparison of present model (colour) with Silva et al. (2012) (black) results.

We proceed by using Filippas & Belibassakis (2014b) simulations comparing deep submergence, calm waters and incident wave cases. Figure 3.12 presents results of their qualitative study of thrust increase, for different wave-heave phase lags  $\phi_w$ . The average thrust is plotted as a portion of its value at finite submergence below the free-surface in calm water, shown with an horizontal bold line at 0%. It concerns a NACA0012 section at  $Fr = 1.5$  with motion parameters  $h_0/c = 1$ ,  $\theta_0 = 35^\circ$ ,  $\omega_0^2 c/g = 3.55$  at submergence  $d^* = 2.5$ , and in waves  $a_0/h_0 = 0.75$ , with flapping frequency equal to encounter frequency. The results of the present model are plotted in the same figure. Firstly, we observe that the effect of the free-surface is to cause a reduction of thrust due to the lift loss as expected. The present model, when compared with Filippas results of a 5% increase for deep submergence, show discrepancies of 20%. It indicates that the model has limitations in the range of values involved, namely low Froude numbers. We conclude that the modelling captures the effect of depth in some degree, needing improvement in future work. The interaction with the free surface introduces complex dynamics, but a further development seems possible. The effects of the phase lag  $\phi_w$  between incident wave and heaving motion can also be seen in Figure 3.12. We notice that the thrust production is maximized at  $\phi_w = -180^\circ$  and minimized at  $\phi_w = 0^\circ$  as expected from Equation (2.49). In Filippa's results, the increment is around 20%. In the first case, the vertical velocities of the wave and the heaving motion have opposite directions resulting in maximum thrust production due to additional energy extraction from the wave. In the second case, the velocities have the same direction and the thrust production is also positive, but lower in comparison with the case of calm water. The present model has a fair agreement, indicating that it captures this effect well.

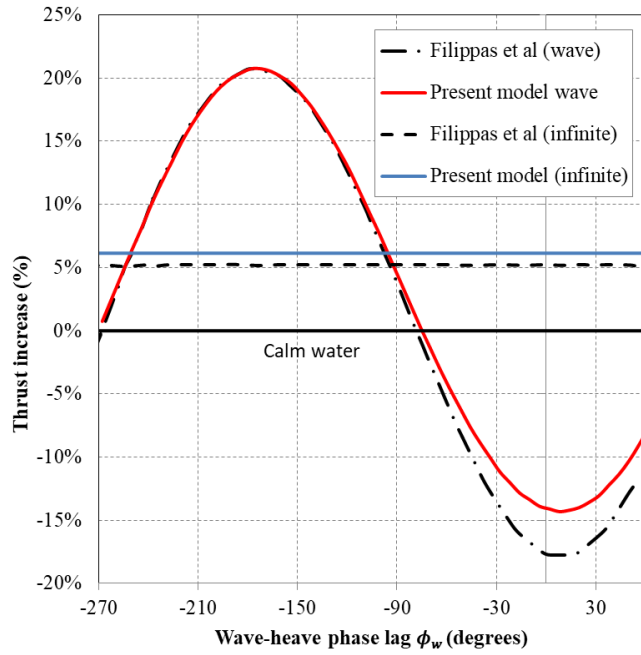


Figure 3.12: Thrust increase for NACA0012 section at  $F_r = 1.5$  with motion parameters  $h_0/c = 1$ ,  $\theta_0 = 35^\circ$ ,  $\omega_0^2 c/g = 3.55$ . Comparison between results in infinite domain, in calm waters at  $d^* = 2.5$ , and in waves  $a_0^* = 1.5$ .

Figure 3.13 shows a comparison of the present model with Silva et al. (2012) time history results of foil thrust and vertical force coefficients, for waves with two different phases mentioned before for the same configuration of Figure 3.11 i.e. NACA0015 section with  $h_0/c = 0.6$ ,  $\theta_0 = 15.65^\circ$  at  $F_r = 0.87$  and  $d^* = 1.28$  with  $a_0/h_0 = 0.238$ ,  $\phi_w = -180^\circ$  and  $\omega_0^2 c/g = 0.69$ . There is a general good agreement, however, the main discrepancies identified in Figure 3.11, namely the difference in the vertical force amplitude for the two strokes and over-prediction in thrust are also visible.

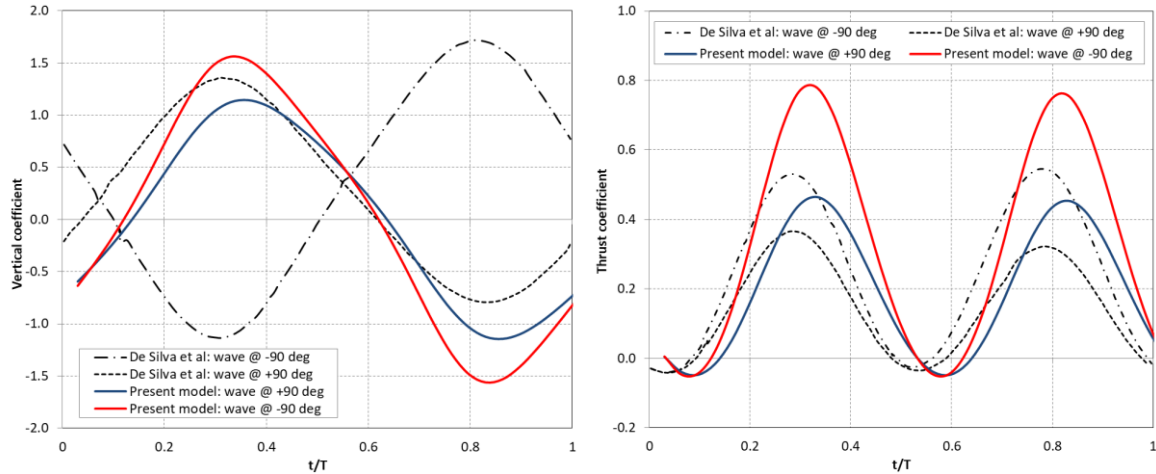


Figure 3.13: a) Vertical force coefficient and b) thrust coefficients time series comparison for NACA0015 at  $F_r = 0.87$  and  $d^* = 1.28$  with motion parameters,  $h_0/c = 0.6$ ,  $\theta_0 = 15.65^\circ$ ,  $\psi = 105^\circ$  with an incident wave with  $\omega_0^2 c/g = 0.69$ ,  $a_0/h_0 = 0.238$ , for two cases: (i), wave phase  $\phi_w = -180^\circ$  (ii) wave phase  $\phi_w = 0^\circ$ .

The vertical force coefficient obtained by the present model shows a discrepancy of +7% relative to average of Silva results, in both cases, while the average thrust coefficient presents +20% over-predictions. It is consistent with the calm water case, indicating that the main cause of the difference is due to the modelling of the submergence effect.

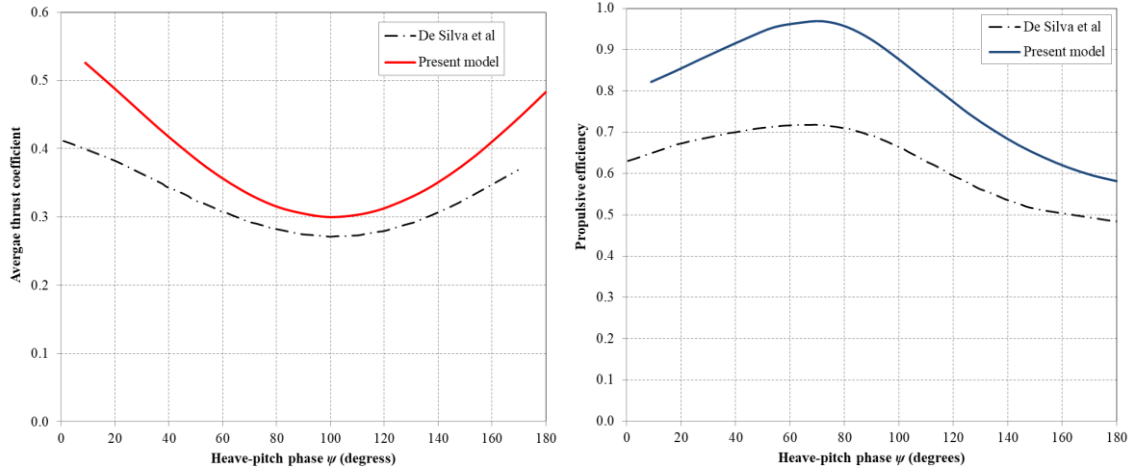


Figure 3.14: a) Average thrust coefficient and b) propulsive efficiency versus heave-pitch phase  $\psi$  at  $F_r = 0.87$  and  $d^* = 1.28$  with  $h_0/c = 0.6$ ,  $\theta_0 = 15.65^\circ$  with an incident wave with  $\omega_0^2 c/g = 0.69$ ,  $a_0/h_0 = 0.238$ ,  $\phi_w = -180^\circ$ .

Figure 3.14, depicts a comparison of the average thrust and propulsive efficiency varying with heave-pitch phase  $\psi$ . The results for the same case with the presence of wave show a completely different behaviour of thrust generation than the infinite domain case studied by Read et al. (2005) in which both thrust, and efficiency had maxima at  $90^\circ$ . In this case the average thrust coefficient shows a minimum near  $100^\circ$ . With a visible qualitative good agreement with Silva's results, the current model presents discrepancies around +9% that increase to +20% with thrust coefficients increase. De Silva et al. found that the efficiency had a maximum near  $60^\circ$  heave-pitch phase, and suggests  $40^\circ$  as a realistic trade-off, keeping high efficiency without much sacrifice of thrust force.

Figure 3.15 shows the variation of thrust coefficient and efficiency with the feathering parameter. As mentioned in Chapter 2 review, for the thrust force to have a positive mean,  $\chi$  should be generally less than 1, since the case of  $\chi = 1$  corresponds to the pitching angle equals to the gliding angle where minimum effective angle of attack is observed. When  $\chi$  is set to zero, the maximum effective angle of attack is obtained, and because of that maximum thrust coefficient is achieved. Silva found that the efficiency initially increases with the increase of the feathering parameter, attaining a maximum value near 0.4. Further increase of feathering parameter results in decrease of the efficiency from 0.6 to 0.1. Therefore, to obtain a higher efficiency and not relinquish the thrust, he proposes the trade-off value of 0.2. The present method is in good agreement with Silva's results presenting again a constant difference in the average thrust coefficient value of 0.11.

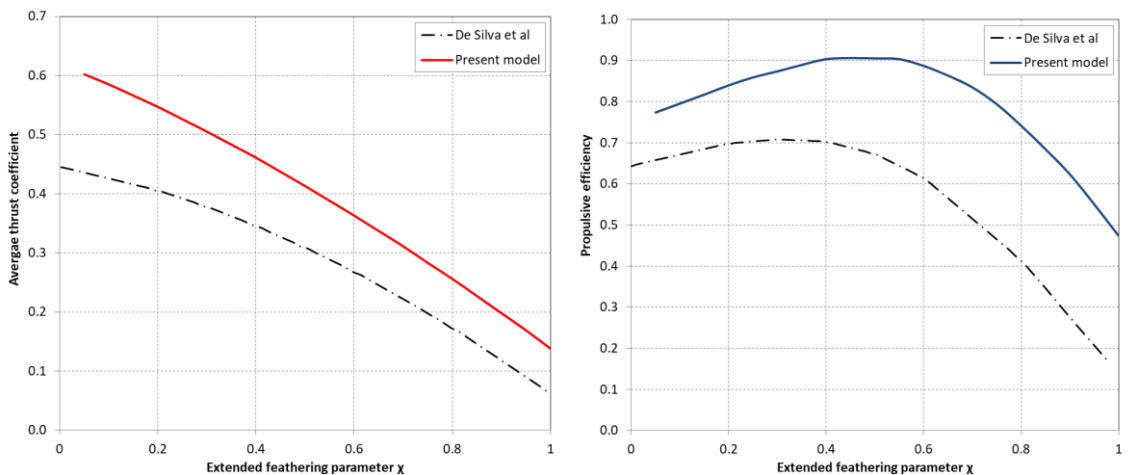


Figure 3.15: a) Average thrust coefficient and b) propulsive versus extended feathering parameter, at  $F_r = 0.87$  and  $d^* = 1.71$ ,  $h_0/c = 0.6$ ,  $\psi = 40^\circ$  with  $\omega_0^2 c/g = 0.69$ ,  $a_0/h_0 = 0.238$ ,  $\phi_w = -180^\circ$ .

The study of the Froude number provides a significant contribution to the wave propulsion understanding because the wave encounter frequencies are highly dependent on the advance velocity of the oscillating foil propulsor. In order to change the Froude number, advance speed and wavelength have to change accordingly. In Figure 3.16 the case with  $h_0/c = 1$ ,  $d^* = 1.28$ ,  $\psi = 40^\circ$ ,  $\chi = 0.2$  with  $a_0/h_0 = 0.238$ ,  $\phi_w = -180^\circ$  and  $\omega_0^2 c/g = 1.5$  is presented. In this simulation the wave encounter frequency and foil oscillation frequency are kept constant, so the wavelength has changed for each Froude number. In the same way to keep the extended feathering parameter at 0.2 the pitching amplitude must change accordingly. It is possible to verify that the thrust coefficient decreases significantly with the  $F_r$ , as expected since the increase of advance velocity decreases the incident flow angle. However, Silva et al. found that the efficiency increased with velocity. It derives from efficiency's direct dependence on velocity. As before Silva proposes a trade-off optimal point between thrust and efficiency for Froude numbers in the range of 0.8 and 1. Similarly to the cases presented before, the results of the current model show good qualitative agreement with Silva's results, presenting greater discrepancies for low  $F_r$  values.

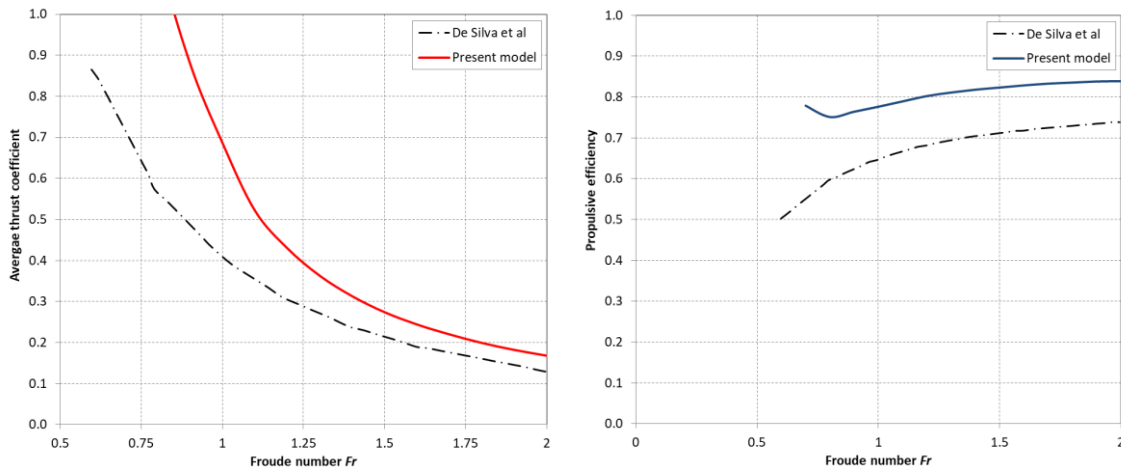


Figure 3.16: a) Average thrust coefficient and b) propulsive efficiency versus Froude number for  $d^* = 1.28$  and  $h_0/c = 0.6$ ,  $\psi = 40^\circ$ ,  $\chi = 0.2$  and wave with  $\omega_0^2 c/g = 1.5$ ,  $a_0/h_0 = 0.238$ ,  $\phi_w = -90^\circ$ .

Finally, we carry out a validation study by comparing it with experimental results. The present literature survey has shown that the only available experiment for wave propulsion was carried out by Isshiki & Murakami (1984) in the Technical Research Institute, Hitachi Zosen Corporation, Osaka. The experiment was carried out in a tank of 25 m length, 1 m width and 0.71 m depth, with a wave maker at one end of the tank. The foil used had a NACA0015 section, 0.4 m chord and 0.96 m span with pivot point at  $1/4$ -chord position and submergence 0.077 m. Waves were incident upon the foil, which moved forward solely due to the thrust caused by the waves (free running test) through a passive spring control system. The average advance speed obtained was 0.40 m/s. Most of the experiment frequencies were above the range of present study. However, in Table 3.1 there is a comparison between the results of the test case at  $\omega_0^2 c/g = 0.38$ , the lower frequency used in the other methods, namely of Silva et al., Grue & Palm (1988) and Isshiki linear theory, with the present method. For this comparison the other methods simulate an active foil propulsor, so the mean horizontal velocity, heave amplitude and pitching amplitude obtained in the experimental results were used.

Table 3.1 Comparison of average thrust coefficient between experimental, numerical, and theoretical methods for  $Fr = 0.2$ ,  $\omega_0^2 c/g = 0.38$  (Silva et al., 2012).

Method	$\bar{C}_T$	Discrepancy to exp.
Isshiki experiment	0.068	
De Silva CFD	0.092	36.30%
Present method	0.112	65.62%
Grue nonlinear theory	0.130	92.65%
Isshiki linear theory	0.157	132.46%

The discrepancies between Silva results and the experiment can be explained both by the limitations of the experiment and by the nonlinearity of the formulation which was neglected in the theoretical studies (Silva et al., 2012). This table gives an idea of the difficulty in obtaining accurate results, both due to the technical difficulties of the experiment and the challenge of modelling such complex physical phenomena.

Despite the limitations in accuracy, the present method proved once more, to be able to provide useful predictions, capturing the main aspects of oscillating foils in incident waves. The improvement of finite submergence modelling was found necessary to increase accuracy. It is worth noting that the computational cost of the present model renders this approach quite competitive and efficient, especially for initial design, optimization, and active control development.

### 3.2.3 Tandem Foils

The results of the model developed are compared with the numerical data from Epps et al. (2016) and Muscutt et al. (2017) from the University of Southampton. They both use a CFD tool called LilyPad (Weymouth, 2015), which solves the full two-dimensional Navier-Stokes equations by applying the Boundary Data Immersion Method (BDIM). This method allows the solid and fluid domains to be combined analytically by using the general integration kernel formulation, resulting in a combined set of equations for the whole domain (Weymouth & Yue, 2011). Far less computing power is required to solve the equations when compared to the original two-domain problem, so fast and accurate solutions can be obtained. This method has second-order convergence, and a Cartesian grid is used.

Figure 3.17 presents the results found in Epps et al. (2016) for a simulation with a tandem foil with NACA0016 two-dimensional profiles pitching at one-quarter-point, with chord length  $c = 1$  m, in a flow speed  $U = 1$  m/s, in infinite domain. The kinematic viscosity was set  $\nu = 10^{-4}$  m<sup>2</sup>/s giving a Reynolds number  $Re = Uc/\nu = 10^4$ . The parameters used in the current simulations are heave amplitude  $h_{01}/c = h_{02}/c = 1$ , pitch amplitude  $\theta_{01} = \theta_{02} = 45^\circ$ , heave-pitch phase  $\psi_1 = \psi_2 = 90^\circ$  and Strouhal number  $St = 0.4$ . The tandem as non-dimensional separation distance between foils of  $s^* = 8$  ( $s^* = s/a$ ) and an inter-foil phase lag of  $\phi_i = 135^\circ$ .

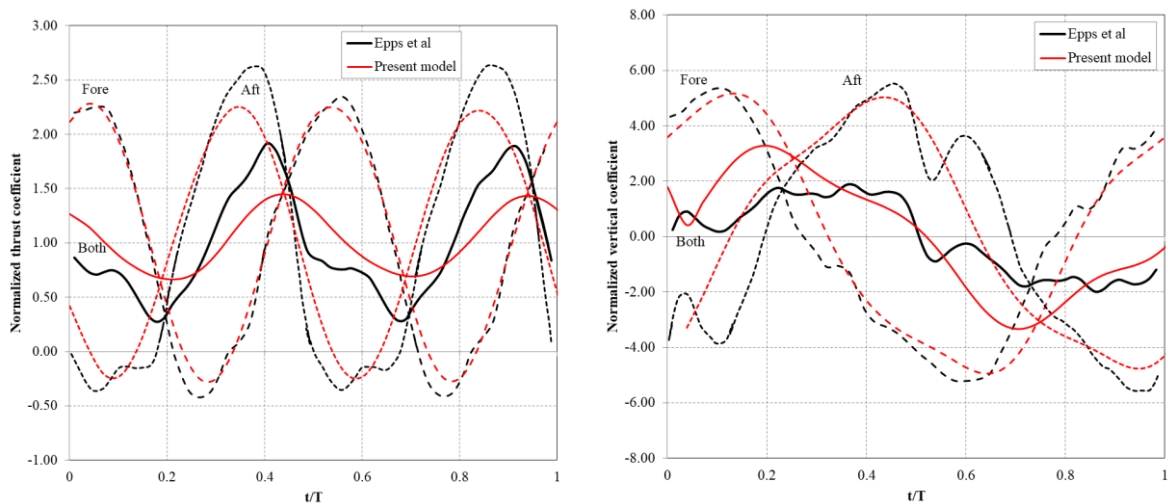


Figure 3.17: a) Comparison of the normalized thrust  $C_T/\bar{C}_T$  and b) normalized vertical force  $C_y/\bar{C}_T$  coefficients between the present model results with numerical results (Epps et al., 2016), with  $h_{0i}/c = 1$ ,  $\theta_{0i} = 45^\circ$ ,  $\psi_i = 90^\circ$ ,  $\phi_i = 135^\circ$ ,  $s^* = 8$ ,  $St = 0.4$ .

This figure shows the instantaneous thrust and vertical force coefficient time history, for the fore and aft foil, normalized by the value of the average thrust coefficient of a single foil. The total of the two foils it is also plotted. This configuration represents a compromise between high thrust and low vertical force amplitudes, which will be further studied during this

section. These results are compared against the present model data with good agreement, especially in the fore foil as expected. It confirms the assumption that the fore foil is minimally affected by the aft foil. The results for the aft foil present some discrepancies, in the vertical force in thrust coefficient, the model not being able to capture the peaks. This could be explained due the limitation of the present model in capturing the full interaction of both foils' vortex wakes. From this observation it is expectable that the thrust coefficient modelled by the present method will be less in comparison to the following case.

Table 2 shows a comparison between Epps values and the present model. For the single foil, and the same parameters, Epps results presents 30% over-prediction against both Read's experiment and Filippas numerical data  $\bar{C}_T = 0.31$  (Section 3.1). If results are taken proportionally, present model underestimates the fore thrust coefficient by 7% and aft by 13%, which seems to be a promising result.

Table 3.2 Comparison of present model results with Epps et al. (2016) numerical results, with  $h_{0i}/c = 1$ ,  $\theta_{0i} = 45^\circ$ ,  $\psi_i = 90^\circ$ ,  $\phi_i = 135^\circ$ ,  $s^* = 8$ ,  $St = 0.4$ .

$\phi_i$	Foil	$\bar{C}_T$	
		Epps et al. (2016)	Present method
90°	Fore	0.43	0.31
	Aft	0.65	0.44
135°	Fore	0.43	0.31
	Aft	0.61	0.41
180°	Fore	0.43	0.31
	Aft	0.55	0.37
	Single	0.39	0.31

Whereas in the single foil case in infinite domain the main space of study was the pitch angle (i.e. the effective angle of attack) and the Strouhal number (frequency), in the tandem foil, the number of parameter combination becomes so large with the introduction of inter-foil separation distance and phase lag, that it is necessary to narrow the study. In the present thesis we follow Muscutt et al. (2017) work, keeping the effective angle of attack the same, exploring first the foil separation – frequency space  $s^* - St$  and then the phase lag. Muscutt studied also a NACA0016 tandem foil in a two-dimensional infinite domain, with chord length  $c = 1$  m, pitching at one-quarter-point at a flow speed  $U = 1$  m/sec. The Reynolds number was set to  $Re = 7000$ . The parameters used in the current simulations are heave amplitude  $h_{0i}/c = 1$ , maximum angle of attack  $\alpha_{0i} = 10^\circ$ , heave-pitch phase  $\psi_i = 90^\circ$ . Figure 3.18 presents a comparison between the present model and Muscutt results. It shows the aft foil average thrust coefficient, normalized with the single foil average thrust, for a range of foil non-dimensional separation  $s^*$  and Strouhal number, with inter-foil phase lag  $\phi_i = 90^\circ$ .

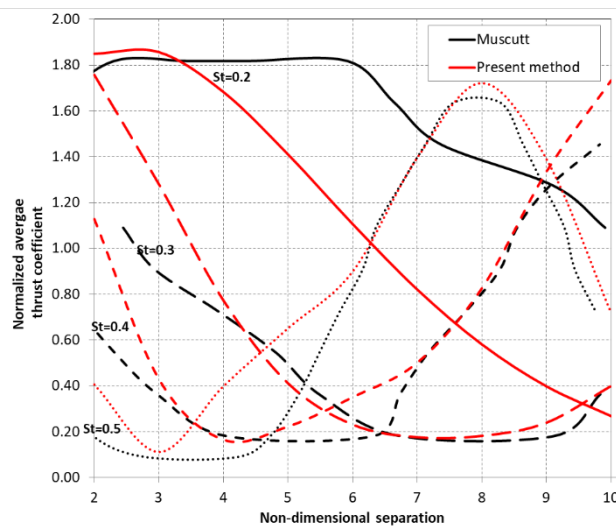


Figure 3.18: Normalized average thrust coefficient varying with non-dimensional separation and Strouhal number, for inter-foil phase lag  $\phi_i = 90^\circ$ , with  $h_{0i}/c = 1$ ,  $\alpha_{0i} = 10^\circ$ ,  $\psi_i = 90^\circ$ . Comparison of the present model with Muscutt et al. (2017) results.

It is possible to observe that for each frequency, depending on the parametric combinations, the tandem arrangement leads to lower thrust ( $\approx 0.2$ ) or almost twice ( $\approx 1.8$ ) the thrust of a single foil. In this latter case, the front and aft foil vortex wake interact constructively. In this high-performance tandem case, the aft foil weaves in between the vortices that are shed from the fore foil. This increases the vorticity on the front surface of the aft foil, and therefore also the strength of the vortices that are shed into the wake. These strong vortices become interspersed with the vortices from the forward foil, pairing up with them and creating a double BvK street. This creates a faster velocity behind the foils than the single foil case, which accounts for the higher thrust. On the other side, in low performance tandem cases, the aft foil comes very close to or crash into the vortices shed by the forward foil, causing a decrease in the strength of the vorticity on the surface of the aft foil, and therefore the strength of the vortices shed in the wake. In this case, a more dispersed and weaker jet is present behind the foils than in the high-performance tandem case (Muscutt, 2017). Examples of the vorticity and flow will be presented in Chapter 5 using CFD model results. The comparison of Muscutt results with the present model clearly shows a qualitative good agreement, with discrepancies around 4.8%, exception for low foil separation ( $s^* < 3$ ) and Strouhal  $St \leq 0.2$ , where significant differences are noted, indicating limitations of the model, due to the assumptions taken. In general, the present model captures both the variation in distance and in frequency.

Figure 3.19 shows further exploration of the parametric study, plotting normalized aft foil average thrust with  $St = 0.2$ ,  $s^* = 6$ , at different inter-foil phase lag values. It is seen that for each frequency-separation pair it is possible to tune the phase lag for high-performance. When comparing the present results with Muscutt's data, it is possible to observe a  $90^\circ$  phase discrepancy, confirming the limitations for low frequencies detected before and indicating that the estimation of the phase could be the problem.

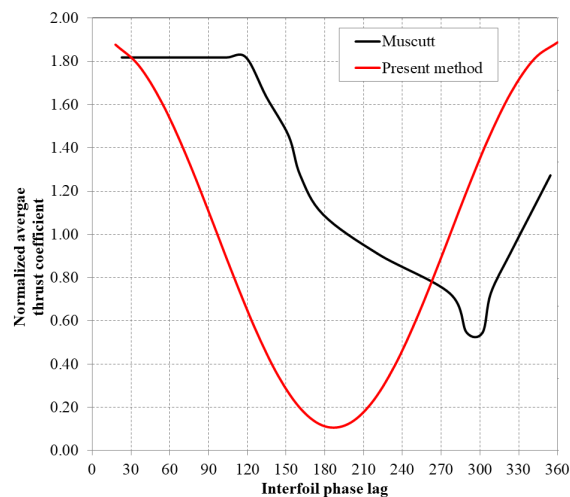


Figure 3.19: Normalized average thrust coefficient varying with inter-foil phase lag,  $St = 0.2$ ,  $s^* = 6$ . Comparison of the present model with Muscutt et al. (2017) results.

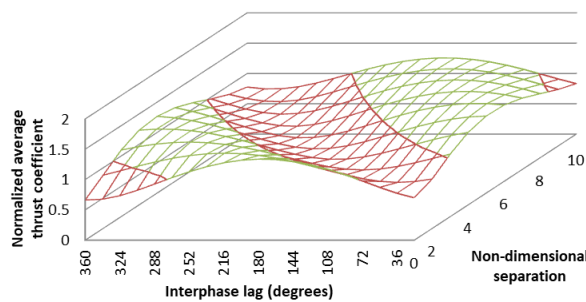


Figure 3.20: Present model results of the normalized aft foil average thrust in the inter-foil phase lag – separation space, for  $St = 0.4$ .

Figure 3.20 shows the results of the present model simulation for  $St = 0.4$  for the different phase lags and separations. As shown by the diagonal bands of high and low thrust, the thrust force is highly dependent on both phase and spacing. These have the form of parallel ‘ridges’ and ‘valleys’ caused by the interaction explained before clearly visible in the figure. In the same way the contours of propulsive efficiency of the aft foil have the same form of diagonal bands as the thrust coefficient contours. In the phase lag-separation combinations that lead to higher thrust the efficiencies are generally the same as the efficiency of a single foil. When the aft foil produces a lower thrust, the efficiencies are much lower than a single foil (Muscutt et al., 2017). Therefore, in the present work the efficiency calculation was found secondary.

Figure 3.21 shows another exploration of the present model where the normalized average thrust of the aft foil is simulated for different separations and frequencies, assuming optimal phase lag i.e., a high-performance tandem case, as explained before.

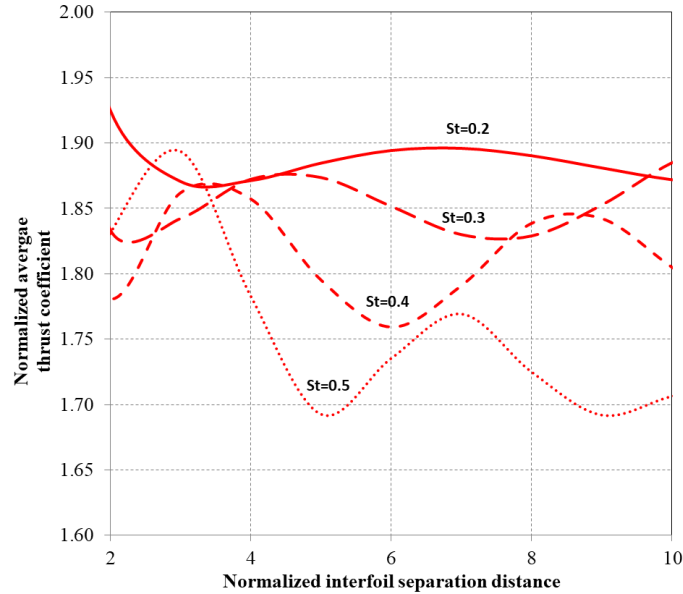


Figure 3.21: Normalized average thrust coefficient varying with inter-foil separation distance  $s^*$  and Strouhal number, for optimal inter-foil phase lag.

It is possible to see that for each frequency the thrust can be again optimized in terms of foil separation being evident in two main ranges,  $s^* = [3, 5]$  and then  $s^* = [7, 9]$ . Besides the absolute value discrepancy found before, these results have a good qualitative agreement with the contour plots presented by Muscutt et al. (2017), indicating that the model also captures well the frequency variation.

The parameter configuration space is enormous. One of them would be to explore the possibilities of improving performance with different flapping amplitudes of the front and aft foils. Another example would be to address thrust force deviation minimization rather than thrust optimization. In terms of tandem performance, Muscutt reports increases of 190% in average thrust and 120% in efficiency for the aft foil, for  $St = 0.2$ ,  $s^* = 6$  and  $\phi_l = 90^\circ$ , showing the possibility to have in the total tandem foil almost the triple of a single foil thrust.



# Chapter 4

## CFD Numerical Modelling

This chapter provides background information regarding the numerical modelling discussed in Chapter 5 and 6. It briefly presents the fundamentals of the viscous flow (CFD) solver ReFRESKO (MARIN, 2022b) used, its governing equations, grid generation and boundary conditions. Likewise, it briefly describes the computing resources used. Since the present work focus on CFD practical application, the numerical details of the solver are not discussed here. This chapter concludes with an overview of the verification & validation methods adopted.

### 4.1 CFD Background

In the attempt to obtain more accurate solutions for the foil propulsion problem, other methods besides linear theory have been employed. An alternative approach is nonlinear theory, in which the vortex distribution solution is found by solving a singular frequency-domain integral equation (e.g., Grue et al. 1988). In the case of numerical methods, potential flow panel method codes calculate the flow around a wing section, based on the replacement of the wing section's geometry by singularity panels, such as source, doublet, and vortex panels. The usual conditions of impermeability and Kutta condition are imposed (e.g., the time-domain panel method used by Filippas & Belibassakis, 2014b). Their accuracy depends on the number, order and choice of panels. Because in panel methods only boundary (i.e., surface) discretization is necessary (known as boundary element method), they are supposed to be fast and easy to implement. However, the non-linearities and viscous effects are not taken in account. Requiring more computing power, more sophisticated and accurate numerical models have been introduced to analyse the performance of the oscillating foil, in particular Computational Fluid Dynamics (CFD). The strategy of CFD is to replace the continuous problem domain with a discrete domain using a grid with a finite number of cells. The continuous governing differential equations that describe the physical processes involved are approximated by a system of discretized algebraic equations. This allows the relevant flow variables to be solved at the centre of each cell, or node, based on the values of its surrounding nodes and using iterative methods. With the availability of super computers, CFD codes can solve finer meshes to achieve high accuracy. Thus, the largest and most complex problems can be solved, such as turbulent flows.

The first step or pre-processing phase in obtaining a CFD numerical solution is to discretize the geometric domain to define a numerical grid using a meshing software e.g., Pointwise ([www.pointwise.com](http://www.pointwise.com)), GridPro ([www.gridpro.com](http://www.gridpro.com)) or Numeca Hexpress ([www.numeca.com/hexpress](http://www.numeca.com/hexpress)), which were used in this work. Assumptions are made concerning the type of flow to be modelled as well as the application of initial and boundary conditions. Then the actual computations are performed by the solver, e.g., Siemens Star-CCM+ ([www.star-ccm.com](http://www.star-ccm.com)), openFOAM ([www.openfoam.com](http://www.openfoam.com)), Ansys Fluent ([www.ansys.com/products/fluids/ansys-fluent](http://www.ansys.com/products/fluids/ansys-fluent)), MARIN ReFRESKO (MARIN, 2022b). Finally, the obtained results are visualized and analysed in the post processing phase. At this stage the results are verified, and conclusions can be drawn based on the obtained results. Finally, post-processing tools like TecPlot ([www.tecplot.com](http://www.tecplot.com)) and ParaView ([www.paraview.org](http://www.paraview.org)) are used to analyse the numerical results. To access the verification of the accuracy of the results, evaluating the error from numerical methods, procedures have to be

carried out at coding level and at solution level. Finally, the model should be validated by comparison the results with experimental data.

In previous chapters results from CFD tools were used for comparison, in particular Fluent (Silva, 2012) and LilyPad (Muscutt, 2017). In this thesis we use ReFRESKO which has been already applied and tested for similar applications namely moving rigid bodies (Rosetti & Vaz, 2017; Fernandes, 2016), propulsion (Rijpkema & Vaz, 2011) as well as free-surface and waves (Klajj et al. 2018; Pereira, 2018). The min graphic tool used in this work is ParaView. It is an open-source, multi-platform data analysis and visualization application, that allows quick building of visualizations using qualitative and quantitative techniques, both interactively in 3D and programmatically.

## 4.2 CFD Solver ReFRESKO

ReFRESKO stands for “Reliable and Fast RANS Equations Code for Ships and Constructions Offshore”, a CFD code that has been under development since 2005, based on state-of-the art numerical algorithms and software features, together with the long-lasting experience in CFD of the Maritime Research Institute Netherlands (MARIN) (MARIN, 2022a). The code is currently being developed and tested at MARIN in collaboration with blueOasis (Portugal), Instituto Superior Técnico (Portugal), University of Southampton (UK) and other institutions around the world.

It is a viscous-flow CFD code that solves multiphase unsteady incompressible flows using the Navier-Stokes equations, complemented with turbulence models and cavitation models (Vaz et al., 2009). The equations are discretized using a finite-volume approach with cell-centred collocated variables. The equations are discretized using a finite-volume approach with cell-centred collocated variables, in strong-conservation form, and a pressure correction equation based on the SIMPLE algorithm (Ferziger & Perić, 2002; Patankar, 1980) is used to ensure mass conservation. Time integration is performed implicitly with first or second-order backward schemes. At each implicit time step, the non-linear system for velocity and pressure is linearized with Picard's method and a segregated approach is adopted for the solution of all transport equations (Klajj & Vuik, 2013). The implementation is face-based, which permits grids with elements consisting of an arbitrary number of faces (hexahedrals, tetrahedrals, prisms, pyramids, etc.). State-of-the-art CFD features such as moving, sliding and deforming grids, as well as automatic grid adaptation (refinement and/or coarsening) are also available. Both rigid-body and flexible-body (fluid-structure interaction) simulations can be performed, Turbulence modelling with both traditional RANS and Scale-Resolving Simulations (SRS) and wave generation potential flow codes (OceanWave3D, SWASH) are implemented. ReFRESKO is written in free-format Fortran, and linked to many state-of-the-art external tools. The code is parallelised using MPI (Message Passing Interface) and sub-domain decomposition and runs on Linux workstations and HPC (High-Performance Computing) clusters. Some of these features will be detailed in the next section.

This code has been chosen in this work because its proven use in a wide range of maritime applications and in similar problems. Its flexibility permits to use of (almost) any grid generator and visualizer. Moreover, it is open-usage and open-source code, developed and maintained by several non-profit organizations. In particular this work was supported by the WavEC – Offshore Renewables ([www.wavec.org](http://www.wavec.org)) that also sponsored this PhD and in particular the blueOASIS ([www.blueoasis.pt](http://www.blueoasis.pt)) team, that are also part of the supervising team. Through them, it was possible to access both the WavEC Linux workstation and the University of Southampton *Iridis* Computer Cluster (Southampton, 2021).

### 4.2.1 Fundamentals of the Governing Equations

As mentioned before, the first step it to discretize the geometric domain to define a numerical grid, which will be detailed later in this section. We start by applying the fundamental laws of

fluid mechanics to obtain the governing equations. First, the continuity equation states that the net flow across any control volume is zero, in the absence of sources or sinks. In an incompressible and one-phase flow, as the change in mass in a control volume is equal to the net flux of mass through the faces, the mass inside a control volume is conserved. The conservation of mass or continuity equation is

$$\nabla \cdot \mathbf{v} = 0. \quad (4.1)$$

In the same way, the conservation of momentum equation is formulated using Navier-Stokes (NS) equation (application of Newton's second law of motion for fluids) given by

$$\frac{\partial}{\partial t}(\rho \mathbf{v}) + \nabla \cdot (\rho \mathbf{v} \mathbf{v}) = -\nabla p + \nabla \cdot \boldsymbol{\tau} + \rho \mathbf{g} + \mathbf{B}. \quad (4.2)$$

Here  $\mathbf{v}$  denotes the velocity vector,  $p$  the pressure and  $\mathbf{B}$  the body-force vector.  $\boldsymbol{\tau}$  is the viscous stress tensor

$$\boldsymbol{\tau} = \mu[\nabla \mathbf{v} + (\nabla \mathbf{v})^T]. \quad (4.3)$$

$\mu$  denotes the dynamic viscosity and the superscript  $T$  represents the transpose of a vector or matrix (Mewes, 2021). These equations form a set of coupled, nonlinear partial differential equations, and its solution gives the velocity and pressure fields. In addition, a transport equation for multiphase flow is needed for free-surface problems. For an arbitrary quantity  $\phi$ , (velocity, pressure, turbulent quantities, etc.) the generic transport equation reads:

$$\frac{\partial}{\partial t} \rho \phi + \nabla \cdot (\rho \phi \mathbf{v}) = \nabla \cdot (\Gamma \nabla \phi) + q_\phi, \quad (4.4)$$

where  $\Gamma$  is the diffusivity of  $\phi$  and  $q_\phi$  a general source or sink term. The first term corresponds to unsteady component, the second to convection, the third to diffusion and the last is the source contribution. In the convection term, the velocity vector is subtracted by the grid velocity vector, not included in the equation. In the finite-volume approach, the integral form of the conservation equations is applied to the control volume defined by a cell, within a fluid domain  $V$  (Figure 4.1),

$$\frac{\partial}{\partial t} \int (\rho \phi) dV + \int (\rho \phi \mathbf{u}) \cdot \mathbf{n} ds - \int (\Gamma \nabla \rho \phi) \cdot \mathbf{n} dS = \int q_\phi dV, \quad (4.5)$$

where  $\Gamma$  is a diffusion coefficient matrix and  $\mathbf{n}$  the normal vector (Pereira, 2018).

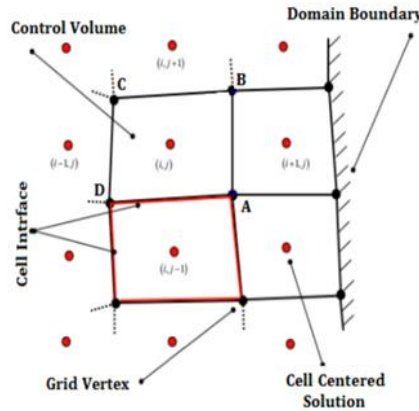


Figure 4.1: Cells in a finite volume approach.

In integral form, the momentum equation reads:

$$\frac{\partial}{\partial t} \int (\rho \mathbf{v}) dV + \int (\rho \mathbf{v} \mathbf{v}) \cdot \mathbf{n} ds = \int \mathbf{T} \cdot \mathbf{n} dS + \int \rho \mathbf{B} dV, \quad (4.6)$$

where  $\mathbf{T}$  denotes the stress tensor for Newtonian fluid,  $\mathbf{B}$  being a body-force vector.

In this work, based on considerations of Section 2.3.1, turbulent flow is assumed. Turbulent flow is characterized by the irregular movement of fluid's particles, in contrast to laminar flow where fluid flows in parallel layers. The turbulence is characterized by high lateral mixing and disruption between the layers, and also by eddies, and apparent randomness, usually present when the inertial forces dominate over the viscous forces. At the moment, the most popular engineering approach to simulate turbulence is based on Reynolds-Averaged Navier-Stokes equations (RANS), and then complemented by turbulence models. The Reynolds-averaging of NS equations implies that the time dependent quantities of the flow are replaced by a mean and a statistical fluctuation quantity, owing to turbulence. For unsteady flow problems, the mean field quantity is obtained by ensemble averaging over  $N$  identical quantities. For the turbulence closure equation, different methods are available in ReFRESKO, but in the present work it is chosen the two-equation  $k - \omega$  turbulence model, i.e., the Shear Stress Transport (SST) version 2003 (Menter, et al., 2003), commonly-used for maritime applications. This model includes two transport equations for the turbulent kinetic energy  $k$  and the dissipation rate per unit kinetic energy  $\omega$ , respectively

$$\frac{\partial}{\partial t} (\rho k) + \nabla \cdot (\rho \mathbf{v} k) = \nabla \cdot \left[ \left( \mu + \frac{\mu_t}{\sigma_k} \right) \nabla k \right] + S^k, \quad (4.7)$$

$$\frac{\partial}{\partial t} (\rho \omega) + \nabla \cdot (\rho \mathbf{v} \omega) = \nabla \cdot \left[ \left( \mu + \frac{\mu_t}{\sigma_\omega} \right) \nabla \omega \right] + S^\omega, \quad (4.8)$$

where  $S^k$ ,  $S^\omega$  and  $\mu_t$  definitions and remaining model constants can be found in Moukalled et al. (2016) and Menter et al. (2003).

#### 4.2.2 Numerical Discretization

Next step after integration of the differential equations over a small volume is the discretization, i.e., its replacement by a set of algebraic equations. ReFRESKO uses a collocated approach, thus all flow variables are defined in cell centres and interpolation practices are used when face values are needed. The volume integrals of quantities  $\phi$  are calculated using the Piecewise Linear method (2<sup>nd</sup> order) as:

$$\int \phi dV \approx \phi_c \Delta V, \quad (4.9)$$

in which  $\phi_c$  is the value of  $\phi$  at the cell centre. The surface integrals are approximated as:

$$\int \phi dS \approx \sum_{i=1}^{N_f} \phi_{fi} S_{fi}, \quad (4.10)$$

where  $\phi_{fi}$  is the variable value in the cell face centre and  $S_{fi}$  is the cell face area.

To deal with each transport equation several interpolation practices or schemes can be used. Higher-order upwind methods (i.e., backward approximation) such as Quadratic Upwind Interpolation for Convective Kinematics (QUICK) (Ferziger & Peric, 2002; Leonard, 1979) are often applied to the convective term, for providing reasonable accuracy and stability. Quadratic interpolation may result in overshoots, especially when jumps in the variable are encountered. For this reason, the scheme applied in this thesis for the momentum equations is the Limited QUICK scheme (Hoekstra, 1999) that uses a flux limiter to ensure that wiggles in the solution are avoided. For turbulence the convective fluxes discretization scheme used is First Order Upwind (FOU), chosen for having more stability. The diffusion term is dealt with the approach proposed by Ferziger & Peric (2002) which consists in splitting the flux into an implicit part and a deferred correction.

Time discretization uses the approximation

$$\frac{\partial}{\partial t} \int \rho \phi dV \approx [c_1(\rho_c \phi_c \Delta V)^n + c_2(\rho_c \phi_c \Delta V)^{n-1} + c_3(\rho_c \phi_c \Delta V)^{n-2}] / \Delta t, \quad (4.11)$$

where  $n$  is the time level and  $\Delta t$  the time step. The coefficients  $c_i$  are defined whether the schemes are the first-order backwards Euler or second-order backward differencing.

### 4.2.3 Free-Surface and Waves Models

In order to deal with two-phase flows i.e., for modelling air-water interfaces, where each fluid is considered constant-density, governing equations are also required. For free-surface type flows, a volume-fraction variable  $\alpha$  is modelled and transported, representing the proportions of air/water in any given cell. The volume of fluid (VOF) equation is:

$$\rho = \alpha \rho_a + (1 - \alpha) \rho_w. \quad (4.12)$$

The diffusion or source/sink terms are neglected and the free-surface transport equation for the volume fraction  $\alpha$  reads

$$\frac{\partial \alpha}{\partial t} + \nabla \cdot \alpha \mathbf{v} = 0. \quad (4.13)$$

The wave height is then calculated for the cells where  $\alpha = 0.5$ . A critical part of this equation is the discretisation of the convective term  $\nabla \cdot \alpha \mathbf{v}$ . The convective fluxes discretization schemes used are ReFRESKO's Interface-Capturing Scheme (Refrics) based on the orientation of interface between phases (Klajj et al., 2018) and Total Variation Diminishing (TVD) SuperBee (Roe, 1985).

The generation of wave's modulation is achieved by employing different boundary conditions. The selected wave model in this work uses the Stokes wave theory to the fifth-order (Stokes5) presented by Skjelbreia and Hendricksson (1960) since their approach has found widespread usage in engineering practice. Vaz et al. (2009) implemented this formulation in ReFRESKO according to the code provided by Lin (2008).

### 4.2.4 Solution Methodologies

The previous section has shown how the flow of a fluid within a domain can be approximated, simulated and modelled via the RANS equations and various additional transport equations, by applying them at each cell centre in a discretized grid. For a typical maritime application, there may be many non-linear, tightly coupled partial differential equations to solve, including those for momentum, continuity, turbulence, free-surface and cavitation modelling.

In ReFRESKO, solving this complex system of conservation equations is done in a segregated manner, i.e., despite being coupled equations, they are solved individually. Each variable assumes the others as known then an iteration procedure restores the coupling of the equations by satisfying all the equations within certain tolerances. These are quantified by means of residuals. In particular, the pressure-velocity coupling is dealt with by the Picard iterative method (Klajj & Vuik, 2013) based on the Semi-Implicit Method for Pressure Linked Equations (SIMPLE) (Ferziger & Perić, 2002; Patankar, 1980). In that manner, linear systems are derived from each transport equation and nested within loops. Moreover, for unsteady computations, the iteration process is to be performed within each time step. There are then three levels of loops: a time loop, an outer loop and the inner loops. The time loop occurs in the unsteady calculations and when finished, time is incremented. Within the outer loop, all equations will be solved and once all conservation equations are satisfied within some tolerance, the outer loop end, and the next time loop starts. Finally, the inner loops take place

when solving iteratively each of the matrix system which results from the discretization of the equations for each component.

In the outer loop the first principle is that of linearization, performed using a Picard's method, whereby the system of non-linear governing equations is converted to their linear counterparts which can be solved iteratively and individually to achieve a correct solution. At the start of each non-linear iteration, Neumann or Dirichlet boundary conditions (which suitably close the system), may need to be updated. A suitable end for the non-linear loop is found by monitoring the maximum ( $L_\infty$ ) or root-mean square ( $L_2$ ) residuals of each equation's linear equation-system

In order to stabilize the iterative process, under-relaxation is applied between each non-linear loop. This damps changes in the solution to prevent rapid divergence and cancels it out when the solution is converged. Relaxation can be applied explicitly or implicitly. Explicit relaxation is applied once a solution vector has been computed, by taking a weighting of the computed value and the old value. Implicit relaxation increases the diagonal dominance of the linear system, making it easier to solve. These are adjusted separately for each test case.

In an unsteady flow, the transient term, which was discretized using one of the schemes mentioned before, must be included within a time loop iteration, with each non-linear (steady) flow solution representing a single time step. In this loop there is a counter, which only advances when the non-linear loop reaches convergence (or after a predefined number of iterations). The second order scheme is used (Implicit 3<sup>rd</sup> Time Level) for time integration in all test cases, except with incident waves where a first order scheme is used (Euler) for convergence reasons.

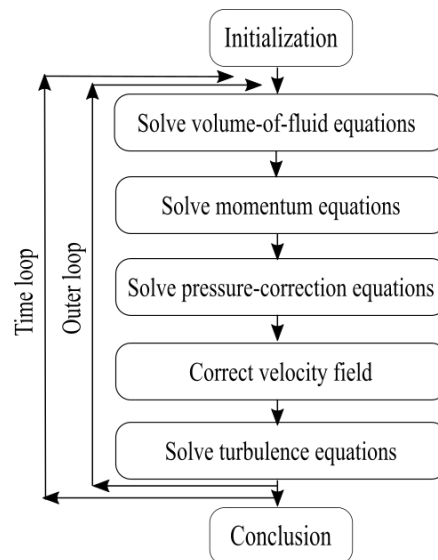


Figure 4.2: SIMPLE algorithm schematics.

Figure 4.2 shows the SIMPLE algorithm, and therefore the two external loops of a typical CFD simulation. The routines within these inner loops are important to examine, from a computational perspective, since they are repeated many hundreds or thousands of times in a particular simulation. In this thesis, the linear systems are first pre-conditioned and then solved iteratively. The momentum equations are pre-conditioned by Jacobi's method (i.e., diagonal scaling) and solved by the Generalized Minimum Residual method (GMRES). The velocity-pressure coupling is achieved by using a segregated, pressure-correction type method. It is the legacy version of the Pressure-Weighted Interpolation method (PWI) (Klaij & Vuik, 2013) which modifies the interpolation of the velocities at the cell faces by adding a pressure term, carefully chosen to suppress spurious modes while maintaining the second-order accuracy of the discretization. The turbulence equation is solved with a Conjugate Gradient method (CG) and pre-conditioned by Block-Jacobi's method (Jacobi is used between blocks of grid partitioning). These methods are presented in Balay et al. (2013) and Ferziger & Peric (2002).

### 4.2.5 High-Performance Computing (HPC)

A supercomputer (i.e., a cluster or a high-performance computer) is a large computer, consisting of many small nodes which resemble individual computers. The nodes are connected using a high-speed inter-nodal network for fast data transfer, and a slower Ethernet connection for management functions. *Iridis5*, the University of Southampton supercomputer (Southampton, 2021), is one of the world’s top 500 supercomputers, using a Infiniband inter-nodal network, grouping approximately 485 nodes together, and connecting these groups via parallel connections in a tree-like hierarchy. Nodes are the coarsest level of parallelization in a supercomputer.

To parallelize scientific code MPI (Message Passing Interface) communication is used in ReFRESKO. Each computational node runs a separate instance (process), or several instances (in the computational nodes), of a parallel application, each with its own memory, sharing data via MPI and memory buffers.

The calculations of this work have been conducted on two HPC clusters: the supercomputer *Iridis5* and the Unix workstation *Wavux-1* own by WavEC – Offshore Renewables. The main features of these clusters influencing the calculation time are summarized in Table 4.1.

Table 4.1: Available details of the machines used in the present work.

Cluster	<i>Iridis5</i>	<i>Wavux-1</i>
Year	2017	2016
Processor	Dual 2.0 GHz Intel Skylake	2 Intel Xeon CPU E5-2680-v4
Cores	20 000	28
Networking	Infiniband	
Memory	192-768 GB (each node)	128GB
Hard drive	2.2 PB	8.2 TB

### 4.3 Grid Generation

A numerical grid or mesh is a discrete representation of the geometric domain on which the problem is to be solved. It divides the solution domain into a finite number of cells based on the physics to be resolved. Depending on the geometry complexity, the user should define the requested mesh type: structured or unstructured. Calculation in structured grids, where grid lines are aligned perpendicular or parallel to the surface meshes, usually takes less time than in unstructured grids because, to date, the existing algorithms are more efficient. Moreover, for simple problems such as an isolated wing, structured grids are generally more accurate per unknown than unstructured. However, for more complex flows, the adaptivity facilitated by an unstructured grid may allow more accurate solutions. Unstructured grid generation is usually much faster than structured grid generation. But, in this last case, if the geometry is only slightly modified from a previously existing geometry, then grid generation can be faster.

For the present work the grid generation software Numeca Hexpress is used ([www.numeca.com/hexpress](http://www.numeca.com/hexpress)). This tool automatically generates unstructured hexahedral meshes in complex 2D and 3D geometries. It is equipped with algorithms for mesh optimization that guarantee that a very large percentage of cells are convex, refining cells locally close to high geometry curvature regions. It allows the insertion of viscous layers, with a robust high aspect cell ratio. Hexpress allows the definition of boundary conditions and also user-specified volume box refinement. Besides Hexpress grids, structured GridPro grids were used at the beginning of this work, in order to check the pros & cons of both in the simpler 2D foil context. This preparatory proceeding made possible higher complexity in the following simulations.

### 4.3.1 Computational Domain and Grid Layout

Most numerical simulations are conducted in a prismatic rectangular computational domain defined in a Cartesian coordinate system ( $xyz$ ). The referential is centred at the middle point of the hydrofoil's trailing edge, or the front foil's trailing edge in case of tandem configuration, with the  $x$  axis aligned with the streamwise flow, the  $y$  axis set in the vertical direction, and the  $z$  axis oriented with the foil's span. The domain has inlet and outlet boundaries in  $x$  axis directions, bottom and top boundaries at  $y$  axis, and two lateral spanwise boundaries. The respective implementation in the numerical setup is detailed in the next section. Table 4.2 presents the dimensions of the computational domain for the different cases. After a few preliminary simulations, these distances were considered sufficient to avoid the reflection of the pressure fields at the boundaries.

For the infinite domain single foil case, detailed in Section 5.1.1 to 5.1.3, the method of unstructured grid generation using Hexpress started with a coarser base mesh having 1 cell per chord refinement ratio and then by adding several refinement sub-regions.

Table 4.2: Dimensions of the computational domains.

Grid type	Case	Dimensions ( $x,y,z$ ) (chord)
Hexpress	2D Infinite Domain	$(20+50) \times (50+50)$
	2D Free-surface	$(20+50) \times (20+50)$
	3D Infinite Domain	$(10+20) \times (50+50) \times (20+20)$
	3D Free-surface	$(10+20) \times (50+50) \times (20+20)$
Grid Pro	2D Infinite Domain	$(50+50) \times (50+50)$

Two square regions of refinement were added, one around the perturbation damping area with  $10 \times 10c$ , the other covering the wake and then a circular refinement zone near the foil with a  $1.1c$  radius, with a refinement ratio of 4, 5 and 6 respectively. Two more regions of refinement were inserted, one at the foil trailing edge and other at the leading edge, where the quantity gradients are greater, with a 12 and 9 refinement ratio, respectively. Figure 4.3 provides several close-up zooms of the grid. Finer grids for more accurate results were obtained by changing the base refinement ratio and then adjusting the different sub-regions refinement ratio. A viscous layer was added based on the Reynold numbers used.

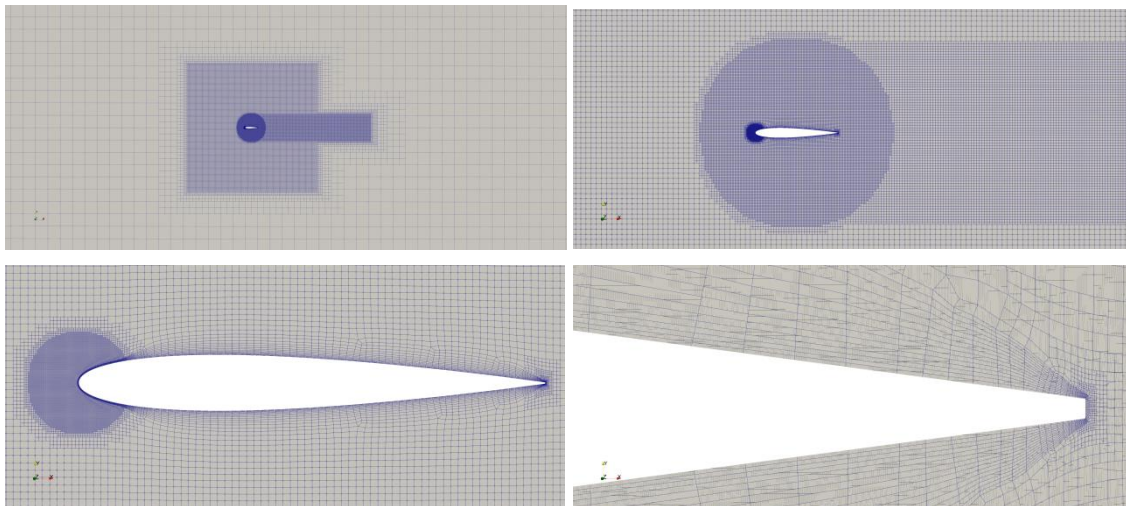


Figure 4.3: Hexpress unstructured mesh refinement regions a) around foil and wake, b) close to the foil, c) leading and trailing edge and d) trailing edge.

In addition to unstructured Hexpress grids, a comparison test case is done with structured GridPro grids provided by MARIN. Figure 4.4 shows an example of a grid that was used, with different details. The trailing edge shape used here is different from Figure 4.3 because of

GridPro restrictions where body shapes should match grid shape. Since the effect is proportional to its dimension relative to chord length, the consequences are negligible.

For test cases with free-surface, with or without incident waves, here only applied to Hexpress grids, an extra refinement region was added around the initial water plane level, allowing enough resolution for wave correct modelling. The topology used here consists of a refinement region from  $0.25c$  above and below the mean water-level. An example is presented in Figure 4.5.

After the grid generation, the grid quality must be addressed, since it is essential to correct CFD simulations. The three parameters used to measure of the grid quality are: the skewness that should be the lowest as possible (or for orthogonal quality as higher possible), in order to avoid slowing down the convergence of simulation and incorrect computations fluxes near walls; the smoothness (cell changing in size) that measures sudden size jumps to be avoided in high gradient regions, in particular near-wall boundaries; and the aspect ratio that should be kept lower in the direction of high gradients. In all the grids used in the present simulations the skewness is higher than 0.2 only for 0.5% of the total number of cells and the concave and deformed cells were kept to zero.

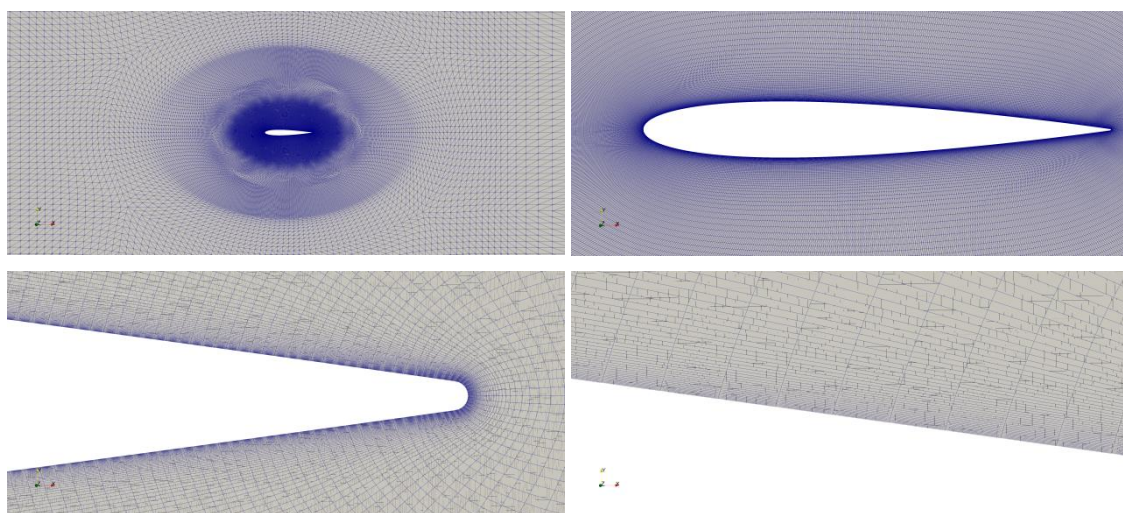


Figure 4.4: GridPro structured grids refinement details a) around foil, b) close to the foil, c) trailing edge and d) foil surface.

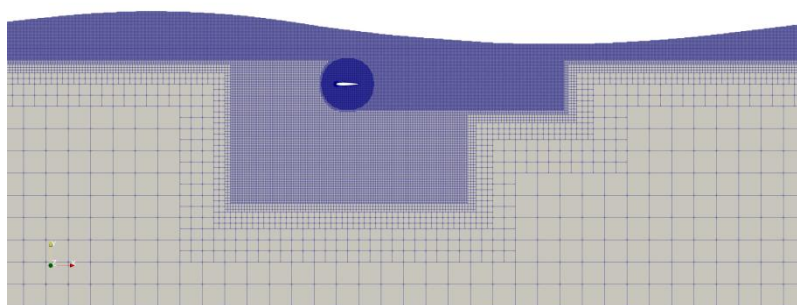


Figure 4.5: Unstructured Hexpress grid for free-surface or incident wave cases: example of the refinement region used.

## 4.4 Numerical Setup

### 4.4.1 Boundary Conditions

The transport equations previously presented in Sections 4.2.1 to 4.2.3 need boundary conditions for all quantities at all boundaries. Physically, boundary conditions used in this work can be categorised as follows:

At the inlet (**inflow boundary condition**) the components of the velocity vector and turbulence quantities are given by a Dirichlet boundary condition, prescribed by a constant, from where the convective fluxes can be calculated. The pressure is extrapolated from the interior of the domain, by approximations based on one-sided difference or extrapolations (zeroth-order extrapolation - Neumann condition). Diffusive fluxes, usually unknown, can be approximated by using the available variable values on the boundary face and one-sided discretization schemes for the gradients.

At the outlet (**outflow boundary condition**) a usual assumption is that in which velocities, turbulent quantities and pressure are extrapolated (zeroth-order is used for developed flow - Neumann-type condition).

At the wall boundaries (**wall boundary condition**) no fluid penetrates the boundary, i.e., convective flux is zero. However, the diffusive fluxes do not vanish and are obtained by approximations. It allows a no-slip condition (fluid is moving with wall velocity) which is the case for the foil surface or a free-slip condition (no frictional losses at the boundary) in the case of the seabed. The modelled turbulence kinetic energy and normal pressure derivative are set equal to zero, while the modelled specific dissipation is given at the centre of the nearest-wall cell.

At sidewalls **symmetry boundary conditions** are used. The convective fluxes of all quantities are zero on that boundary, as well as the normal gradients of the velocity components parallel to the symmetry plane and of the scalar quantities (mixed Dirichlet/Neumann conditions).

At the top and bottom (**pressure boundary condition**), the pressure is prescribed as a constant or varying value for the complete pressure boundary. The velocities and other quantities are extrapolated from the interior as in the outflow boundary condition.

The **wave boundary condition** is an inflow boundary condition used to simulate the effects of waves entering the domain. The wave is generated by prescribing both particle velocities and the volume fraction, as well as all other convective fluxes, with the result conforming to the wave model used. The components of the velocity vector are given by a Dirichlet boundary condition, while the pressure is extrapolated from the interior.

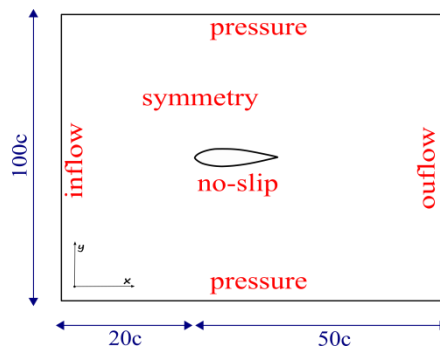


Figure 4.6: Schematic representation of the 2D computational domain and prescribed boundary conditions, for the infinite domain single foil case.

**Wave absorption zones** can be prescribed to minimize wave reflections on the inlet and outlet. ReFRESKO allows the definition of zones, where absorption is progressively increased to a maximum value. In these absorption zones the volume fraction is forced towards the undisturbed wave solution using either body forces in the air volume fraction equation, or by relaxation of air volume fraction at the end of each time step (See Perić & Abdel-Maksoud, (2016) for active wave absorption techniques). A trade-off in the maximum absorption value

should be sought off since low values may lead to reflections from the boundary, while high values may cause reflection from the zone itself due to a too high forcing.

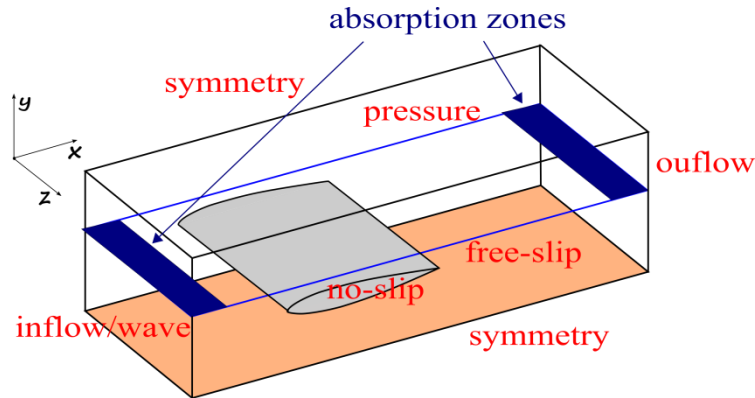


Figure 4.7 Schematic representation of 2D domain with boundary conditions, free-surface and damping zones, for the submerged single foil case (not to scale).

As for the **initial conditions**, the foil is at rest at its middle position, the initial velocity field is assumed uniform with magnitude equal to the streamwise velocity, and pressure to be zero. Likewise, the turbulent quantities are uniform, deduced from a laminar initial field. In the cases with waves, the free-surface is at rest with zero elevation.

In all test cases of this work presented in next chapters, a no-slip wall boundary condition is specified on the foil's surface in body fixed reference system. The freestream velocity is set in the inlet boundary with an earth fixed reference system. Symmetry boundary conditions are used on sidewalls, and an outflow boundary condition in the outlet. In Chapter 5, for infinite domain test cases, both top and bottom boundaries use a zero pressure condition because more pressure constrains allows the solving to be quicker. The computational domain is schematically represented in Figure 4.6, together with the boundary conditions used. The tandem foil uses the same setting.

In free-surface and incident wave domain test cases in Chapter 6, the bottom boundary conditions is replaced by a slip wall condition. Furthermore, a wave damping zone is set, next to the boundary limits of the domain using the free-surface equation parameter setting. It uses the body forces technique with cosine function variation (Rapuc et al., 2018). Although the width of the absorption zone is advised to be of same order of the wave period, to limit the number of cells in the computational domain, it was found that a  $3.0c \approx \lambda/20$  width damping zone with an absorption coefficient of 100 was enough to avoid reflections (see Figure 6.5 in Section 6.1.2). In particular, for incident wave test cases, a wave condition replaces the inflow at the inlet. Figure 4.7 presents a schematic representation of the 3D domain with free-surface and absorption zones. Table 4.3 lists the boundary condition settings for the different topologies studied in this work.

Table 4.3 Boundary condition settings for the different test cases both with single foil and tandem foil.

Boundaries	2D Inf. domain	3D Inf. domain	2D Free-surface	3D Free-surface	2D With waves
Foil(s)	No-slip	No-slip	No-slip	No-slip	No-slip
Inlet	Inflow	Inflow	Inflow	Inflow	Wave
Outlet	Outflow	Outflow	Outflow	Outflow	Outflow
Top	Pressure	Pressure	Pressure	Pressure	Pressure
Bottom	Pressure	Pressure	Free-slip	Free-slip	Free-slip
Absorption zone	-	-	Yes	Yes	Yes

## 4.4.2 Body Motion

In order to model a general rigid-body motion (translation and/or rotation) of one object within URANS, different approaches for grid-motion handling are possible a) the relative-formulation where the fluid transport equations are written and solved in the moving or relative reference frame, b) the absolute-formulation, where the fluid transport equations are solved in the moving reference frame but written in terms of absolute or inertial reference frame quantities and c) the moving-grid-formulation, where the fluid transport equations are written and solved in the earth-fixed reference frame. In the latter, due to the motion of the objects, the equations are inherently unsteady, even for steady motions. There are two different grid motion methods, i.e., move grid (MVG) and deforming grid (DG) in combination with an imposed periodic rotation and/or translation of the body, in this case the hydrofoil. In this work we use DG method based on the grid deformation of individual grid nodes (vertices) in combination with an imposed periodic rotation and/or translation of the hydrofoil (Le Roy et al., 2021). Therefore, a part of the grid remains undistorted. Two methods are available to control deformation, i.e., Radial Basis Functions (RBF) (Boer et al., 2009; Lombardi et al. 2013) and Inverse Distance Weighting (IDW) (Witteveen & Bijl, 2013). The former method is employed, using interpolation functions to guarantee no grid deformation outside a defined support radius. This method is robust and permitted all deformations, even the largest considered, without deteriorating the grid quality, and therefore ensuring well converged solutions. Figure 4.8 presents two examples of the extent of grid deformation applied here.

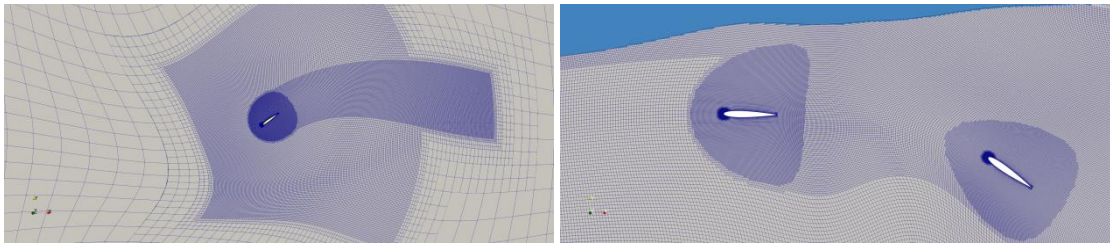


Figure 4.8: Grid deformation example in present case. a) single foil b) tandem foils.

## 4.4.3 Numerical Settings

In the present work, in order to guarantee that iterative errors are negligible when compared to discretization errors, the iterative convergence criteria  $c_{it}$  required that the  $L_\infty$  norm (maximum value) of the normalized residual of all transport equations is smaller than  $10^{-4}$ , which normally leads to a  $L_2$  norm lower than  $10^{-6}$ . Because  $L_\infty$  calculates the maxima found in the domain, and it could be located at non-important zones,  $L_2$  norm, which concerns residuals in the complete domain, is evaluated for the different test cases results. A second-order scheme (Implicit 3<sup>rd</sup> Time Level) is used for time integration, except for test cases with incident waves that use first order schemes (FOU) which although less accurate are more stable. Momentum convection discretization uses second order scheme (Limited QUICK). The assumption, based on previous chapters, is that of transition flow on the boundary layer and turbulent on the wake. Thus, the turbulence is applied with a first order scheme (FOU) which was found acceptable by Pereira (2018) in a similar application. Turbulence modelling is not used in 3D cases because of time costs. Free-surface discretization uses two schemes according to the absence (SuperBEE) or existence (Refrics) of wave generation. The ramp-up time for waves is set to zero.

Concerning body motion, imposed vertical translation, and rotation motions are set in a fixed body reference system with a deform grid scheme, with amplitudes, frequency, phases, and rotating axis according to the settings of each case (see Figure 4.8 for example).

Eight different main cases are tested: For 2D infinite domain, free-surface with calm water and with incident waves, both for single foil and tandem foil configurations; for 3D settings,

there are only two cases, a single foil with and without free-surface. Table 4.4 and Table 4.5 present a summary of the main numerical settings.

Table 4.4: Numerical settings for the different test cases with a single foil.

Equations	2D Inf. domain	2D Free-surface	2D With waves	3D Inf. domain	3D Free-surface
Time	2 <sup>nd</sup> order*	2 <sup>nd</sup> order*	Euler	2 <sup>nd</sup> order*	2 <sup>nd</sup> order*
Moment	Limited_QUICK	Limited_QUICK	Limited_QUICK	Limited_QUICK	Limited_QUICK
Free-surface	n.a.	SuperBEE	Refrics	n.a.	SuperBEE
Turbulence	n.u./SST_2003**	SST_2003**	SST_2003**	not used	not used

\* Implicit 3rd Time Level \*\* 1<sup>st</sup> order (FOU)

Table 4.5 Numerical settings for the different test cases with tandem foils.

Equations	2D Inf. domain	2D Free-surface	2D With waves	3D Inf. domain	3D Free-surface
Time	2 <sup>nd</sup> order*	2 <sup>nd</sup> order*	Euler	-	-
Moment	Limited_QUICK	Limited_QUICK	Limited_QUICK	-	-
Free-surface	n.a.	SuperBEE	Refrics	-	-
Turbulence	SST_2003/FOU	SST_2003/FOU	SST_2003/FOU	-	-

\* Implicit 3rd Time Level

## 4.5 Verification & Validation

To assess whether computational results are reliable and accurate, verification and validation procedures are required. Verification can be divided in two parts: code verification in which it is verified whether a code correctly solves the equations of the model, and solution verification that is a mathematical exercise intended to determine the numerical uncertainty resultant from the numerical procedures to solve the mathematical model. Validation evaluates the suitability of a mathematical model to represent a determined physical phenomenon. This thesis focuses on solution verification and validation following the work of Pereira (2018). Two quantities are used: errors and uncertainties, designated by respectively  $E$  and  $U$ . An error is defined as the difference between a simulated or measured value  $\Phi$  and a comparison value  $\Phi_0$  (sometimes called the true or exact value), and thus, it is a quantity that has a sign and magnitude:

$$E(\Phi) = \Phi - \Phi_0 . \quad (4.14)$$

When the evaluation of an exact solution is not known, the uncertainty  $U(\Phi)$  is estimated, providing an interval where the exact solution is contained within a certain degree of confidence. To obtain the uncertainty one needs to start by estimating the error under study. For numerical models, the computational or total error  $E_t(\Phi)$  of a numerical solution  $\Phi$  is the combination of input  $E_i(\Phi)$ , modelling  $E_m(\Phi)$  and numerical  $E_n(\Phi)$  errors

$$E_t(\Phi) = E_i(\Phi) + E_m(\Phi) + E_n(\Phi) , \quad (4.15)$$

which are illustrated in Figure 4.9.

The input error  $E_i(\Phi)$  derives from differences between the conditions and parameters of the numerical and physical problems, i.e., it is caused by assumptions taken when formulating the numerical problem, or lack of precise data on the physical problem. It affects the validation, but to simplify this it is assumed that the input error is not significant. The modelling error  $E_m(\Phi)$  is the difference between the exact solution  $\Phi_o$  of the model and the physical phenomenon  $\Phi_p$ , which in turn is generally only accessible through experimental observation, subject to an error  $E_e(\Phi)$ . For this reason, the quantification of the modelling error requires the estimation of a validation uncertainty  $U_v(\Phi)$ . The procedures used in the estimation of  $E_m(\Phi)$  are discussed later in this section and evaluate how the mathematical model represents the flow fields.

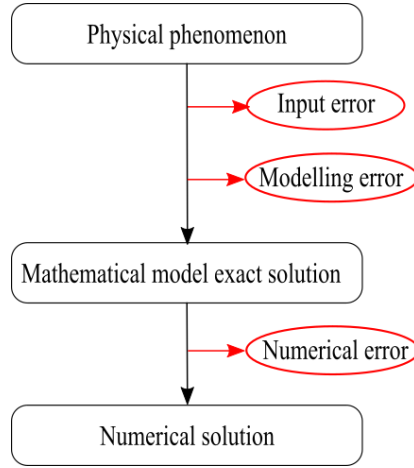


Figure 4.9: Sources of computational errors.

The numerical errors  $E_n(\Phi)$  result from the numerical calculations, and its components are the discretization  $E_d(\Phi)$ , iterative  $E_{it}(\Phi)$ , round-off  $E_r(\Phi)$ , and statistical  $E_s(\Phi)$  errors:

$$E_n(\Phi) = E_d(\Phi) + E_{it}(\Phi) + E_r(\Phi) + E_s(\Phi). \quad (4.16)$$

The discretization error  $E_d(\Phi)$  arises from the discretization of the governing equations. It depends on the discretization scheme, the spatio-temporal grid resolution and quality, and the model. The iterative error  $E_{it}(\Phi)$ , results from the methods used to compute the solution of the discretized governing equations, e.g. non-linearity or iterative solvers, whereas the round-off error  $E_r(\Phi)$  is due to the limited precision of machines to execute mathematical operations. All computations are executed on double-precision to guarantee, when compared with the other sources of the numerical error, a negligible influence of the round-off error. Thus, this source of errors is not addressed in this work. Finally, the statistical error  $E_s(\Phi)$  arises from the initial conditions and the calculation of the flow statistics. A sufficient extensive sampling time is therefore required to converge the flow statistics and minimize statistical error. The techniques employed in this work to evaluate each component of the computational error are described in the following sections.

#### 4.5.1 Numerical Error

The iterative error is the consequence of the utilization of iterative schemes to resolve the algebraic system of governing equations, which is controlled by the iterative convergence criterion defined before, in this case infinity norm,  $L_\infty$ . Simulations at successive tighter iterative convergence criteria have been conducted to evaluate the influence of this type of error. The iterative error is then estimated from,

$$E_{it}(\Phi) = \Phi_{cit} - \Phi_{ref}, \quad (4.17)$$

where  $\Phi_{cit}$  is the numerical solution obtained at a given  $L_\infty$ , and  $\Phi_{ref}$  is the reference solution computed with the tightest iterative convergence criterion. The iterative convergence criteria tested in this work varied from  $10^{-3}$  to  $10^{-6}$  and is discussed in Chapter 5.

The discretization error is usually the major source of numerical errors thus its estimation is important. Currently, there are two main strategies to quantify it. The first execute spatial and temporal grid refinement studies (Stern et al., 2001; Rosetti et al., 2012) to estimate the exact solution, order of grid convergence, and discretization error. The second calculates the discretization error directly from an error transport equation (Celik & Hu, 2004). Whereas the first approach requires a minimum of three solutions/grids, the second method involves estimating the error with a higher order of accuracy than that used in the discretization of the

governing equations. After estimating the discretization error, both strategies calculate the respective discretization uncertainty. The procedure of the first type proposed by Eça and Hoekstra (2014) is employed here. This method first defines an interval containing the exact solution  $\Phi_0$  with 95% coverage,

$$\Phi - U_d(\Phi) \leq \Phi_0 \leq \Phi + U_d(\Phi), \quad (4.18)$$

where  $U_d(\Phi)$  is the discretization uncertainty calculated from the estimate of the discretization error  $E_d(\Phi)$

$$E_d(\Phi) \equiv \Phi - \Phi_0 \approx \alpha_s \Delta h_i^{p_s} + \alpha_t \Delta t_i^{p_t}, \quad (4.19)$$

where the indexes  $s$  and  $t$  denote spatial and temporal components,  $\alpha$  is the error constant,  $\Delta h$  and  $\Delta t$  are respectively, the characteristic spatial and temporal (time-step) grid resolution, and  $p$  is the order of accuracy of the discretization scheme. For simplicity, the Numerical Uncertainty Analysis tool, developed from Eça and Hoekstra's work (2014) is used here to determine the order of accuracy and numerical uncertainty.

The statistical error has its origin in initial conditions and the calculation of the flow statistics. This important source of computational errors is here evaluated using a simple procedure in which the statistics of integral and local flow quantities are calculated from the time history of the solution (i.e., signal), backwards, with successive larger time intervals  $\Delta T$ , here referred to as sampling. After removing the transient period, the statistical error can be measured from

$$E_s(\Phi) = \Phi(\Delta T) - \Phi(\Delta T_{max}), \quad (4.20)$$

where  $\Phi(\Delta T_{max})$  is the reference solution computed with the largest time interval available. In this work this error is evaluated with the python module Transient Scanning Technique presented in Brouwer et al. (2013, 2015 and 2019) developed at MARIN. It allows easy detection of a transient portion of a signal and then measures the statistical uncertainty with that portion removed. This procedure is illustrated in Figure 4.10.

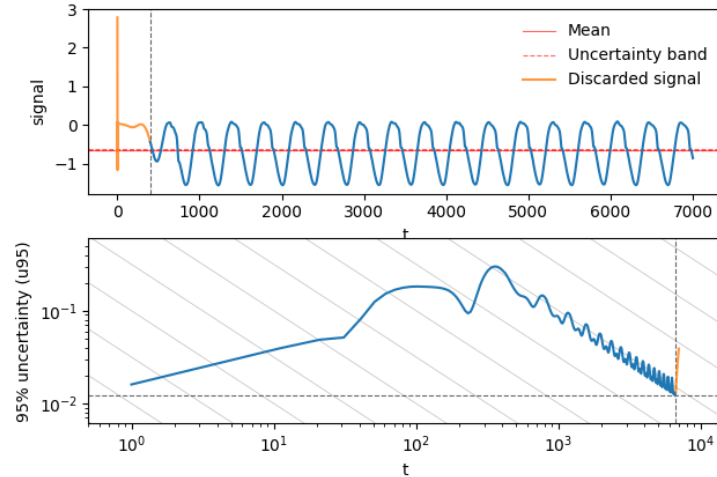


Figure 4.10: Statistical error evaluation (transient state in yellow, statistically converged state in blue).

#### 4.5.2 Modelling Error

The modelling error can be estimated using the procedures proposed by the American Society of Mechanical Engineers (2009), where the interval containing the modelling error  $E_m(\Phi)$  in the estimation of any flow quantity for 95 out of 100 cases is given by

$$E_c(\Phi) - U_v(\Phi) \leq E_m(\Phi) \leq E_c(\Phi) + U_v(\Phi), \quad (4.21)$$

where the comparison error  $E_c(\Phi)$  is the difference between the simulated result  $\Phi$  and the experimental measurement  $\Phi_e$ , and  $U_v(\Phi)$  is the validation uncertainty, since neither  $\Phi$  nor  $\Phi_e$  are exact values. Assuming that these uncertainties are not correlated, it is calculated from the numerical and experimental uncertainties:

$$U_v(\Phi)^2 = U_n(\Phi)^2 + U_e(\Phi)^2. \quad (4.22)$$

# Chapter 5

## Oscillating Foils Thrusters in Infinite Domain

This chapter examines the outcome of the numerical modelling of the single foil and tandem foil test cases in infinite domain and evaluates the modelling accuracy through the verification and validation methodology presented in the previous chapter. The model is also compared with the semi-analytical model. The test cases and their results are presented in this chapter, reflecting the step-by-step stages in which the work progressed both in the model development and the familiarization with the CFD tool. The different errors and simulations accuracies are studied in more detail, following the V&V procedures, for the first, less demanding cases, to establish a basis for understanding the model capabilities and limitations. Then more complex cases are studied, aiming at practical application configurations, where different physical effects are introduced.

In these cases, the emphasis is on the comparison with the semi-analytical model and on identifying its limitations, by understanding the physical phenomena involved. Therefore, according to the possibilities in terms of computational time and requirements, the V&V is further simplified or even the results are addressed only qualitatively. In each case issues like grid sensitivity, grid deformation for large oscillations, the flow solutions, and hydrodynamic forces are discussed.

### 5.1 Single Foil

#### 5.1.1 Small Oscillations – Grid Study

This section investigates the flow around a 2D single foil in small oscillations, using two types of grids. This is an important phase to comprehend the selected modelling strategies, and extend their application to cases of practical interest. This case's objectives are to analyse and compare the modelling accuracy and precision of the different grids and to draw conclusions about the numerical errors involved.

The 2D computational domain and boundary conditions used are the ones explained in Chapter 4, with dimensions  $70c \times 100c$ , with inflow velocity at the inlet and outflow at the outlet, at  $-20c$  and  $50c$  respectively, top and bottom zero pressure at  $\pm 50c$ , and no-slip wall at the foil's surface. Concerning the numerical settings, time integration uses the implicit second-order scheme, iterative error criteria is set to  $L_\infty = 10^{-4}$ , and momentum convection and diffusion discretization uses the second-order scheme. The motion handling uses the deforming grid method with deformation radius of  $2c$ . The dynamic viscosity was adjusted to keep the Reynolds number at  $Re = 40\,000$ . Although it is expected some turbulence, for this Reynolds (see Figure 2.9 on Section 2.3.1), turbulence modelling is not yet used in this section, and it will be address in the next test case. The motion parameters are shown in Table 5.1.

One stability criterion for time integration methods is the one-dimensional Courant number (Courant-Friedrichs-Lewy) CFL:

$$CFL = \frac{u\Delta t}{\Delta x}. \quad (5.1)$$

Here,  $u$  denotes the one-dimensional velocity scalar and  $\Delta x$  the cell size in the corresponding direction and  $\Delta t$  the time step. Explicit methods need for stability that  $CFL < 1$ , while implicit methods can be stable for larger CFL numbers. Because CFL numbers show the balance between space and time refinement, for implicit methods they are an accuracy indicator and should be kept in order of magnitude of 1. The Courant number can be controlled by altering the time or space interval. When the space interval is reduced or time interval is increased, the courant number increases. Because the 1<sup>st</sup> and 2<sup>nd</sup> order time integration schemes used in this work are both implicit, the condition that CFL is less than one was not applied. However, CFL was kept as low as possible, by lowering time step  $t_i$ , but looking for a compromise between stability and computational cost (Klajj et al. 2018).

Table 5.1: Small oscillations test case simulation parameters.

Parameter	Value
Inflow velocity, $U$	1.0 m/s
Chord, $c$	1.0 m
Pitching axis, $b^*$	1/3-point
Heave amplitude, $h_0$	0.25 m
Pitch amplitude, $\theta_0$	28.3° ( $\alpha_0 \approx 15^\circ$ )
Heave-pitch phase, $\psi$	90°
Period, $T$	1.67 s ( $St = 0.3$ )
Reynolds number, $Re$	40 000

Two types of grids were compared. First, a set of GridPro structured grids (31k-478k cells) provided by MARIN were used at the beginning of the work to gain familiarization with ReFRESKO solver and understand the challenges of the modelling problem. Then a set of unstructured grids (53k-711k cells) were produced using Hexpress. The same tool was used for the generation of the rest of the grids in the current work. Table 5.2 presents the grids and time steps used

Table 5.2: Simulation grid and time refinement: total number of cells  $N_c$ , space refinement ratio  $h_i/h_1$ , number of timesteps per period  $n_i/T$ , time refinement ratio  $t_i/t_1$  and  $CFL_{max}$  for GridPro (GP) and Hexpress (HE) grids. Motion parameters  $h_0/c = 0.25$ ,  $\alpha_0 = 15^\circ$ ,  $\psi = 90^\circ$ ,  $St = 0.3$ .

Grid	$N_c$	$n_i/T$	$h_i/h_1$	$t_i/t_1$	$CFL_{max}$
GP_A	478104	16667	1.00	1.0	3.65
GP_B	269820	8333	0.75	2.0	3.86
GP_B	269820	5556	0.75	2.0	5.79
GP_C	121916	8333	0.50	2.0	5.64
GP_D	31372	4167	0.26	4.0	3.99
HE_A	771248	16667	1.00	2.0	9.32
HE_B	296274	33333	1.61	1.0	0.29
HE_B	296274	16667	1.61	2.0	0.59
HE_B	296274	8333	1.61	4.0	1.19
HE_C	112998	8333	2.61	4.0	4.02
HE_D	53621	3704	3.79	9.0	7.14

As discussed in Chapter 4, the numerical error comprises statistical, iterative and discretization components, assuming that the use of double-precision is sufficient to make the magnitude of the round-off error negligible. First, the statistical error is quantified using the python module Transient Scanning Technique (TST) (Brouwer et al., 2019) to detect the transient portion of a signal. Figure 5.1 shows an example of statistical analysis for the grid HE\_B and  $t_i/t_1 = 4$  case, using the horizontal force time series. It is worth reminding that the negative horizontal force corresponds to positive thrust, and it has the double frequency of the oscillation cycle. It is possible to see the discarded transient state and the statistical converged

state in both graphs. In the uncertainty  $u_{95}$  graph, diagonal grid lines are added to identify slopes of minus one ( $T^{-1}$ ). The optimal selection is the minimum within the range where the  $u_{95}$  decays with the inverse of  $T$ , i.e., where the signal is stationary.

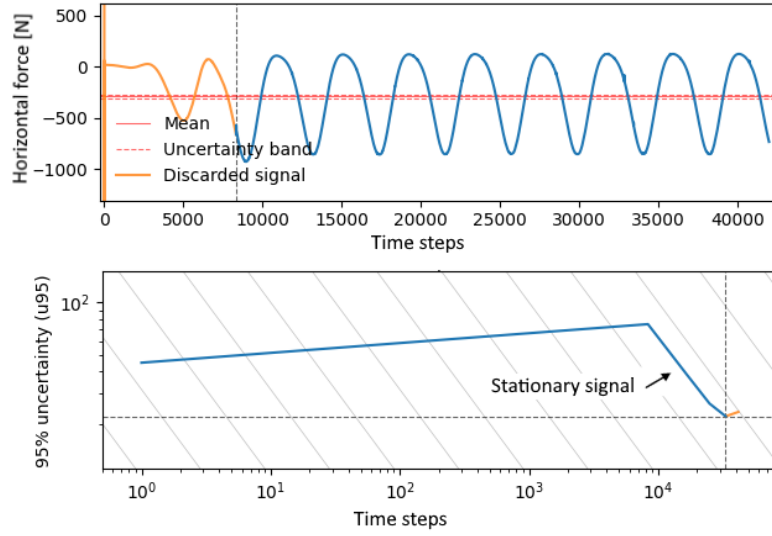


Figure 5.1: Small oscillations test case statistical signal evaluation for simulation with Grid HE\_B and  $\Delta t_i/\Delta t_l = 4$ , with the discarded transient state in orange and the statistical converged state in blue. (a) The horizontal force time series for total iterations and (b) the uncertainty calculated backwards, showing the method of selection of optimal point of transient signal discard.

After removing the transient period, the statistical error was studied for two cases (HE\_B  $t_i/t_l = 4$  and HE\_D,  $t_i/t_l = 9$ ), verifying that the statistical error  $E_s$  drops below 0.4% (see Equation (4.20) for samplings with at least two oscillation cycles.

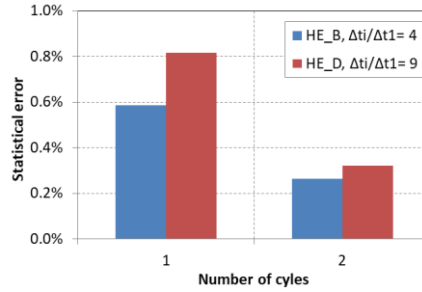


Figure 5.2: Statistical error evaluation with number of sampling cycles for 2 simulations with Hexpress grids. Motion parameters  $h_0/c = 0.25$ ,  $\alpha_0 = 15^\circ$ ,  $\psi = 90^\circ$ ,  $St = 0.3$ .

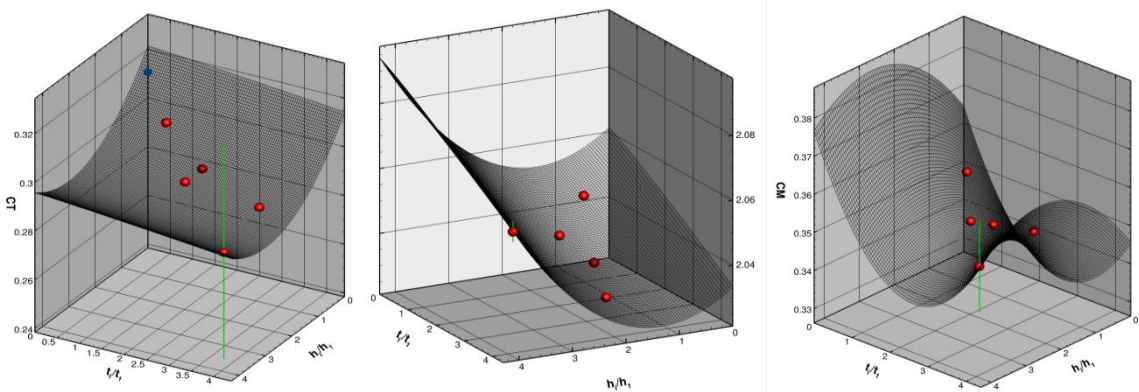


Figure 5.3 Results for 5 simulations using GridPro structured grids (a) average thrust coefficient with experimental data in blue (b) vertical force coefficient (c) moment coefficient. The data points are defined with the grid space refinement ratio  $h_i/h_l$  and time refinement ratio  $t_i/t_l$  and the uncertainty bar is included. Motion parameters  $h_0/c = 0.25$ ,  $\alpha_0 = 15^\circ$ ,  $\psi = 90^\circ$ ,  $St = 0.3$ .

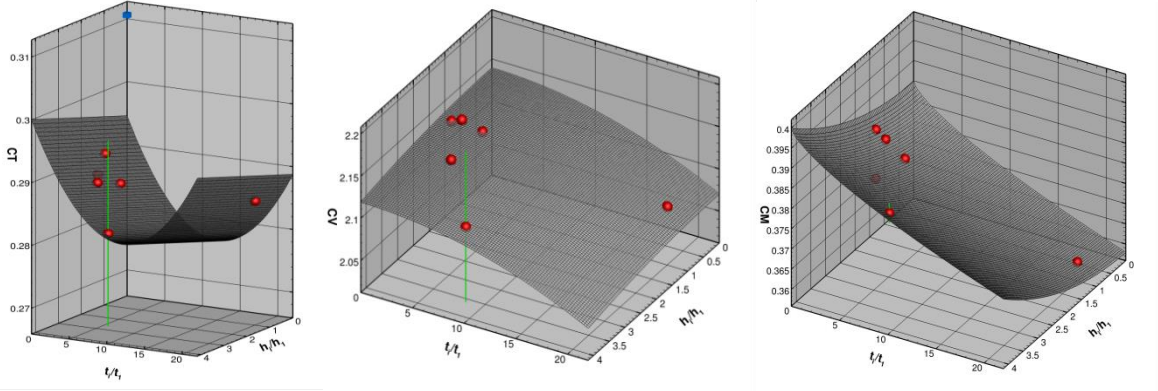


Figure 5.4: Results for 6 simulations using Hexpress unstructured grids (a) average thrust coefficient with experimental data in blue (b) vertical force coefficient (c) moment coefficient. The data points are defined with the grid space refinement ratio  $h_i/h_1$ , time refinement ratio  $t_i/t_1$  and the uncertainty bar is included. Motion parameters  $h_0/c = 0.25$ ,  $\alpha_0 = 15^\circ$ ,  $\psi = 90^\circ$ ,  $St = 0.3$ .

The estimation of the exact solution, discretization error and uncertainty was performed using the Numerical Uncertainty Analysis tool (Eça & Hoekstra, 2014) by computing solutions with different spatial and time refinements. The results for the average thrust, vertical force, and moment coefficients are presented in Figure 5.3 and Figure 5.4. The extrapolated value, error, and uncertainties are shown in Table 5.3.

Table 5.3: Results for discretization error and uncertainty for the different data sets. The errors are given in percentage based on extrapolated value. Motion parameters  $h_0/c = 0.25$ ,  $\alpha_0 = 15^\circ$ ,  $\psi = 90^\circ$ ,  $St = 0.3$ .

Data set	Var	Extrapolated value $\phi_0$	Finest exact solution $\phi_1$	Error $E_d$ [%]	Uncertainty $U_d$ [%]	Order of convergence	
						$p_x$	$q_t$
GP, 5 simulations	$\bar{C}_T$	0.31	0.29	10.9	15.2	1,2	1.1
	$C_V$	2.07	2.06	0.4	0.2	1,2	1.1
	$C_M$	0.36	0.36	2.4	1.2	1,2	0.02
HE, 6 simulations	$\bar{C}_T$	0.30	0.28	4.1	5.2	1	1,2
	$C_V$	2.14	2.11	1.4	4.2	2	2
	$C_M$	0.39	0.38	0.5	0.7	2	0.69

The results for the error and uncertainty estimation scatter, however it is possible to see that the extrapolated values differ by 3-8% between the two data sets/types of grids, revealing a good accuracy of the model, even if it has a difference in the number of points. The uncertainty for average thrust coefficient for GridPro setting is larger as average thrust results showed more oscillatory behaviour of the signal. The discretization error for the average thrust coefficient  $\bar{C}_T$  ranges from 4.1% to 10.9% which is much more significant than the statistical error. The form of the fitted plane changes from an almost straight to a curved shape, according to the different cases. GridPro data set in general presents greater sensitivity to time refinement, in the Hexpress data set the space refinement appears to be more important. The remaining term for the error, the iterative error will be addressed in the next section.

Table 5.4. Comparison between present numerical model and experimental data (Anderson et al., 1998). Motion parameters  $h_0/c = 0.25$ ,  $\alpha_0 = 15^\circ$ ,  $\psi = 90^\circ$ ,  $St = 0.3$ .

Method	$\bar{C}_T$	$E_n$ [%]	$U_v$ [%]	$C_V$	$C_M$
CFD model (grids HE)	0.304	10.9%	5.2%	2.14	0.30
Semi-Analytical	0.387	-	-	2.22	0.74
Experimental	0.311	-	-	-	-

Table 5.4 presents the comparison between the values obtained with the CFD model, HE data set, with measured data from Anderson et al. (1998), and results from the semi-analytical model presented in Chapters 2 and 3. Although there is no reference of experimental uncertainty, Schouveiler et al. (2003) reported  $U_e = 4\%$  for similar experiments with the same apparatus. Assuming that the numerical and the experimental uncertainty are not correlated, using Equation (4.22) it is possible to obtain a modelling validation uncertainty of 5.2%.

The very similar results produced by the two types of grids, with differences of 3% in thrust and vertical coefficients and 7% in moment coefficient, verify the use of Hexpress for the next stages of the work, as well the numerical modelling error of 7.5% which was obtained.

### 5.1.2 Large Oscillations – Validation & Verification Study

This section explores the case for 2D single oscillating foil propulsor where the heave amplitude is  $h_0/c = 1$ , which is the core value studied in the vast majority of the published studies and experiments. The large oscillations allow higher thrust performance and efficiencies. However, the numerical modelling is more demanding in terms of grid deformation. This can cause problems of grid quality that have to be addressed. Furthermore, large magnitudes and variation rates can bring convergence problems. Also, in this section the effect of turbulence is introduced. Finally, to determine the importance of viscous and turbulent stresses a grid refinement region is added near the foil surface. In this section grid quality and convergence parameters are investigated. The iteration error is now evaluated to complete the procedure of verification & validation since it was not accounted for in the previous section.

The computational domain is two-dimensional and boundary conditions and numerical setup used are as in the previous section, with inflow velocity at the inlet and outflow at the outlet, top and bottom zero pressure. The time integration uses a second-order scheme and iterative error criteria  $L_\infty = 10^{-4}$ . The Reynolds number is kept at  $Re = 40\,000$ . Simulations are in general done without turbulence modelling, except one to access the influence of this effect in the result. The motion parameters are shown in Table 5.5. All the grids used in this section were produced with Hexpress and a viscous sub-layer was added in the cells adjacent to the foil surface using the non-dimensional wall distance  $y^+ = 1$  (Eça et al., 2018) denoted by

$$y^+ = \frac{yu_\tau}{\nu}, \quad (5.2)$$

where  $u_\tau$  is the friction velocity,  $y$  is the absolute distance from the wall and  $\nu$  the kinematic viscosity. In the viscous layer, the fluid is dominated by the viscous effect, and it can be assumed that the Reynolds shear stress is negligible. After the computation the  $y^+$  value should be checked if  $y^+_{max} < 5$  in order to confirm grid quality. Four grids were produced with 81k-394k cells.

Concerning the deforming grid issues caused by the large oscillations, it was concluded that the deformation radius, initially set at  $1c$ , was constraining the deformation in a too near range to the foil. This setting forced the cells in the periphery of that region to large deformations, causing the simulations to diverge. It was then found for this case that a deforming radius of  $2c$  i.e., a wider zone of deformation, allowed a smoother cell deformation and simulation convergence was achieved.

The evaluation of the grid quality is done using two ReFRESKO built-in parameters. One is the *MeshQuality* calculated using the cell Jacobian, where the minimum quality should be greater than 0.3. The other is the *nonOrtho\_f\_c* that measures the angle of the line between the two cells centres, whose results are presented further in this section.

In this test case, a data set with 7 simulations is used with different refinements in space and time, described in Table 5.6. As in the previous section, the statistical error is assessed.

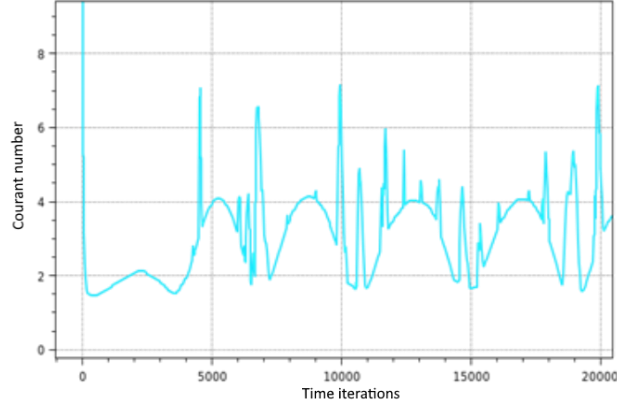
Table 5.5: Large oscillations test case simulation parameters.

Parameter	Value
Inflow velocity, $U$	1.0 m/s
Chord, $c$	1.0 m
Pitching axis, $b^*$	1/3-point
Heave amplitude, $h_0$	1.0 m
Pitch amplitude, $\theta_0$	$28.3^\circ$ ( $\alpha_0 \approx 15^\circ$ )
Heave-pitch phase, $\psi$	$90^\circ$
Period, $T$	6.67 s ( $St = 0.3$ )
Reynolds number, $Re$	40 000

Table 5.6: Large oscillations test case simulation grid and time refinement: total number of cells  $N_c$ , space refinement ratio  $h_i/h_1$ , number of timesteps per period  $n_i/T$ , time refinement ratio  $t_i/t_1$  and CFL. Motion parameters  $h_0/c = 1.0$ ,  $\alpha_0 = 15^\circ$ ,  $\psi = 90^\circ$ ,  $St = 0.3$ .

Grid	$N_c$	$n_i/T$	$h_i/h_1$	$t_i/t_1$	$CFL_{max}$
A	394373	4167	1.00	2.0	12.1
B	124661	4167	1.78	2.0	6.48
C	85364	4167	2.15	2.0	6.38
C	85364	1042	2.15	8.0	24.9
C	85364	2083	2.15	4.0	12.0
C	85364	8333	2.15	1.0	3.10
D	81932	4167	2.19	2.0	3.60

The maximum Courant numbers for the different simulations can be seen in Table 5.6 and an example of the CFL variation with simulation time in Figure 5.5. The worst case is the grid C with  $t_i/t_1 = 8$  with the largest CFL that presents an averaged residuals for vertical velocity of  $3.3e-06$  for norm  $L_2$  and  $9.5e-05$  for norm  $L_{inf}$ , showing that good convergence is achieved even with large CFLs.

Figure 5.5 Average Courant number for grid C and  $t_i/t_1 = 2$ . Motion parameters  $h_0/c = 1.0$ ,  $\alpha_0 = 15^\circ$ ,  $\psi = 90^\circ$ ,  $St = 0.3$ .

Concerning the iteration error investigation, Figure 5.6 shows an example of iterative convergence presenting the  $L_2$  and  $L_\infty$  norm residuals of the simulation for the grid C with  $t_i/t_1 = 2$ . The results show convergence below  $10^{-5}$  in  $L_2$  and  $10^{-3}$  in  $L_\infty$ . The highest residuals were found for the vertical velocity. They were in the leading and trailing edges of the foil, showing the importance of refining those regions during grid generation to prevent convergence problems. Figure 5.7 shows the number of iterations used to solve the equations. It is possible to see that the more demanding case is the pressure, although it never reached the limit set to 500 maximum iterations. Different convergence criteria were also investigated for this case. Figure 5.8 presents the results of the average over time effective residuals obtained for the following convergence criteria:  $L_\infty < 10^{-3}$ ,  $L_\infty < 10^{-4}$ ,  $L_\infty < 10^{-5}$ , and  $L_\infty < 10^{-6}$ . It is possible to see that the criteria  $L_\infty < 10^{-4}$  is enough to guarantee an iteration error  $E_{it}$  below

0.01%. Although not being exact, because of time limitations, we then assume that the iterative convergence is the same in the other cases.

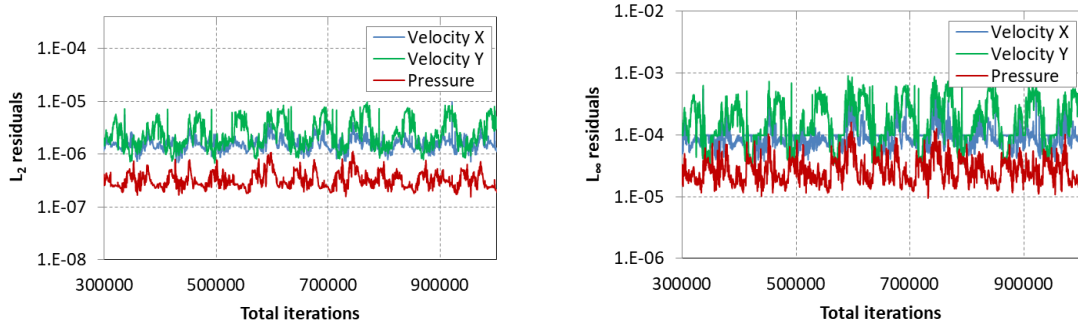


Figure 5.6: Residuals for the (a)  $L_2$  and (a)  $L_\infty$  norm for the grid C and  $t_i/t_1 = 2$ . Motion parameters  $h_0/c = 1.0$ ,  $\alpha_0 = 15^\circ$ ,  $\psi = 90^\circ$ ,  $St = 0.3$ .

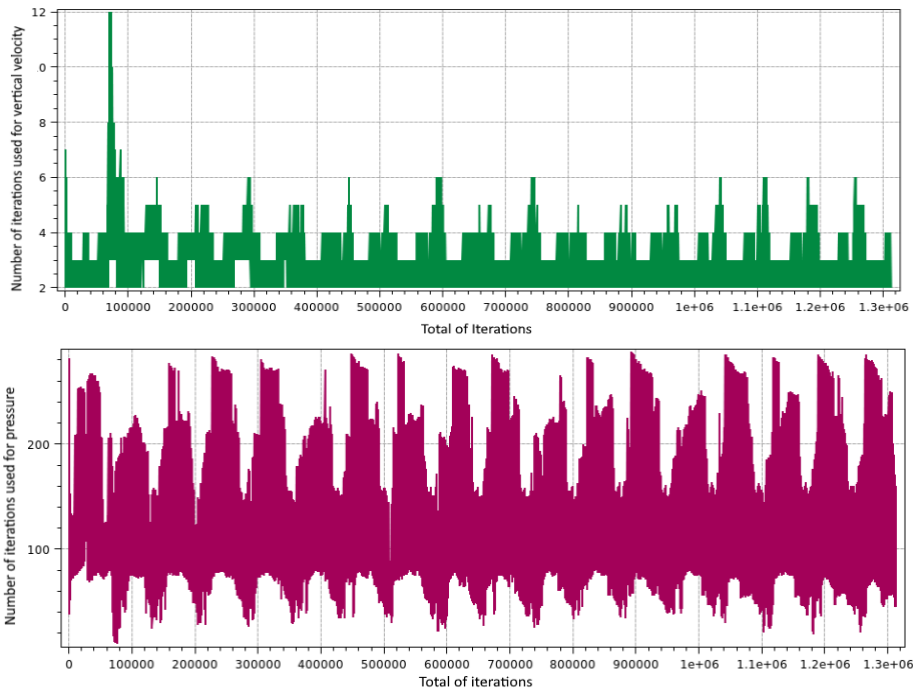


Figure 5.7: Number of used iterations to the equations for (a) vertical velocity and (b) pressure, using the grid C and  $t_i/t_1 = 2$ . Motion parameters  $h_0/c = 1.0$ ,  $\alpha_0 = 15^\circ$ ,  $\psi = 90^\circ$ ,  $St = 0.3$ .

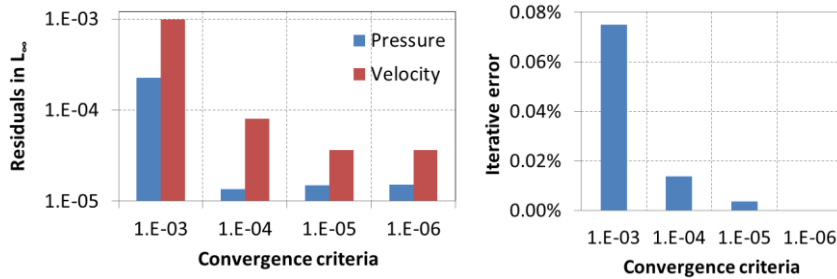


Figure 5.8: (a) Residuals averaged over time, for vertical velocity and pressure and (b) average thrust iterative error, for different convergence criteria using the grid C and  $t_i/t_1 = 2$ . Motion parameters  $h_0/c = 1.0$ ,  $\alpha_0 = 15^\circ$ ,  $\psi = 90^\circ$ ,  $St = 0.3$ .

Figure 5.9 shows the selection of the statistical converged state for the case of grid C with  $t_i/t_1 = 2$ , and Figure 5.10 the variation of statistical uncertainty, using the horizontal force time series. It was found that using a time interval of  $\Delta T = 4$  periods of the statistical converged

state was enough to guarantee an uncertainty of 0.014%. The respective statistical error  $E_s$  is 0.05%, lower than the cases in the previous section as the time interval includes more cycles.

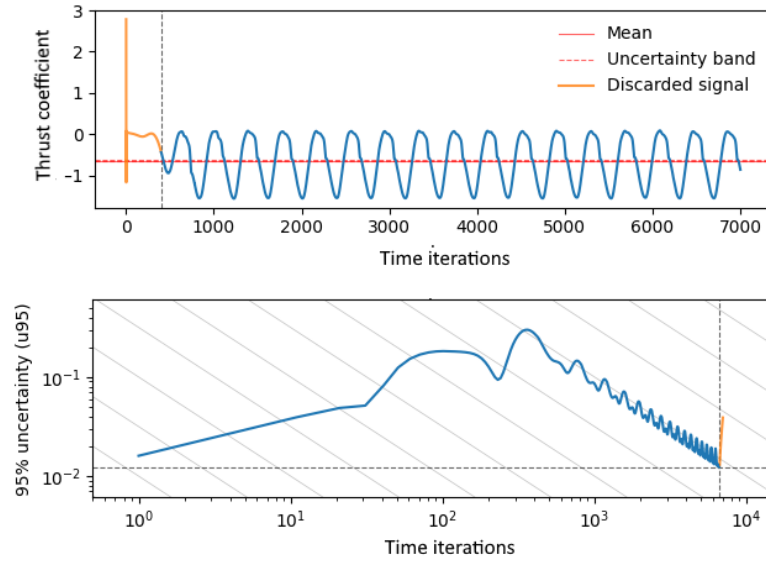


Figure 5.9: Large oscillations test case statistical error evaluation for simulation with grid C and  $t_i/t_f = 2$ , with the discarded transient state in orange and the statistical converged state in blue. (a) The thrust coefficient time series for total iterations and (b) the uncertainty calculated backwards, showing the method of selection of optimal point of transient signal discard.

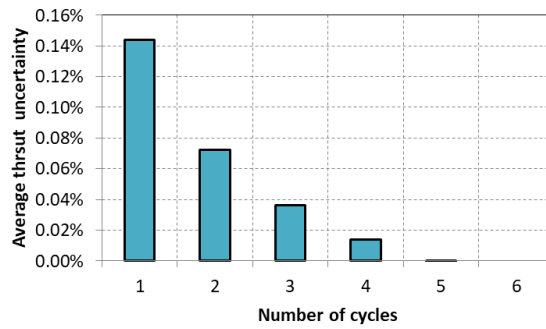


Figure 5.10: Variation of statistical uncertainty for the average thrust with sampling cycles/periods for grid C and  $t_i/t_f = 2$  simulation. Motion parameters  $h_0/c = 1.0$ ,  $\alpha_0 = 15^\circ$ ,  $\psi = 90^\circ$ ,  $St = 0.3$ .

The discretization error evaluation follows the same procedure as the previous section. Figure 5.11 and Table 5.7 present the results for discretization error and uncertainty for the large oscillations case data set. It is possible to see that the order of convergence in space is linear while the order of convergence in time is quadratic. As before, it is evident that extrapolated value is much more dependent on space refinement than on time refinement.

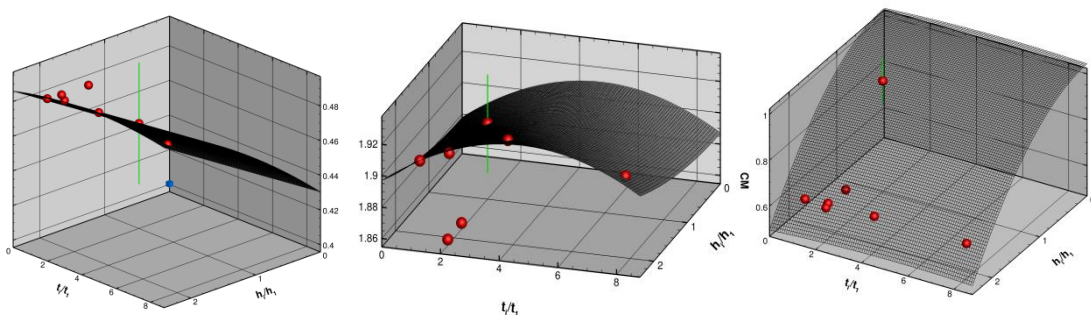


Figure 5.11: Results for 7 simulations (a) average thrust coefficient with experimental data in blue (b) vertical force coefficient (c) moment coefficient. Motion parameters  $h_0/c = 1.0$ ,  $\alpha_0 = 15^\circ$ ,  $\psi = 90^\circ$ ,  $St = 0.3$ .

The discretization error  $E_d$  ranges from 6.5% to 7.7%, same order of the previous section, being much more significant than both the statistical error and the iteration error. Since the modelling error  $E_m$  can only be evaluated for the average thrust coefficient because of data availability, it is possible to obtain a modelling validation uncertainty  $U_v$  of 7.6%. This accuracy value seems very promising. In terms of comparison error, the numerical result presents a discrepancy of +7% relatively to experimental data. The modelling error is thus less than 14.6%. A discussion on the experimental results and detailed comparison with the semi-analytical results is done in the following section.

Table 5.7: Results for discretization error and uncertainty of the data set for the large oscillations test case. The errors are given in percentage based on extrapolated value. Comparison with semi-analytical results and measured data (Read et al. 2003). Motion parameters  $h_0/c = 1.0$ ,  $\alpha_0 = 15^\circ$ ,  $\psi = 90^\circ$ ,  $St = 0.3$ .

Var	Extrapolated value $\phi_0$	Finest exact solution $\phi_1$	Error $E_d$ [%]	Uncertainty $U_\phi$ [%]	Order of convergence	
					$p_x$	$q_t$
$\bar{C}_T$	0.43	0.46	6.5	7.7	1	2
$C_V$	1.88	1.90	1.1	1.6	1	2
$C_M$	1.03	0.95	7.7	10.6	1	2
$\bar{C}_T$ (semi-analytic)	0.45	-	-	-	-	-
$\bar{C}_T$ (experimental)	0.40	-	-	-	-	-

The deformation of the grid is shown in Figure 5.12 where it is possible to have a visual confirmation of the good quality of the grid. Figure 5.13 shows the results after computation for the average ReFRESCO *MeshQuality* parameter and the maximum wall distance. It is possible to see that both parameters are kept within the criteria defined above, except for the transient stage, ( $MeshQuality > 0.86$  and  $y^+_{max} < 2.49$ ), indicating the good quality of the mesh and the validity of the viscous layer. The non-orthogonally parameter was 0.016 for this simulation, confirming the other results. We draw attention to the slow degradation of the mesh quality with the number of iterations due to the successive grid recalculation in the deform grid method. For very long simulations this might be a problem. In this case, it is not relevant since it was established that a few cycles were enough to maintain a low value of the statistical error.

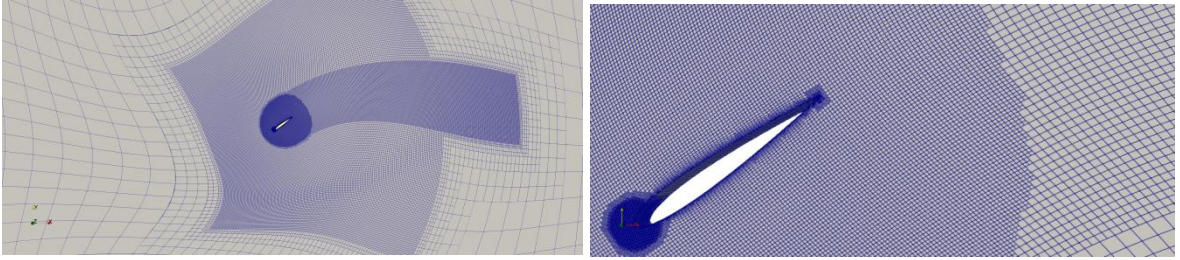


Figure 5.12: Example of grid deformation (a) general view and (b) detail of the mesh around the foil.

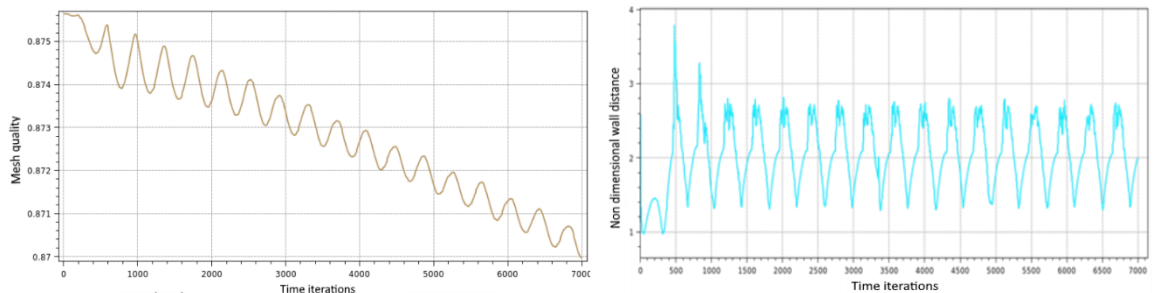


Figure 5.13: (a) Average *MeshQuality* parameter and (b) maximum non-dimensional wall distance  $y^+_{max}$  for grid C and  $t_i/t_1 = 2$ . Motion parameters  $h_0/c = 1.0$ ,  $\alpha_0 = 15^\circ$ ,  $\psi = 90^\circ$ ,  $St = 0.3$ .

Figure 5.14 shows the eddy viscosity ratio for the simulation with  $h_i/h_l = 2.15$  and  $t_i/t_l = 2.0$ . The eddy viscosity ratio i.e., the ratio of turbulent to molecular viscosity indicates how strong the Reynolds stresses are, compared to the molecular stresses. Typically, the eddy viscosity ratio of more than 10 to 100 indicates turbulent flow. It is possible to see the laminar flow in dark blue ( $< 0$ , log scale), the transition range (0 to 2) in light blue to yellow, and also the absence of fully turbulent flow ( $> 2$ ) in orange and red. This result shows that although the flow is not very turbulent on the foil boundary layer, the turbulence in the wake is significant enough to require the use of turbulence modelling. Table 5.8 confirms this conclusion, showing the comparison with and without turbulence model, with differences from 0.4% to 11.8%.

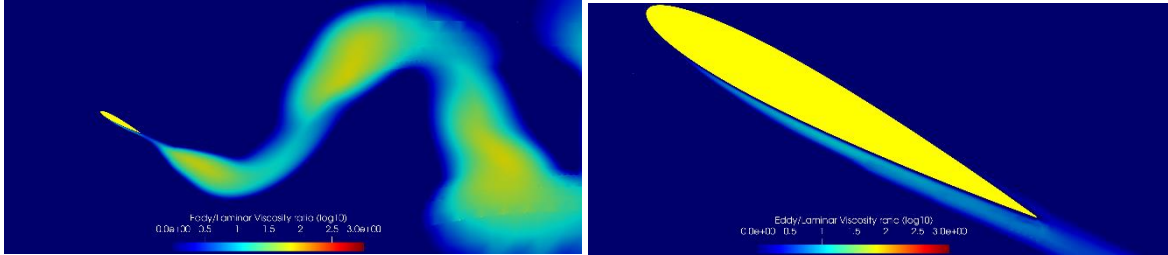


Figure 5.14: Eddy viscosity ratio (log scale) for the single foil in large oscillations case for the simulation with  $h_i/h_l = 2.15$  and  $t_i/t_l = 2.0$ . (a) wake (b) foil boundary layer. Motion parameters  $h_0/c = 1.0$ ,  $\alpha_0 = 15^\circ$ ,  $\psi = 90^\circ$ ,  $St = 0.3$ . Laminar flow in dark blue and fully turbulent flow in red.

Table 5.8: Comparison of the results with and without turbulence model for the large oscillations test case, for the simulation with  $h_i/h_l = 2.15$  and  $t_i/t_l = 2.0$ . Motion parameters  $h_0/c = 1.0$ ,  $\alpha_0 = 15^\circ$ ,  $\psi = 90^\circ$ ,  $St = 0.3$ .

Var	W/out turbulence model	With turbulence model	Difference [%]
$\bar{C}_T$	0.49	0.48	2.0
$C_V$	1.91	1.69	11.8
$C_M$	0.62	0.62	1.2

### 5.1.3 High-Performance – Forces and Flow Analysis

The objective of this section is first to discuss the flow and the results of the hydrodynamic forces obtained with the CFD numerical model. Then, compare them with the results obtained with the different modelling methods. For time reasons, the validation and verification procedures performed in the two previous sections and conclusions are assumed to be applicable in this new case. We proceed with a demonstration case in which the different features and physical processes of the oscillating foil propulsor are more evident. The test case is set for a 2D single foil in large oscillations, both in heave and pitch, with higher frequency and consequently with large average thrust and propulsive efficiency values, i.e., high-performance. The computational domain, boundary conditions and numerical setup used are as those considered in the previous section. All the grids used in this section were unstructured, with dimensions scaled to match Read et al. (2003) experiment and maintain the inclusion of the viscous sublayer and the refinement used in the grids of the previous section (85k – 124k cells). As before, the simulations are run without turbulence model, with exception of one, used to compare. The simulation parameters are shown in Table 5.9. The simulation data set comprised 5 grids, shown in Table 5.10. The respective maximum CFL numbers and the grid quality parameters are also included, presenting acceptable values, with the large Courant numbers not being a limitation for convergence.

Table 5.9: Simulation parameters for the single foil high-performance case.

Parameter	Value
Inflow velocity, $U$	0.4 m/s
Chord, $c$	0.1 m
Pitching axis, $b^*$	1/3-point
Heave amplitude, $h_o$	0.1 m
Pitch amplitude, $\theta_o$	$35^\circ$ ( $\alpha_o \approx 16.5^\circ$ )
Heave-pitch phase, $\psi$	$90^\circ$
Period, $T$	1.25 s ( $St = 0.4$ )
Reynolds number, $Re$	40 000

Table 5.10: Simulation grid and time refinement: total number of cells  $NC$ , space refinement ratio  $h_i/h_j$ , number of timesteps per period  $n_i/T$ , time refinement ratio  $t_i/t_j$ ,  $CFL_{max}$  and grid quality values. Motion parameters  $h_o/c = 1.0$ ,  $\alpha_o = 16.5^\circ$ ,  $\psi = 90^\circ$ ,  $St = 0.4$ .

Grid	$N_c$	$n_i/T$	$h_i/h_j$	$t_i/t_j$	$CFL_{max}$	Mesh quality
A	124661	781	1.00	4.00	37.0	0.86
C	85364	3125	1.21	1.00	7.6	0.86
C	85364	1563	1.21	2.00	14.7	0.86
C	85364	781	1.21	4.00	31.1	0.87
C	85364	625	1.21	5.00	38.9	0.84

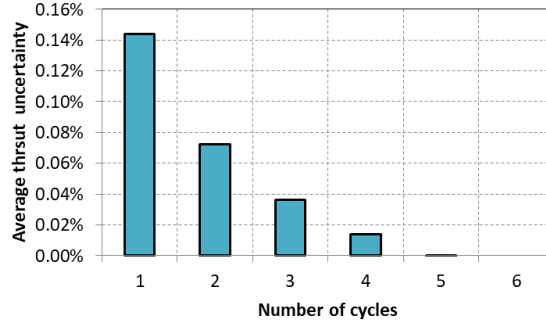


Figure 5.15: Variation of statistical uncertainty for the average thrust with sampling cycles/periods for grid C and  $t_i/t_j = 1$  simulation. Motion parameters  $h_o/c = 1.0$ ,  $\alpha_o = 16.5^\circ$ ,  $\psi = 90^\circ$ ,  $St = 0.4$ .

While keeping the previous procedure, the statistical error estimation and the iteration error were found to be the same as before, with average residuals for the vertical velocity  $< 10^{-4}$ . The results of the discretization error evaluation can be found in Table 5.11, with errors ranging from 0.2-6.0% and uncertainties from 0.3-8.0%. The comparison of the different modelling methods are addressed at the end of the section.

Table 5.11 Results for discretization error and uncertainty of the data set for the flow & forces study test case. The errors are given in percentage based on the extrapolated value. Motion parameters  $h_o/c = 1.0$ ,  $\alpha_o = 16.5^\circ$ ,  $\psi = 90^\circ$ ,  $St = 0.4$ .

Var	Extrapolated value $\phi_0$	Finest exact solution $\phi_1$	Error $E_d$ [%]	Uncertainty $U_\phi$ [%]	Order of convergence	
					$p_x$	$q_t$
$\bar{C}_T$	0.88	0.83	6.0	8.0	1.1	1.1
$C_V$	2.68	2.77	3.4	3.9	2.0	2.0
$C_M$	1.08	1.08	0.2	0.3	1.50	1.28
$\bar{C}_{Texp}$	0.74	-	-	-	-	-

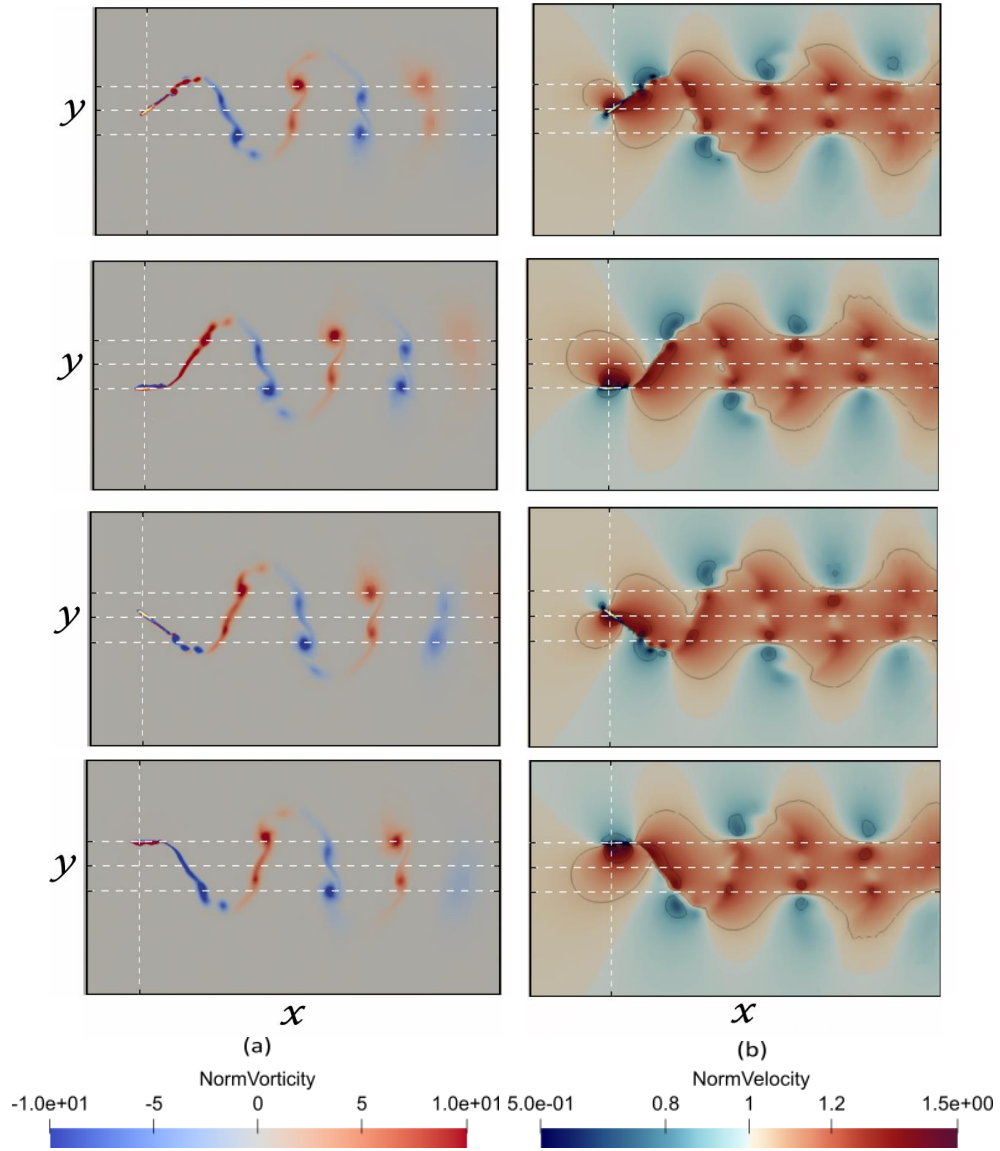


Figure 5.16: Snapshots of (a) normalized vorticity and (b) normalized velocity fields contours at cycle increments of  $t/T = 1/4$  where  $T = 1/f$ , for a single foil with motion parameters  $h_0/c = 1.0$ ,  $\alpha_0 = 16.5^\circ$ ,  $\psi = 90^\circ$ ,  $St = 0.4$ . Clockwise vorticity is indicated with blue, and anticlockwise with red. In all figures, the vertical lines show the location of 1/3 point pitching axis of the foils. The horizontal lines show the mid foil position as well as the upper and lower limits of heave motion. A video of the vorticity field can be found in the on-line supplementary materials listed in the Appendix H and is entitled ‘Single Foil in Infinite Domain’.

Figure 5.16 and Figure 5.17 show a sequence of snapshots of the instantaneous vorticity and velocity fields for a single foil at high-performance configuration ( $h_0/c = 1.0$ ,  $\alpha_0 = 16.5^\circ$ ,  $\psi = 90^\circ$ ,  $St = 0.4$ ) at quarter cycle instant increments. The velocity is normalized with the streamwise flow velocity. It is possible to see the typical flow structure of a thrust-producing flapping foil consisting of two primary vortices of alternating sign shed by the foil per cycle. Following the approach of Joshi & Mysa (2021), we now analyse the flow dynamics. A flapping cycle consists of a foil downstroke followed by an upstroke. A leading edge clockwise vortex LEV- (coloured in blue) is formed on the upper surface of the foil during the downstroke, whereas LEV+ is an anticlockwise vortex (coloured in red) that forms on the lower side of the foil during the upstroke. Due to the oscillating path of the foil, these vortices are shed on the opposite side of a natural BvK vortex street, in reference to the wake midline. Thus, the signs of the vortices on each side of the street are reversed, creating the reverse BvK wake vortex street, which induces a thrust producing jet behind the foil, clearly visible on the velocity field snapshots. The instantaneous vorticity field shows that these primary vortices exist along with smaller secondary vortices that appear as the shear layers roll up. These secondary vortices form a natural BvK and thus cause drag.

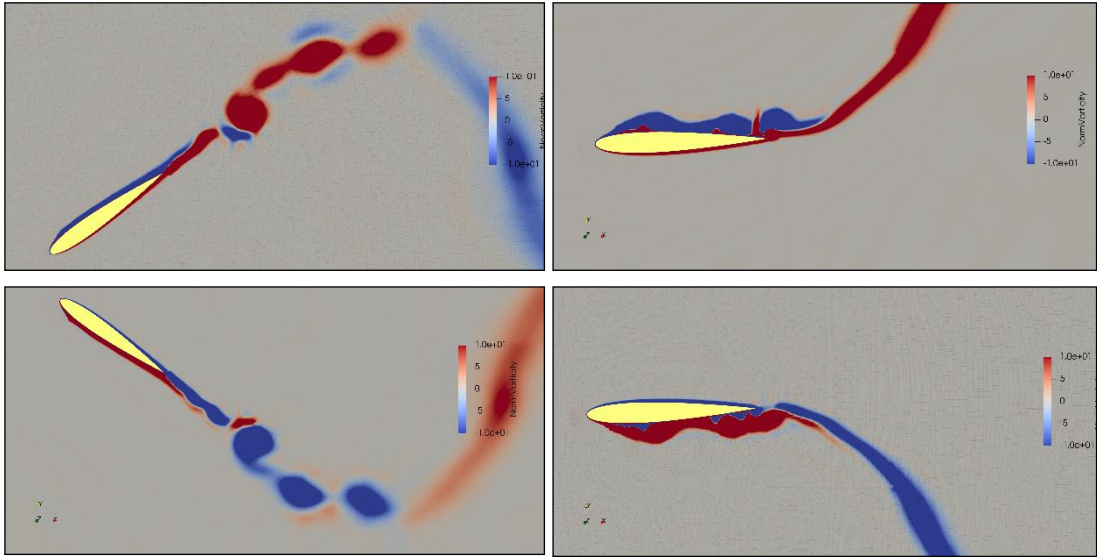


Figure 5.17: Detail of vorticity close to the foil for the snapshots of Figure 5.16. Motion parameters  $h_0/c = 1.0$ ,  $\alpha_0 = 16.5^\circ$ ,  $\psi = 90^\circ$ ,  $St = 0.4$ .

To go into further detail, at time instant ( $t/T = 0$ ) in the downstroke, an anticlockwise LEV+ has just been shed at the highest position, and fully develops in the following instants ( $t/T = 0.25, 0.5, 0.75$ ). As the foil progresses in the downstroke, a trailing edge vortex TEV+ is observed in the trailing wake of the foil, which detaches itself from the lower foil surface at  $t/T = 0.25$ . The LEV is circular in shape, while the TEV is an elongated vortex. The elongated TEV dissipates faster compared to the LEV, which can be observed for the TEV generated during earlier strokes and so on. During the upstroke (from  $t/T=0.25$  to  $t/T=0.75$ ), a LEV+ develops (red in colour with positive vorticity) at the lower surface of the foil near the leading edge and convects along the lower surface of the foil as the upstroke progresses. This vortex region at the lower surface of the foil is responsible for a suction pressure (negative pressure) at the lower surface whereas, there is positive pressure at the upper surface. In this configuration, during upstroke, this pressure differential leads to a net thrust force on the foil. During the same period, an elongated TEV- detaches from the trailing edge, decreasing the pressure differential and causing drag. From  $t/T = 0.75$  on the LEV+ is then shed from the trailing edge, completing the cycle. A similar mechanism, but with clockwise LEV- (blue in colour with negative vorticity) occurs during the downstroke.

The primary leading edge vortices generated during this flapping motion of the foil are the main source of thrust, depending on the dynamics of the foil. It is also important to remark that, in this case, once shed, the vortices maintain their trajectory, denoting that the influence between them is negligible, because they are too far and not strong enough for that to occur. If the frequency is increased to an asymmetric wake regime, the vorticity becomes strong enough to couple the vortices and alter the wake pattern. The secondary trailing edge vortices are shed on the opposite side of the wake midline thus increasing drag.

Figure 5.18 shows the vertical force, horizontal force and moment time history for a full-cycle, with the four-time instants of the snapshot sequenced marked.

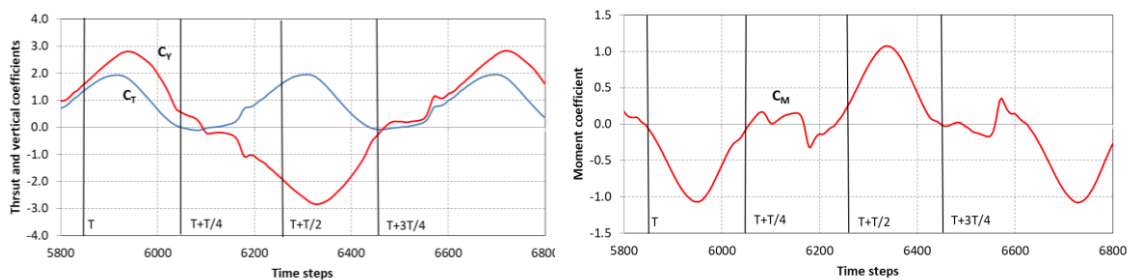


Figure 5.18: (a) Thrust and vertical forces coefficient and (b) moment coefficient instantaneous values for the single foil in high frequency test case. The four-time instants marked correspond to the snapshots of Figure 5.16. Motion parameters  $h_0/c = 1.0$ ,  $\alpha_0 = 16.5^\circ$ ,  $\psi = 90^\circ$ ,  $St = 0.4$ .

It is possible to see that the maximum magnitude of the forces and moment happens in the second half of the foil stroke, after the shedding of the primary LEV, occurring when the foil begins the up or downstroke movement. To remark that due to the apparent flow incident angle resulting from this foil motion, the positive lift or vertical force happens in the downstroke and vice-versa.

Forthwith, the results obtained are compared with the results from the semi-analytical model, the experimental data from Read et al. (2003), and the numerical panel method from Filippas & Belibassakis (2014b). Table 5.12 presents the final values for the average thrust coefficient, vertical force coefficient, moment coefficient, and propulsive efficiency. It is visible a fair agreement between the values obtained with the different methods, with average thrust coefficient discrepancies to the experimental values of 17.5% for the numerical model, 9.5% for the panel model and -5.4% for the semi-analytical model. Uncertainty range lower limit is very close to Filippas' result. We bring to mind what was discussed in Chapter 3 in which it was proposed that span effects and apparatus drag could be interfering with Read's experiment, opening the possibility of the real values to be higher, closer to the numerical methods results. In terms of propulsive efficiency, the discrepancies are 8.4% and 18.6% for the numerical and semi-analytical model. Again, bringing to mind that the propulsive efficiency uncertainty in the experiments is 7% (Schouveiler, 2005), it confirms the fact that the actual efficiency could be higher than the measured values. The high efficiency discrepancy of the semi-analytical model can be explained by looking into the values of vertical force and moment coefficient. These values are clearly under-estimated when compared with CFD model's results and so leading to over-prediction of the efficiency. Since it is not reflected in the average thrust, this might be related to the evaluation of the added-mass, and the discrepancy might be derived from not accounting the second-order terms. This is aligned with the conclusions of Chapter 3.

Table 5.12: Comparison of the average thrust coefficient, vertical force coefficients, moment coefficient and propulsive efficiency between the semi-analytical and CFD model developed in the present work with experimental measured values from Read et al. (2003). Motion parameters  $h_0/c = 1.0$ ,  $\alpha_0 = 16.5^\circ$ ,  $\psi = 90^\circ$ ,  $St = 0.4$ .

Method	$\bar{C}_T$	$C_V$	$C_M$	$Eff$	$U_{CT}$	$E_{dCT}$
CFD	0.88	2.77	1.08	65%	8.0%	6.0%
Semi-analytical	0.70	1.60	0.33	70%	-	-
Experimental (Read et al., 2003)	0.74	-	-	59%	4%	-
Panel method (Filippas & Belibassakis, 2014b)	0.81	-	-	-	-	-

The general fair-to-good agreement that could be observed in the results obtained for both modelling methods developed, namely the estimation of the average thrust coefficient with discretization error of 6.0% establishes the basis that enables to approach more complex cases.

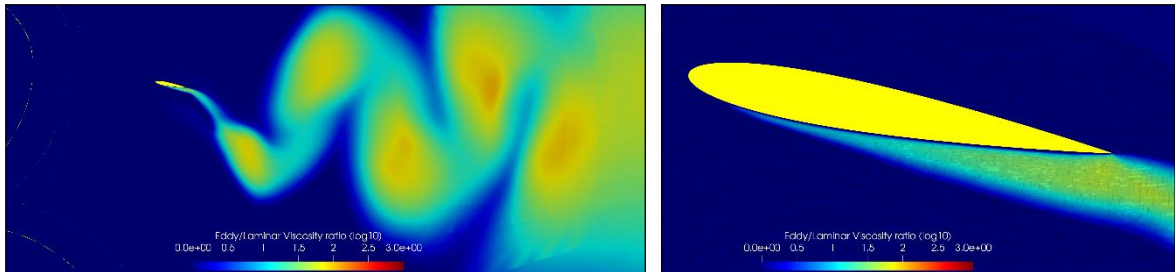


Figure 5.19: Eddy viscosity ratio (log scale) for the single foil in the high-performance test case. Motion parameters  $h_0/c = 1.0$ ,  $\alpha_0 = 16.5^\circ$ ,  $\psi = 90^\circ$ ,  $St = 0.4$ . Laminar flow in dark blue and fully turbulent flow in red.

Figure 5.19 shows the eddy viscosity ratio for the simulation with  $h_i/h_1 = 1.21$  and  $t_i/t_1 = 5.0$ . The results are similar to the previous Section, but turbulence is both higher in the foil's boundary layer and in the wake, as well as the flow separation, due to the increase of vorticity caused by higher Strouhal number. This confirms that the turbulence in the wake is significant

enough to require the use of turbulence modelling. This will be adopted in all following test cases. Table 5.13 compares the results with and without turbulence model, with differences from 1.1% to 8.1%.

Table 5.13: Comparison of the results with and without turbulence model for the single foil in the high-performance test case, for the simulation with  $h_i/h_l = 1.21$  and  $t_i/t_l = 5.0$ . Motion parameters  $h_0/c = 1.0$ ,  $\alpha_0 = 16.5^\circ$ ,  $\psi = 90^\circ$ ,  $St = 0.4$ .

Var	W/out turbulence model	With turbulence model	Difference [%]
$\bar{C}_T$	0.81	0.80	1.1
$C_V$	2.81	2.58	8.1
$C_M$	1.08	1.07	0.6

### 5.1.4 Three Dimensional Case – Span Effects Analysis

The objective of this section is to study ReFRESKO capability to model 3D oscillating foils simulations, as a step towards the approach of the 3D free-surface case studied in the next Chapter. Since the simulations are very time-consuming, only one case is run. Likewise, only a qualitative comparative study is carried out to evaluate the span effects, not including the V&V procedures. In this section, the motion parameters of Section 5.1.2 are used, the large oscillations case, less demanding than the last section's high-performance case. The 3D computational domain and boundary conditions used are as explained in Chapter 4, with dimensions  $70c \times 100c \times 40c$ , with inflow velocity at the inlet and outflow at the outlet, at  $-20c$  and  $50c$  respectively, top and bottom zero pressure at  $\pm 50c$ , and no-slip wall at foil's surface, with  $8c$  span. The symmetry conditions are placed at  $\pm 20c$ . Regarding the numerical settings, time integration uses the implicit second-order scheme, iterative error criteria is set to  $L_\infty = 10^{-4}$ , and moment discretization uses second order scheme. Due to time costs, the turbulence model is not used here. The motion handling uses deforming grid method, but the deformation radius had to be adjusted to  $4.5c$  because of convergence issues. The cells close to foil tips were too deformed with the previous value of  $2c$ . The motion parameters are shown in Table 5.14. The dynamic viscosity was adjusted to keep  $Re = 40\,000$ . The number of cells, time step for this simulation, and the calculated maximum CFL number can be found in Table 5.15. Table 5.16 presents a comparison between the results of this case with the CFD model, the semi-analytical model, and the results of the different methods for the 2D case studied in Section 5.1.2.

Table 5.14: Simulation parameters for the span effect test case.

Parameter	Value
Inflow velocity, $U$	1 m/s
Chord, $c$	1 m
Pitching axis, $b^*$	1/3-point
Span, $s$	8 m
Pitch amplitude, $\theta_0$	$28.3^\circ$ ( $\alpha_0 \approx 15^\circ$ )
Heave-pitch phase, $\psi$	$90^\circ$
Period, $T$	6.67 s ( $St = 0.3$ )
Reynolds number, $Re$	40 000

Table 5.15: Simulation refinement and  $CFL_{max}$ : total number of cells  $N_c$ , space refinement ratio  $h_i/h_l$ , number of timesteps per period  $n_r/T$ , time refinement ratio  $t_i/t_l$  and  $CFL_{max}$ . Motion parameters  $h_0/c = 1.0$ ,  $\alpha_0 = 15^\circ$ ,  $\psi = 90^\circ$ ,  $St = 0.3$ ,  $s/c = 8$ .

Grid	$N_c$	$n_r/T$	$CFL_{max}$
A	2.85M	333	50.9

The experimental results show the lowest value, and it was proposed in Chapter 3 that 3D span effects might be interfering with the experiment. Taking the 2D results obtained with the

CFD model as a reference, the panel method presents a discrepancy on average thrust coefficient of 16%, while the semi-analytical model and measured data present a discrepancy of 10%. This was considered acceptable because the focus of the section is on qualitative conclusions rather than absolute accuracy. The results obtained are in good agreement with the results of the semi-analytical model confirming that the span effect is well captured in this last one.

Table 5.16: Comparison of the average thrust, vertical force and moment coefficients results between the CFD and semi-analytical models for the 3D with the results for the 2D case from CFD model, semi-analytical model, experimental data from Read et al. (2003) and panel model results from Filippas & Belibassakis (2014b). Motion parameters  $h_0/c = 1.0$ ,  $\alpha_0 = 15^\circ$ ,  $\psi = 90^\circ$ ,  $St = 0.3$ ,  $s/c = 8$ .

Case	Method	$\bar{C}_T$	$C_V$	$C_M$
3D large oscillations	CFD model	0.36	1.30	0.45
	Semi Analytical model	0.34	1.01	0.20
2D large oscillations (Section 5.1.2)	CFD model (Finest exact solution)	0.46	1.90	0.95
	CFD model (Extrapolated value)	0.43	1.88	1.03
	Semi Analytical model	0.45	1.31	0.23
	Experimental (Read et al., 2003)	0.40	-	-
	Panel method (Filippas & Belibassakis, 2014b)	0.50	-	-

## 5.2 Tandem Foils

This section investigates the oscillating foil propulsor configuration using two oscillating foils, one in front of the other, in the same plane, and in a 2D infinite domain. This configuration has been proposed in the review to enhance the thrust and efficiency of the single foil. By optimizing the set of parameters, including the inter-foil separation distance and phase lag, the vortices shed by the two foils can interact constructively and produce total tandem thrust higher than the sum of the isolated foils. The optimization space becomes very large when compared with the single foil case. If the fore and aft foils are equal and have the same motion parameters, two extra parameters are introduced, the foils separation distance and their motion phase lag. The objectives of this test case are to develop an understanding of the vortices and flow dynamics in the two foil wake interaction, compare the modelling accuracy with the available data, and discuss the results from the analytical model. Due to the demanding computational costs for these complex simulations, only two cases are studied, the first chosen to be an intermediate situation with low performance and the second a high-performance configuration.

### 5.2.1 Low Performance – Flow and Forces Analysis

The computational domain and boundary conditions are the same as in 2D cases used before, with dimensions  $70c \times 100c$ , with the inlet and outlet boundaries at  $-20c$  and  $50c$  respectively with top and bottom zero pressure boundaries at  $\pm 50c$ . Three grids were produced with Hexpress, with the fore and aft foils placed at origin and  $5c$ , respectively, with 38k-197k cells. All the numerical setup was kept the same as the single foil test case, with inflow velocity in the inlet and outflow in the outlet, top and bottom zero pressure, second-order time integration and  $L_\infty = 10^{-4}$  iteration criteria. The dynamic viscosity was adjusted to keep  $Re = 40\,000$ . A turbulence model was used for all simulations. The motion parameters are shown in Table 5.17 and the individual foil motions and their separation distance are set to match Epps et al. (2016) case. The inter-foil phase lag is selected for a case with low performance so that the negative interference of the wakes could be studied.

Table 5.17: Tandem foil low performance test case simulation parameters.

Parameter	Value
Inflow velocity, $U$	1 m/s
Chord, $c$	1 m
Pitching axis, $b^*$	1/3-point
Heave amplitude, $h_o$	1 m
Pitch amplitude, $\theta_o$	$45^\circ$ ( $\alpha_0 \approx 6.5^\circ$ )
Heave-pitch phase, $\psi$	$90^\circ$
Inter-foil separation, $s$	4 m
Inter-foil phase lag, $\phi_t$	$270^\circ$
Period, $T$	5 s ( $S_t = 0.4$ )
Reynolds number, $Re$	40 000

The time step in each simulation was chosen trying to keep the Courant in order of 1. Although, as concluded in previous sections, CFL do not need to be less than one since the time integration uses an implicit scheme.

Table 5.18: Simulation parameter details: total number of cells  $N_c$ , number of timesteps per period  $n_t/T$ , space refinement ratio  $h_i/h_j$ , time refinement ratio  $t_i/t_j$ ,  $CFL_{\max}$  and  $y^+_{\max}$ . Motion parameters  $h_o/c = 1.0$ ,  $\alpha_0 = 6.5^\circ$ ,  $\psi = 90^\circ$ ,  $St = 0.4$ ,  $s^* = 8$ ,  $\phi_t = 270^\circ$ .

Grid	$N_c$	$n_t/T$	$h_i/h_j$	$t_i/t_j$	$CFL_{\max}$	$y^+_{\max}$
HE_A	197632	104167	1.00	1.00	2.3	1.76
HE_B	131765	8333	1.22	1.25	7.3	1.57
HE_B	131765	69444	1.22	1.50	2.5	1.84
HE_B	131765	69444	1.22	1.67	3.4	1.54
HE_C	38900	8333	2.25	1.25	2.4	1.54

Table 5.19 Results for discretization error and uncertainty of the data set for the tandem foil low performance test case. Motion parameters  $h_o/c = 1.0$ ,  $\alpha_0 = 6.5^\circ$ ,  $\psi = 90^\circ$ ,  $St = 0.4$ ,  $s^* = 8$ ,  $\phi_t = 270^\circ$ .

Foil	Var	Extrapolated value $\phi_0$	Finest exact solution $\phi_1$	Uncertainty $U_\phi$ [%]	Error $E_d$ [%]	Order of convergence	
						$p_x$	$q_t$
Fore	$\bar{C}_T$	0.40	0.38	8.3	6.0	1.1	1.1
	$C_V$	2.15	2.14	1.0	12.3	1.1	1.1
	$C_M$	0.69	0.71	4.9	0.5	1,2	1,2
Aft	$\bar{C}_T$	0.11	0.12	20.4	32.5	1.1	1.1
	$C_V$	3.35	2.26	18.5	4.1	1,2	1,2
	$C_M$	0.83	0.80	4.4	3.5	1.1	1.1

After the computation it was verified that the non-dimensional wall distance  $y^+_{\max}$  was less than 1.84, that was considered acceptable enough, and that the mesh quality average was 0.89, confirming the good performance of the grid. The parameters used in the simulations for this test case and the  $CFL_{\max}$  registered are shown in Table 5.18.

Figure 5.20 shows a sequence of snapshots of the instantaneous vorticity and velocity fields for this test case ( $h_o/c = 1.0$ ,  $\theta_{oi} = 45^\circ$ ,  $\psi_i = 90^\circ$ ,  $\phi_t = 270^\circ$ ,  $s^* = 8$ ) at quarter cycle instant increments. By first analysing the fore foil it is possible to see, when compared with the previous test case (Figure 5.16) that although the heave amplitude and frequency are the same, the primary vortices are shed much closer to the motion midline. The reason is that the pitch amplitude is larger in this case i.e., the maximum effective angle of attack is smaller ( $\alpha_0 = 6.5^\circ$  instead of  $15^\circ$ ). It agrees with what it is stated in Chapter 3, that when the AoA approaches zero, the vortices align in wake midline, entering into the drag regime.

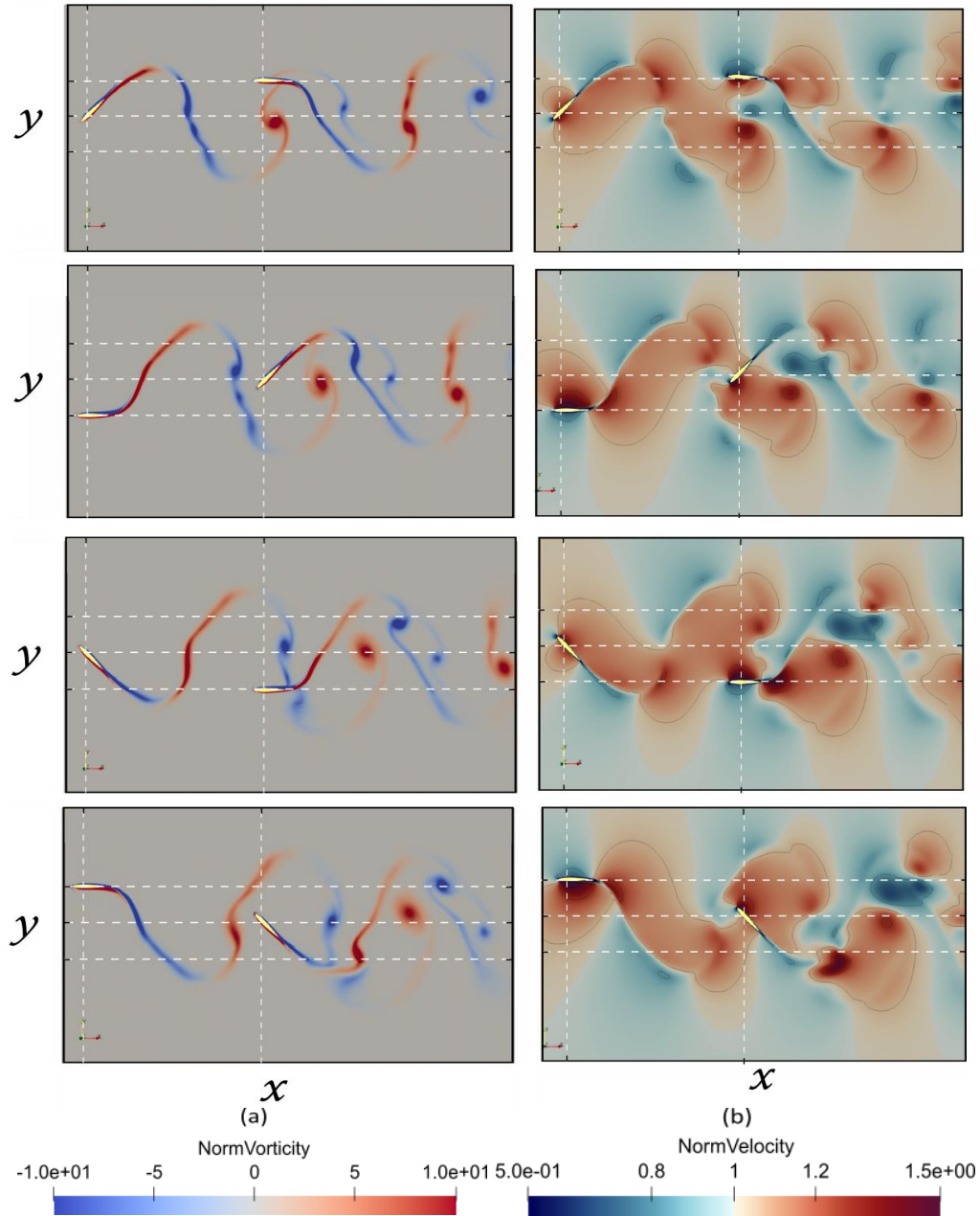


Figure 5.20: Snapshots of (a) normalized vorticity and (b) normalized velocity fields contours at cycle increments of  $t/T = 1/4$  where  $T = 1/f$ , for a tandem foil low performance case with motion parameters  $h_0/c = 1.0$ ,  $\alpha_0 = 6.5^\circ$ ,  $\psi = 90^\circ$ ,  $St = 0.4$ ,  $s^* = 8$ ,  $\phi_t = 270^\circ$ . Clockwise vorticity is indicated with blue, and anticlockwise with red. In all figures, the vertical lines show the location of 1/3 point pitching axis of the foils. The horizontal lines show the mid foil position and the upper and lower limits of heave motion.

In this intermediate low performance case, the fore foil anticlockwise leading edge vortex  $LEV_{f+}$  (red in colour) and the aft foil clockwise leading edge vortex  $LEV_{a-}$  (blue in colour) are pulled together and become coupled. It is the most visible feature of the interaction of the two foils. Thus, deflecting their trajectory and disrupting the BvK vortex street (from  $t/T = 0.25$  to  $t/T = 0.75$ ). To provide further detail on this process, at  $t/T = 0.25$  the aft foil starts to interact with the  $LEV_{f-}$  (blue colour) shed from a previous cycle of the fore foil. As it interacts with the upper surface of the aft foil near the leading edge with opposite signed shear layer (red colour), it lifts the positive shear layer to form  $LEV_{a+}$  at the middle region of the upper surface, leading to high suction. This results in an early or premature shedding of the  $LEV_{a+}$  (red colour) from  $t/T=0.5$  to  $t/T=0.75$ , the shear negative pressure on the upper surface causes negative suction and thus drag. Between  $t/T = 0.25$  and  $t/T = 0.5$ , because of the aft foil interaction with the  $LEV_{f-}$ , the suction pressures are lower on the downstream foil's upper surface compared to the single foil, leading to a small positive thrust.

Table 5.19 presents the results obtained for the average thrust coefficient, vertical force coefficient and moment coefficient, for both the fore and aft foil. The results for the fore foil show a discretization error similar to the previous cases with a single foil up to 6.0%, but when concerning the aft foil, it reaches 32.5%. This might indicate that the grid should be further refined near the aft foil.

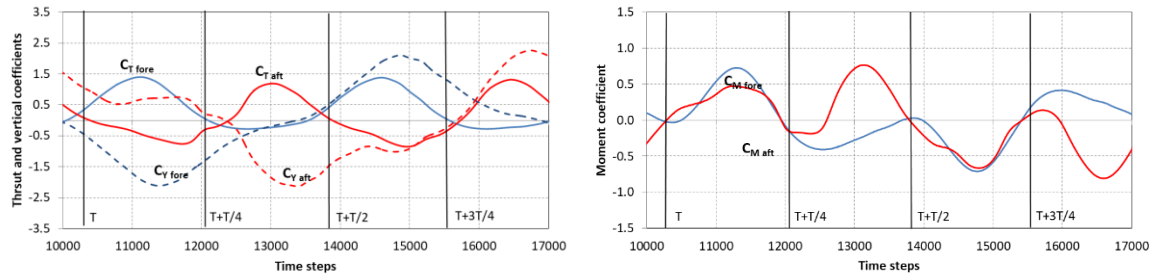


Figure 5.21: (a) Thrust and vertical coefficients and (b) moment coefficient instantaneous values for the forward foil and aft foil in the tandem low performance test case. The four time instants marked correspond to the snapshots of Figure 5.20. Motion parameters  $h_0/c = 1.0$ ,  $\alpha_0 = 6.5^\circ$ ,  $\psi = 90^\circ$ ,  $St = 0.4$ ,  $s^* = 8$ ,  $\phi_t = 270^\circ$ .

The results obtained allow to see that both the aft foil vertical force and the moment are only slightly affected by the fore foil wake, showing small differences within the uncertainties obtained (see also Figure 5.21). The outcomes mainly evidence that the average thrust in the aft foil is much less than in the fore foil, showing that it is an intermediate performance case where the fore foil wake is cancelling part of the thrust produced by the aft foil. Table 5.20 presents a comparison with average thrust coefficient results with the semi-analytical model and the CFD results presented by Epps et al. (2016). There are visible discrepancies between the values. The first is, for the case of a single foil, a 22% over estimation from Epps in comparison with measured data. That might indicate that both Epps' fore and aft foil average thrust coefficients are also over predicted, and results from the present CFD model might be more accurate.

Table 5.20: Comparison of the average thrust coefficient for single, fore, aft and total tandem foils between the CFD model, semi-analytical model and CFD LilyPad solver numerical data (Epps et al., 2016) and experimental data (Read et al., 2003). Results for tandem foil propulsive efficiency. Motion parameters  $h_0/c = 1.0$ ,  $\alpha_0 = 6.5^\circ$ ,  $\psi = 90^\circ$ ,  $St = 0.4$ ,  $s^* = 8$ ,  $\phi_t = 270^\circ$ .

Method	$\bar{C}_T$				$\eta_p$ [%]
	Single foil	Fore foil	Aft foil	Tandem foil	Tandem foil
CFD model	-	0.37	0.07	0.44	60.5
Semi-analytical model	0.27	0.27	0.25	0.52	-
CFD LilyPad (Epps et al., 2016)	0.39	0.43	0.16	0.59	-
Experimental (Read et al., 2003)	0.32	-	-	-	-

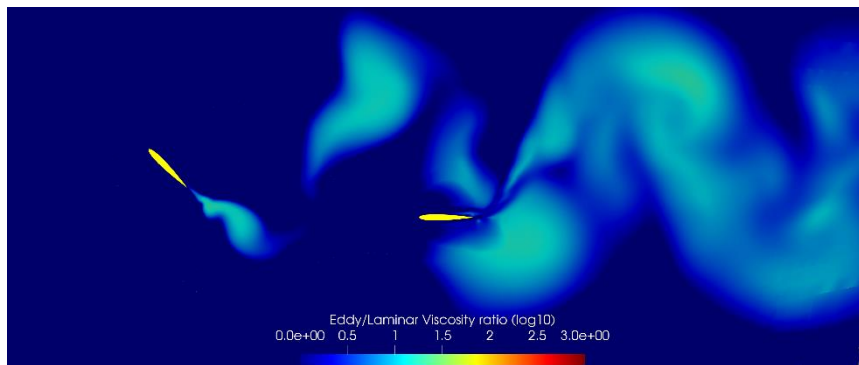


Figure 5.22: Eddy viscosity ratio (log scale) for the tandem foil in low performance case. Motion parameters  $h_0/c = 1.0$ ,  $\alpha_0 = 6.5^\circ$ ,  $\psi = 90^\circ$ ,  $St = 0.4$ ,  $s^* = 8$ ,  $\phi_t = 270^\circ$ . Laminar flow in dark blue and fully turbulent flow in red.

Results from the semi-analytical model for the aft foil have visible discrepancies. The total tandem foil average thrust coefficient and propulsive efficiency are also shown. They are not much higher than the performance of a single foil with the same motion parameters ( $\bar{C}_T \approx 0.3$ ,  $\eta_p \approx 40\%$ , see Figure 5.21). Figure 5.22 shows the eddy viscosity ratio.

## 5.2.2 High-Performance – Flow and Forces Analysis

This case aims to study a 2D tandem foil in parameter configuration for high thrust and propulsive efficiency. The computational domain and boundary conditions are as in the previous section. Solely one grid was produced with Hexpress, with the fore and aft foils placed at origin and  $5c$ , respectively, with 132k cells. All the numerical set-up was kept the same as the tandem low performance test case. The dynamic viscosity was adjusted to keep Reynolds number at  $Re = 40\,000$  and a turbulence model was used. Table 5.21 shows the motion parameters and the individual foil motions. Their separation distance is chosen to match the study case of Muscutt et al. (2017). Both foils oscillate with a maximum AoA of  $10^\circ$ , and the inter-foil phase lag is selected for a case with high-performance so the positive interference of the wakes can be studied. Table 5.22 shows the parameters used in the simulations for this test case and the  $CFL_{max}$  registered.

Table 5.21: Simulation parameters for the tandem foil high-performance test case.

Parameter	Value
Inflow velocity, $U$	1 m/s
Chord, $c$	1 m
Pitching axis, $b^*$	1/3-point
Heave amplitude, $h_o$	1 m
Pitch amplitude, $\theta_o$	$41.5^\circ$ ( $\alpha \approx 10^\circ$ )
Heave-pitch phase, $\psi$	$90^\circ$
Inter-foil separation, $s$	4 m
Inter-foil phase lag, $\phi_t$	$180^\circ$
Period, $T$	5 s ( $St = 0.4$ )
Reynolds number, $Re$	40 000

Table 5.22: Simulation parameter details: total number of cells  $N_c$ , number of timesteps per period  $n_i/T$ , space refinement ratio  $h_i/h_j$ , time refinement ratio  $t_i/t_j$  and  $CFL_{max}$ . Motion parameters  $h_o/c = 1.0$ ,  $\alpha_o = 10^\circ$ ,  $\psi = 90^\circ$ ,  $St = 0.4$ ,  $s^* = 8$ ,  $\phi_t = 180^\circ$ .

Grid	$N_c$	$n_i/T$	$CFL_{max}$
A	131765	6844	2.56

Figure 5.23 shows a sequence of snapshots of the instantaneous vorticity and velocity fields for this test case ( $h_{oi}/c = 1.0$ ,  $\alpha_{oi} = 10^\circ$ ,  $\psi_i = 90^\circ$ ,  $St = 0.4$ ,  $s^* = 8$ ,  $\phi_t = 180^\circ$ ) at quarter cycle instant increments. By first analysing the fore foil, it is possible to see that the primary vortices are now shed at the heave maximum amplitude if compared with the previous test case (Figure 5.15) This outcome is expected because the effective angle of attack is higher, creating a clear reverse BVK wake street, and smaller secondary vortices are shed on the opposite side of the street. As mentioned before, while the first contributes to thrust, the secondary contributes to drag and are probably caused by the beginning of leading edge separation effect.

Regarding the interaction of the two foils, in this high-performance case, the aft foil is weaving in between the primary vortices that are shed from the fore foil. It is possible to see that this increases the vorticity on the front surface of the aft foil, and for this reason also the strength of its vortices shed into the wake. These strong vortices become interspersed with the vortices shed from the fore foil, enough apart not to become coupled, forming vertically pairs and creating a double reversed BvK street. It creates a faster velocity behind the foils than the single foil case, which accounts for the higher thrust.

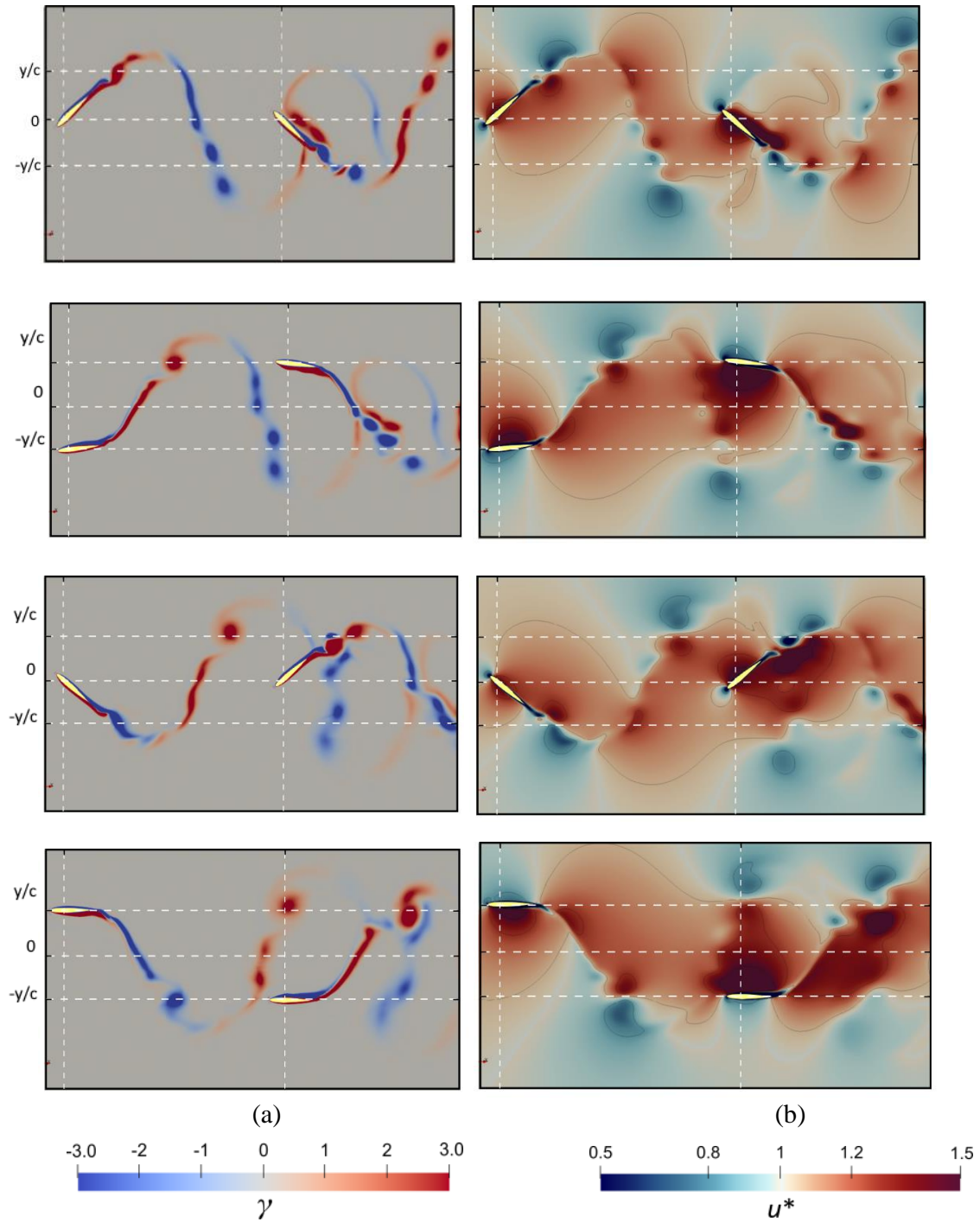


Figure 5.23: Snapshots of (a) vorticity and (b) normalized velocity fields contours at cycle increments of  $t/T = 1/4$  where  $T = 1/f$ , for a tandem foil high-performance case with motion parameters  $h_0/c = 1.0$ ,  $\alpha_0 = 10^\circ$ ,  $\psi = 90^\circ$ ,  $St = 0.4$ ,  $s^* = 8$ ,  $\phi_t = 180^\circ$ . Clockwise vorticity is indicated with blue, and anticlockwise with red. In all figures, the vertical lines show the location of 1/3 point pitching axis of the foils. The horizontal lines show the mid foil position and the upper and lower limits of heave motion. A video of the vorticity field can be found in the on-line supplementary materials listed in the Appendix H and is entitled ‘Tandem Foil in Infinite Domain’.

To explain the vortex dynamics of the aft foil, at  $t/T = 0$ , it is possible to observe the clockwise leading vortex  $LEV_{f-}$  (blue in colour) at the lowest foil position and the elongated trailing edge vortex  $TEV_{f-}$  (blue in colour) shed by the upstroke of the previous cycle. Between  $t/T = 0.25$  and  $t/T = 0.5$ , the  $TEV_{f-}$  from the fore foil directly interacts with the leading edge of the aft foil that is in its downstroke, resulting in a separation of the  $TEV_{f-}$ . At  $t/T=0.5$ , the upper part of the  $TEV_{f-}$ , which is a negative shear flow, supplies vorticity to the negative shear layer on the upper surface of the aft foil, enhancing the suction on this foil. The lower part of  $TEV_{f-}$  couples favourably with the leading edge vortex  $LEV_{a+}$  (red in colour) that is convecting along the lower surface of the aft foil, supplying vorticity, which leads to the

formation of  $LEV_{a+}$ , which has a larger strength compared to  $LEV_{a+}$  of the single foil. This larger  $LEV_{a+}$ , which is spread throughout the lower surface of the aft foil, leads to higher suction pressure and thrust augmentation ( $t/T = 0.75$ ). On the other hand, the interaction of the lower side of the aft foil with the  $TEV_{f-}$  drives it out of the way in the wake, avoiding the drag effects that they cause in the isolated single foil. Thus, two favourable conditions help to generate thrust during a downstroke of the flapping foil, the strengthening of the aft foil primary vortices and the repositioning of the fore secondary vortices. With progress in time, the aft foil undergoes upstroke motion where a similar vortex interaction is observed for reversed sign of vorticity.

For the velocity field snapshots, it is possible to see that the jet velocity behind the fore foil is little affected by comparing the tandem high-performance, the tandem low performance, and the single foil cases (Figure 5.17, Figure 5.15, and Figure 5.13, respectively). It implies that the vortex advection speed between the foils is constant for each Strouhal number and independent of the inter-foil phase lag and separation. This streamwise velocity behind the fore foil is always higher than the freestream so it will always act to increase the induced velocity of the aft foil regardless of its specific kinematics. On the other hand, the crossflow velocity alternates between every primary vortex. If it is in the same direction as the heave velocity of the aft foil, then the magnitude of the induced vertical velocity is reduced. Therefore, to increase its induced vertical velocity, the aft foil needs to move in opposite direction to this crossflow velocity, which is why it must weave between the incoming vortices for the highest thrust production.

Figure 5.24 shows the instantaneous thrust, vertical, and moment coefficients for both fore and aft foils. The time instant of the Figure 5.23 snapshots are indicated. It is possible to see the augmentation of the aft thrust coefficient relative to the fore foil.

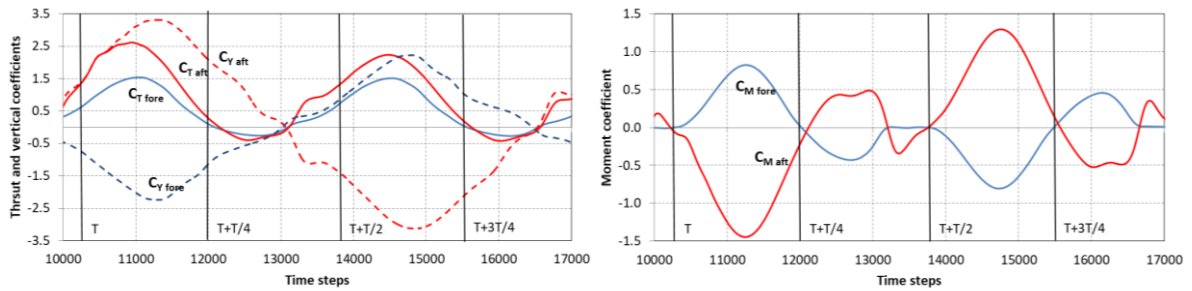


Figure 5.24: (a) Thrust and vertical and (b) moment coefficients instantaneous values for the forward foil and aft foil in tandem test case. The four time instants marked correspond to the snapshots of Figure 5.20  $t/T = 0, 0.25, 0.5, 0.75$ . Motion parameters  $h_0/c = 1.0$ ,  $\alpha_0 = 10^\circ$ ,  $\psi = 90^\circ$ ,  $St = 0.4$ ,  $s^* = 8$ ,  $\phi_t = 180^\circ$ .

Table 5.23 presents the results of the average thrust for both fore and aft foils and total tandem configuration and propulsive efficiency with discrepancies of 28% on mean thrust coefficient. In Table 5.24 the normalized CFD model values of the aft foil  $C_T$  and  $\eta_p$  are compared with Muscutt results with a very good agreement (Muscutt assumes that the values for the fore foil are approximately the same for the single foil case), with 0.6% and 5.6% discrepancies for the average thrust and propulsive efficiency, respectively.

Table 5.23: Results of the average thrust coefficient and propulsive efficiency for the fore, aft and tandem foil. Motion parameters  $h_0/c = 1.0$ ,  $\alpha_0 = 10^\circ$ ,  $\psi = 90^\circ$ ,  $St = 0.4$ ,  $s^* = 8$ ,  $\phi_t = 180^\circ$ .

Method		Fore foil	Aft foil	Tandem foil
CFD model	$\bar{C}_T$	0.51	0.87	1.37
	$\eta_p$ [%]	77.2	82.1	80.1
Semi-analytical model	$\bar{C}_T$	0.39	0.59	0.98
	$\eta_p$ [%]	74.5	90.7	82.6

Table 5.24: Comparison of the normalized aft foil average thrust coefficient and efficiency between CFD model, the semi-analytical model and CFD LilyPad solver numerical data (Muscutt et al., 2017). Motion parameters  $h_0/c = 1.0$ ,  $\alpha_0 = 10^\circ$ ,  $\psi = 90^\circ$ ,  $St = 0.4$ ,  $s^* = 8$ ,  $\phi_t = 180^\circ$ .

Method	$\bar{C}_{T\ aft}/\bar{C}_{T\ fore}$	$\eta_{p\ aft}/\eta_{p\ fore}$
CFD model	1.57	1.06
Semi-analytical model	1.52	1.21
CFD LilyPad (Muscutt et al., 2017)	1.56	1.00

In this configuration the aft foil mean thrust is augmented by 157% through its interaction with the fore foil wake resulting in the whole tandem having mean thrust values 2.6 times larger than the single foil, while the propulsive efficiency increases 6.3% in the aft foil and 3.8% in the tandem. Nevertheless, the good agreement with Muscutt results in terms of normalized values, the discretization error and uncertainty of the solutions obtained was not quantified, requiring more simulations with different grid and time step refinements. But even qualitatively, the results seem promising compared to the best high-performance case for a single foil found in Section 3.2.1 ( $h_0/c = 1.0$ ,  $\alpha_0 = 20^\circ$ ,  $\psi = 90^\circ$ ,  $St = 0.5$ ) where the tandem presents 80.1 % and  $C_T = 1.37$  against 60% and  $C_T = 1.2$ .

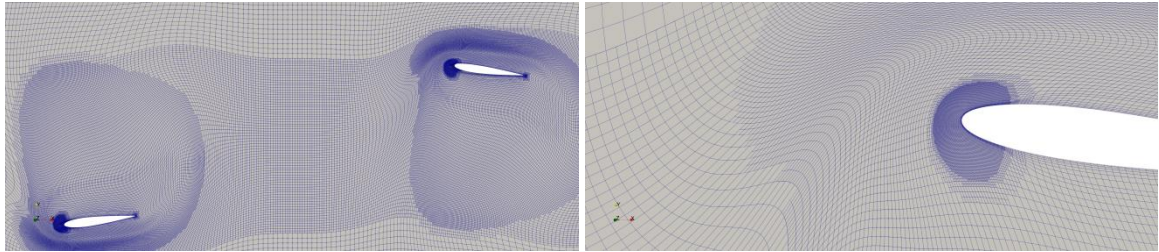


Figure 5.25: Example of grid deformation (a) general view and (b) detail of the mesh around the aft foil.

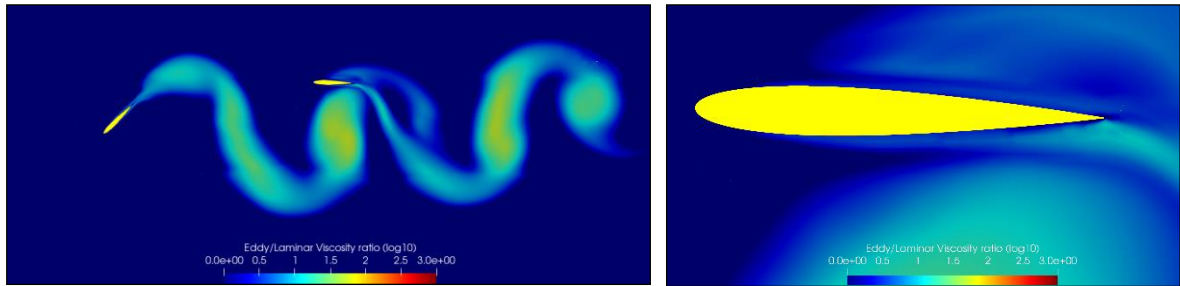


Figure 5.26: Eddy viscosity ratio (log scale) for the high-performance tandem foil case. (a) wake (b) Aft foil boundary layer. Motion parameters  $h_0/c = 1.0$ ,  $\alpha_0 = 10^\circ$ ,  $\psi = 90^\circ$ ,  $St = 0.4$ ,  $s^* = 8$ ,  $\phi_t = 180^\circ$ . Laminar flow in dark blue and fully turbulent flow in red.

The deformation of the grid is shown in Figure 5.25 where it is possible to have a visual confirmation of the good performance of the deforming grid used, maintaining the quality of the grid in the critical areas like the foils' leading end trailing edge. Figure 5.26 shows the eddy viscosity ratio. It is possible to see, as the case with single foil, the transitional regime in the wake and low turbulence in the boundary layer, and also the absence of fully developed turbulent flow.



# Chapter 6

## Oscillating Foil Thrusters with Free-Surface and Waves

This Chapter first assesses the results for a submerged single foil in calm waters and then in incident waves, followed by an exploratory study of the tandem foil physical processes and performance, again in calm waters and incident waves. A more thorough and detailed investigation is left for future studies because of the increased complexity of the physical processes, the large parameter space, and the demanding time computational costs. This Chapter intends to be a preliminary approach, demonstrating and discussing the capabilities of the numerical model. Thus, only one configuration is computed for each test case, considered sufficient to pursue a qualitative study, and to discuss the flow solutions and hydrodynamic forces. In general, the study of the test cases follows the same approach and structure of the previous Chapter.

### 6.1 Single Foil

#### 6.1.1 Free-Surface – 2D Study

This section investigates a 2D single foil in large oscillations with a free-surface. The simulation parameters are chosen to match the test case of a single foil in infinite domain in large oscillations, presented in Section 5.1.2. The computational domain and boundary conditions are similar to those of in Chapter 4, with dimensions  $70c \times 100c$ , with inflow velocity at the inlet and outflow at the outlet, at  $-20c$  and  $50c$  respectively, top pressure at  $+20c$ , bottom free-slip at  $-50c$ , and no-slip wall at foil's surface. Two wave absorption zones are used,  $3c$  length from the inlet and outlet. Just one grid was produced with Hexpress, with 397k cells. Concerning the numerical settings, time integration uses the implicit second-order scheme, iterative error criteria is set to  $L_{\infty} = 10^{-4}$ , and momentum discretization uses a second-order scheme. The dynamic viscosity was adjusted to keep the Reynolds number at  $Re = 40\,000$  and a turbulence model was used. The motion handling uses the deforming grid method with a deformation radius of  $2c$ . The motion parameters are shown in Table 6.1. For this test case, the simulations' parameters and the  $CFL_{\max}$  are shown in Table 6.2.

Table 6.1: Submerged single foil test case simulation parameters

Parameter	Value
Inflow velocity, $U$	1.0 m/s
Chord, $c$	1.0 m
Pitching axis, $b^*$	1/3-point
Heave amplitude, $h_o$	1.0 m
Pitch amplitude, $\theta_o$	$28.3^\circ$ ( $\alpha_o \approx 15^\circ$ )
Heave-pitch phase, $\psi$	$90^\circ$
Submergence, $d$	1.25 m
Period, $T$	6.67 s ( $S_r = 0.3$ )
Reynolds number, $Re$	40 000

Table 6.2: Simulation parameter details: total number of cells  $N_c$ , number of timesteps per period  $n_f/T$ , space refinement ratio  $h_f/h_1$ , time refinement ratio  $t_f/t_1$  and  $CFL_{max}$ . Motion parameters  $h_0/c = 1.0$ ,  $\alpha_0 = 15^\circ$ ,  $\psi = 90^\circ$ ,  $St = 0.3$ ,  $d^* = 1.25$ .

Grid	$N_c$	$n_f/T$	$CFL_{max}$
A	397178	4167	3.5

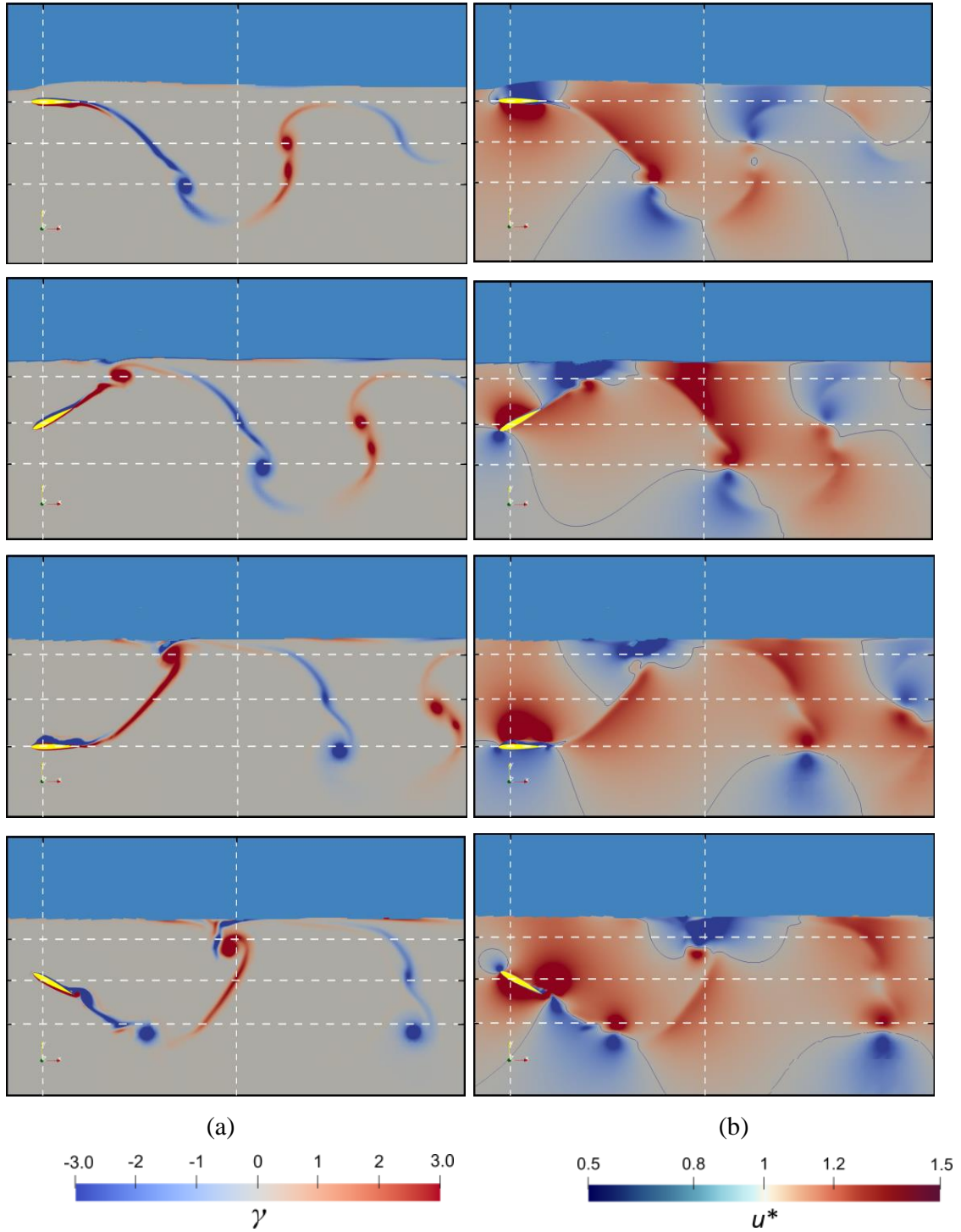


Figure 6.1: Snapshots of (a) vorticity and (b) normalized velocity fields contours at cycle increments of  $t/T = 1/4$  where  $T = 1/f$ , for a submerged foil in large oscillations with motion parameters  $h_0/c = 1.0$ ,  $\alpha_0 = 15^\circ$ ,  $\psi = 90^\circ$ ,  $St = 0.3$ ,  $d^* = 1.25$ . Clockwise vorticity is indicated with blue, and anticlockwise with red. In all figures, the vertical lines show the location of 1/3 point pitching axis of the foils. The horizontal lines show the mid foil position and the upper and lower limits of heave motion. A video of the vorticity field can be found in the on-line supplementary materials listed in the Appendix H and is entitled ‘Single Foil with Free-Surface’.

Figure 6.1 shows a sequence of snapshots of the instantaneous vorticity and velocity fields for this test case ( $h_0/c = 1.0$ ,  $\alpha_0 = 15^\circ$ ,  $\psi = 90^\circ$ ,  $St = 0.3$ ,  $d^* = 1.25$ ) at quarter cycle instant increments. It is possible to see the alternate shedding of primary and then secondary elongated vortices, typical of reversed BvK street wake, observed in the different cases of Chapter 5 (e.g., see Figure 5.20). In particular it is visible the interaction of the foil with the free-surface, causing its deformation and wave generation. During the downstroke, from instants  $t/T = 0.25$  to  $t/T = 0.75$ , from the free-surface, a clockwise vortex (in blue) develops coupled with the primary anticlockwise vortex (in red). This causes its weakening and displacement towards the wake midline, thus decreasing thrust. The decrease in velocity produced by the downstroke, when compared with the upstroke, can also be seen in the normalized velocity field snapshots.

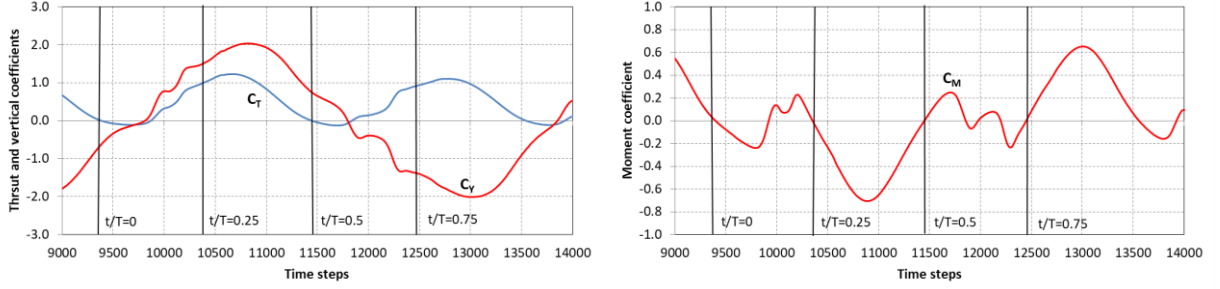


Figure 6.2: (a) Thrust and vertical and (b) moment coefficients instantaneous values for the forward foil and aft foil in tandem test case. The four time instants marked correspond to the snapshots of Figure 6.1  $t/T = 0, 0.25, 0.5, 0.75$ . Motion parameters  $h_0/c = 1.0$ ,  $\alpha_0 = 15^\circ$ ,  $\psi = 90^\circ$ ,  $St = 0.3$ ,  $d^* = 1.25$ .

Figure 6.2 shows the instantaneous thrust, vertical and moment coefficients. The time instant of the Figure 6.1 snapshots are indicated. Although not very significant it is possible to see the differences in the thrust coefficient between the upstroke and downstroke. Table 6.3 presents a comparison of the average thrust results with those of the analytical model and with the infinite domain test case of Section 5.1.2. Although the free-surface is expected to cause a small decrease (4.4% for the analytical model), the CFD model results present instead a slight increase (1.2%). It can indicate that the grid refinement around the surface is not capable to fully capture the waves with small height generated by the foil oscillation. Nevertheless, in the context of the qualitative analysis aimed in this section, the results were found acceptable.

Table 6.3: Comparison of the average thrust coefficient, between the semi-analytical and numerical model developed in the present work with respective results in an infinite domain of Section 5.1.2. Motion parameters  $h_0/c = 1.0$ ,  $\alpha_0 = 15^\circ$ ,  $\psi = 90^\circ$ ,  $St = 0.3$ ,  $d^* = 1.25$ .

Case	Method	$\bar{C}_T$
2D free-surface	CFD model	0.44
	Semi-analytical model	0.43
2D infinite domain (Section 5.1.2)	CFD model	0.43
	Semi-analytical model	0.45

Figure 6.3 shows the eddy viscosity ratio. It is possible to see, as the case with single foil in infinite domain, that turbulence occurs mainly in the wake. It is important to remark that the turbulence near the free-surface is numerical and does not translate a physical phenomenon. This might be explained by low refinement near the free-surface, causing the VOF equations to generate vorticity, that artificially creates turbulence. This is a known issue called *numerical eddy viscosity due to VOF poor accuracy* (Klajic et al., 2018; Kamath et al., 2019), which resolution needs special and complex filters in the code. Because of its complexity, it was not done in this work. Figure 6.4 shows an example for a wave with non-dimensional wavelength  $ka = 0.118$  and amplitude  $a_0/a = 1.5$ , plotting the normalized vorticity, eddy viscosity ratio (turbulence), turbulent kinetic energy and  $k$  the dissipation rate per unit kinetic energy  $\omega$ . It is possible to see the numerical vorticity (positive in red and negative in blue) in the all the area

close to the free-surface in (a), causing  $k$  and  $\omega$  quantities in (c) and (d) not to be zero in the same area, and finally resulting in the appearance of turbulence (b).

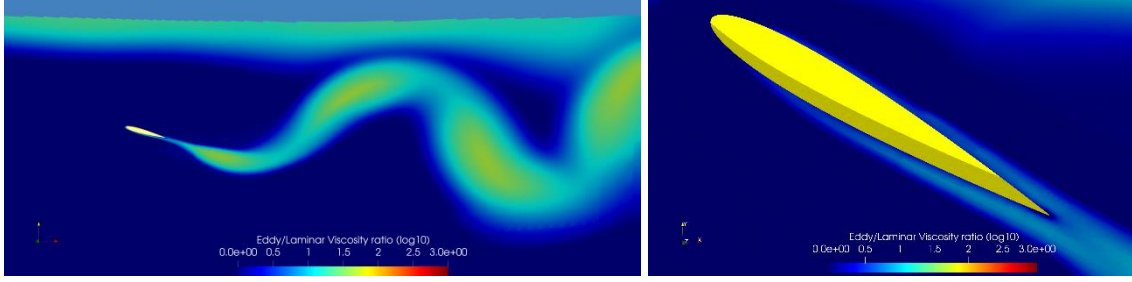


Figure 6.3: Eddy viscosity ratio (log scale) for the submerged single foil case: (a) wake (b) foil boundary layer. Motion parameters  $h_0/c = 1.0$ ,  $\alpha_0 = 15^\circ$ ,  $\psi = 90^\circ$ ,  $St = 0.3$ ,  $d^* = 1.25$ . Laminar flow in dark blue and fully turbulent flow in red.

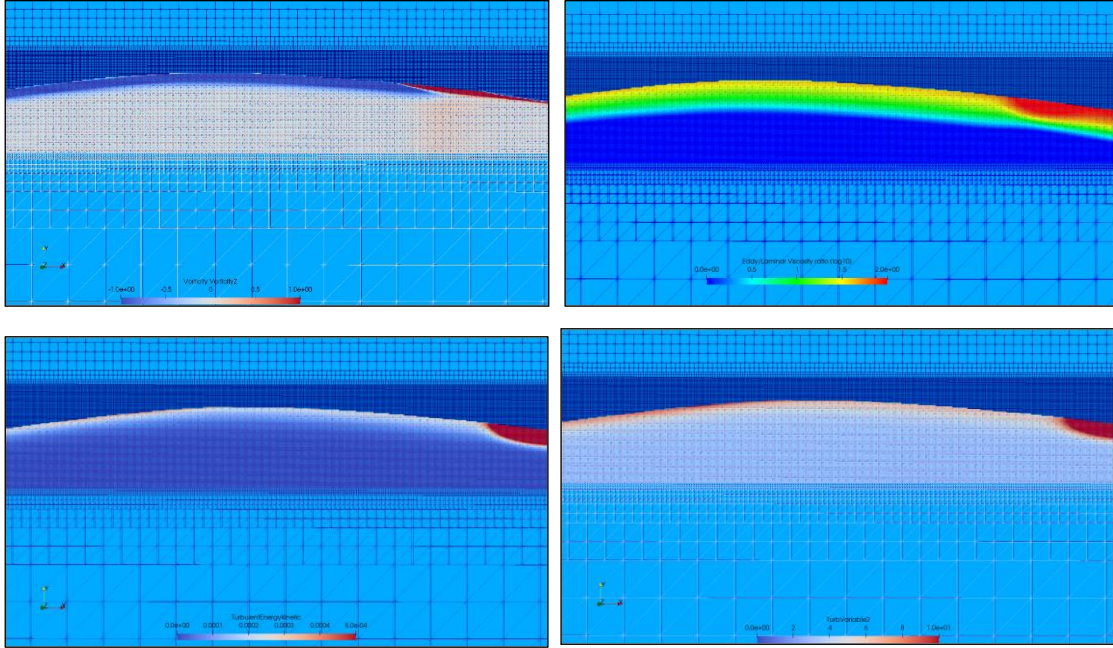


Figure 6.4: Grid refinement near the free-surface for a wave with non-dimensional wavelength  $ka = 0.118$  and amplitude  $a_0/a = 1.5$ : (a) Normalized vorticity (b) Eddy viscosity ratio (turbulence) (c) Turbulent kinetic energy  $k$  (d) Dissipation rate per unit kinetic energy  $\omega$ .

### 6.1.2 Free-Surface – 3D Study

This section studies ReFRESH capability to model 3D oscillating foil with a free-surface. In this section, the motion parameters are the same as in the previous Section, the large oscillations case, which also matches the 3D test case for an infinite domain of Section 5.1.3. The 3D computational domain and boundary conditions used are as explained in Section 5.1.3, with dimensions  $70c \times 100c \times 40c$ , with inflow velocity at the inlet and outflow at the outlet, at  $-20c$  and  $50c$  respectively, top and bottom zero pressure at  $\pm 50c$ , and no-slip wall at foil's surface, with  $8c$  span. The symmetry conditions are placed at  $\pm 20c$ . An elliptical wave absorption zone is used, centred on the foil,  $3c$  length from the boundaries, with a cosine absorption function. Concerning the numerical settings, time integration uses the implicit second-order scheme, iterative error criteria is set to  $L_\infty = 10^{-4}$ , and momentum discretization uses a second-order scheme. For time reasons, the turbulence model is not used here. The motion handling uses the deforming grid method, but the deformation radius had to be adjusted to  $4.5c$  because of convergence issues, as the cells close to foil tips were too deformed with the previous value of  $2c$ . The dynamic viscosity was adjusted to keep  $Re = 40\,000$ . The motion

parameters are shown in Table 6.4. The number of cells, time step for this simulation and the calculated maximum CFL number are found in Table 6.5.

Table 6.4: Simulation parameters for the free-surface span effect test case.

Parameter	Value
Inflow velocity, $U$	1 m/s
Chord, $c$	1 m
Pitching axis, $b^*$	1/3-point
Span, $s$	8 m
Heave amplitude, $h_o$	1.0 m
Pitch amplitude, $\theta_o$	$28.3^\circ$ ( $\alpha_o \approx 15^\circ$ )
Heave-pitch phase, $\psi$	$90^\circ$
Submergence, $d$	1.25 m
Period, $T$	6.67 s ( $St = 0.3$ )
Reynolds number, $Re$	40 000

Table 6.5: Simulation parameter details: total number of cells  $N_c$ , number of timesteps per period  $n_r/T$ . Motion parameters  $h_o/c = 1.0$ ,  $\alpha_o = 15^\circ$ ,  $\psi = 90^\circ$ ,  $St = 0.3$ ,  $d^* = 1.25$ ,  $s/c = 8$ .

Grid	$N_c$	$n_r/T$
A	3.7M	333

Figure 6.5 presents a time sequence of snapshots of surface elevation for this test case ( $h_o/c = 1.0$ ,  $\alpha_o = 15^\circ$ ,  $\psi = 90^\circ$ ,  $St = 0.3$ ,  $d^* = 1.25$ ,  $s/c = 8$ ), showing the wave radiation by the submerged oscillating foil, and its subsequent damping in the absorption zone. For this case, the critical wavenumber is below  $1/4$  ( $F_r^2 k_f = 0.09$ ). Thus, all four types of radiated waves exist (see Section 3.2.2), behind and in front of the foil, visible in the images. The elongated wave pattern visible behind the foil is caused by the forward travelling velocity of the foil. The radiated waves then reach the absorption zone near the boundaries of the domain where they are quickly attenuated, avoiding reflections.

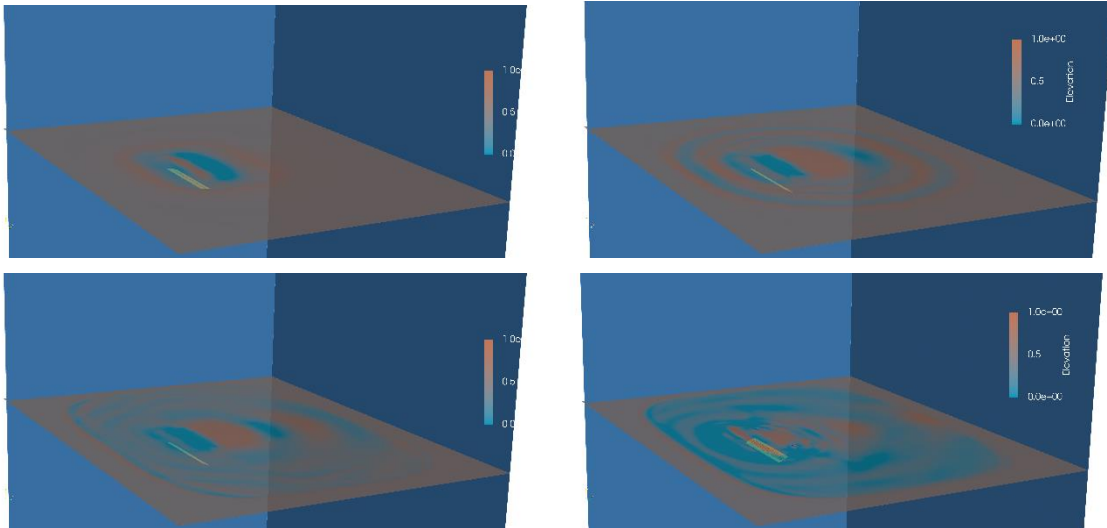


Figure 6.5: a) to d) Sequence of snapshots of surface elevation, showing wave radiation by the submerged oscillating foil, and wave damping in the absorption zone. Motion parameters  $h_o/c = 1.0$ ,  $\alpha_o = 15^\circ$ ,  $\psi = 90^\circ$ ,  $St = 0.3$ ,  $d^* = 1.25$ ,  $s/c = 8$ .

Table 6.6 shows a comparison between the average thrust coefficient results obtained with both the CFD and the semi-analytical models, with the test cases of 3D infinite domain (Section 5.1.4), the 2D free-surface (Section 6.1.1) and the 2D infinite domain (Section 5.1.2). It is possible to see the good agreement with the results between the two types of models, with discrepancies of less than 5%. The effect of the span is visibly more important than the free-surface effect, causing a reduction in the average thrust of 21.7% and 3.7%, respectively.

Table 6.6: Comparison of the average thrust coefficient, between the semi-analytical and numerical model developed in the present work with respective results in 3D infinite domain, 2D free-surface and 2D infinite domain. Motion parameters  $h_0/c = 1.0$ ,  $\alpha_0 = 15^\circ$ ,  $\psi = 90^\circ$ ,  $St = 0.3$ ,  $d^* = 1.25$ ,  $s/c = 8$ .

Case	Method	$\bar{C}_T$
3D free-surface	CFD model	0.26
	Semi-analytical model	0.27
3D infinite domain (Section 5.1.4)	CFD model	0.34
	Semi-analytical model	0.34
2D free-surface (Section 6.1.1)	CFD model	0.44
	Semi-analytical model	0.43
2D infinite domain (Section 5.1.2)	CFD model	0.43
	Semi-analytical model	0.45

### 6.1.3 Incident Waves – No Oscillations Study

The aim of this section is to study the simplified problem of a fixed foil with heading incident waves, contributing to approaching the higher complexity case of an oscillating foil in incident waves. Both the implementation issues and flow and forces analysis are addressed. In this section a fixed 2D NACA0012 foil is considered, within the same computational domain of Section 6.1.1. The inlet and outlet boundaries are at a distance of  $20c$  and  $50c$  from the coordinate origin at the leading edge of the foil. A wave boundary condition is prescribed at the inlet for wave generation and freestream velocity of  $F_r = 0.39$  while an outflow boundary condition is satisfied at the outlet. The top and bottom boundaries are at  $20c$  and  $50c$  where pressure and free-slip boundary conditions are imposed respectively. The symmetry conditions are placed at  $\pm 20c$  and a no-slip condition is imposed at the foil surface. The dynamic viscosity was adjusted to keep the foil subjected to flow at  $Re = 40\,000$ . With respect to the numerical settings, time integration uses the implicit second-order scheme, iterative error criteria is set to  $L_\infty = 10^{-4}$ , and momentum discretization uses second order scheme. Because of the vertical wave orbital velocity acting on the foil's surface, the turbulence model is used as well. The motion handling uses the deforming grid method, with deformation adjusted to  $2c$ . A free-surface equation is used to prescribe the submergence at  $d^* = 2.5$  and the wave generation, with Stokes 5<sup>th</sup> order formulation, with wave amplitude  $a_0^* = 1.5$  m and wave period  $T_w = 1.51$  s. Wave absorption is set within a range of  $3c$  from both inlet and outlet. The motion parameters are shown in Table 6.7.

Table 6.7: Simulation parameters for the fixed foil in incident waves test case.

Parameter	Value
Inflow velocity, $U$	0.38 m/s
Chord, $c$	0.1 m
Submergence, $d$	0.25 m
Wave amplitude, $a_0$	0.075
Wave period, $T_w$	1.51 s
Reynolds number, $Re$	40 000

Table 6.8: Simulation parameter details: total number of cells  $N_c$ , number of timesteps per period  $n_t/T$ , and  $CFL_{max}$ . Parameters  $a_0^* = 1.5$ ,  $d^* = 2.5$ .

Grid	$N_c$	$n_t/T$	$CFL_{max}$
A	85364	2607	11.0

The number of cells, time step for this simulation and the calculated maximum CFL number can be found in Table 6.8, where  $T$  is taken to be the encounter wave period.

Figure 6.6 shows a sequence of snapshots of the instantaneous vorticity and velocity fields for this test case ( $a_0^* = 1.5$ ,  $d^* = 2.5$ ) at a quarter cycle instant increment. These four time

instants correspond to the travelling heading wave upward midpoint, crest, downward midpoint, and trough (see Figure 6.8c). At  $t/T = 0$ , the upward crosswise flow velocity causes a negative shear flow on the upper surface of the foil, creating negative vorticity that is convected along its surface until  $t/T = 0.25$ , then shedding a primary clockwise leading edge vortex LEV- (blue in colour) at  $t/T = 0.5$ , followed by the shedding of an elongated clockwise trailing edge vortex LEV- (blue in colour). A similar process with anticlockwise vortices (red in colour) is observed for reversed sign of vorticity in the second part of the cycle, in the same way of an oscillating foil in infinite domain, creating a reverse BvK wake street.

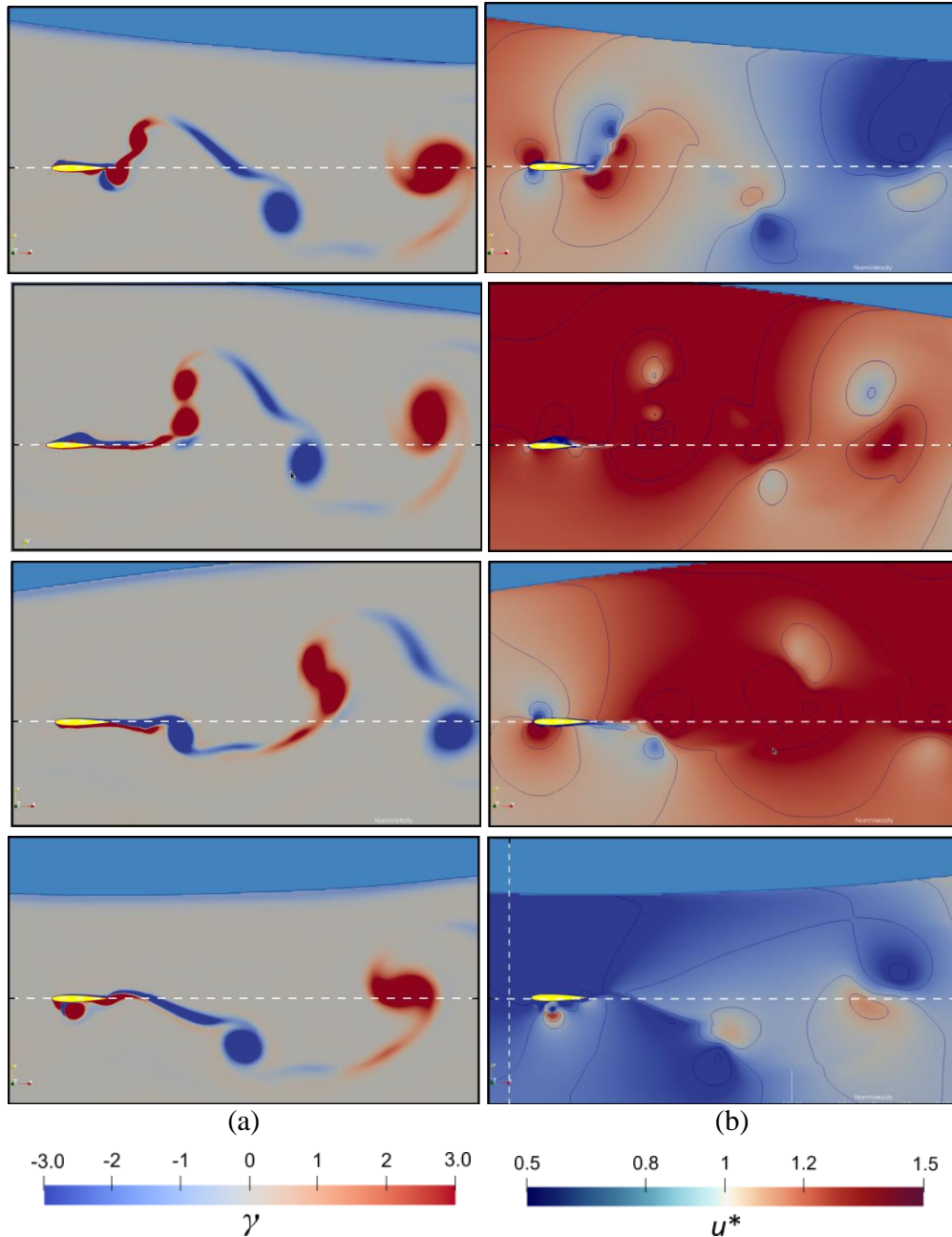


Figure 6.6: Snapshots of (a) vorticity and (b) normalized velocity fields contours at cycle increments of  $t/T = 1/4$  where  $T = 1/f$ , for a fixed foil in incident waves with parameters  $a_0^* = 1.5$ ,  $d^* = 2.5$ . The blue indicates the clockwise vorticity, and the red the anticlockwise vorticity.

This pattern corresponds approximately to the wake pattern of a foil in small oscillations, with the vortices close to the wake midline. Otherwise, in the case of the oscillating foil in an infinite domain, the vortices move, due to the crosswise flow induced by the wave. Due to the free-surface proximity, it is also possible to observe that the primary LEV+ (red in colour), are separated but stronger than the LEV- (blue in colour) that are more similar to the single infinite domain vortices. It explains the differences in the thrust coefficient on two parts of the cycle

observed in Figure 6.7. This figure shows the instantaneous thrust, vertical, moment coefficients with the time instants of the Figure 6.6.

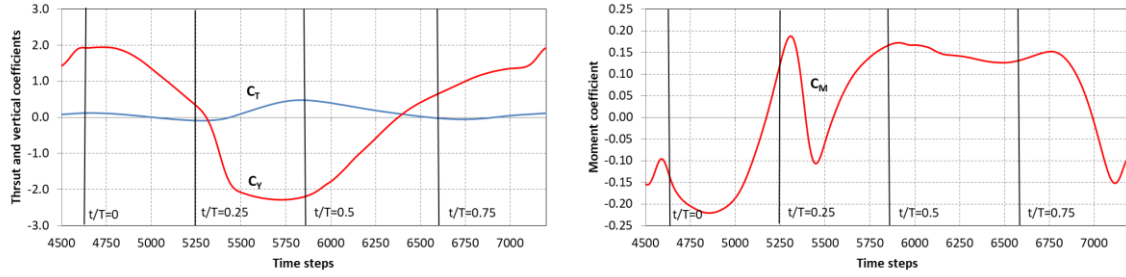


Figure 6.7: (a) Thrust and vertical coefficient and (b) moment coefficient for the fixed foil in incident waves test case. The four time instants marked correspond to the snapshots of Figure 5.20  $t/T = 0, 0.25, 0.5, 0.75$ . Parameters are  $a_0^* = 1.5, d^* = 2.5$ .

Figure 6.8 shows the wave height at  $x = 1/3$ -chord, with the time instant of the Figure 6.6 snapshots indicated, and Table 6.9 presents the results for average thrust, vertical and moment coefficients, with thrust generation even in the absence of oscillations. Semi analytical model results show a significant average thrust coefficient over prediction to the numerical simulation, expected as seen in Chapter 3.

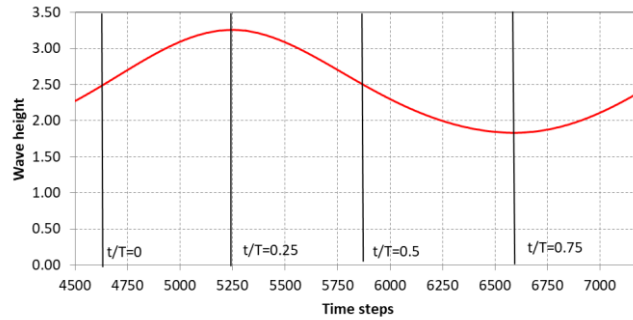


Figure 6.8: Wave height at  $x = 1/3$ -chord for the fixed foil in waves test case. The four time instants marked correspond to the snapshots of Figure 5.20  $t/T = 0, 0.25, 0.5, 0.75$ . Parameters are  $a_0^* = 1.5, d^* = 2.5$ .

Table 6.9: Results of the average thrust, vertical and moment coefficients for the fixed foil in waves and comparison with the semi-analytical model. Parameters are  $a_0^* = 1.5, d^* = 2.5$ .

Method	$\bar{C}_T$	$C_V$	$C_M$
CFD model	0.12	1.99	0.19
Semi-analytical model	0.29	2.02	0.286

The grid refinement for the free-surface used is shown in Figure 6.9 where it is possible to have a visual confirmation that it is adequate for the wave amplitude used.

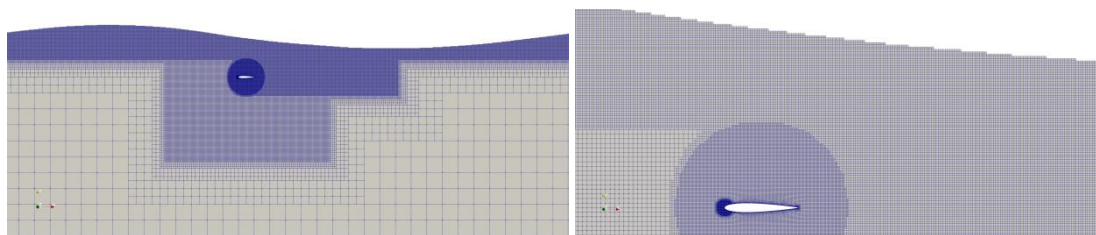


Figure 6.9: Grid refinement for an incident wave with a fixed foil a) general view b) detail near the foil. Parameters are  $a_0^* = 1.5, d^* = 2.5$ .

Figure 6.10 shows the eddy viscosity ratio, where turbulence is clearly visible in both wake and boundary layer. There is also a clear flow separation in the boundary layer. As explained before in Section 6.1.1, the turbulence near the surface is of numerical origin due to VOF poor accuracy, probably accentuated by the use of first order time discretization.

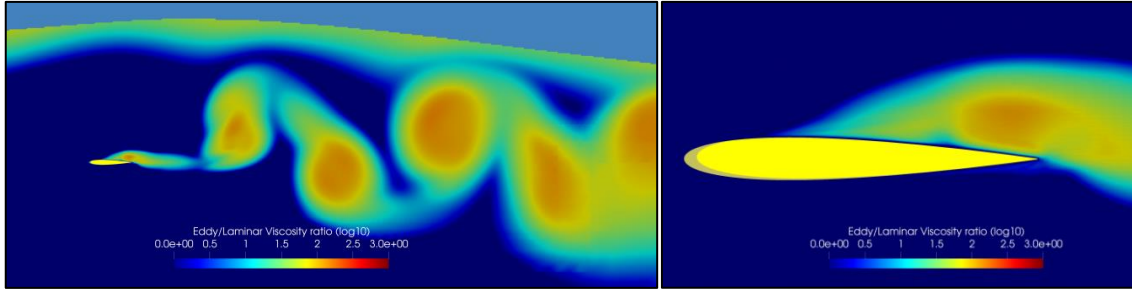


Figure 6.10: Eddy viscosity ratio (log scale) for the submerged fixed single foil case: (a) wake (b) foil boundary layer. Parameters are  $a_0^* = 1.5$ ,  $d^* = 2.5$ . Laminar flow in dark blue and fully turbulent flow in red.

#### 6.1.4 Incident Waves – Large Oscillations Study

The aim of this section is to analyse the flow and forces of an active oscillating foil in heading incident waves. The wave and motion parameters are set to allow comparison with the FLUENT results of Silva et al. (2012) addressed in Section 3.2.2, using a 1:70 scale. In this section a 2D NACA0012 profile is considered, within the same computational domain of the previous section. The wave boundary condition is prescribed at the inlet for wave generation and freestream velocity of  $F_r = 0.87$ . The flow passing the foil has a Reynolds number  $Re = 8500$ . Concerning the numerical settings, time integration uses the implicit first-order scheme (Euler), with lower accuracy but more robust than the second-order scheme, found necessary to achieve iterative convergence, keeping the iterative error criteria is set to  $L_\infty = 10^{-4}$ , and moment discretization uses a second-order scheme. Despite the low Reynolds number, the turbulence model was kept. The motion handling uses the deforming grid method, with deformation adjusted to  $2c$ . A free-surface equation with a SuperBEE discretization scheme is used to prescribe the submergence at  $d^* = 1.28$  and the heading wave generation, with Stokes 5<sup>th</sup> order formulation, wave amplitude  $a_0/h_0 = 0.238$ , wave period  $T_w = 1.13$  s, and wave heave phase  $\phi_w = -180^\circ$ . The non-dimensional frequency of flapping is equal to encounter frequency  $\omega_0^2 c/g = 0.69$ . The phase difference between the heaving and the pitching motion is selected as  $\psi = 90^\circ$ . The heaving amplitude is  $h_0/c = 0.6$  and the pitching amplitude is adjusted to  $\theta_0 = 15.2^\circ$ , to keep the same encounter frequency. The motion parameters are shown in Table 6.10. The number of cells, time step for this simulation and the calculated maximum CFL number are found in Table 6.11.

Table 6.10: Simulation parameters for oscillating foil in incident wave test case.

Parameter	Value
Inflow velocity, $U$	0.86 m/s
Chord, $c$	0.1 m
Pitching axis, $b^*$	1/3-point
Heave amplitude, $h_0$	0.06 m
Pitch amplitude, $\theta_0$	$15.2^\circ$
Heave-pitch phase, $\psi$	$90^\circ$
Oscillation period, $T$	0.76 s
Submergence, $d$	0.128 m
Wave amplitude, $a_0$	0.075
Wave period, $T_w$	1.13 s
Wave-heave phase $\phi_w$	$-90^\circ$
Reynolds number, $Re$	8500

Table 6.11: Simulation parameter details: total number of cells  $N_c$ , number of timesteps per period  $n/T$ , and  $CFL_{max}$ . Motion and wave parameters  $h_0/c = 0.6$ ,  $\theta_0 = 15.2^\circ$ ,  $\psi = 90^\circ$ ,  $\omega_0^2 c/g = 0.69$ ,  $d^* = 1.28$ ,  $a_0/h_0 = 0.238$ .

Grid	$N_c$	$n/T$	$CFL_{max}$
A	849994	2540	16.5

Figure 6.11 shows a sequence of snapshots of the instantaneous vorticity and velocity fields for this test case ( $h_0/c = 0.6$ ,  $\theta_0 = 15.2^\circ$ ,  $\psi = 90^\circ$ ,  $\omega_0^2 c/g = 0.69$ ,  $d^* = 1.28$ ,  $a_0/h_0 = 0.238$ ) at quarter cycle instant increments.

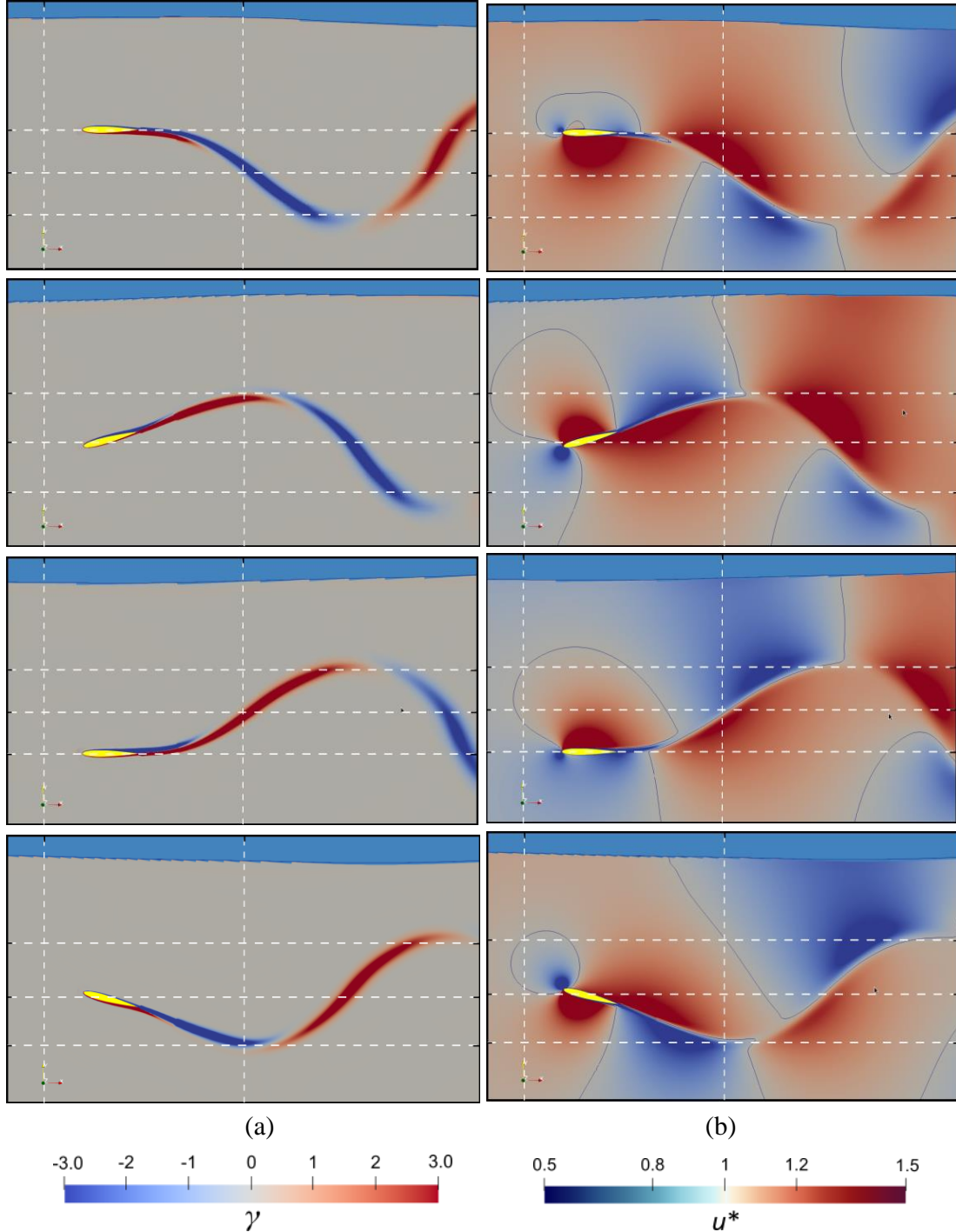


Figure 6.11: Snapshots of (a) vorticity and (b) normalized velocity fields contours at cycle increments of  $t/T = 1/4$  where  $T = 1/f$ , for a single foil in incident waves with motion and wave parameters  $h_0/c = 0.6$ ,  $\theta_0 = 15.2^\circ$ ,  $\psi = 90^\circ$ ,  $\omega_0^2 c/g = 0.69$ ,  $d^* = 1.28$ ,  $a_0/h_0 = 0.238$ . Clockwise vorticity is indicated with blue, and anticlockwise with red. In all figures, the vertical lines show the location of 1/3 point pitching axis of the foils. The horizontal lines show the mid foil position and the upper and lower limits of heave motion. A video of the vorticity field can be found in the on-line supplementary materials listed in the Appendix H and is entitled ‘Single Foil in Waves’.

If compared with the previous test cases, it shows that the primary vortices are now elongated and close to the wake midline and the reverse BvK wake street is not well defined. This can be explained because of the higher values of the Froude number, small heave amplitude and very small wave amplitude. This corresponds to the lower limits of propulsion regime addressed in Section 3.2.1, i.e., a low performance case. In the velocity field snapshots, it becomes possible that the orbital wave velocity, with its negative and positive areas (see the travelling red and blue areas near the free-surface), mixes with the velocity field of the wake, reinforcing ( $t/T = 0$ ,  $t/T = 0.75$ ) and weakening ( $t/T = 0.25$ ,  $t/T = 0.5$ ) the jet behind the foil.

Figure 6.12 shows the instantaneous thrust, vertical and moment coefficients. The time instant of the Figure 6.11 snapshots are indicated. Table 6.12 presents a comparison between CFD model results with the semi-analytical model and FLUENT (Silva et al., 2012) results studied in Section 3.2.2.

CFD model results compare well with FLUENT data, with differences of 12% for average thrust coefficient and 21% for propulsive efficiency that might be explained by the different settings of the two methods. The higher discrepancies in the propulsive efficiency are expected, due to the cumulative error in the vertical and moment coefficients. The semi-analytical model over-estimates the values as seen in Section 3.2.2.

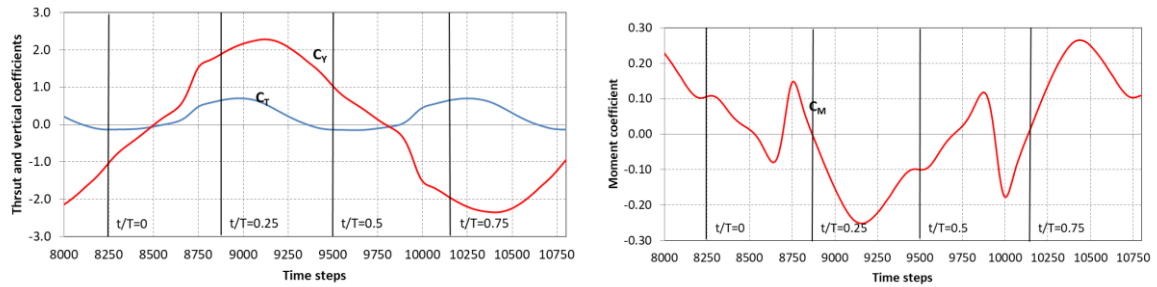


Figure 6.12: (a) Thrust and vertical and (b) moment coefficients instantaneous values for the forward foil and aft foil in tandem test case. The four time instants marked correspond to the snapshots of Figure 6.11  $t/T = 0, 0.25, 0.5, 0.75$ . Motion and wave parameters  $h_0/c = 0.6$ ,  $\theta_0 = 15.2^\circ$ ,  $\psi = 90^\circ$ ,  $\omega_0^2 c/g = 0.69$ ,  $d^* = 1.28$ ,  $a_0/h_0 = 0.238$ .

Table 6.12: Comparison of the average thrust coefficients results between the CFD, semi-analytical models and FLUENT results from Silva et al. (2012). Motion and wave parameters  $h_0/c = 0.6$ ,  $\theta_0 = 15.2^\circ$ ,  $\psi = 90^\circ$ ,  $\omega_0^2 c/g = 0.69$ ,  $d^* = 1.28$ ,  $a_0/h_0 = 0.238$ .

Method	$\bar{C}_T$	$\eta_p$ [%]
CFD model	0.24	49.8
Semi Analytical model	0.31	91.3
FLUENT (Silva et al., 2012)	0.27	69.1

Figure 6.13 shows the eddy viscosity ratio for this case, with low turbulence, explained by low Reynolds. As mentioned before in Section 6.1.1, the turbulence near the surface is of numerical origin due to VOF poor accuracy.

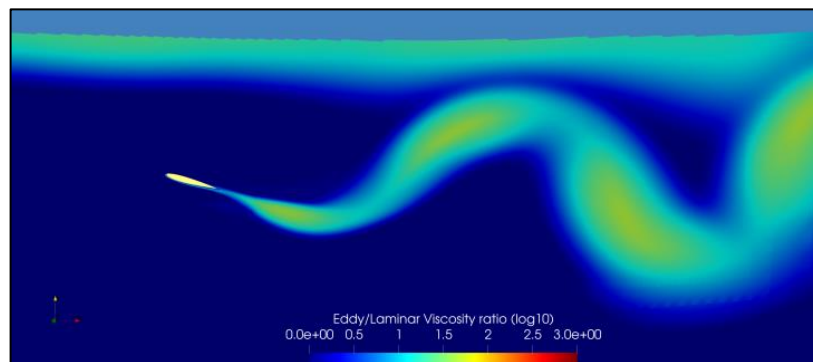


Figure 6.13: Eddy viscosity ratio (log scale) for the single foil in incident waves case. Motion and wave parameters  $h_0/c = 0.6$ ,  $\theta_0 = 15.2^\circ$ ,  $\psi = 90^\circ$ ,  $\omega_0^2 c/g = 0.69$ ,  $d^* = 1.28$ ,  $a_0/h_0 = 0.238$ . Laminar flow in blue and turbulent flow in red.

## 6.2 Tandem Foils

### 6.2.1 Free-Surface

In this section, the tandem configuration of submerged oscillating NACA0012 foils is numerically studied to understand the effects of the presence of a free-surface on the propulsive performance. For the current study we select a set of motion and tandem parameters to allow comparison with the results of the tandem in an infinite domain in Section 5.2.2. In this simulation fore and aft foil leading edges with the same chord length  $c$  are placed at origin and  $5c$  (i.e.,  $4c$  separation distance), respectively, within a 2D computational domain. The inlet and outlet boundaries are at a distance of  $20c$  and  $50c$  from the origin. An inflow condition is prescribed at the inlet with a freestream velocity of  $F_r = 0.32$  while an outflow condition is satisfied at the outlet. The top and bottom boundaries are at  $20c$  and  $50c$  where pressure and slip boundary conditions are imposed respectively. Symmetry conditions are placed at the sides and a non-slip condition is imposed at the foil surface. The flow passing the foil has a Reynolds number  $Re = 40\,000$ . For the numerical settings, time integration uses the implicit second-order scheme, iterative error criteria is set to  $L_\infty = 10^{-4}$ , and momentum discretization uses the second-order scheme. The turbulence model was used. The motion handling uses deforming grid method, with deformation adjusted to  $2c$ . A free-surface equation is used to prescribe the submergence at  $d^* = 1.25$ . Wave absorption is set within a range of  $3c$  from both inlet and outlet, with a cosine absorption function. Both fore and aft foils motion parameters are the same, denoted by  $i = f, a$  respectively. The non-dimensional frequency of oscillation, the Strouhal number is set to  $St = 0.4$ . The phase difference between the heaving and the pitching motion is selected to be  $\psi_i = 90^\circ$ . The heaving and pitching amplitudes are  $h_{oi}/c = 1.0$  and  $\theta_{oi} = 41.5^\circ$  (i.e., an approximately maximum AoA of  $10^\circ$ ), respectively. The inter-foil phase lag  $\phi_t = 180^\circ$  is selected for a case with high-performance, so the positive interference of the wakes can be analysed. The motion parameters are shown in Table 6.13. Grid sub-region refinement around the foil is performed and the number of cells, time step for this simulation and the calculated maximum CFL number can be found in Table 6.14.

Table 6.13: Simulation parameters for the submerged tandem foil test case.

Parameter	Value
Inflow velocity, $U$	1 m/s
Chord, $c$	1 m
Pitching axis, $b^*$	1/3-point
Heave amplitude, $h_o$	1.0 m
Pitch amplitude, $\theta_o$	$41.5^\circ$ ( $\alpha_0 \approx 10^\circ$ )
Heave-pitch phase, $\psi$	$90^\circ$
Period, $T$	5.0 s ( $S_r = 0.4$ )
Submergence, $d$	1.25 m
Foil separation, $s$	4 m
Inter-foil phase lag, $\phi_t$	$180^\circ$
Reynolds number, $Re$	40 000

Table 6.14: Simulation parameter details: total number of cells  $N_c$ , number of timesteps per period  $n_r/T$ , and  $CFL_{max}$ . Motion parameters  $h_o/c_i = 1.0$ ,  $\alpha_{oi} = 10^\circ$ ,  $\psi_i = 90^\circ$ ,  $St = 0.4$ ,  $d^* = 2.5$ ,  $s^* = 8$ ,  $\phi_{ti} = 180^\circ$ .

Grid	$N_c$	$n_r/T$	$CFL_{max}$	$y^+_{max}$
A	529994	8333	2.2	0.21

Figure 6.14 shows a sequence of snapshots of the instantaneous vorticity and velocity fields for this test case ( $h_o/c_i = 1.0$ ,  $\alpha_{oi} = 10^\circ$ ,  $\psi_i = 90^\circ$ ,  $St = 0.4$ ,  $d^* = 2.5$ ,  $s^* = 8$ ,  $\phi_{ti} = 180^\circ$ .) at quarter cycle instant increments. It is possible to see in Figure 6.14 that the fore foil wake dynamics follows the same pattern that the submerged single foil in Section 6.1.1, with primary leading edge vortices shed at the heave maximum amplitude, creating a clear reversed BvK wake street, and smaller secondary elongated trailing edge vortices are shed in the opposite side of the street. The difference here to an oscillating foil in infinite domain, as stated before, is that the interaction of the fore foil with the free-surface in the end of the upstroke,

causes the increase of the positive pressure on the lower surface of the foil, augmenting the positive vorticity and resulting in the shedding of a stronger counterclockwise leading edge vortex  $LEV_{f+}$  (colour in red). Regarding the interaction of the two foils, in this high-performance case, the aft foil is weaving in between the primary vortices that are shed from the fore foil, observed at  $t/T=0.25$ . The aft foil have the same dynamics as the fore foil, but its vortices are stronger and become interspersed with the fore foil vortices, distant enough to not become coupled, forming vertically pairs and creating a double reversed BvK street. This creates a faster velocity behind the foils than the single foil case, which accounts for the higher thrust.

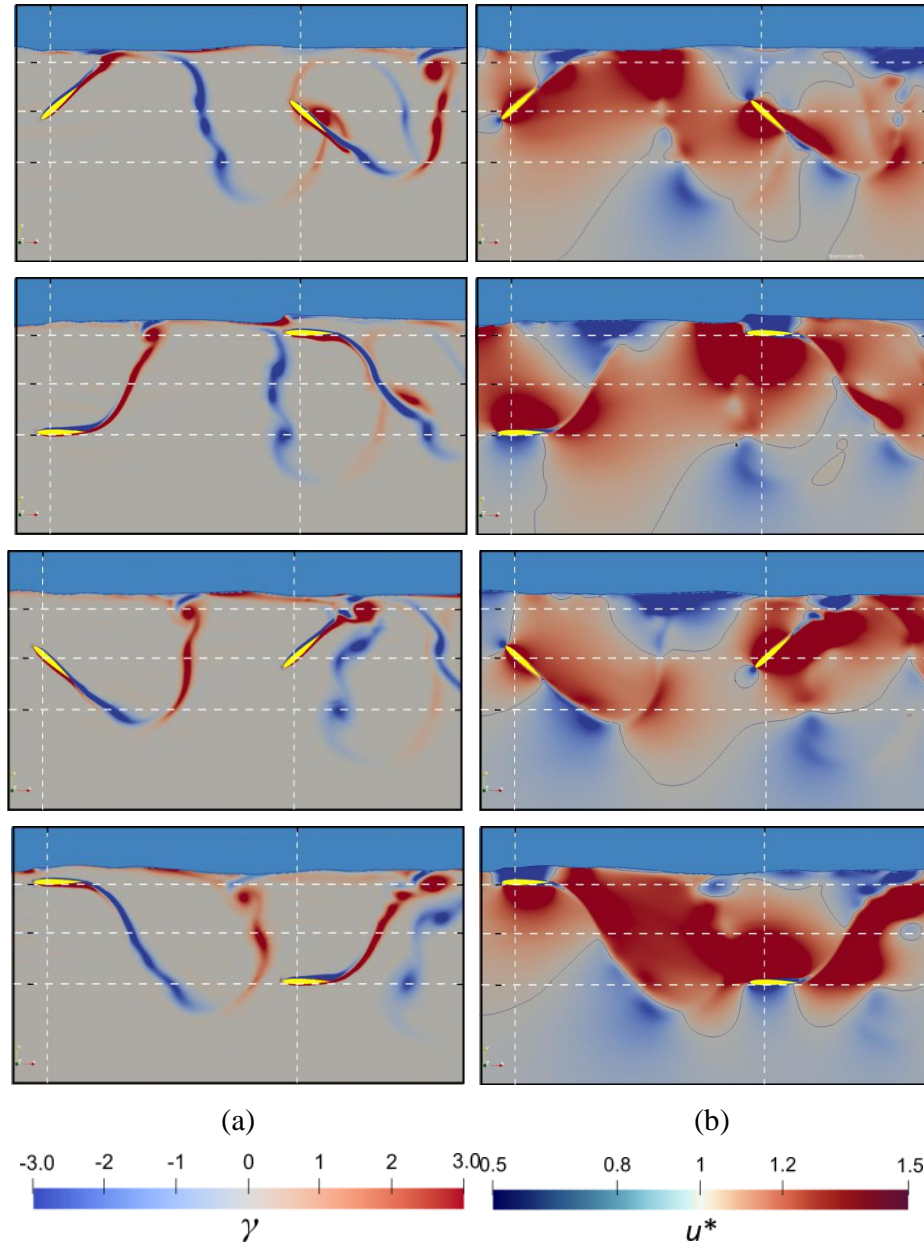


Figure 6.14: Snapshots of (a) vorticity and (b) normalized velocity fields contours at cycle increments of  $t/T = 1/4$  where  $T = 1/f$ , for a tandem foil in large oscillations with motion parameters  $h_0/c_i = 1.0$ ,  $\alpha_{0i} = 10^\circ$ ,  $\psi_i = 90^\circ$ ,  $St = 0.4$ ,  $d^* = 2.5$ ,  $s^* = 8$ ,  $\phi_r = 180^\circ$ . Clockwise vorticity is indicated with blue, and anticlockwise with red. In all figures, the vertical lines show the location of 1/3 point pitching axis of the foils, and the horizontal lines show the mid foil position and the upper and lower limits of heave motion. A video of the vorticity field can be found in the on-line supplementary materials listed in the Appendix H and is entitled ‘Tandem Foil with Free-Surface’.

To explain the vortex dynamics of the aft foil, at  $t/T = 0.25$ , it is possible to observe the clockwise leading vortex  $LEV_{f-}$  (blue in colour) at the lowest foil position and the elongated trailing edge vortex  $TEV_{f-}$  (blue in colour) shed by the upstroke of the previous cycle. Between  $t/T = 0.25$  and  $t/T = 0.5$  the  $TEV_{f-}$  couples favourably with the leading edge vortex  $LEV_{a+}$  (red in colour) that is convecting along the lower surface of the aft foil, supplying vorticity,

resulting in the formation of  $LEV_{a+}$ , which has a larger strength compared to  $LEV_{a+}$  of the single foil. This larger  $LEV_{a+}$ , which is spread throughout the lower surface of the aft foil, leads to higher suction pressure and thrust augmentation ( $t/T = 0.75$ ). With progress in time, the aft foil undergoes upstroke motion where a similar vortex interaction is observed for reversed sign of vorticity. Concerning the velocity field snapshots, by comparing the tandem with free-surface and in infinite domain in Section 5.2.2, we observe that the jet velocity behind the fore foil is little affected but becomes flattened on top side. The main result of the free-surface is that the wake, relative to its midline, becomes asymmetrical.

Figure 6.15 shows the instantaneous thrust, vertical and moment coefficients for both fore and aft foils. The time instant of the Figure 6.14 snapshots are indicated. It is possible to see the augmentation of the aft thrust coefficient relatively to the fore foil, especially in the aft foil upstroke ( $t/T=0$  to  $t/T=0.25$ ). Table 6.15 presents the results for the average thrust coefficient for the fore, aft foils and total tandem and compares it with results of the tandem foil in infinite domain studied in Section 5.2.2 as well as the results of the semi-analytical model. The fore foil presents a decrease in thrust of 6% while the aft foil thrust reduces 15%. This indicates that part of the augmentation in thrust gained by the aft foil is being lost in wave radiation. The semi-analytical model presents discrepancies of 9.4%.

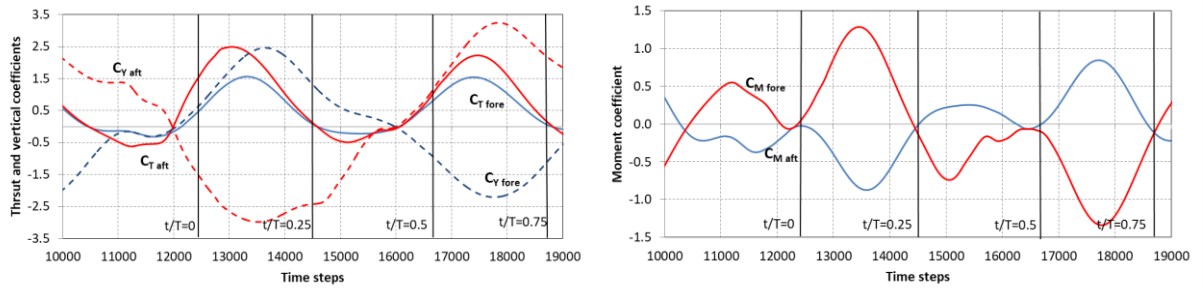


Figure 6.15. (a) Thrust and vertical and (b) moment coefficients instantaneous values for the forward foil and aft foil in submerged tandem test case. The four time instants marked correspond to the snapshots of Figure 6.14  $t/T = 0, 0.25, 0.5, 0.75$ . Motion parameters  $h_0/c_i = 1.0, \alpha_{0i} = 10^\circ, \psi_i = 90^\circ, St = 0.4, d^* = 2.5, s^* = 8, \phi_i = 180^\circ$ .

Table 6.15: Results of the average thrust coefficient for the fore, aft and tandem foil. Motion parameters  $h_0/c_i = 1.0, \alpha_{0i} = 10^\circ, \psi_i = 90^\circ, St = 0.4, d^* = 2.5, s^* = 8, \phi_i = 180^\circ$ .

Method	Case	$\bar{C}_T$		
		Fore foil	Aft foil	Tandem foil
CFD model	Free-surface	0.48	0.74	1.22
	Infinite domain (Section 5.2.2)	0.51	0.87	1.37
Semi-Analytical model	Free-surface	0.45	0.67	1.12

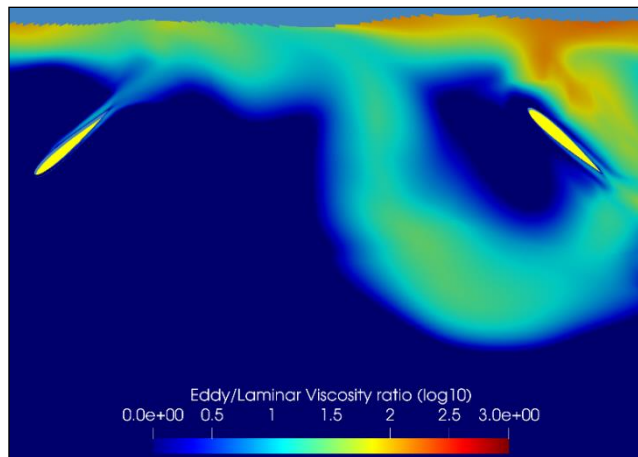


Figure 6.16: Eddy viscosity ratio (log scale) for the submerged tandem foil case. Motion parameters  $h_0/c_i = 1.0, \alpha_{0i} = 10^\circ, \psi_i = 90^\circ, St = 0.4, d^* = 2.5, s^* = 8, \phi_i = 180^\circ$ . Laminar flow in blue and turbulent flow in red.

Figure 6.16 shows the eddy viscosity ratio, where turbulence is relatively low in both wake and boundary layer. As explained before in Section 6.1.1, the turbulence near the surface is of numerical origin due to VOF poor accuracy.

## 6.2.2 Incident Waves

In this section we numerically study the tandem configuration of oscillating 2D NACA0012 profiles with a heading incident wave to understand the effects of the wave on the propulsive performance. This test case is the key engineering application of the active oscillating tandem foil propulsor, in the open sea. There are almost no published studies on this case. Therefore, since the focus of the thesis is on the modelling tools development, here we present a typical demonstrative case, and a preliminary discussion of the physical phenomena involved, leaving a thorough investigation of this case for future work. The computational domain and boundary conditions are the same as in the previous section. A wave boundary condition is prescribed at the inlet for wave generation and freestream velocity of  $F_r = 0.39$ . The flow passing the foil has a Reynolds number  $Re = 4e4$ . Concerning the numerical settings, time integration uses the implicit second-order scheme, iterative error criteria is set to  $L_{\infty} = 10^{-4}$ , and momentum discretization uses a second-order scheme. The turbulence model is used. The motion handling uses the deforming grid method, with deformation adjusted to  $2c$ . A free-surface equation with a Refrics discretization scheme is used for faster convergence. Both fore and aft foils motion parameters are the same, denoted by  $i = f, a$  respectively. The non-dimensional frequency of flapping is equal to encounter frequency  $\omega_0^2 c/g = 0.24$ . The phase difference between the heaving and the pitching motion is selected as  $\psi_i = 90^\circ$ . The heaving amplitude and extended feathering parameter are  $h_{oi}/c = 1.0$  and  $\chi_{oi} = 0.41$ , respectively. The inter-foil phase lag  $\phi_t = 180^\circ$  is selected following the case with high-performance in an infinite domain so the positive interference of the wakes can be studied. The submergence is set at  $d^* = 2.5$ , the heading wave generation to wave amplitude  $a_0/h_0 = 0.75$  m, wave period  $T_w = 1.51$  s, and wave-heave phase  $\phi_w = -90^\circ$ . The wave and motion parameters are shown in Table 6.16. The number of cells, time step for this simulation and the calculated maximum CFL number can be found in Table 6.17.

Table 6.16: Simulation parameters for the tandem foil in waves test case.

Parameter	Value
Inflow velocity, $U$	0.38 m/s
Chord, $c$	0.1 m
Pitching axis, $b^*$	1/3-point
Heave amplitude, $h_{oi}$	0.1 m
Pitch amplitude, $\theta_{oi}$	$35^\circ$
Heave-pitch phase, $\psi_i$	$90^\circ$
Oscillating period, $T$	1.30 s
Submergence, $d$	0.25 m
Foil separation, $s$	0.4 m
Inter-foil phase lag, $\phi_t$	$180^\circ$
Wave amplitude, $a_0$	0.075 m
Wave period, $T_w$	1.51 s
Wave-heave phase, $\phi_w$	$-90^\circ$
Reynolds number, $Re$	40 000

Table 6.17: Simulation parameter details: total number of cells  $N_c$ , number of timesteps per period  $n_r/T$ , and  $CFL_{max}$ . Motion parameters  $h_0/c_i = 1.0$ ,  $\chi_{oi} = 0.41$ ,  $\psi_i = 90^\circ$ ,  $\omega_0^2 c/g = 0.24$ ,  $s^* = 8$ ,  $\phi_t = 180^\circ$ ,  $d^* = 2.5$ ,  $a_0/h_0 = 0.75$ ,  $\phi_w = -90$ .

Grid	$N_c$	$n_r/T$	$CFL_{max}$
A	1030698	2607	31.2

Figure 6.17 shows a sequence of snapshots of the instantaneous vorticity and velocity fields for this test case ( $h_0/c_i = 1.0$ ,  $\chi_{oi} = 0.41$ ,  $\psi_i = 90^\circ$ ,  $\omega_0^2 c/g = 0.24$ ,  $s^* = 8$ ,  $\phi_t = 180^\circ$ ,  $d^* = 2.5$ ,  $a_0/h_0 = 0.75$ ,  $\phi_w = -90$ .) at quarter cycle instant increments. It is possible to observe the

alternating shedding of clockwise and anticlockwise vortices, both primary and secondary, of both fore and aft foils, as seen in previous sections. The key difference here is a significant change in the wake's pattern caused by the orbital wave velocity field. For the fore foil, in the downstroke, the secondary anticlockwise trailing edge vortex  $TEV_{f+}$  (red in colour), visible in  $t/T = 0.75$  and  $t/T = 0$  (previous cycle), with the motion of the wave, is drawn near and absorbed into the primary vortex  $LEV_{f+}$  (red in colour) increasing its strength. On the other side, in the upstroke, the wave causes the separation of the two clockwise vortices, the primary  $LEV_{f-}$  and the secondary  $TEV_{f-}$  (both in blue)  $t/T=0.25$  to  $0.75$ . Thus, the  $TEV_{f-}$  stays between the  $LEV_{f+}$  reducing the jet velocity and the thrust. This creates a pattern of three vortices, instead of the four observed previously. Regarding the interaction of the two foils' wakes, in this case, the aft foil is weaving in between the primary vortices that are shed from the fore foil. However, because of the fore foil wake pattern change, the interaction of vortices become very complex. The interaction of the aft foil  $LEV_{a-}$  (blue) with fore foil  $LEV_{f+}$  (red) seems to cause the dissipation of both, weakening thrust  $t/T = 0.25$  to  $0.75$ . The interaction of the  $LEV_{a+}$  (red) with  $TEV_{f-}$  (blue) appears to strengthen the first, thus increasing thrust.

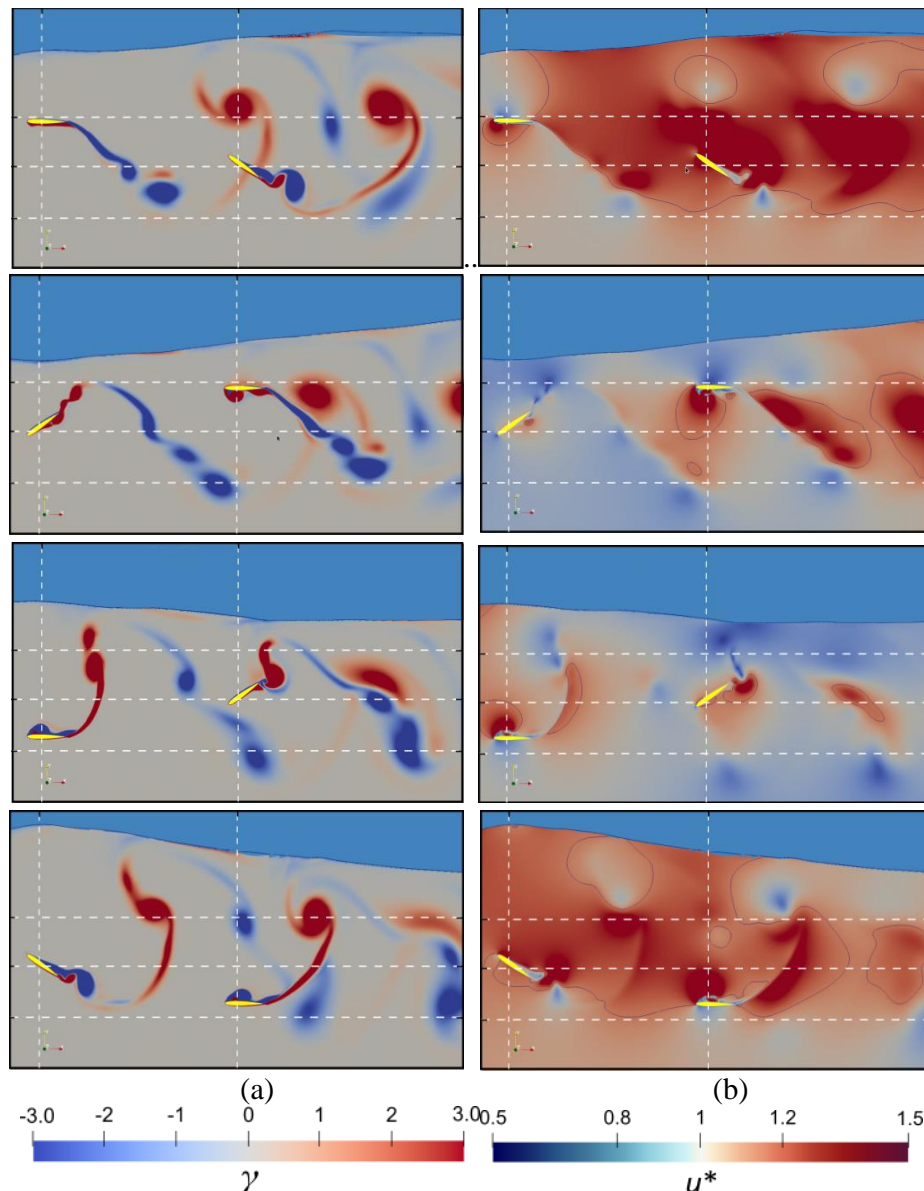


Figure 6.17: Snapshots of (a) vorticity and (b) normalized velocity fields contours at cycle increments of  $t/T = 1/4$  where  $T = 1/f$ , for a tandem foil oscillating in waves with motion parameters  $h_0/c_i = 1.0$ ,  $\chi_{0i} = 0.41$ ,  $\psi_i = 90^\circ$ ,  $\omega_0^2 c/g = 0.24$ ,  $s^* = 8$ ,  $\phi_i = 180^\circ$ ,  $d^* = 2.5$ ,  $a_0/h_o = 0.75$ ,  $\phi_w = -90$ . Clockwise vorticity is indicated with blue, and anticlockwise with red. In all figures, the vertical lines show the location of 1/3-point pitching axis of the foils. The horizontal lines show the mid foil position and the upper and lower limits of heave motion. A video of the vorticity field can be found in the on-line supplementary materials listed in the Appendix H and is entitled ‘Tandem Foil in Waves’.

In the velocity field snapshots, it is visible that the jet velocity behind the fore foil is higher with the crest and lower with the trough, as well asymmetrical. During the most of the rising and downing of the wave crest the velocity behind the aft foil is greatly increased, indicating that, despite the positive and negative interferences of the different vortices just described, the two foils are overall interacting positively.

Figure 6.18 shows the instantaneous thrust, vertical and moment coefficients for both fore and aft foils. The time instant of the Figure 6.17 snapshots are indicated. It is possible to see the augmentation of the aft thrust coefficient relative to the fore foil and the differences in the thrust coefficient in the two parts of the cycle, where from  $t/T=0.5$  to  $0.75$  the thrust becomes significantly negative, because of the effect of the  $TEV_{f-}$ . Given the results, this might be classified as a mid-performance case.

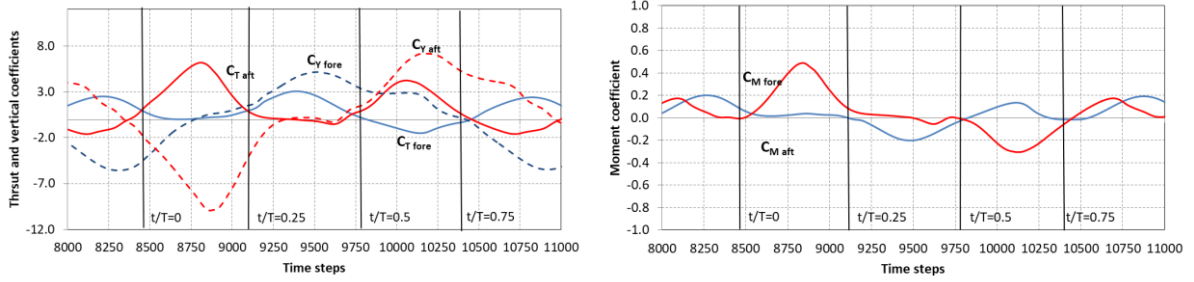


Figure 6.18: (a) Thrust and vertical and (b) moment coefficients instantaneous values for the forward foil and aft foil in tandem in waves test case. The four time instants marked correspond to the snapshots of Figure 6.17  $t/T = 0, 0.25, 0.5, 0.75$ . Motion parameters  $h_0/c_i = 1.0$ ,  $\chi_{0i} = 0.41$ ,  $\psi_i = 90^\circ$ ,  $\omega_0^2 c/g = 0.24$ ,  $s^* = 8$ ,  $\phi_i = 180^\circ$ ,  $d^* = 2.5$ ,  $a_0/h_o = 0.75$ ,  $\phi_w = -90^\circ$ .

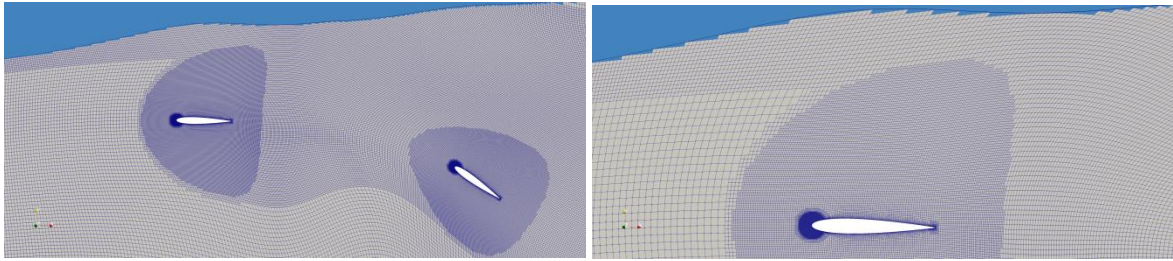


Figure 6.19: Example of grid deformation for the tandem foil in waves (a) general view and (b) detail of the mesh around the aft foil.

Table 6.18: Results of the average thrust coefficient and propulsive efficiency for the fore, aft and tandem foil. Motion and wave parameters  $h_0/c_i = 1.0$ ,  $\chi_{0i} = 0.41$ ,  $\psi_i = 90^\circ$ ,  $\omega_0^2 c/g = 0.24$ ,  $s^* = 8$ ,  $s^* = 8$ ,  $\phi_i = 180^\circ$ ,  $d^* = 2.5$ ,  $a_0/h_o = 0.75$ ,  $\phi_w = -90^\circ$ .

Method		Fore foil	Aft foil	Tandem foil
CFD model	$\bar{C}_T$	0.81	1.43	2.23
	$\eta_p$ [%]	64.7	88.0	67.5
Semi-analytical model	$\bar{C}_T$	1.87	2.65	4.52

Table 6.18 presents the results of the average thrust coefficient and propulsive efficiency for both the numerical and semi-analytical models. Concerning CFD model results, the aft foil presents an increase of 77% and 36% of average thrust and propulsive efficiency, respectively, when compared with the fore foil. The total tandem foil configuration, when compared with the single/fore foil has mean thrust values 2.75 times higher and presents an increase of 4.3% in propulsive efficiency. Although no V&V procedures were done, higher discrepancies in the propulsive efficiency are expected, due to the cumulative error in the vertical and moment coefficients, but the configuration seems very promising. The semi-analytical model provides significant discrepancies to the numerical results. The over predictions might be explained by the losses in lift due to the full separation of the flow (see Figure 6.20) that are not accounted in the model. Another reason is the model low accuracy of the free-surface effect for low Froude numbers (here  $F_r = 0.39$ ) already observed in previous sections.

The deformation of the grid is shown in Figure 6.19 where it is possible to have a visual confirmation of the good performance of the deforming grid method used, maintaining the quality of the grid in the critical areas like the foils' leading end trailing edge and foil interspace. Figure 6.20 shows the eddy viscosity ratio, where the flow in the wake is fully turbulent. There is also a clear flow full separation in the boundary layer of the fore foil. It is visible turbulence created near the leading edge of the aft foil, possibly due to a leading edge vortex. As explained before in Section 6.1.1, the turbulence near the surface is of numerical origin due to VOF poor accuracy.

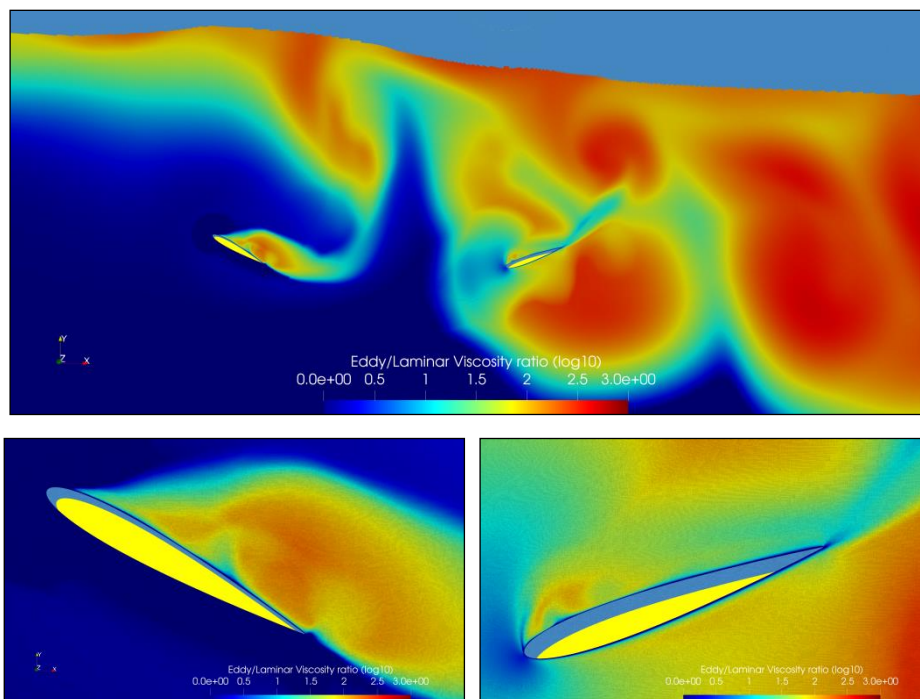


Figure 6.20: Eddy viscosity ratio (log scale) for the tandem foil case in waves. (a) general view (b) detail of the fore foil (c) and detail on the aft foil. Motion and wave parameters  $h_0/c_i = 1.0$ ,  $\chi_{0i} = 0.41$ ,  $\psi_i = 90^\circ$ ,  $\omega_0^2 c/g = 0.24$ ,  $s^* = 8$ ,  $\phi_t = 180^\circ$ ,  $d^* = 2.5$ ,  $a_0/h_o = 0.75$ ,  $\phi_w = -90^\circ$ . Laminar flow in blue and turbulent flow in red.

# Chapter 7

## Conclusions

### 7.1 Main Conclusions

#### 7.1.1 Introduction

The main aim of this thesis was to contribute to the development of automated surface vehicles propulsion on waves. Two configurations were considered, an active oscillating foil propulsor and an enhancement of this concept using two foils in tandem. Infinite domain, free-surface and incident waves case tests were addressed. The research focused on the investigation and implementation of modelling tools to study these configurations. It proposes using theoretical and numerical models in a complementary manner. Conclusions concern both the adequacy of the models, as well as the flow dynamics and performance of the foil propulsor. Based on the findings several recommendations are given for further research directions.

#### 7.1.2 Semi-Analytical Model

The semi-analytical model developed here is an enhancement of the classical thin wing theory. It started by integrating several analytical unsteady theories with empirical quasi-steady expressions in order to achieve an extensive modelling of the physical phenomena involved. The model was then simplified, considering the parameter's ranges for practical application, providing a simple, fast and intuitive tool to estimate the hydrodynamic forces and explore the parameter space in question. The following results were obtained for the different case models:

- Single foil in infinite domain model: it presents good agreement with the several experimental and numerical results available in the literature. It constitutes a promising development of classical theory models. It presents slope over-predictions of 4% and average coefficient amplitudes discrepancies less than 9% at high AoA up to  $20^\circ$  and Strouhal numbers up to  $St = 0.45$ . The overall results suggest that the model captures with sufficient precision the different effects involved, covering the main operating region of propulsion regime at large heave amplitudes  $h_0/c = 1$  which occupies  $St = 0.20-0.50$  and pitch amplitudes  $\theta_0 = 15^\circ-60^\circ$ , considered satisfactory for the present purpose.
- Free-surface model: it presents a fair-to-good qualitative agreement with the available data, with significant discrepancies for  $F_r < 0.8$  and  $d/c < 1$ , concerning the lift loss caused by the presence of the free-surface. Despite this limitation in accuracy, the model enables a qualitative study of the effects of the free-surface.
- Wave model: It has a visible qualitative good agreement with CFD numerical and experimental published results, presenting fair-to-good discrepancies around 7% to 20%. Despite its limitations in accuracy, if compared with other methods, linear theory, non-linear, numerical and experimental, it presented visible good results, surpassing non-

linear methods. Because the difficulty in obtaining accurate results, both due to the technical difficulties of the experiment and the challenge of modelling such complex physical phenomena is still an actual challenge not much explored. The discrepancies in the model might be explained by the alterations of the wake pattern caused by the orbital velocity field of the wave. These pattern changes are not captured by the theory used in this work. Once again, the present method is considered capable of providing valid predictions, capturing the main aspects of the oscillating foils in incident waves. The computational cost of this method makes this approach quite competitive and efficient, especially for initial design, optimization and active control development.

- Tandem foil model: An innovative analytical model was proposed in this work, by extending the classical formulation of Newman (1978) to include the effects of the two foil wake's interaction. The model provides a promising good agreement with extensive results of the aft foil average thrust coefficient obtained by Muscutt et al. (2017) using CFD, indicating that the model captures well the motion frequency, separation distance, and inter-foil lag variation. It shows discrepancies around 5% in the majority of the range studied but have visible limitations for low frequencies and separation values.

The semi-analytical model provides an innovative tool with sufficient precision in almost the entire range of applications, suitable for use in engineering design and optimization. It presents simulation times less than one minute for the most complex test cases, using a personal computer, while for the same test cases the CFD model calculations can last up to 10 days using the *Iridis5* supercomputer. The semi-analytical model allows identifying the main relevant parameters and response curves, as well as cases of interest. In particular it can be coupled with parameter optimization tools, to perform parameter sensitivity analysis and provide input for CFD modelling and experimental tests.

### 7.1.3 CFD Numerical Model

For the numerical modelling we used the CFD code ReFRESKO, a tested and resourceful tool that uses RANS to achieve high accuracy and allows flow dynamics visualization. In particular, a deforming grid method is used for body motion modelling, enabling the simulation of cases with large motions. Turbulence, free-surface and wave models provided in ReFRESKO are employed. Background information on the application of CFD techniques to this hydrodynamic problem was addressed, discussing the governing equations of fluid flow, their Reynolds averaging, the rigid body motions and wave models, and numerical solving schemes. In face of the range of Reynolds numbers, the flow was considered turbulent, thus a turbulence model is included. For verification & validation, iterative convergence was monitored in terms of residual norms; discretisation errors and exact solutions were estimated using spatial and temporal grid refinement; and statistical error was evaluated with transient scanning. V&V procedures are mainly applied for the infinite domain test cases, while for free-surface and incident wave test cases the focus was on flow dynamics analysis. The conclusions observed for the different settings of the numerical simulations are:

- Grid and numerical settings: Both structured and unstructured types of grid, for the simple case of a single foil in infinite domain, produced very similar results, with differences of 3% in thrust and vertical coefficients and 7% in moment coefficient. Hexpress unstructured grid generator software was found to be a suitable tool for this type of study. In all the grids used, in terms of quality, the skewness is higher than 0.2 only for 0.5% of the total number of cells, with no concave or deformed cells. Viscous sub-layers were found to be necessary to improve accuracy. Domain dimensions were set  $50c$  distant from the foil, found enough to avoid reflections on the boundaries, especially top, bottom and outlet. 3D grids/test cases required a number of cells over 2M, however, have high computational time costs. The setting of the grid deformation radius for the body motion method played an important role for numerical convergence. Deforming radius within the range of  $2c$  to  $4.5c$ , according to the test cases, was found

sufficient to allow a smooth cell deformation and guarantee grid quality. CFL was kept as low as possible, with maximum values ranging from 2 to 30, for the different test cases, by refining the time step, nevertheless looking for a compromise between stability and computational cost.

- **Accuracy:** The infinite norm criteria  $L_\infty < 10^{-4}$  resulted in an iteration error below 0.01%, and a minimum sampling of 4 periods of the statistical converged state allowed achieving statistical errors around 0.05%, for the case with large oscillations. For the 2D single foil in an infinite domain, the discretization error, using 5 to 7 sets with different spatial and temporal refinement, ranged from 6.5% to 7.7%. It is more significant than both the statistical and iteration errors. The estimation of the modelling error, considering the few experimental data available, led to 14.6%. An important outcome of the work is that a general fair-to-good agreement could be observed in the results obtained for both the modelling methods developed, the semi-analytical and the numerical. In particular concerning the estimation of the average thrust coefficient, uncertainties of 6.2% for the single foil at high-performance were achieved. The tandem foil case, also at high-performance, presented discrepancies of 15% between the predictions of the two models. The discrepancies were higher on the aft than on the fore foil, suggesting that further grid refinement should be done near the aft foil.
- **Captured Effects:** The 3D results obtained are in good agreement with the results of the semi-analytical model, presenting a 21% decrease in the mean thrust coefficient for an aspect ratio  $\Lambda = 8$  foil, confirming that the span effect is well captured in this last model. In the cases with free-surface it was noticed numerical eddy viscosity interfering with the results due to VOF poor accuracy. Despite this limitation, in the single foil test case it was found a good agreement in the results between the two types of model, with discrepancies of less than 5%. The effect of span was markedly more relevant than the free-surface effect, with losses in the average thrust of 21.7% and 3.7%, respectively. In the incident wave test case, discrepancies are higher, reaching 12% for mean average thrust, between the present CFD model and the results of Silva et al. (2012). Since only one set was tested in the CFD model, further discretization error investigation would be necessary. Turbulence analysis confirmed that, for the Reynold numbers in this work, this effect was more important in the wake, with low turbulence in the boundary layer for the most of cases studied. It became increasingly turbulent for cases with larger wave or oscillation amplitudes or frequencies. For the scope of this work, it was reasonable to use the  $k-\omega$  SST model but introducing more refined turbulence models may improve the accuracy in future work.

ReFRESKO proved to be highly suitable to investigate the hydrodynamic problem of the wave oscillating foil propulsor. With the CFD model it was possible to do the validation and detailed study of the flow, providing information for further refinement of the semi-analytical model.

#### **7.1.4 Findings Related to Flow Dynamics and Performance**

The analysis of the flow dynamics, namely vorticity and velocity field, for single foil in infinite domain, enabled the observation of the reverse BvK street wake pattern, with two stronger primary leading edge vortices in the oscillating motion extrema, and two secondary elongated and weaker trailing edge vortices closer to wake midline. The first pair is responsible for thrust, with the jet located in the wake periphery, and the second pair contributes for drag, causing a velocity decrease in the wake midline. The maximum magnitude of the forces and moment happens in the second half of the foil stroke cycle, after the primary vortex shedding. High-performance is possible for heave amplitudes of one chord length, and large angles of attack.

The results of the free-surface model suggest that it is possible to identify delimited ranges of advance velocity values where the lift loss has significant maxima. The model also identified two regimes of wave radiation for the oscillating foil. One is below a critical velocity, where waves propagate behind and in front of the foil, and the other one is above this critical value where there are only waves behind the foil. For the practical application ranges, the wave resistance appears to be relevant only for velocities near the critical value.

In agreement with the conclusions of Silva et al. (2012), we verified that the problem of the oscillating foil in waves has some different features than the foil in an infinite domain. One of the main findings of this work is that, for the foil in waves, there is a significant pattern change in the wake caused by the orbital wave velocity field. For the high amplitude test case studied, a wake pattern of three vortices is created, instead of four, as we previously observed. One of primary vortices is strengthened by absorbing one of the secondary vortices, and the other secondary vortex becomes more defined. This creates unevenness in the wake, reinforcing thrust in one stroke and drag in the other. Another main conclusion is that the semi-analytical model of the foil in an infinite domain can be applied directly to the case of incident waves by replacing the non-dimensional heave amplitude with the proposed non-dimensional wave heave amplitude that accounts for the incident wave parameters.

In the case of the tandem foil in infinite domain, the effect of the aft foil in the fore foil was found to be negligible in this range, which allows the fore foil to be modelled as a single foil, and the total hydrodynamic forces of the tandem foil to be calculated by the linear combination of both fore and aft solutions. It was found that high-performance happens when the primary vortices of the aft foil become interspersed with the vortices shed from the fore foil, forming vertically pairs and creating a double reversed BvK street. This is achieved when the aft foil is weaving in between the primary vortices shed by the fore foil, especially when the aft foil collides favourably with the secondary vortices shed by the fore foil, strengthening aft foil primary vortices and repositioning of the fore secondary vortices.

The main findings on performance per test case were:

- A promising high-performance configuration for the single foil in infinite domain propulsor was observed, selecting a trade-off between thrust and efficiency, at AoA amplitudes of  $20^\circ$  and  $St = 0.5$ . For these parameters, values of propulsive efficiency  $\eta_p$  of 60% and swept area mean thrust coefficient  $\bar{C}_{TSA}$  of 0.6 ( $\bar{C}_{TSA} = -F_x/\rho U^2 h_0$ ) can be achieved. With this setting the oscillating foil propulsor compares with the standard screw propeller that can achieve efficiencies in the range 65–75% for thrust coefficients in the range 0.25–0.75 (Epps et al., 2016). The viscous effect was found to be negligible, and the separation to play a significant role for AoA  $> 15^\circ$ .
- With incident waves, since wave orbital vertical velocities, if properly tuned, add to heave velocities, higher mean thrust coefficients are possible. Thrust increases up to 20% are achieved even with small amplitude waves ( $a_0/h_0 = 0.75$ ) for heading waves with wave-heave phase  $\phi_w = 180^\circ$ . The energy absorbed from the wave allows propulsive efficiency augmentation. To obtain higher efficiencies and not relinquish thrust, trade-off parameter values have to be carefully chosen. For the case studied, heave-pitch phase of  $40^\circ$  and extended feathering parameter of 0.2, with  $h_0/c = 0.6$  and  $a_0/h_0 = 0.24$  waves, result in  $\eta_p$  of 70% and swept area mean thrust coefficient  $\bar{C}_{TSA}$  of 0.33, comparable with the range of values of the standard screw propeller mentioned before (Epps et al., 2016).
- In the tandem foil in infinite domain, the aft foil thrust force is highly dependent on both inter-foil phase lag and separation. The contours in this parameter space have a pattern of diagonal bands of high and low thrust, forming parallel ‘ridges’ and ‘valleys’ caused by the wake interaction. In the same way the propulsive efficiency of the aft foil follows the same pattern. For each frequency the thrust can be again optimized in terms of foils distance separation with two main favourable ranges,  $1.5c$  to  $2.5c$ , and  $3.5c$  to  $4.5c$ . In terms of tandem performance, increases of 185% are found in the average thrust for the aft foil, for  $St = 0.2$ ,  $s^* = 6$  and inter-foil phase lag  $\phi_t = 90^\circ$ , showing the possibility to have in the total tandem foil almost the triple of a single foil thrust. Because the single foil highest thrust performances are at different frequencies ( $St = 0.5$ ), compromises should be sought between single foil performance and fore-aft wake interaction

performance. The results seems promising when compared with the best high-performance case for a single foil found in Section 3.2.1 ( $h_o/c = 1.0$ ,  $AoA_{max} = 20^\circ$ ,  $St = 0.5$ ) where the tandem presents propulsive efficiency 80.1 % and  $\bar{C}_{TSA} = 0.69$  against 60% and  $\bar{C}_{TSA} = 0.6$ .

- The case of the tandem foil in waves showed very promising results. A high-performance configuration, based on the previous test case in an infinite domain, was tested, experiencing increases in thrust, when compared with a single foil, of 2.75 times. It reaches high thrust values of  $\bar{C}_{TSA} = 1.11$  with 67.5% propulsive efficiency. The flow dynamics visualization obtained in this research offers an important contribution to understanding the complexity of wake pattern and vortices interaction. In a preliminary analysis, we can conclude that even better performances might be possible. For example, by making the aft foil collide with the fore secondary vortex, to weaken its effect and or by trying to avoid the unfavourable interaction of the aft secondary foil with fore main primary vortices. This case is remarkably relevant for future studies of practical applications of interest, with almost no published data on the subject.

## 7.2 Future Work

Next steps of research should address further improvement of the semi-analytical model through detailed study of each component. Each physical effect model component needs to be individually investigated and compared with the CFD model, and a thorough a detailed assessment of the errors and limits of the model should be established. Attention must be given to the improvement of vertical forces and moments calculation to allow accurate propulsive efficiency estimation.

Enhancements can be made to the single foil model, by introducing a dynamic stall model (e.g., see the work of Bøckman, 2014), and furthering research to understand the discrepancies identified in the propulsion-drag wake regime transition. Another possible extension is to try to capture the switch from the wake propulsion regime to the deflected regime. One possible idea is to empirically relate the vortex strength with the angle of the jet deflection and estimate the horizontal component of the thrust force. Further development of the tandem model should focus on improving the limitations for low separation and frequencies and might include the estimation of the increase in velocity at the fore foil jet and investigation on the propulsive efficiency prediction.

Moreover, in the CFD model, discretization, iteration, and statistical errors for the cases with free-surface and waves also need to be assessed to obtain a total computation error and uncertainty. Grid refinement near free-surface and the aft foil should be studied. The investigation on the use of more refined turbulence models is also relevant. The problem of numerical turbulence near the free-surface should also be addressed. Further research should address the study of the flow dynamics in cases with waves. Parameter study and optimization are necessary for a better understanding of this hydrodynamic problem in order to allow optimization strategies for obtaining higher performances.

Finally, the next step to the development of this concept is the modelling of a passive-type wave foil propulsor integrated in a vessel. That entails the research on the coupling of the semi-analytical model with the spring control system. In particular the study of the active foil in incident waves, both single and tandem foil, can help to identify optimal performance cases, which can be used as reference for the system control design. To integrate with vessel ship, dynamics studies are necessary. Another important study is the application to irregular waves to assess its effect on the modelling and performance. These investigations need to be made in parallel with the CFD model.



# References

- Abramowitz and Stegun 1972. *Handbook of Mathematical Functions with Formulas, Graphs, and Mathematical Tables*.
- Akhtar, I., Mittal, R., Lauder, G.V. and Drucker, E. 2007. Hydrodynamics of a biologically inspired tandem flapping foil configuration. *Theoretical and Computational Fluid Dynamics*, 21, 155–170.
- Alexander, D. E. 1984 Unusual phase relationships between the forewings and hindwings in flying dragonflies. *Journal Exp. Biol.*, 109, 379-383.
- Anderson, J., Streitlien, K., Barrett, D. and Triantafyllou, M. 1998. Oscillating foils of high propulsive efficiency. *Journal of Fluid Mechanics*, 360, 41–72.
- Anon 1983. Wave power for ship propulsion. *The Motor Ship*, 64 (757), 67-69.
- Ashraf, M. A., Young, J., Lai J. C. S. and Platzer, M. F. 2011. Numerical Analysis of an Oscillating-Wing Wind and Hydropower Generator. *AIAA Journal*, 49 (7), 1374-1386.
- AutoNaut Ltd 2021. *AutoNaut*. ([www.autonautusv.com](http://www.autonautusv.com)) (Accessed August 2021).
- Balay, S., Abhyankar, S., Adams, M.F., Brown, J., Brune, P., Buschelman, K., Dalcin, L., Dener, A., Eijkhout, V., Gropp, W.D., Karpseyev, D., Kaushik, D., Knepley, M.G., May, D.A., McInnes, L.C., Mills, R.T., Munson, T., Rupp, K., Sanan, P., Smith, B.F., Zampini, S., Zhang, H. and Zhang, H. 2020. *PETSc User's Manual*. Technical Report ANL-95/11 Revision 3.13, Argonne National Laboratory.
- Belibassakis, K.A., Politis, G.K. and Triantafyllou, M.S., 1997. Application of the Vortex Lattice Method to the propulsive performance of a pair of oscillating wing-tails. *Proceedings of Eighth International Conference on Comp. Methods and Experimental Measurements*, CMEM'97, Rhodes, Greece.
- Belibassakis, K.A. 2011. A panel method based on vorticity distribution for the calculation of free surface flows around ship hull configurations with lifting bodies. *Sustain. Marit. Trans. Exploit. Sea Resour.*, 79 (86), 79–86.
- Belibassakis, K.A. and Politis, G.K. 2013. Hydrodynamic performance of flapping wings for augmenting ship propulsion in waves. *Ocean Eng.*, 72, 227–240.
- Belibassakis, K.A. and Filippas, E.S. 2015. Ship propulsion in waves by actively controlled flapping foils. *Appl. Ocean Res.*, 52, 1–11.
- Berg, A. 1985. Trials with passive foil propulsion on M/S "Kystfangst". *Project no. 672.138*. Fiskeriteknologisk Forskningsinstitutt, Trondheim, Norway.
- Boer A., Zuijlen V.H., Bijl H. 2009. Radial Basis Functions for Interface Interpolation and Mesh Deformation. *Advanced Computational Methods in Science and Engineering*, 143-178.
- Boschitsch, B.M., Dewey, P.A. and Smits, A.J. 2014. Propulsive performance of unsteady tandem hydrofoils in an in-line configuration. *Physics of Fluids*, 26, 131-139.

- Bose, N. and Lien, J. 1990. Energy absorption from ocean waves: a free ride for cetaceans. *Proceedings of the Royal Society of London. B. Biological Sciences*, 240 (1299), 591-605.
- Bose, N. 1992. A time-domain panel method for analysis of foils in unsteady motion as oscillating propulsors. *Proceedings of the 11th Australian Fluid Mechanics Conference*, University of Tasmania, Hobart, 1201–1204.
- Bøckmann, E. and Steen, S. 2013. The effect of a fixed foil on ship propulsion and motions. *Proceedings of the Third International Symposium on Marine Propulsors*, 553–561.
- Bøckmann, E. and Steen, S. 2014. Experiments with actively pitch-controlled and springloaded oscillating foils. *Appl. Ocean Res.*, 48, 227–235.
- Bøckmann, E. 2015. *Wave propulsion of ships*, PhD thesis, Norwegian University of Science and Technology, Trondheim, Norway.
- Bøckmann, E. and Steen, S., 2016. Model test and simulation of a ship with wavefoils. *Appl. Ocean Res.*, 57, 8–18.
- Bowker, J.A., Townsend N.C., Tan M. and Sheno R.A. 2015. Experimental study of a wave energy scavenging system onboard autonomous surface vessels (ASVs). *Proceeding of OCEANS 2015*, Genova.
- Broering, T.M. & Lian, Y. 2010 Numerical investigation of energy extraction in a tandem flapping wing configuration. *48th AIAA Aerospace Sciences Meeting*.
- Broering, T.M., Lian, Y. and Henshaw, W. 2012. Numerical study of two flapping airfoils in tandem configuration. *AIAA Journal*, 50, 2295-2307.
- Brouwer, J., Tukker, J.C., Rijsbergen, M. 2013. Uncertainty Analysis of Finite Length Time Measurement Signals. *3rd International Conference on Advanced Model Measurement Technologies for the EU Maritime Industry*
- Brouwer, J., Tukker, J.C., Rijsbergen, M. 2015. Uncertainty Analysis and Stationarity Test of Finite Length Time Series Signals. *AMT'15 4th International Conference on Advanced Model Measurement Technologies for the Maritime Industry*, 28 - 30
- Brouwer, J., Tukker, J.C., Klinkenberg, Y.J., & van Rijsbergen, M. 2019. Random uncertainty of statistical moments in testing: Mean. *Ocean Engineering* ,182, 563-576.
- Caccia, M. & Bono, R. 2005. Design and preliminary sea trials of SESAMO: an autonomous surface vessel for the study and characterization of the air-sea interface, *IEEE ICRA 2005*, 3582-3587.
- Celik, I. & Hu, G. 2004. Single Grid Error Estimation Using Error Transport Equation. *J. of Fluids Engineering*, 126 (5), 778-790.
- Coffey, D. L. 1977. *Dolphins, Whales and Porpoises*. MacMillan Press, New York
- Curcio, J., Leonard, J. & Patrikalakis, A. 2005. SCOUT – A Low Cost Autonomous Surface Platform for Research in Cooperative Autonomy, *MTS/IEEE OCEANS 2005*, 1, 725-729.
- Cibalia Scheepsbouw & Reparatie B.V. 2021. *M/S “Triade”*. (<http://cibalia.nl/onze-projecten/projecten/ms-triade/>) (Accessed September 2021).
- Deng, J., Shao, X.M. and Yu, Z.S. 2007. Hydrodynamic studies of two wavy foils in tandem arrangement. *Physics of Fluids*, 19, 113104.

- Doctors, L.J. 1986. Effects of a finite Froude Number on a supercavitating hydrofoil. *J. of Ship Research*, 30 (1), 1-11.
- Duarte T.M. 2011. Experimental Study of a 2D Hydrofoil for Application in Ocean Mooring Systems. *9th EWTEC conference*, Southampton, England.
- DuCane, P.D. 1972. *High Speed Small Craft*, David & Charles, Newton Abbot.
- Dybdahl, K. 1988. Foilpropellen kan revolusjonere skipsfarten. *Teknisk Ukeblad/Teknikk*, 135 (39):10-11.
- Eça, L. & Hoekstra, M. 2014. A procedure for the estimation of the numerical uncertainty of CFD calculations based on grid refinement studies. *J. of Computational Physics*, 262, 104–130.
- Eça, L., Pereira, F. and Vaz, G. 2018. Viscous flow simulations at high Reynolds numbers without wall functions: Is  $y^+ \approx 1$  enough for the near-wall cells? *Computers & Fluids*, 170.
- Egorov, I.T. & Sokolov, V.T. 1965. *Hydrodynamics of Fast Craft*, In Russian (English translation: NTIS AD A032120, 1976).
- Epps, B.P., Muscutt, L., Roesler, B. and Weymouth, G. 2016 On the Interfoil Spacing and Phase Lag of Tandem Flapping Foil Propulsors. *J. of Ship Production and Design*, 33 (4), 1–7.
- Eloy, C. 2012 Optimal Strouhal number for swimming animals. *J. of Fluid and Structures*, 30, 205-218.
- Faltinsen, O.M. 2005. *Hydrodynamics of High-Speed Marine Vehicles*. Cambridge University Press.
- Fernandes, G., Kapsenberg, G.K., Kerkvliet, M. and Walree, F. van 2016. Towards Accurate Computations of Active Stabiliser Fins, focusing on Dynamic Stall. *15th International Ship Stability Workshop*, 51-58, Stockholm, Sweden
- Ferziger, J.H. & Perić, M. 2002. *Computational Methods for Fluid Dynamics*, 3rd edition. Berlin, Germany. Springer-Verlag.
- Filippas, E.S. & Belibassakis, K.A. 2013. Free surface effects on hydrodynamic analysis of flapping foil thrusters in waves. *Proceedings of the ASME 2013 32nd International Conference on Ocean, Offshore and Arctic Engineering*, 5, Ocean Engineering.
- Filippas, E.S. & Belibassakis, K.A. 2014a. A boundary element method for the hydrodynamic analysis of flapping-foil thrusters operating beneath the free surface and in waves. *Developments in Maritime Transportation and Exploitation of Sea Resources*, 1, 3-11.
- Filippas, E.S. & Belibassakis, K.A. 2014b. Hydrodynamic analysis of flapping foil thrusters operating beneath the free surface and in waves. *Engineering Analysis with Boundary Elements*, 41, 47-59.
- Filippas, E.S., Gerostathis, T.P. and Belibassakis, K.A., 2018. Semi-activated oscillating hydrofoil as a nearshore biomimetic energy system in waves and currents. *Ocean Eng.*, 154, 396–415.
- Fish, F.E. and Hui, C.A. 1991. Dolphin Swimming—A Review. *Mamm. Rev.*, 21,181–195.

- Fish, F.E. 1997. Biological designs for enhanced manoeuvrability: Analysis of marine mammal performance. *10th International Symposium on Unmanned Untethered Submersible Technology*, 10 pp.
- Fish, F.E. 1998. Biomechanical perspective on the origin of cetacean flukes. *The Emergence of Whales: Patterns in the Origin of Cetacea*. J. G. M. Thewissen, ed., 303–324. Plenum Press, New York.
- Floch, F., Phoemsaphawee, S., Laurens and J.M., Leroux, J.B., 2012. Porpoising foil as a propulsion system. *Ocean Eng.*, 39, 53–61.
- Garrick, I.E. 1936. Propulsion of a flapping and oscillating airfoil. *NACA Report No. 567*.
- Geoghegan, J.J., 2008. *Boat, Moved Only by Waves, Sails to a Seafaring First* ([www.nytimes.com/2008/07/08/science/08wave.html](http://www.nytimes.com/2008/07/08/science/08wave.html)) (Accessed July 2022).
- Gong, W.Q., Jia, B.B. and Xi, G. 2015. Experimental study on mean thrust of two plunging wings in tandem. *AIAA Journal*, 53 (6).
- Gong, W.Q., Jia, B.B. and Xi, G. 2016. Experimental study on instantaneous thrust and lift of two plunging wings in tandem. *Experimental Fluids*, 57.
- Godoy-Diana, R., Aider, J. and Wesfreid, J.E. 2008. Transitions in the wake of a flapping foil. *Phys. Rev. E*, 77, 016308.
- Grue, J., Mo, A. and Palm, E. 1988. Propulsion of a foil moving in water waves. *J Fluid Mech*, 186, 393–417.
- Hauge, J. 2013. *Oscillating foil propulsion*, MSc Thesis, Norwegian University of Science and Technology, Trondheim, Norway.
- Hoekstra M. 1999. *Numerical simulation of ship stern flows with a space-marching Navier-Stokes method*. PhD thesis, Delft University of Technology.
- Hoerner, S.F. 1965, *Fluid Dynamic Drag*. Hoerner Fluid Dynamics, Bricktown, New Jersey.
- Hough, G. 1969. Froude number effects on two-dimensional hydrofoils. *Journal of Ship Research*, 13 (1), 53–60.
- Hover, F.S., Haugsdal, Ø. and Triantafyllou, M.S. 2004. Effect of angle of attack profiles in flapping foil propulsion. *Journal of Fluids and Structures*, 19 (1), 37-47.
- Isshiki, H. 1982. A theory of wave devouring propulsion (1st Report). Thrust Generation by a Linear Wells Turbine. *J. Soc. Nav. Archit. Jpn.*, 151, 54–64.
- Isshiki, H. & Murakami, M. 1983 A theory of wave devouring propulsion (3rd report). An experimental verification of thrust generation by a passive-type hydrofoil propulsor. *J. Soc. Nav. Arch. Japan*, 154, 125
- Isshiki, H. & Murakami, M. 1984. A theory of wave devouring propulsion (4th Report): A comparison between theory and experiment in case of a passive-type hydrofoil propulsor. *Journal of the Society of Naval Architects of Japan*, 156, 102–114.
- Jakobsen, E. 1981. The foilpropeller, wave power for propulsion. *2<sup>nd</sup> International Symposium on Wave & Tidal Energy, BHRA Fluid Engineering*, 363-369.
- Joshi V. & Mysa R.C. 2021, Mechanism of wake-induced flow dynamics in tandem flapping foils: Effect of the chord and gap ratios on propulsion. *Phys. Fluids*, 33, 087104.

- Kamath, A., Fleit, G., and Bihs, H. 2019. Investigation of Free Surface Turbulence Damping in RANS Simulations for Complex Free Surface Flows. *Water*, 11 (3). 456.
- Kesel, A.B., 2000. Aerodynamic characteristics of dragonfly wing sections compared with technical aerofoils. *Journal of Experimental Biology*, 203, 3125–3135.
- Kinsey, T., Dumas, G., Lalande, G., Ruel, J., Mehut, A., Viarogue, P., Lemay, J. and Jean, Y. 2011. Prototype testing of a hydrokinetic turbine based on oscillating hydrofoils. *Renewable Energy*, 36, 1710–1718.
- Kinsey, T. & Dumas, G. 2012. Optimal tandem configuration for oscillating-foils hydrokinetic turbine. *Journal of Fluids Engineering*, 134, 031103.
- Klajj, C. M. & Vuik, C. 2013. Simple-type Preconditioners for Cell-centered, Colocated Finite Volume Discretization of Incompressible Reynolds-averaged Navier-stokes Equations. *International Journal for Numerical Methods in Fluids*, 71 (7), 830–849.
- Klajj, C., Hoekstra, M., and Vaz, G. 2018. Design, analysis and verification of a Volume-of-Fluid model with interface-capturing scheme. *Computers and Fluids*, 170, 324–340.
- Kumar, A.G. and Hu, H. 2011. An experimental investigation on the wake flow characteristics of tandem flapping wings. *6th AIAA Theoretical Fluid Mechanics Conference*.
- Küssner, H. 1935. Augenblicklicher Entwicklungs-stand der Frage des Flügelflatterns. *Luftfahrtforschung*, 6, 193-209.
- Lagolopoulos N., Weymouth G. and Ganapathisubramani B. 2020. Deflected Wake Interaction of Tandem Flapping Foils. *Journal of Fluid Mechanics*, 903, A9.
- Lai P.S.K., Bose, N. and McGregor, R.C. 1993. Wave propulsion from flexible-armed, rigid-foil propulsor. *Marine Technol.*, 30 (1), 28–36.
- Le, T.Q., Ko, J.H. and Byun, D.Y. 2013. Morphological effect of a scallop shell on a flapping-type tidal stream generator. *Bioinspiration and Biomimetics*, 8, 036009.
- Leishman, J.G. 2006. *Principles of helicopter aerodynamics*. Cambridge University Press.
- Leonard, B. 1979. A Stable and Accurate Convective Modelling Procedure Based on Quadratic Upstream Interpolation. *Computer Methods in Applied Mech. and Engineering*, 19, 59-98.
- Le Roy, C., Amadori, D., Charberet, S., Windt, J., Muijres, F. T., Llaurens, V. and Debat, V. (2021). Adaptive evolution of flight in Morpho butterflies. *Science* (New York), 374 (6571), 1158–1162.
- Lian, Y., Broering, T. M., Hord, K. and Prater, R. 2014. The characterisation of tandem and corrugated wings. *Progress in Aerospace Sciences*, 65, 41-69
- Licht S.C., Wibawa M.S., Hover F.S. and Triantafyllou M.S. 2010. In-line motion causes high thrust and efficiency in flapping foils that use power downstroke. *The Journal of Experimental Biology*, 213, 63-71.
- Lighthill, M.J. 1960. Note on the swimming of slender fish. *J. Fluid Mech*, 9 (02), 305-317.
- Lighthill, M.J. 1970. Aquatic animal propulsion of high hydromechanical efficiency. *J. Fluid Mech*, 44, 265–301.
- Linden, H., 1895. Improved combination with floating bodies, of fins adapted to effect their propulsion, *UK Patent 14630*.

- Lin, P. 2008. *Numerical Modeling of Water Waves*. London and New York: CRC Press, Taylor & Francis.
- Liu, W.D., Xiao, Q. and Cheng, F. 2013. A bio-inspired study on tidal energy extraction with flexible flapping wings. *Bioinspiration and Biomimetics*, 8, 1–16.
- Liu, Z., Qu, H. and Shi, H. 2019. Numerical study on hydrodynamic performance of a fully passive flow-driven pitching hydrofoil. *Ocean Eng.*, 177, 70–84.
- Lombardi M., Parolini N., Quarteroni A. 2013. Radial basis functions for inter-grid interpolation and mesh motion in FSI problems. *Computer Methods in Applied Mechanics and Engineering*, 256, 117-131.
- Lopes, D.B.S., Falcão de Campos, J.A.C. and Sarmiento, A.J.N.A. 2018. An analytical model study of a flapping hydrofoil for wave propulsion. *ASME 37th International Ocean, Offshore and Arctic Engineering OMAE 2018*, Madrid, Spain.
- Lopes D.B.S., Falcão de Campos J.A.C., Sarmiento A.J.N.A., Vaz. G. 2022. Analytical and numerical modelling of tandem oscillating foils propulsors. *Ocean Engineering*, manuscript submitted for publication.
- Lopes D.B.S., Falcão de Campos J.A.C., Sarmiento A.J.N.A., Vaz. G. 2022. Modelling of Oscillating Foil Propulsors in Waves. *Ocean Engineering*, manuscript submitted for publication.
- Manley, J. & Willcox, S. 2010. The Wave Glider: A Persistent Platform for Ocean Science, *IEEE OCEANS 2010*.
- Mannen J.D.V. & Oossanen P.V. 1989 Propulsion. *Principles of Naval Architecture V.2/Ed. E.V. Lewis*, Jersey City, 127–254.
- MARIN, 2022a. *Maritime Research Institute Netherlands*, ([www.marin.nl](http://www.marin.nl)) (accessed July 1, 2022).
- MARIN, 2022b. *ReFRESKO*, ([www.marin.nl/en/facilities-and-tools/software/refresco](http://www.marin.nl/en/facilities-and-tools/software/refresco)) (accessed July 1, 2022).
- Maruo, H. 1963. Resistance in waves. *Researches on seakeeping qualities of ships in Japan. The Society of Naval Architects of Japan*, Tokyo, 67–102.
- Mathworks 2021. *MATLAB*, ([www.mathworks.com/products/matlab.html](http://www.mathworks.com/products/matlab.html)) (accessed July 1, 2022).
- Menter F.R., Kuntz, M. and Langtry, R. 2003. Ten Years of Industrial Experience with the SST Turbulence Model. *Proceedings of the 4th Turbulence, Heat and Mass Transfer*, 625-632.
- Mewes, S. 2021. *Numerical Prediction of Hydrodynamic Loads and Damping of a Floating Offshore Wind Turbine*. PhD thesis, Universität Duisburg-Essen. Germany.
- Migeotte, G, 1997. *Development of Hydrofoil Supported Catamarans with Semi-Displacement Hulls*. MSc Thesis, University of Stellenbosch, Stellenbosch, South Africa.
- Moukalled, F., Mangnani, L., and Darwish, M. 2016. *The Finite Volume Method in Computational Fluid Dynamics*. Springer International Publishing.
- Muscutt, L., Ganapathisubramani, B., and Weymouth, G. 2014 Characteristics of the flow around tandem flapping wings. *Bulletin of the American Physical Society*, 59.

- Muscutt, L., Dyke, G., Weymouth, G., Naish, D., Palmer, C. and Ganapathisubramani, B. 2017a. The four-flipper swimming method of plesiosaurs enabled efficient and effective locomotion. *Proc. of the Royal Society B: Biological Sciences*, 284 (1861), 20170951.
- Muscutt, L., Weymouth, G. and Ganapathisubramani, B. 2017. Performance augmentation mechanism of in-line tandem flapping foils. *Journal of Fluid Mechanics*, 827, 484505.
- Nagata, S., Imai, Y., Toyota, K. and Isshiki, H. 2010. Thrust generation by waves. *Proc. of the Ninth (2010) ISOPE Pacific/Asia Offshore Mechanics Symposium*, 155-162.
- Newman, J. N. 1978. *Marine Hydrodynamics*. Cambridge, MIT Press.
- Ohtake, T., Nakae, Y. and Motohashi, T. 2007. Nonlinearity of the Aerodynamic Characteristics of NACA0012 Airfoil at Low Reynolds Numbers. *Journal of the Japan Society for Aeronautical and Space Sciences*, 55, 439-445. (In Japanese)
- Paknys R. 2016. *Applied Frequency Domain Electromagnetics*. John Wiley & Sons Ltd.
- Patankar, S. 1980. *Numerical Heat Transfer and Fluid Flow*. Routledge.
- Pereira, F. 2018. *Towards Predictive Scale-Resolving Simulations of Turbulent External Flows*. PhD thesis, Instituto Superior Técnico, Lisboa, Portugal.
- Perić, R. & Abdel-Maksoud, M. 2016. Reliable damping of free-surface waves in numerical simulations. *Ship Technology Research - Schiffstechnik*, 63.
- Politis, G.K. 2004. Simulation of unsteady motion of a propeller in a fluid including free wake modeling. *Eng. Anal. Bound. Elem.*, 28 (6), 633–653.
- Politis, G.K. 2009. A BEM code for the calculation of flow around systems of independently moving bodies including free shear layer dynamics. *Advances in Boundary Element Techniques X*, Athens, Greece, 381–388.
- Politis, G.K. 2011. Application of a BEM time stepping algorithm in understanding complex unsteady propulsion hydrodynamic phenomena. *Ocean Eng.*, 38 (4), 699–711.
- Politis, G. & Politis, K 2014. Biomimetic propulsion under random heaving conditions, using active pitch control. *J. Fluids Struct.*, 47, 139–149.
- Politis, G.K. & Tsarsitalidis, V.T. 2009. Simulating biomimetic (flapping foil) flows for comprehension, reverse engineering and design. *1st International Symposium on Marine Propulsors, SMP'09*, Trondheim, Norway.
- Politis, G.K. & Tsarsitalidis, V.T. 2013. Biomimetic propulsion using twin oscillating wings. *3rd International Symposium on Marine Propulsors, SMP'13*, Tasmania, Australia.
- Politis, G.K., & Tsarsitalidis, V.T. 2014. Flapping wing propulsor design: an approach based on systematic 3D-BEM simulations. *Ocean Eng.*, 84, 98–123.
- Rapuc, S., Crepier, P., Jaouen, F., Bunnik, T., Regnier, P. 2018. Towards Guidelines for Consistent Wave Propagation in CFD Simulations. *19th International Conference on Ship & Maritime Research (NAV2018)*, Trieste, Italy
- Read, D.A., Hover, F.S. and Triantafyllou, M.S. 2003. Forces on oscillating foils for propulsion and manoeuvring. *J. Fluids Struct.*, 17, 163–83.
- Rijkema, M.D. & Vaz, C. 2011. Accurate model and full-scale viscous flow computations on propulsors. *The Naval Architect*, 52-55.

- Rival, D., Hass, G. and Tropea, C. 2011. Recovery of energy from leading and trailing edge vortices in tandem airfoil configurations. *Journal of Aircraft*, 48, 203-211
- Rochholz, T. 2012. *Wave-Powered Unmanned Surface Vehicle as a Station-Keeping Gateway Node for Undersea Distributed Networks*. MSc thesis, Naval Postgraduate School, Monterey, California.
- Roe, P. L. 1985. Some contributions to the modelling of discontinuous flows. *Lectures in Applied Mathematics*, 22, 163-193.
- Rosetti, G. F. & Vaz, G. 2017. On the numerical simulations of captive, driven and freely moving cylinder. *Journal of Fluids and Structures*, 74, 492–519
- Rosetti, G. F., Vaz, G., and Fajarra, A. L. C. 2012. URANS Calculations for Smooth Circular Cylinder Flow in a Wide Range of Reynolds Numbers: Solution Verification and Validation. *ASME J. Fluids Eng*, 134 (12): 121103.
- Rozhdestvensky K.V. & Ryzhov V.A. 2003. Aerohydrodynamics of flapping-wing propulsors. *Progress in Aerospace Sciences*, 39, 585–633.
- Rozhdestvensky K.V. & Htet Z.M. 2021. A Mathematical Model of a Ship with Wings Propelled by Waves. *Journal of Marine Science and Application*, 20, 595–620.
- Schouveiler L., Hover F.S. and Triantafyllou M.S. 2005. Performance of flapping foil propulsion. *Journal of Fluids and Structures*, 20, 949–959.
- Skjelbreia, L. & Hendrickson, J. 1960. Fifth order gravity wave theory. *Proc. Coastal Engineering Conf.*, 184-196.
- Silva, L.W.A.D. & Yamaguchi, H. 2012. Numerical study on active wave devouring propulsion, *Journal Marine Science & Technology*, 17 (3), 261-275.
- Smith, R. & Das, J. 2011. Predicting wave glider speed from environmental measurements. *Proceeding of MTS/IEEE Oceans 2011*.
- Southampton University 2021. *The Iridis Compute Cluster*, ([www.southampton.ac.uk/isolutions/staff/iridis.page](http://www.southampton.ac.uk/isolutions/staff/iridis.page)) (accessed July 1, 2022).
- Stern, F., Wilson, R.V., Coleman, H.W. and Paterson, E.G. 2001. Comprehensive Approach to Verification and Validation of CFD Simulations (Part 1): Methodology and Procedures. *Journal of Fluids Engineering*, 123 (4), 793-802.
- Terao, Y. and Isshiki, H. 1991. Wave devouring propulsion sea trial, *18<sup>th</sup> Symposium on Naval Hydrodynamics*, 287-296.
- Thaweewat, N., Phoemsaphawee, S., and Juntasaro, V. 2018. Semi-active flapping foil for marine propulsion. *Ocean Eng.*, 147, 556–564.
- The American Society of Mechanical Engineers (ASME) 2009. *Standard for Verification and Validation in Computational Fluid Dynamics and Heat Transfer - ASME V&V 20-2009*, United States of America.
- Theodorsen, T. 1935. General theory of aerodynamic instability and the mechanism of flutter. *NACA Tech. Rep.* 496.

- Thomas, A.L.R., Taylor, G.K., Srygley, R.B., Nudds, R.L. and Bomphrey, R.J. 2004. Dragonfly flight: free-flight and tethered flow visualizations reveal a diverse array of unsteady lift-generating mechanism, controlled primarily via angle of attack. *The Journal of Experimental Biology*, 207, 4299-4323.
- Triantafyllou, G.S., Triantafyllou, M.S., and Grosenbaugh, M.A. 1993. Optimal thrust development in oscillating foils with application to fish propulsion. *Journal of Fluids and Structures*, 7 (2), 205-224.
- Tsarsitalidis, V. & Politis, G. 2015. Simulating Biomimetic Propulsors under spring loading and/or active control for the pitching motion of the wings. *Proceedings of 4th International Symposium on Marine Propulsors, SMP'15*, Austin, Texas, USA.
- Usherwood, J.R. & Lehmann, F.O. 2008. Phasing of dragonfly wings can improve aerodynamic efficiency by removing swirl. *Journal of the Royal Society Interface*, 5 (28), 1303–1307.
- Vaz, G., Jaouen, F. and Hoekstra, M. 2009. Free-Surface Viscous Flow Computations. Validation of URANS code FreSCo, *OMAE 2009*, Hawaii, Honolulu, USA.
- van Dyke M. 1975. *Perturbation Methods in Fluid Mechanics*, 2nd ed., Stanford, Parabolic Press.
- von Kármán, T. & Sears, W. R. 1938. Airfoil theory for non-uniform motion. *Journal of the Aeronautical Sciences*, 5 (10), 379-390.
- Vrooman, D. 1858. *Vibrating Propeller*, US Patent 22097.
- Walree van, F. 1999. *Computational Methods for Hydrofoil Craft in Steady and Unsteady Flow*. PhD Thesis. Delft University of Technology. The Netherlands.
- Wagner, H. 1925. Über die Entstehung des dynamischen Auftriebes von Tragflügeln. *ZAMM - Journal of Applied Mathematics and Mechanics/Zeitschrift für Angewandte Mathematik und Mechanik*, 5 (1), 17-35.
- Wang, Y., Anvar, A. and Hu, E. 2013. A Feasibility Study on the Design, Development and Operation of an Automated Oceanic Wave Surface Glider Robot. *20th International Congress on Modelling and Simulation*. Adelaide, Australia.
- Warkentin, J. & DeLaurier, J. 2007. Experimental aerodynamic study of tandem flapping membrane wings. *Journal of Aircraft*, 44 (5), 1653–1661.
- WavEC – Offshore Renewables 2015. *West Coast of Portugal from ONDATLAS monitoring program* (Unpublished report), WavEC – Offshore Renewables, Lisbon.
- Weymouth, G.D. & Yue, D.K.P. 2011. Boundary data immersion method for Cartesian-grid simulations of fluid-body interaction problems. *Journal of Computational Physics*, 230 (16), 6233-6247.
- Weymouth, G. D. 2015. Lily Pad: Towards real-time interactive computational fluid dynamics. *18th Numerical Towing Tank Symposium*.
- Witteveen, J. & Bijl, H. 2009. Explicit Mesh Deformation Using Inverse Distance Weighting Interpolation. *19<sup>th</sup> AIAA Computational Fluid Dynamics*, San Antonio, Texas.
- Wu, T.Y. 1961. Swimming of a waving plate. *J Fluid Mech*, 10, 321–344.

- Wu, T.Y. 1971a. Hydromechanics of swimming propulsion (Part 1): Swimming of a Two-Dimensional Flexible Plate at Variable Forward Speeds in an Inviscid Fluid. *J Fluid Mech*, 46, 337–355.
- Wu, T.Y. 1971b. Hydromechanics of swimming propulsion (Part 2): Some optimum shape problems. *J Fluid Mech*, 46, 521–544.
- Wu, T.Y. & Chang, A.T. 1975. Extraction of flow energy by fish and birds in a wavy stream. *Swimming and flying in nature*. Springer, 687-702.
- Wu, X., Zhang X., Tian, X., Li, X. and Lu W. 2020. A review on fluid dynamics of flapping foils. *Ocean Engineering*, 195, 106712.
- Xiao, Q. & Zhu, Q. 2014. A review on flow energy harvesters based on flapping foils. *Journal of Fluids and Structures*, 46, 174–191.
- Yamaguchi, H. and Bose, N. 1994. Oscillating foils for marine propulsion. *Proceedings of the 4th International Offshore and Polar Engineering Conference*, Osaka, 539–544.
- Zhenjiang, Y., Zhongqiang, Z., Xiaoguang, Y. and Zongyu, C. 2016. Dynamic Analysis of Propulsion Mechanism Directly Driven by Wave Energy for Marine Mobile Buoy, *Chinese Journal of Mechanical Engineering*, 29, 4, 1-6.
- Zhu, Q., 2012. Energy harvesting by a purely passive flapping foil from shear flows. *Journal of Fluids and Structures*, 34, 157–169.

# Appendix A

## 2D Hydrofoil Potential Flow Theory

This appendix chapter is dedicated to the review of the formulation of the potential flow theory for hydrofoils used in Section 2.2 following the account given by Newman (1978). It is considered a two-dimensional symmetrical foil advancing with constant speed and performing harmonic oscillation in combined heave and pitch motions.

**Formulation of the potential flow problem:** We consider a two-dimensional infinite long thin hydrofoil moving in unbounded ideal fluid at rest at infinity, with the fundamental assumption that the camber of the foil is small compared to its chord. The foil travels at constant forward velocity  $U$  directed to the negative  $x_0$  axis of a space-fixed Cartesian coordinate system  $(x_0, y_0)$ , and has small lateral motion in the  $y_0$  direction. A moving coordinate system  $(x, y)$  with constant velocity  $U$  is defined by the transformation

$$x = x_0 + Ut, y = y_0. \quad (\text{A.1})$$

We consider the origin of the coordinate system  $(x, y)$  to be at the mid-chord of the foil. The instantaneous camber line is given by  $y = (x, t)$ ,  $-a \leq x \leq a$ ,  $a = c/2$ ,  $c$  being the chord length. We will assume that  $\eta$  is much smaller than the chord length and that the slope of the instantaneous foil surface, is small  $|d\eta/dx| \ll 1$ , with respect to the  $x$  axis. The fluid motion due to the unsteady motion of the foil will be described by the gradient of a perturbation velocity potential  $(x, y, t)$  to the free-stream potential  $Ux$ , satisfying the Laplace equation in the fluid domain. The perturbation velocity is  $\nabla\phi = (u, v)$ . The potential must satisfy the kinematic boundary condition on the foil surface, a dynamic boundary condition on the vortex sheet shed from the foil trailing edge and should tend to zero at large distances away from the foil. In addition, a Kutta condition should be imposed on the foil sharp trailing edge. The boundary value problem for the perturbation potential may be formulated by requiring the potential to first satisfy the Laplace equation

$$\nabla^2\phi = 0. \quad (\text{A.2})$$

Because perturbations are assumed to be small, we may linearize the kinematic boundary condition on the foil surface and separate the effect of thickness from the effect of camber. Transferring the boundary condition to the  $x$  axis, we obtain on the chord cut

$$\frac{\partial\phi}{\partial y} = \frac{\partial\eta}{\partial t} + U \frac{\partial\eta}{\partial x} \equiv v_0(t) \text{ on } |x| < a, \quad (\text{A.3})$$

where  $v_0(t)$  is the vertical velocity of the foil surface. The perturbation potential must tend to zero at infinity

$$\phi \rightarrow 0 \text{ as } (x^2 + y^2)^{1/2} \rightarrow \infty, \quad (\text{A.4})$$

and the Kutta condition is imposed by requiring that the velocity remains finite at the foil's trailing edge

$$\nabla\phi < \infty \text{ at } x = a. \quad (\text{A.5})$$

As to the dynamic boundary condition of zero pressure across the vortex sheet surface,

$$\Delta p = p^+ - p^- = 0 \text{ on } x > -a, \quad (\text{A.6})$$

where  $p^+$  and  $p^-$  denote the pressure on each side of the vortex sheet. The linearized unsteady Bernoulli equation writes

$$\frac{p - p_\infty}{\rho} = \left( \frac{\partial\phi}{\partial t} + U \frac{\partial\phi}{\partial x} \right), \quad (\text{A.7})$$

where  $p_\infty$  is the undisturbed pressure and  $\rho$  the fluid density. Applying Eq. (A.7) to the dynamic boundary condition Eq. (A.6) we obtain

$$\frac{\partial\gamma}{\partial t} + U \frac{\partial\gamma}{\partial x} = 0, \quad (\text{A.8})$$

where  $\gamma$  is the strength of the vortex sheet along the  $x$  axis. The solution of Eq (A.8) is

$$\gamma(x, t) = \gamma(x - Ut), \quad (\text{A.9})$$

showing that the vorticity in the vortex sheet is convected with the velocity  $U$  and remains constant in a reference frame moving with the fluid at that speed. The initial condition states that the total circulation of foil and wake must be zero. The foil circulation is

$$\Gamma = \int_{-a}^a \gamma(x, t) dx. \quad (\text{A.10})$$

Then

$$\frac{\partial\Gamma}{\partial t} = -U\gamma(x, t). \quad (\text{A.11})$$

Thus, the linearized boundary value problem consists in finding the potential satisfying the Laplace equation Eq. (A.2) the kinematic boundary condition Eq. (A.3) on the foil cut and the condition at infinity Eq. (A.4). This can be achieved with a vortex distribution  $\gamma(x, t)$ ,  $x > -a$  along the  $x$  axis, where the vorticity in the wake satisfies Eq. (A.9), with the initial condition Eq. (A.11) at  $x = a$ .

**The Hilbert problem:** The boundary condition on the foil Eq. (A.3) is written in terms of the vortex distribution on the  $x$  axis as

$$v_0(x, t) + \frac{1}{2\pi} \int_a^\infty \frac{\gamma(a\xi - Ut)}{\xi - x} d\xi = -\frac{1}{2\pi} \int_{-a}^a \frac{\gamma(\xi, t)}{\xi - x} d\xi, \quad (\text{A.12})$$

with  $\xi$  the distance to mid-chord, and where the second integral is to be taken in the Cauchy principal value sense. This is a singular integral equation for the vortex strength. With the coordinates made non-dimensional on the basis of half-chord, it is possible to obtain the solution for this singular integral equation on the cut  $|x| < 1$ .

$$\gamma(x, t) = \frac{2}{\pi(1-x^2)^{1/2}} \left\{ \int_{-1}^1 \frac{(1-\xi^2)^{1/2}}{\xi-x} v_0(\xi, t) d\xi - \frac{1}{2} \int_1^\infty \frac{(\xi^2-1)^{1/2}}{\xi-x} \gamma(a\xi-Ut) d\xi \right\}. \quad (\text{A.13})$$

The Kutta condition of finite velocity at the trailing edge  $x = 1$ , requires the term between brackets to vanish, i.e.,

$$\int_1^\infty \left( \frac{\xi+1}{\xi-1} \right)^{1/2} \gamma(a\xi-Ut) d\xi = -2 \int_{-1}^1 \left( \frac{1+\xi}{1-\xi} \right)^{1/2} v_0(\xi, t) d\xi. \quad (\text{A.14})$$

Applying this to Eq. (A.13), the solution may be written as

$$\gamma(x, t) = \frac{1}{\pi} \left( \frac{1-x}{1+x} \right)^{1/2} \left\{ \int_{-1}^1 \left( \frac{1+\xi}{1-\xi} \right)^{1/2} \frac{2v_0(\xi, t)}{\xi-x} d\xi + \int_1^\infty \left( \frac{\xi+1}{\xi-1} \right)^{1/2} \frac{\gamma(a\xi-Ut)}{\xi-x} d\xi \right\}, \quad (\text{A.15})$$

where the first term is the quasi-steady vorticity distribution that is needed to cancel the  $v_0(\xi, t)$  in steady flow, and the second term is the vorticity induced by the wake.

**Expressions for the lift and moment:** We evaluate the lift by integrating the pressure distribution on the foil. From the linearized unsteady Bernoulli equation Eq. (A.7) we get for the lift

$$L = \rho a \int_{-1}^1 \left( \frac{\partial \Delta \phi}{\partial t} + \frac{U}{a} \frac{\partial \Delta \phi}{\partial x} \right) dx. \quad (\text{A.16})$$

The moment with respect to origin at mid-chord is

$$M = \rho a^2 \int_{-1}^1 \left( \frac{\partial \Delta \phi}{\partial t} + \frac{U}{a} \frac{\partial \Delta \phi}{\partial x} \right) x dx. \quad (\text{A.17})$$

Since we have

$$\frac{\partial \Delta \phi}{a \partial x} = -\gamma(x, t), \quad (\text{A.18})$$

and that at leading edge  $x = -1$  we have  $\Delta \phi = 0$ , using the integration by parts Eqs. (A.16) and Eq. (A.17) can be reduced to

$$L = -\rho a \int_{-1}^1 \left[ a(1-x) \frac{\partial \gamma}{\partial t} + U\gamma \right] dx, \quad (\text{A.19})$$

and respectively

$$M = -\rho a^2 \int_{-1}^1 \left[ \frac{1}{2} a(1-x) \frac{\partial \gamma}{\partial t} + U\gamma x \right] dx. \quad (\text{A.20})$$

Applying the solution of Eq. (A.15) and further developing these expressions, we obtain

$$L = -2\rho a \int_{-1}^1 a(1-\xi^2)^{1/2} \frac{\partial v_0(\xi, t)}{\partial t} d\xi + \rho U a \int_1^\infty \frac{\xi}{(\xi^2-1)^{1/2}} \gamma(a\xi-Ut) d\xi. \quad (\text{A.21})$$

The first term gives the non-circulatory lift, or the added-mass force associated with generalized vertical acceleration along the foil. The second term renders the circulatory lift, which represents the effect of the wake, the memory effects that depend on past history of the motion. Similarly, for the expression for the moment about mid-chord,

$$M_{1/2} = -\rho a^2 \int_{-1}^1 a(1 - \xi^2)^{1/2} \frac{\partial v_0(\xi, t)}{\partial t} d\xi + 2\rho U a^2 \int_{-1}^1 (1 - \xi^2)^{1/2} v_0(\xi, t) d\xi \quad (\text{A.22})$$

$$+ \frac{1}{2} \rho U a^2 \int_1^\infty \frac{\gamma(a\xi - Ut) d\xi}{(\xi^2 - 1)^{1/2}}.$$

The first term represents the added moment of inertia, the second term is the quasi-steady moment, and the third term is the moment that depends explicitly on the wake. If we evaluate the moment about the chord quarter point the memory effects of the wake vanish,

$$M_{1/4}(t) = M(t) + \frac{1}{2} aL(t) \quad (\text{A.23})$$

$$= -\rho a^2 \int_{-1}^1 a(1 - \xi^2)^{1/2} (1 + \xi) \frac{\partial v_0(\xi, t)}{\partial t} d\xi$$

$$+ \rho U a^2 \int_{-1}^1 (1 - 2\xi) \left( \frac{1 + \xi}{1 - \xi} \right)^{1/2} v_0(\xi, t) d\xi.$$

If the motion of the foil is known,  $v_0(\xi, t)$  is known, the moment about the quarter point may be calculated without considering the wake effects.

**Oscillatory time dependence:** Since the motion is considered to have harmonic time dependence

$$v_0(x, t) = v_0(x) e^{i\omega_0 t}. \quad (\text{A.24})$$

With the convention that we take the real part of the right-hand-side we allow  $v_0(x)$  to be a complex amplitude of the harmonic component with angular frequency  $\omega$ . The wake vorticity must be of the form

$$\gamma(ax - Ut) = \gamma_0 e^{i(\omega_0 t - k_f x)}, \quad (\text{A.25})$$

where  $k_f = \omega_0 a/U$  is the reduced frequency. By substituting Eqs. (A.24) and (A.25) in Eq. (A.15) we obtained

$$\gamma_0 = -2 \int_{-1}^1 \left( \frac{1 + \xi}{1 - \xi} \right)^{1/2} v_0(\xi) d\xi / \int_1^\infty \left( \frac{\xi + 1}{\xi - 1} \right)^{1/2} e^{-ik_f \xi} d\xi. \quad (\text{A.26})$$

The integral in the denominator can be written as

$$\int_1^\infty \left( \frac{\xi + 1}{\xi - 1} \right)^{1/2} e^{-ik_f \xi} d\xi = \int_1^\infty \frac{\xi}{(\xi^2 - 1)^{1/2}} e^{-ik_f \xi} d\xi + \int_1^\infty \frac{e^{-ik_f \xi}}{(\xi^2 - 1)^{1/2}} d\xi. \quad (\text{A.27})$$

These integrals can be expressed in terms of the Hankel function  $H_0^{(2)}(k_f)$  and  $H_1^{(2)}(k_f)$  respectively (see Newman (1978), Ch. 5 and Abramowitz & Stegun, 9.6.23 and 9.6.4):

$$\int_1^\infty \frac{\xi}{(\xi^2 - 1)^{1/2}} e^{-ik_f \xi} d\xi = -\frac{\pi}{2} H_1^{(2)}(k_f), \quad (\text{A.28})$$

$$\int_1^{\infty} \left(\frac{\xi+1}{\xi-1}\right)^{1/2} e^{-ik_f\xi} d\xi = -\frac{\pi}{2} [iH_0^{(2)}(k_f) + H_1^{(2)}(k_f)], \quad (\text{A.29})$$

so, Eq. (A.26) writes

$$\gamma_0 = -2 \int_{-1}^1 \left(\frac{1+\xi}{1-\xi}\right)^{1/2} v_0(\xi) d\xi / \left[-\frac{\pi}{2} (iH_0^{(2)} + H_1^{(2)})\right]. \quad (\text{A.30})$$

For the case of a combined heave and pitch motion oscillation

$$h(t) = h_0 e^{i\omega_0 t} \text{ and } \theta(t) = \theta_0 e^{i\omega_0 t}, \quad (\text{A.31})$$

where  $h_0$  and  $\theta_0$  are complex constant amplitudes, with  $\theta > 0$  measured clockwise from the  $x$  axis (nose up). Considering  $b$ , the distance of the rotating axis to mid-chord, leading edge positive,

$$v_0(x) = \dot{h} - (x-b)\dot{\theta} - U\theta. \quad (\text{A.32})$$

With non-dimensional heave amplitude  $h_0^* = h_0/a$  and  $b^* = b/a$ , we have

$$\int_{-1}^1 \left(\frac{1+\xi}{1-\xi}\right)^{1/2} v_0(\xi) d\xi = \pi \left[ i\omega_0 a h_0^* - i\omega_0 a \left(\frac{1}{2} - b^*\right) \theta_0 - U\theta_0 \right], \quad (\text{A.33})$$

$$\int_{-1}^1 (1-\xi^2)^{1/2} v_0(\xi) d\xi = \frac{\pi}{2} [i\omega_0 a h_0^* + i\omega_0 a b^* \theta_0 - U\theta_0]. \quad (\text{A.34})$$

We finally obtain the vortex expression

$$\gamma_0(x, t) = \left\{ -4U \left[ ik_f h_0^* - ik_f \left(\frac{1}{2} - b^*\right) \theta_0 - \theta_0 \right] e^{-ik_f x} / [H_1^{(2)} + iH_0^{(2)}] \right\} e^{i\omega_0 t}. \quad (\text{A.35})$$

Hence using the same procedure on (A.21) we obtain the expression for the circulatory lift

$$L_c(t) = (\rho a U^2) [-2\pi C(k_f) h_0^*] \left\{ ik_f \left[ 1 + \left(b^* - \frac{1}{2}\right) \theta_0^* \right] - \theta_0^* \right\} e^{i\omega_0 t}, \quad (\text{A.36})$$

and for the non-circulatory lift

$$L_{Nc}(t) = (\rho a U^2) [-\pi h_0^*] \left\{ -k_f^2 [1 + b^* \theta_0^*] - ik_f \theta_0^* \right\} e^{i\omega_0 t}, \quad (\text{A.37})$$

with  $\theta_0^* = \theta_0/h_0^*$  and where  $C(k_f)$  is the Theodorsen's function, given by

$$C(k_f) = \frac{H_1^{(2)}(k_f)}{H_1^{(2)}(k_f) + iH_0^{(2)}(k_f)}. \quad (\text{A.38})$$

For small reduced frequencies  $C(k_f) \approx 1$  and this contribution reduces to the quasi-steady lift. For  $k_f \rightarrow \infty$   $C(k_f) \rightarrow 0.5$  this contribution is in phase with the quasi-steady lift and the non-circulatory term dominates (see Figure A.1). For intermediate values of the reduced frequency, the phase of  $C(k_f)$  is negative so the circulatory lift lags the quasi-steady lift.

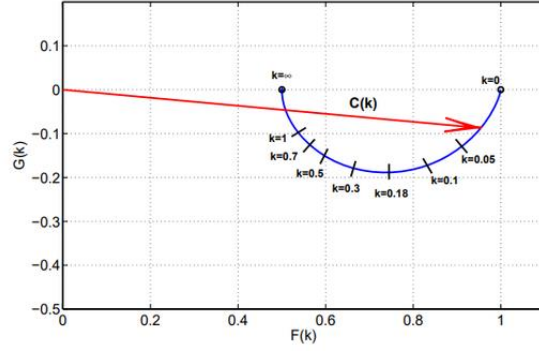


Figure A.1: Theodorsen's function  $C(k) = F(k) + iG(k)$ .

Similarly, the expressions for the moment about point  $b$  are given by

$$M_c(t) = -a \left( b^* + \frac{1}{2} \right) L_c(t), \quad (\text{A.39})$$

$$M_{Nc}(t) = (2\rho a^2 U^2) \left[ \frac{\pi}{2} h_0^* \right] \left\{ -k_f^2 \left[ b^* + \left( b^{*2} + \frac{1}{8} \right) \theta_0^* \right] - ik_f \left( b^* - \frac{1}{2} \right) \theta_0^* \right\} e^{i\omega_0 t}. \quad (\text{A.40})$$

These expressions can be easily adapted to use the Strouhal number applying the relation

$$\pi S_t = h_0^* k_f. \quad (\text{A.41})$$

# Appendix B

## Wu's Theory Formulation

This appendix is a brief introduction of Wu's unsteady theory for an oscillating two-dimensional hydrofoil in waves as presented in Section 2.3.3 based on Isshiki's work (1982). It is considered a two-dimensional foil with chord  $c = 2a$  at a depth  $d$  advancing with constant speed  $U$  in a heading sinusoidal gravity wave of amplitude  $a_0$  and wavelength  $\lambda$ , in the deep sea. In terms of body coordinate system  $(x, y)$  with origin at mid-chord, the heading wave profile  $\zeta_0$ , the velocity potential  $Ux + \phi_0(x, y, t)$  and pressure  $p_0(x, y, t)$  can be given by

$$\zeta_0(x, t) = a_0 e^{i(\omega_0 t - kx)}, \quad (\text{B.1})$$

$$\phi_0(x, y, t) = \frac{ga_0}{\sqrt{gk}} e^{[i(\omega_0 t - kx) + k(y-d)]}, \quad (\text{B.2})$$

$$p_0(x, y, t) = \rho g a_0 e^{[i(\omega_0 t - kx) + k(y-d)]} - \rho g(y - d), \quad (\text{B.3})$$

with wavenumber  $k = 2\pi/\lambda$ ,  $\omega_0 = \sqrt{gk} + kU$  is the encounter frequency, for heading waves, and  $\rho$  for the water density. The wave amplitude is assumed small  $ka_0 \ll 1$ . For the present analysis, it is considered independent of the free-surface effects, and assumed that the fluid is only disturbed at depth  $d$ . The vertical component of wave velocity at the foil is

$$V_0(x, t) = \frac{\partial \phi_0}{\partial y} = iA_0 e^{i(\omega_0 t - kx)}, \quad (\text{B.4})$$

where

$$A_0 = \sqrt{gk} a_0 e^{-kd}. \quad (\text{B.5})$$

It is also assumed that the streamwise component of the wave orbital velocity may be neglected in comparison with  $U$  and foil thickness as well.

**Formulation of the problem:** Because the assumed linearity in this appendix we consider a fixed foil, and the total solution for an oscillating foil in waves as the sum of the present solution with the one obtained in Appendix A. The total pressure  $p$  it is taken to be sum of the undisturbed pressure  $p_0$  and the perturbation pressure  $p_1$ . However, the pressure  $p_0$  generates no hydrodynamic force or moment on the foil since it is continuous across the foil of zero thickness. The problem to obtain  $p_1$  is specified by the Laplace equation in the fluid, the linearized kinematic boundary condition on the foil, the Kutta condition on the trailing edge, the infinite condition and the free-surface conditions, respectively:

$$\nabla^2 p_1 = 0 \text{ in the fluid,} \quad (\text{B.6})$$

$$-\frac{1}{\rho} \frac{\partial p_1}{\partial y} = \left( \frac{\partial}{\partial t} + U \frac{\partial}{\partial x} \right) [-V_0(x, t)] \text{ on } |x| < a, y = \pm 0, \quad (\text{B.7})$$

$$p_1 = 0 \text{ at } x = a, y = \pm 0, \quad (\text{B.8})$$

$$p_1 \rightarrow 0 \text{ as } (x^2 + y^2)^{1/2} \rightarrow \infty, \quad (\text{B.9})$$

$$\left[ \left( \frac{\partial}{\partial t} + U \frac{\partial}{\partial x} \right)^2 + g \frac{\partial}{\partial y} \right] p_1 = 0 \text{ on } y = d. \quad (\text{B.10})$$

For the first order approximation, the free-surface condition may be neglected, as assumed before, and the solution for this problem is known (Wu, 1971a). The value of  $p_1(x, t)$  at the foil can be given by

$$\begin{aligned} -\frac{1}{\rho} p_1(x, t) = & -\frac{U}{2} [b_1 - C(k_f)(b_0 + b_1)] \left( \frac{a-x}{a+x} \right)^{\frac{1}{2}} \\ & + \frac{\pi}{2} \oint_{-a}^a \left( \frac{a^2 - x^2}{a^2 - \xi^2} \right)^{\frac{1}{2}} \left( \frac{\partial}{\partial t} + U \frac{\partial}{\partial x} \right) \int_{-a}^x V_0(\xi', t) d\xi' \frac{1}{\xi - x} d\xi, \end{aligned} \quad (\text{B.11})$$

where the integral assumes its Cauchy principal value;  $C(k_f) = \mathcal{F}(k_f) + i\mathcal{G}(k_f)$  is the Theodorsen's function,  $k_f = \omega_0 a / U$  the reduced frequency, and with  $b_n$  defined in terms of Bessel functions of the first kind  $J_n(ka)$

$$b_n = 2A_0(-i)^{n-1} J_n(ka) e^{i\omega_0 t}. \quad (\text{B.12})$$

When the foil is oscillating at encounter frequency, the reduced frequency and the wavenumber are related by

$$k_f = ka + \frac{\sqrt{ka}}{\sqrt{2}F_r}, \quad (\text{B.13})$$

with Froude number  $F_r = U/\sqrt{gc}$ .

Expressions for the lift and moment: The integral representation of the lift and moment about mid-chord (positive nose down) along the chord are, considering  $p^+ - p^- = 2p_1^+$

$$L = \int_{-a}^a 2p_1^+(x, t) dx, \quad (\text{B.14})$$

$$M_{1/2} = - \int_{-a}^a 2p_1^+(x, t) x dx, \quad (\text{B.15})$$

Substituting Equation (B.11) in Equations (B.14) and (B.15) we obtain the expressions for the lift and moment

$$L(t) = (\rho a U^2) [-2\pi] i \frac{A_0}{U} \left[ W_1(k_f) - iW_2(k_f) + \left( \frac{k_f}{ka} - 1 \right) J_1(ka) \right] e^{i\omega_0 t}, \quad (\text{B.16})$$

$$M_{\frac{1}{2}}(t) = (2\rho a^2 U^2) \left[ -\frac{\pi}{2} \right] i \frac{A_0}{U} \left[ W_1(k_f) - iW_2(k_f) + i \left( \frac{k_f}{ka} - 1 \right) J_2(ka) \right] e^{i\omega_0 t}, \quad (\text{B.17})$$

where

$$W_1(k_f) = [1 - \mathcal{F}(k_f)] J_1(ka) + \mathcal{G}(k_f) J_0(ka), \quad (\text{B.18})$$

$$W_2(k_f) = \mathcal{F}(k_f)J_0(ka) + \mathcal{G}(k_f)J_1(ka). \quad (\text{B.19})$$

These can be easily simplified to

$$L_C(t) = (\rho a U^2)[-2\pi]C(k_f) \left[ -i \frac{A_0}{U} (J_0(ka) - iJ_1(ka)) \right] e^{i\omega_0 t}, \quad (\text{B.20})$$

$$L_{NC}(t) = (\rho a U^2)[- \pi] \left[ k_f \frac{A_0}{U} \left( \frac{2J_1(ka)}{ka} \right) \right] e^{i\omega_0 t}, \quad (\text{B.21})$$

$$M_{C1/2}(t) = (2\rho a^2 U^2) \left[ -\frac{\pi}{2} \right] C(k_f) \left[ -i \frac{A_0}{U} (J_0(ka) - iJ_1(ka)) \right] e^{i\omega_0 t}, \quad (\text{B.22})$$

$$M_{NC1/2}(t) = (2\rho a^2 U^2) \left[ -\frac{\pi}{2} \right] \left\{ -\frac{A_0}{U} \left[ ik_f \frac{J_2(ka)}{ka} - (J_1(ka) - iJ_2(ka)) \right] \right\} e^{i\omega_0 t}. \quad (\text{B.23})$$



# Appendix C

## Tandem Foil Model Formulation

This appendix describes the problem formulation and method to obtain the solution for the lift of the aft foil of a tandem foil configuration, in the model developed in this work. We consider two hydrofoils, one aft the other, travelling in unbounded fluid and oscillating in heave and pitch.

**Formulation of the problem:** We consider two identical 2D infinite long thin hydrofoils moving in unbounded ideal fluid at rest at infinity, separated by a distance length  $s$ , and with a phase lag in their motion of  $\phi_t$ , with the fundamental assumption that their camber is small compared to its chord  $c = 2a$ . The tandem foil travels at constant forward velocity  $U$  directed to the negative  $x_0$  axis of a space-fixed Cartesian coordinate system  $(x_0, y_0)$ , with origin in aft foil mid-chord, and the small lateral motion in the  $y_0$  direction. The motion is considered to have harmonic time dependence so the heave and pitching motions for the fore and aft foil are defined as, with  $i = 1, 2$ , respectively:

$$h_i = h_{0i}e^{i(\omega_0 t)} \text{ and } \theta_i = \theta_{0i}e^{i(\omega_0 t)}. \quad (\text{C.1})$$

The pitching axis is set in both foils at  $b^* = b/a$  distance from their respective mid-chord, leading edge positive.

The fore-aft foil interaction effects are accounted in the following way: i) the horizontal constant flow velocity for the aft foil is the vortex advection velocity of the jet of the fore foil; ii) there is a vertical velocity component induced on the aft foil by the fore foil vorticity that only affects the fore foil apparent inflow angle; iii) it is also asserted that the aft foil wake effect in the forward foil is minimal, if there is sufficient inter-foil distance (Epps et al. 2016); iv) it is assumed that the main additional effect of the fore foil the aft foil is the interference of the wakes, where the superimposition of the vortices shed by both foils starts on the trailing edge of the aft foil, and continues downstream.

The horizontal vortex advection velocity can be related to stream velocity using the ratio  $r_{va} = U_{for}/U$ . Here we propose the empirical value  $r_{va} = 1.2$  from Epps et al. (2016).

To estimate the induced apparent inflow angle we consider that the fore foil is modelled by a single vortex with circulation  $\Gamma$ , that is related with lift coefficient, using the Kutta-Joukowski theorem, by

$$\Gamma = aUC_L, \quad (\text{C.2})$$

These circulations will cause a perturbation on velocity field of the aft foil, resulting, in an induced downwash velocity that is given by:

$$v_2 = -\frac{\Gamma}{2\pi(s + 2a)}, \quad (\text{C.3})$$

that results in induced apparent inflow angle

$$\varphi_{i2} = \text{atan}\left(\frac{v_2}{U}\right). \quad (\text{C.4})$$

Combining these expressions with Equation (2.17) it is possible to obtain

$$\varphi_2 = \text{atan}\left(ik_f h_0^* \left[1 + \left(b^* - \frac{1}{2}\right)\theta_0^*\right] - \frac{C_L^S}{2\pi(s^* + 2)}\right) e^{i\omega_0 t}, \quad (\text{C.5})$$

where  $s^* = s/a$  and  $C_L^S$  the lift coefficient for a single foil that can be obtain from Equation (2.13).

To estimate the interference of the wakes, we recall the lift expression for a single foil given in Eq. (A.21):

$$L = -2\rho a \int_{-1}^1 a(1 - \xi^2)^{1/2} \frac{\partial v_0(\xi, t)}{\partial t} d\xi + \rho U a \int_1^\infty \frac{\xi}{(\xi^2 - 1)^{1/2}} \gamma(a\xi - Ut) d\xi, \quad (\text{C.6})$$

where  $v_0(\xi, t)$  is the vertical velocity of the foil surface,  $\gamma(\xi + Ut)$  the vortices and  $\xi$  the distance to mid-chord, with the coordinates made non-dimensional on the basis of half-chord. The first term gives the non-circulatory lift, independent of the wake, and second term the circulatory lift. For the tandem foil it is assumed that the vortex shedding is independent for the two foils so the Kutta condition applies locally to each of them. Each vortex solution can be written, assuming the origin in the aft foil mid-chord, by:

$$\gamma_1(x, t) = \gamma_{o1}(t) e^{-ik_f(x+s^*+2)} \text{ and } \gamma_2(x, t) = \gamma_{o2}(t) e^{-ik_f x}, \quad (\text{C.7})$$

where  $s^* = s/a$ , and with  $\gamma_{oi}(t)$  given by Equation (A.35):

$$\gamma_{oi}(t) = \left\{ -4U \left[ ik_f h_{oi}^* - ik_f \left( \frac{1}{2} - b^* \right) \theta_{oi} - \theta_{oi} \right] / [H_1^{(2)} + iH_0^{(2)}] \right\} e^{i\omega_0 t}. \quad (\text{C.8})$$

The phase difference is  $\phi_t = \arg[\gamma_{o2}] - \arg[\gamma_{o1}]$ . Due to the linearity, the effect of the two wakes on the aft foil can be added. The circulatory lift for the tandem aft foil becomes:

$$L_{C2}^t = \rho U a \left[ \int_1^\infty \frac{\xi}{(\xi^2 - 1)^{1/2}} \gamma_2(a\xi - Ut) d\xi + \int_{-(s^*+1)}^\infty \frac{\xi}{(\xi^2 - 1)^{1/2}} \gamma_1(a\xi - Ut) d\xi \right]. \quad (\text{C.9})$$

The second term of this equation can be decomposed in two parts:

$$L_{C2}^t = \rho U a \left[ \int_1^\infty \frac{\xi \gamma_2(a\xi - Ut)}{(\xi^2 - 1)^{1/2}} d\xi + \int_1^\infty \frac{\xi \gamma_1(a\xi - Ut)}{(\xi^2 - 1)^{1/2}} d\xi + \int_{-(s^*+1)}^1 \frac{\xi \gamma_1(a\xi - Ut)}{(\xi^2 - 1)^{1/2}} d\xi \right]. \quad (\text{C.10})$$

This equation can be simplified in the following way:

$$L_{C2}^t = L_{C2}^s + \left[ L_{C1}^s + \rho U a \gamma_{o1} \int_{-(s^*+1)}^1 \frac{\xi e^{-ik_f \xi}}{(\xi^2 - 1)^{1/2}} d\xi e^{i\omega_0 t} \right] e^{-ik_f(s^*+2)}, \quad (\text{C.11})$$

where the upper  $t$  denotes tandem and  $s$  single foil. The physical interpretation of this expression is that if the inter-foil distance is  $s^* = -2$  so the two wakes coincide, the second term in the brackets vanishes and the aft foil circulatory lift will be simply the sum of the two

single foils circulatory lifts. If the distance tends to infinity the second term in brackets will cancel the first term, leaving only the circulatory lift of the single second foil. The integral in Equation (C.11) is not convergent due to its oscillatory nature. One technique for avoiding this difficulty is to assume that the forward foil wake is symmetrical around aft foil mid-chord, so it cancels itself between aft foil leading and trailing edges. It allows Equation (C.11) to be rewritten, with  $s^* > 0$ , as:

$$L_{C2}^t = L_{C2}^s + \left[ L_{C1}^s + \rho U a \gamma_{o1} \int_{-(s^*+1)}^{-1} \frac{\xi e^{-ik_f \xi}}{(\xi^2 - 1)^{1/2}} d\xi e^{i\omega_0 t} \right] e^{-ik_f(s^*+2)}. \quad (C.12)$$

Rewriting the integral by integrating in  $k_f$  and using:

$$L_{C2}^t = L_{C2}^s + L_{C1}^s \left[ 1 - \frac{E(k_f, s^*)}{C(k_f)} \right] e^{-ik_f(s^*+2)}, \quad (C.13)$$

where  $C(k_f)$  is the Theodorsen's function,  $E(k_f, s^*)$  is given by:

$$E(k_f, s^*) = \frac{2/\pi}{H_1^{(2)} + iH_0^{(2)}} i \frac{d}{dk_f} \int_{-(s^*+1)}^{-1} \frac{e^{-ik_f \xi}}{(\xi^2 - 1)^{1/2}} d\xi. \quad (C.14)$$

Because  $L_{C1}^s$  translates the effect of fore on the aft foil, its reference is the vortex advection velocity thus is related with the single foil by  $L_{C1}^s = r_{va}^2 L_C^s$ . From Eqs (A.28) and (A.29) we have

$$\int_1^\infty \frac{e^{-ik_f \xi}}{(\xi^2 - 1)^{1/2}} d\xi = -\frac{\pi}{2} i H_0^{(2)}(k_f), \quad (C.15)$$

and if  $k_f$  is not small (Paknys, 2016, Eq. C.15):

$$\frac{d}{dk_f} H_0^{(2)}(k_f) = i H_0^{(2)}(k_f) + O(k_f^{-3/2}). \quad (C.16)$$

Assuming also that if inter-foil distance  $s^*$  is not small, Equation (C.14) can be approximated by:

$$E(k_f, s^*) \approx -\frac{2/\pi}{H_1^{(2)} + iH_0^{(2)}} \left[ \int_{-(s^*+1)}^{-1} \frac{e^{-ik_f \xi}}{(\xi^2 - 1)^{1/2}} d\xi + E_0 k_f^{-3/2} \right]. \quad (C.17)$$

By solving the equation  $E(k_f, s^* \rightarrow \infty) = C(k_f)$  numerically the following expression was obtained

$$E(k_f, s^*) \approx -\frac{2/\pi}{H_1^{(2)} + iH_0^{(2)}} \left[ \int_{-(s^*+1)}^{-1} \frac{e^{-ik_f \xi}}{(\xi^2 - 1)^{1/2}} d\xi - 2.5538 k_f^{-0.649} \right], \quad (C.18)$$

with errors less than 7% and 3% for  $k_f > 0.05$  and  $k_f > 0.5$  respectively.

Considering heave and pitch amplitudes and heave-pitch phases are set equal in both foils, and their phase difference, and replacing  $U$  by  $V_A = U/\cos \varphi_2$ , Equation (C.13) becomes:

$$L_{C,2}^t = \frac{L_C^s}{\cos^2 \varphi_2} \left\{ 1 + r_{va}^2 \left[ 1 - \frac{E(k_f, s^*)}{C(k_f)} \right] e^{i[\phi_t - k_f(s^*+2)]} \right\}. \quad (C.19)$$



# Appendix D

## Chapter 3 Cases

<b>Single foil</b>						
Hydrofoil	Motion		Other		Observations	
NACA profile	0012	Heave amplitude, $h_0/c$	0.1			Infinite domain
Chord length, $c$	-	Pitch amplitude, $\theta_0$	10°			Small oscillations
Axis position, $b^*$	0	Heave-pitch phase, $\psi$	90°			Frequency study
Advancing speed, $U$	-	Reduced frequency, $Kf$	0-3			<b>Fig. 3.3</b>
Reynolds number, $Re$	-					
NACA profile	0012	Heave amplitude, $h_0/c$	1.0			Infinite domain
Chord length, $c$	0.1 m	Pitch amplitude, $\theta_0$	10-55°			Large oscillations
Span length (equiv.) $s$	1.2 m	Heave-pitch phase, $\psi$	90°			Pitch amplitude study
Axis position, $b^*$	1/3	Strouhal number, $St$	0.2-0.45			Frequency study
Advancing speed, $U$	0.4 m					<b>Fig. 3.4 &amp; 3.5</b>
Reynolds number, $Re$	4e4					
NACA profile	0012	Heave amplitude, $h_0/c$	0.75			Infinite domain
Chord length, $c$	0.1 m	Pitch amplitude, $\theta_0$	23.3°			Large oscillations
Span length (equiv.) $s$	1.2 m	Heave-pitch phase, $\psi$	90°			Time series study
Axis position, $b^*$	1/3	Strouhal number, $St$	0.3			<b>Fig. 3.6</b>
Advancing speed, $U$	0.4 m					
Reynolds number, $Re$	4e4					
NACA profile	0015	Heave amplitude, $h_0/c$	1.9	Submergence, $d/c$	1.286	Large oscillations
Chord length, $c$	7 m	Pitch amplitude, $\theta_0$	35°			Free-surface
Axis position, $b^*$	1/3	Heave-pitch phase, $\psi$	90°			Time series study
Froude number, $F_r$	0.87	Encounter frequency, $\omega_0^2 c/g$	0.25			<b>Fig. 3.11</b>
Reynolds number, $Re$	5e7					
NACA profile	0012	Heave amplitude, $h_0/c$	1.0	Submergence, $d/c$	2.5	Large oscillations
Chord length, $c$	0.1	Pitch amplitude, $\theta_0$	35°	Wave amplitude, $a_0/c$	0.75	Free-surface & waves
Axis position, $b^*$	1/3	Heave-pitch phase, $\psi$	90°	Wave-heave phase $\phi$	0-360°	Wave-heave phase study
Froude number, $F_r$	1.5	Encounter frequency, $\omega_0^2 c/g$	3.55			<b>Fig. 3.12</b>
Reynolds number, $Re$	1.5e5					
NACA profile	0015	Heave amplitude, $h_0/c$	0.6	Submergence, $d/c$	1.286	Average oscillations
Chord length, $c$	7	Pitch amplitude, $\theta_0$	15.7°	Wave amplitude, $a_0/c$	0.143	Free-surface & waves
Axis position, $b^*$	1/3	Feathering parameter, $\chi$	0.43	Wave-heave phase $\phi$	-90°	Time series study
Froude number, $F_r$	0.87	Heave-pitch phase, $\psi$	0-180°			Heave-pitch angle study
Reynolds number, $Re$	5e7	Encounter frequency, $\omega_0^2 c/g$	0.69			<b>Fig. 3.13 &amp; 3.14</b>
NACA profile	0015	Heave amplitude, $h_0/c$	0.6	Submergence, $d/c$	1.71	Average oscillations
Chord length, $c$	7	Feathering parameter, $\chi$	0-1	Wave amplitude, $a_0/c$	0.143	Free-surface & waves
Axis position, $b^*$	1/3	Heave-pitch phase, $\psi$	40°	Wave-heave phase $\phi$	-90°	Pitching amplitude study
Froude number, $F_r$	0.87	Encounter frequency, $\omega_0^2 c/g$	0.69			<b>Fig. 3.15</b>
Reynolds number, $Re$	5e7					
NACA profile	0015	Heave amplitude, $h_0/c$	0.6	Submergence, $d/c$	1.28	Average oscillations
Chord length, $c$	7 m	Feathering parameter, $\chi$	0.2	Wave amplitude, $a_0/c$	0.143	Free-surface & waves
Axis position, $b^*$	1/3	Heave-pitch phase, $\psi$	40°	Wave-heave phase $\phi$	-90°	Advancing speed study
Froude number, $F_r$	0.5-2	Encounter frequency, $\omega_0^2 c/g$	1.5			<b>Fig. 3.16</b>
Reynolds number, $Re$	-					
<b>Tandem foil</b>						
Hydrofoil	Motion		Other		Observations	
NACA profile	0016	Heave amplitude, $h_0/c$	1.0	Foil separation, $s/c$	4	Infinite domain
Chord length, $c$	1 m	Pitch amplitude, $\theta_0$	45°	Foil phase lag, $\phi$	135°	Large oscillations
Axis position, $b^*$	1/4	Heave-pitch phase, $\psi$	90°			Time series study
Advancing speed, $U$	1 m/s	Strouhal number, $St$	0.4			<b>Fig. 3.17</b>
Reynolds number, $Re$	1e4					
NACA profile	0016	Heave amplitude, $h_0/c$	1.0	Foil separation, $s/c$	1-5	Infinite domain
Chord length, $c$	1 m	Pitch amplitude, $\theta_0$	45°	Foil phase lag, $\phi$	0-360°	Large oscillations
Axis position, $b^*$	1/4	Heave-pitch phase, $\psi$	90°			Frequency study
Advancing speed, $U$	1 m/s	Strouhal number, $St$	0.2-0.5			Separation study
Reynolds number, $Re$	1e4					Foil phase lag study
						<b>Fig. 3.18</b>



# Appendix E

## Chapter 5 Cases

2D Single foil						
Hydrofoil		Motion		Other		Observations
NACA profile	0012	Heave amplitude, $h_0/c$	0.25	GridPro grids		<b>Section 5.1.1</b>
Chord length, $c$	1 m	Pitch amplitude, $\theta_0$	28.3°	Number of cells, $N_c$	32k-478k	
Axis position, $b^*$	1/3	Max. angle of attack, $\alpha_o$	15°	N° iter per period, $n_i/T$	833-33.3k	Infinite domain
Advancing speed, $U$	1 m/s	Heave-pitch phase, $\psi$	90°	Hexpress grids		Small oscillations
Reynolds number, $Re$	4e4	Strouhal number, $St$	0.3	Number of cells, $N_c$	53k-771k	Grid study
		Period, $T$	1.667 s	N° iter per period, $n_i/T$	833-16.6k	
NACA profile	0012	Heave amplitude, $h_0/c$	1.0	Number of cells, $N_c$	82k-394k	<b>Section 5.1.2</b>
Chord length, $c$	1 m	Pitch amplitude, $\theta_0$	28.3°	N° iter per period, $n_i/T$	2.1k-4.2k	
Axis position, $b^*$	1/3	Max. angle of attack, $\alpha_o$	15°			Infinite domain
Advancing speed, $U$	1 m/s	Heave-pitch phase, $\psi$	90°			Large oscillations
Reynolds number, $Re$	4e4	Strouhal number, $St$	0.3			V&V study
		Period, $T$	6.667 s			
NACA profile	0012	Heave amplitude, $h_0/c$	1.0	Number of cells, $N_c$	82k-394k	<b>Section 5.1.3</b>
Chord length, $c$	0.1 m	Pitch amplitude, $\theta_0$	35.0°	N° iter per period, $n_i/T$	2.1k-4.2k	
Axis position, $b^*$	1/3	Max. angle of attack, $\alpha_o$	16.5°			Infinite domain
Advancing speed, $U$	0.4m/s	Heave-pitch phase, $\psi$	90°			Large oscillations
Reynolds number, $Re$	4e4	Strouhal number, $St$	0.4			High-performance
		Period, $T$	1.250 s			Forces&Flow study
3D Single foil						
Hydrofoil		Motion		Other		Observations
NACA profile	0012	Heave amplitude, $h_0/c$	1.0	Number of cells, $N_c$	2.85M	<b>Section 5.1.4</b>
Chord length, $c$	1 m	Pitch amplitude, $\theta_0$	28.3°	N° iter per period, $n_i/T$	333	
Axis position, $b^*$	1/3	Max. angle of attack, $\alpha_o$	15°			Infinite domain
Span length, $s$	8 m	Heave-pitch phase, $\psi$	90°			Large oscillations
Advancing speed, $U$	1 m/s	Strouhal number, $St$	0.3			Span effects
Reynolds number, $Re$	4e4	Period, $T$	6.667 s			
2D Tandem foil						
Hydrofoil		Motion		Other		Observations
NACA profile	0012	Heave amplitude, $h_0/c$	1.0	Number of cells, $N_c$	39k-131k	<b>Section 5.2.1</b>
Chord length, $c$	1 m	Pitch amplitude, $\theta_0$	45°	N° iter per period, $n_i/T$	8k-104k	
Axis position, $b^*$	1/3	Max. angle of attack, $\alpha_o$	6.5°	Foil separation, $s^*$	4	Infinite domain
Span length, $s$	8 m	Heave-pitch phase, $\psi$	90°	Foil phase lag, $\phi_i$	270°	Large oscillations
Advancing speed, $U$	1 m/s	Strouhal number, $St$	0.4			Low performance
Reynolds number, $Re$	4e4	Period, $T$	5 s			Tandem study
NACA profile	0012	Heave amplitude, $h_0/c$	1.0	Number of cells, $N_c$	39k-131k	<b>Section 5.2.2</b>
Chord length, $c$	1 m	Pitch amplitude, $\theta_0$	41.5°	N° iter per period, $n_i/T$	8k-104k	
Axis position, $b^*$	1/3	Max. angle of attack, $\alpha_o$	10°	Foil separation, $s^*$	4	Infinite domain
Span length, $s$	8 m	Heave-pitch phase, $\psi$	90°	Foil phase lag, $\phi_i$	180°	Large oscillations
Advancing speed, $U$	1 m/s	Strouhal number, $St$	0.4			High-performance
Reynolds number, $Re$	4e4	Period, $T$	5 s			Tandem study



# Appendix F

## Chapter 6 Cases

2D Single foil						
Hydrofoil		Motion		Other		Observations
NACA profile	0012	Heave amplitude, $h_0/c$	1.0	Submergence, $d/c$	2.5	<b>Section 6.1.1</b>
Chord length, $c$	1 m	Pitch amplitude, $\theta_0$	35°	Number of cells, $N_c$	397k	
Axis position, $b^*$	1/3	Max. angle of attack, $\alpha_0$	15°	N° iter per period, $n_p/T$	4167	Free-surface
Advancing speed, $U$	1 m/s	Heave-pitch phase, $\psi$	90°			Large oscillations
Reynolds number, $Re$	4e4	Strouhal number, $St$	0.3			
Froude number, $Fr$	0.32	Period, $T$	6.67 s			
3D Single foil						
Hydrofoil		Motion		Other		Observations
NACA profile	0012	Heave amplitude, $h_0/c$	1.0	Submergence, $d/c$	1.25	<b>Section 6.1.2</b>
Chord length, $c$	1 m	Pitch amplitude, $\theta_0$	28.3°	Number of cells, $N_c$	3.7M	
Axis position, $b^*$	1/3	Max. angle of attack, $\alpha_0$	15°	N° iter per period, $n_p/T$	333	Free-surface
Span length, $s$	8 m	Heave-pitch phase, $\psi$	90°			Large oscillations
Advancing speed, $U$	1 m/s	Strouhal number, $St$	0.3			
Froude number, $Fr$	0.32	Strouhal number, $St$	0.3			
Reynolds number, $Re$	4e4	Period, $T$	6.667 s			
2D Single foil						
Hydrofoil		Motion		Other		Observations
NACA profile	0012	Heave amplitude, $h_0/c$	0.0	Submergence, $d/c$	2.5	<b>Section 6.1.3</b>
Chord length, $c$	0.1 m	Pitch amplitude, $\theta_0$	0°	Wave amplitude, $a_0/c$	0.75	
Axis position, $b^*$	1/3	Period, $T$	0 s	Wave period, $T_w$	1.51 s	Incident waves
Advancing speed, $U$	0.38m/s			Number of cells, $N_c$	850k	No oscillations
Froude number, $Fr$	0.38			N° iter per period, $n_p/T$	2607	
Reynolds number, $Re$	4e4					
NACA profile	0012	Heave amplitude, $h_0/c$	0.6	Submergence, $d/c$	2.5	<b>Section 6.1.4</b>
Chord length, $c$	0.1 m	Pitch amplitude, $\theta_0$	15.2°	Wave amplitude, $a_0/c$	0.14	
Axis position, $b^*$	1/3	Heave-pitch phase, $\psi$	40°	Wave period, $T_w$	1.13s	Infinite domain
Advancing speed, $U$	0.86m/s	Strouhal number, $St$	0.18	Wave-heave phase $\phi$	-90°	Large oscillations
Froude number, $Fr$	0.87	Period, $T$	0.76 s	Number of cells, $N_c$	850k	De Silva
Reynolds number, $Re$	8.5e3			N° iter per period, $n_p/T$	4298	
2D Tandem foil						
Hydrofoil		Motion		Other		Observations
NACA profile	0012	Heave amplitude, $h_0/c$	1.0	Foil separation, $s/c$	4	<b>Section 6.2.1</b>
Chord length, $c$	1 m	Pitch amplitude, $\theta_0$	41.5°	Foil phase lag, $\phi$	180°	
Axis position, $b^*$	1/3	Max. angle of attack, $\alpha_0$	10°	Submergence, $d/c$	1.25	Free-surface
Advancing speed, $U$	1 m/s	Heave-pitch phase, $\psi$	90°	Number of cells, $N_c$	529k	Large oscillations
Froude number, $Fr$	0.32	Strouhal number, $St$	0.4	N° iter per period, $n_p/T$	8333	Tandem foil
Reynolds number, $Re$	4e4	Period, $T$	5.0 s			Muscutt
NACA profile	0012	Heave amplitude, $h_0/c$	1.0	Foil separation, $s/c$	4	<b>Section 6.2.2</b>
Chord length, $c$	0.1 m	Pitch amplitude, $\theta_0$	35°	Foil phase lag, $\phi$	180°	
Axis position, $b^*$	1/3	Heave-pitch phase, $\psi$	90°	Submergence, $d/c$	2.5	Incident waves
Advancing speed, $U$	0.38m/s	Strouhal number, $St$	0.4	Wave amplitude, $a_0/c$	0.75	Large oscillations
Froude number, $Fr$	0.39	Period, $T$	1.3 s	Wave period, $T_w$	1.51 s	Tandem foil
Reynolds number, $Re$	4e4			Wave-heave phase $\phi$	-90°	
				Number of cells, $N_c$	1.0M	
				N° iter per period, $n_p/T$	2607	



# Appendix G

## Summary of Results

Comparison of the results, for the mean thrust coefficient, of the semi-analytical model (S-A) with those of CFD model, and the latest with published data (CFD, panel method and experimental). For the tandem foil configurations, aft foil normalized values are used.

$\bar{C}_T$			Thesis Models			Published Data			
	Case	Subcase	S-A	CFD	Diff.	CFD	Panel	Exper.	Diff. to CFD
Infinite Domain	Single Foil	Small Oscillations	0.39	0.30	30%			0.31	-3%
		Large Oscillations	0.45	0.43	5%		0.48	0.40	7%
		High-Performance	0.70	0.80	-13%		0.81	0.74	8%
		Span Effects/3D	0.34	0.36	-6%				
	Tandem Foils	Low Performance	0.93	0.19	389%	0.37			-49%
		High-Performance	1.52	1.57	-3%	1.56			1%
Free-Surface	Single Foil	Large Oscillations	0.43	0.44	-2%		0.45		-2%
		Span Effects/3D	0.27	0.26	4%				
	Tandem	High-Performance	1.49	1.54	-3%				
Incident Waves	Single Foil	Large Oscillations	0.31	0.24	29%	0.27			-11%
	Tandem	High-Performance	1.42	1.77	-20%				



# Appendix H

## Supplementary Material

This appendix provides the links to access the videos of the vorticity fields for different test cases:

**Single Foil in Infinite Domain – Section 5.1.3**

<https://youtu.be/P-RJ1VQM02E>

**Single Foil with Free-Surface – Section 6.1.1**

[https://youtu.be/5ewzJK\\_CXeM](https://youtu.be/5ewzJK_CXeM)

**Single Foil in Waves – Section 6.1.4**

<https://youtu.be/0Njo44hs1SY>

**Tandem Foils in Infinite Domain – Section 5.2.2**

<https://youtu.be/ZTqMYDvgUQA>

**Tandem Foils with Free-Surface – Section 6.2.1**

<https://youtu.be/K8d92rmH7rg>

**Tandem Foils in Waves – Section 6.2.2**

<https://youtu.be/-WDiy-aV6ZA>

